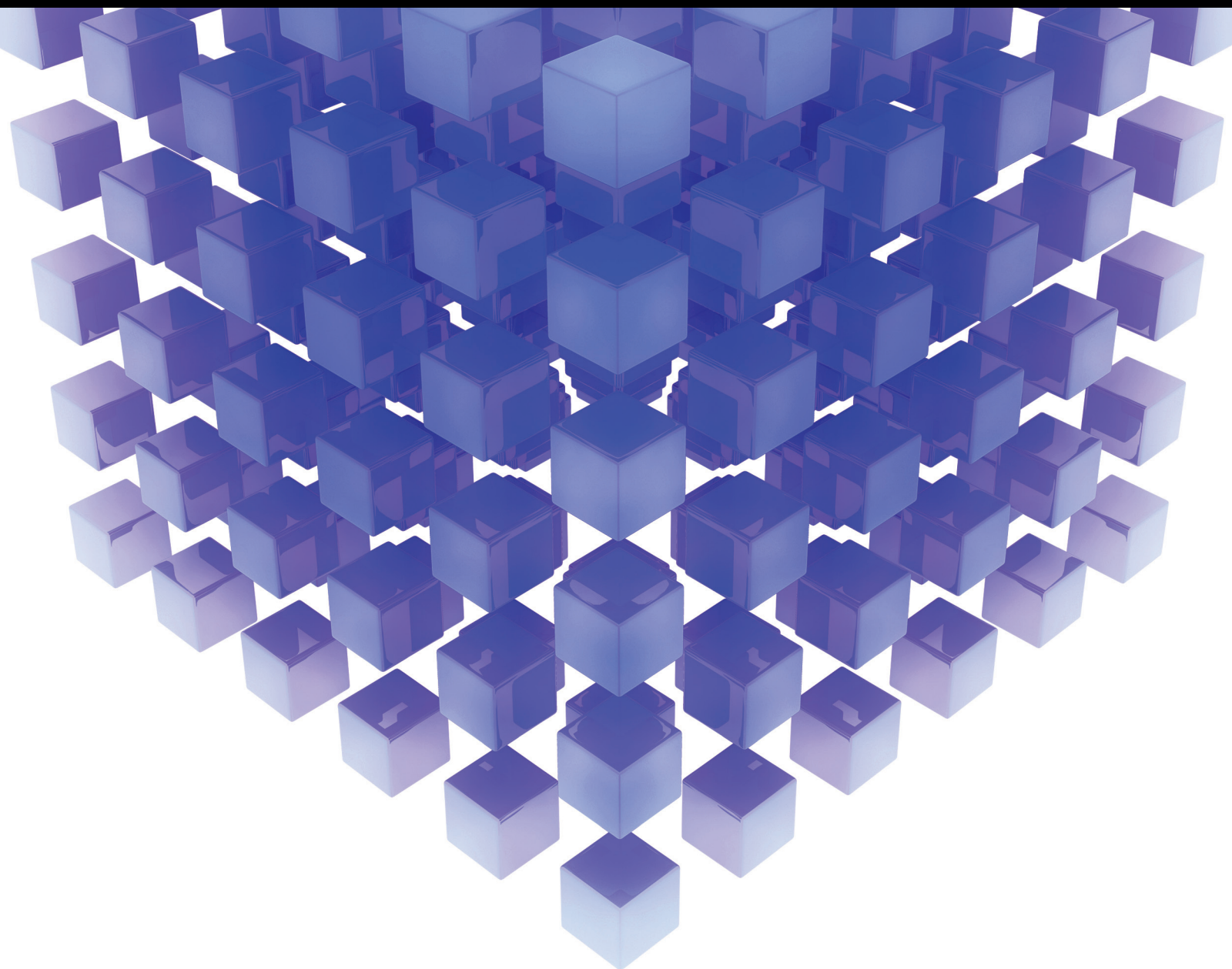


Mathematical Problems in Engineering

Advanced Control Methods for Systems with Fast-Varying Disturbances and Applications

Lead Guest Editor: Ton D. Do

Guest Editors: Hancheol Cho, Hamed J. Asl, and Tran H. Linh





Advanced Control Methods for Systems with Fast-Varying Disturbances and Applications

Mathematical Problems in Engineering

**Advanced Control Methods for Systems with
Fast-Varying Disturbances and Applications**

Lead Guest Editor: Ton D. Do

Guest Editors: Hancheol Cho, Hamed J. Asl, and Tran H. Linh



Copyright © 2018 Hindawi. All rights reserved.

This is a special issue published in “Mathematical Problems in Engineering.” All articles are open access articles distributed under the Creative Commons Attribution License, which permits unrestricted use, distribution, and reproduction in any medium, provided the original work is properly cited.

Editorial Board

- Mohamed Abd El Aziz, Egypt
AITOUCHE Abdelouhab, France
Leonardo Acho, Spain
José A. Acosta, Spain
Paolo Adesso, Italy
Claudia Adduce, Italy
Ramesh Agarwal, USA
Francesco Aggogeri, Italy
Juan C. Agüero, Australia
R Aguilar-López, Mexico
Tarek Ahmed-Ali, France
Elias Aifantis, USA
Muhammad N. Akram, Norway
Guido Ala, Italy
Andrea Alaimo, Italy
Reza Alam, USA
Nicholas Alexander, UK
Salvatore Alfonzetti, Italy
Mohammad D. Aliyu, Canada
Juan A. Almendral, Spain
José Domingo Álvarez, Spain
Cláudio Alves, Portugal
J. P. Amezquita-Sanchez, Mexico
Lionel Amodeo, France
Sebastian Anita, Romania
Renata Archetti, Italy
Felice Arena, Italy
Sabri Arik, Turkey
Francesco Aristodemo, Italy
Fausto Arpino, Italy
Alessandro Arsie, USA
Edoardo Artioli, Italy
Fumihiko Ashida, Japan
Farhad Aslani, Australia
Mohsen Asle Zaem, USA
Romain Aubry, USA
Matteo Aureli, USA
Richard I. Avery, USA
Viktor Avrutin, Germany
Francesco Aymerich, Italy
Sajad Azizi, Belgium
Michele Baccocchi, Italy
Seungik Baek, USA
Adil Bagirov, Australia
Khaled Bahlali, France
Laurent Bako, France
Pedro Balaguer, Spain
Stefan Balint, Romania
Ines Tejado Balsera, Spain
Alfonso Banos, Spain
Jerzy Baranowski, Poland
Roberto Baratti, Italy
Andrzej Bartoszewicz, Poland
David Bassir, France
Chiara Bedon, Italy
Azeddine Beghdadi, France
Denis Benasciutti, Italy
Ivano Benedetti, Italy
Rosa M. Benito, Spain
Elena Benvenuti, Italy
Giovanni Berselli, Italy
Michele Betti, Italy
Jean-Charles Beugnot, France
Pietro Bia, Italy
Carlo Bianca, France
Simone Bianco, Italy
Vincenzo Bianco, Italy
Vittorio Bianco, Italy
Gennaro N. Bifulco, Italy
David Bigaud, France
Antonio Bilotta, Italy
Paul Bogdan, USA
Guido Bolognesi, UK
Rodolfo Bontempo, Italy
Alberto Borboni, Italy
Paolo Boscaroli, Italy
Daniela Boso, Italy
Guillermo Botella-Juan, Spain
Boulaïd Boulkroune, Belgium
Fabio Bovenga, Italy
Francesco Braghin, Italy
Ricardo Branco, Portugal
Maurizio Brocchini, Italy
Julien Bruchon, France
Matteo Bruggi, Italy
Michele Brun, Italy
Vasilis Burganos, Greece
Tito Busani, USA
Raquel Caballero-Águila, Spain
Filippo Cacace, Italy
Pierfrancesco Cacciola, UK
Salvatore Caddemi, Italy
Roberto Caldelli, Italy
Alberto Campagnolo, Italy
Eric Campos-Canton, Mexico
Marko Canadija, Croatia
Salvatore Cannella, Italy
Francesco Cannizzaro, Italy
Javier Cara, Spain
Ana Carpio, Spain
Caterina Casavola, Italy
Sara Casciati, Italy
Federica Caselli, Italy
Carmen Castillo, Spain
Inmaculada T. Castro, Spain
Miguel Castro, Portugal
Giuseppe Catalanotti, UK
Nicola Caterino, Italy
Alberto Cavallo, Italy
Gabriele Cazzulani, Italy
Luis Cea, Spain
Miguel Cerrolaza, Venezuela
M. Chadli, France
Gregory Chagnon, France
Ludovic Chamoin, France
Ching-Ter Chang, Taiwan
Qing Chang, USA
Michael J. Chappell, UK
Kacem Chehdi, France
Peter N. Cheimets, USA
Xinkai Chen, Japan
Luca Chiapponi, Italy
Francisco Chicano, Spain
Nicholas Chileshe, Australia
Adrian Chmielewski, Poland
Ioannis T. Christou, Greece
Hung-Yuan Chung, Taiwan
Simone Cinquemani, Italy
Roberto G. Citarella, Italy
Joaquim Ciurana, Spain
John D. Clayton, USA
Francesco Clementi, Italy

Piero Colajanni, Italy
Giuseppina Colicchio, Italy
Vassilios Constantoudis, Greece
Enrico Conte, Italy
Francesco Conte, Italy
Alessandro Contento, USA
Mario Cools, Belgium
José A. Correia, Portugal
Jean-Pierre Corriou, France
J.-C. Cortés, Spain
Carlo Cosentino, Italy
Paolo Crippa, Italy
Andrea Crivellini, Italy
Frederico R. B. Cruz, Brazil
Erik Cuevas, Mexico
Maria C. Cunha, Portugal
Peter Dabnichki, Australia
Luca D'Acierno, Italy
Weizhong Dai, USA
Andrea Dall'Asta, Italy
Purushothaman Damodaran, USA
Farhang Daneshmand, Canada
Giuseppe D'Aniello, Italy
Sergey N. Dashkovskiy, Germany
Fabio De Angelis, Italy
Samuele De Bartolo, Italy
Pietro De Lellis, Italy
Luciano R. O. de Lima, Brazil
Alessandro De Luca, Italy
Stefano de Miranda, Italy
Filippo de Monte, Italy
Maria do Rosário de Pinho, Portugal
Michael Defoort, France
Alessandro Della Corte, Italy
Xavier Delorme, France
Laurent Dewasme, Belgium
Angelo Di Egidio, Italy
Roberta Di Pace, Italy
Ramón I. Diego, Spain
Yannis Dimakopoulos, Greece
Zhengtao Ding, UK
M. Djemai, France
Alexandre B. Dolgui, France
Georgios Dounias, Greece
Florent Duchaine, France
George S. Dulikravich, USA
Bogdan Dumitrescu, Romania
Horst Ecker, Austria
Saeed Eftekhari Azam, USA
Ahmed El Hajjaji, France
Antonio Elipe, Spain
Fouad Erchiqui, Canada
Anders Eriksson, Sweden
R. Emre Erkmen, Australia
Gilberto Espinosa-Paredes, Italy
Andrea L. Facci, Italy
Giacomo Falcucci, Italy
Giovanni Falsone, Italy
Hua Fan, China
Nicholas Fantuzzi, Italy
Yann Favennec, France
Fiorenzo A. Fazzolari, UK
Giuseppe Fedele, Italy
Roberto Fedele, Italy
Arturo J. Fernández, Spain
Jesus M. Fernandez Oro, Spain
Massimiliano Ferrara, Italy
Francesco Ferrise, Italy
Eric Feulvarch, France
Barak Fishbain, Israel
S. Douwe Flapper, Netherlands
Thierry Floquet, France
Eric Florentin, France
Alessandro Formisano, Italy
Francesco Franco, Italy
Elisa Francomano, Italy
Tomonari Furukawa, USA
Juan C. G. Prada, Spain
Mohamed Gadala, Canada
Matteo Gaeta, Italy
Mauro Gaggero, Italy
Zoran Gajic, USA
Erez Gal, Israel
Jaime Gallardo-Alvarado, Mexico
Ugo Galvanetto, Italy
Akemi Gálvez, Spain
Rita Gamberini, Italy
Maria L. Gandarias, Spain
Arman Ganji, Canada
Zhiwei Gao, UK
Zhong-Ke Gao, China
Giovanni Garcea, Italy
Luis Rodolfo Garcia Carrillo, USA
Jose M. Garcia-Aznar, Spain
Akhil Garg, China
Alessandro Gasparetto, Italy
Oleg V. Gendelman, Israel
Stylianos Georgantzinos, Greece
Fotios Georgiades, UK
Mergen H. Ghayesh, Australia
Georgios I. Giannopoulos, Greece
Agathoklis Giaralis, UK
Pablo Gil, Spain
Anna M. Gil-Lafuente, Spain
Ivan Giorgio, Italy
Gaetano Giunta, Luxembourg
Alessio Gizzi, Italy
Jefferson L.M.A. Gomes, UK
Emilio Gómez-Déniz, Spain
Antonio M. Gonçalves de Lima, Brazil
David González, Spain
Chris Goodrich, USA
Rama S. R. Gorla, USA
Nicolas Gourdain, France
Kannan Govindan, Denmark
Antoine Grall, France
George A. Gravvanis, Greece
Fabrizio Greco, Italy
Simonetta Grilli, Italy
Jason Gu, Canada
Federico Guarracino, Italy
Michele Guida, Italy
José L. Guzmán, Spain
Quang Phuc Ha, Australia
Petr Hájek, Czech Republic
Zhen-Lai Han, China
Thomas Hanne, Switzerland
Mohammad A. Hariri-Ardebili, USA
Xiao-Qiao He, China
Sebastian Heidenreich, Germany
Luca Heltai, Italy
Alfredo G. Hernández-Díaz, Spain
M.I. Herreros, Spain
Eckhard Hitzer, Japan
Paul Honeine, France
Jaromir Horacek, Czech Republic
Muneo Hori, Japan
András Horváth, Italy
S. Hassan Hosseinnia, Netherlands
Mengqi Hu, USA
Gordon Huang, Canada

Sajid Hussain, Canada
 Asier Ibeas, Spain
 Orest V. Iftime, Netherlands
 Przemyslaw Ignaciuk, Poland
 Giacomo Innocenti, Italy
 Emilio Insfran Pelozo, Spain
 Alessio Ishizaka, UK
 Nazrul Islam, USA
 Benoit Jung, France
 Benjamin Ivorra, Spain
 Payman Jalali, Finland
 Mahdi Jalili, Australia
 Łukasz Jankowski, Poland
 Samuel N. Jator, USA
 Juan C. Jauregui-Correa, Mexico
 Reza Jazar, Australia
 Khalide Jbilou, France
 Piotr Jędrzejowicz, Poland
 Isabel S. Jesus, Portugal
 Linni Jian, China
 Bin Jiang, China
 Zhongping Jiang, USA
 Emilio Jiménez Macías, Spain
 Ningde Jin, China
 Xiaoliang Jin, USA
 Liang Jing, Canada
 Dylan F. Jones, UK
 Palle E. Jorgensen, USA
 Vyacheslav Kalashnikov, Mexico
 Tamas Kalmar-Nagy, Hungary
 Tomasz Kapitaniak, Poland
 Julius Kaplunov, UK
 Haranath Kar, India
 Konstantinos Karamanos, Belgium
 Krzysztof Kecik, Poland
 Jean-Pierre Kenne, Canada
 Chaudry M. Khalique, South Africa
 Do Wan Kim, Republic of Korea
 Nam-Il Kim, Republic of Korea
 Jan Koci, Czech Republic
 Ioannis Kostavelis, Greece
 Sotiris B. Kotsiantis, Greece
 Manfred Krafczyk, Germany
 Frederic Kratz, France
 Petr Krysl, USA
 Krzysztof S. Kulpa, Poland
 Shailesh I. Kundalwal, India
 Jurgen Kurths, Germany
 Kyandoghere Kyamakya, Austria
 Davide La Torre, Italy
 Risto Lahdelma, Finland
 Hak-Keung Lam, UK
 Giovanni Lancioni, Italy
 Jimmy Lauber, France
 Antonino Laudani, Italy
 Hervé Laurent, France
 Aimé Lay-Ekuakille, Italy
 Nicolas J. Leconte, France
 Dimitri Lefebvre, France
 Eric Lefevre, France
 Marek Lefik, Poland
 Yaguo Lei, China
 Kauko Leiviskä, Finland
 Thibault Lemaire, France
 Roman Lewandowski, Poland
 Chen-Feng Li, China
 Jian Li, China
 En-Qiang Lin, USA
 Zhiyun Lin, China
 Peide Liu, China
 Peter Liu, Taiwan
 Wanquan Liu, Australia
 Bonifacio Llamazares, Spain
 Alessandro Lo Schiavo, Italy
 Jean Jacques Loiseau, France
 Francesco Lolli, Italy
 Paolo Lonetti, Italy
 Sandro Longo, Italy
 Sebastian López, Spain
 Pablo Lopez-Crespo, Spain
 Luis M. López-Ochoa, Spain
 Ezequiel López-Rubio, Spain
 Vassilios C. Loukopoulos, Greece
 Jose A. Lozano-Galant, Spain
 Helen Lu, Australia
 Gabriel Luque, Spain
 Valentin Lychagin, Norway
 Antonio Madeo, Italy
 José María Maestre, Spain
 Alessandro Magnani, Italy
 Fazal M. Mahomed, South Africa
 Noureddine Manamanni, France
 Paolo Manfredi, Italy
 Didier Maquin, France
 Giuseppe Carlo Marano, Italy
 Damijan Markovic, France
 Francesco Marotti de Sciarra, Italy
 Rui Cunha Marques, Portugal
 Luis Martínez, Spain
 Rodrigo Martinez-Bejar, Spain
 Guiomar Martín-Herrán, Spain
 Denizar Cruz Martins, Brazil
 Benoit Marx, France
 Elio Masciari, Italy
 Franck Massa, France
 Paolo Massioni, France
 Alessandro Mauro, Italy
 Fabio Mazza, Italy
 Laura Mazzola, Italy
 Driss Mehdi, France
 Roderick Melnik, Canada
 Pasquale Memmolo, Italy
 Xiangyu Meng, USA
 Jose Merodio, Spain
 Alessio Merola, Italy
 Mahmoud Mesbah, Iran
 Luciano Mescia, Italy
 Laurent Mevel, France
 Mariusz Michta, Poland
 Leandro F. F. MIGUEL, Brazil
 Aki Mikkola, Finland
 Giovanni Minafò, Italy
 Hiroyuki Mino, Japan
 Pablo Mira, Spain
 Dimitrios Mitsotakis, New Zealand
 Vito Mocella, Italy
 Sara Montagna, Italy
 Roberto Montanini, Italy
 Francisco J. Montáns, Spain
 Luiz H. A. Monteiro, Brazil
 Gisele Mophou, France
 Rafael Morales, Spain
 Marco Morandini, Italy
 Javier Moreno-Valenzuela, Mexico
 Simone Morganti, Italy
 Caroline Mota, Brazil
 Aziz Moukrim, France
 Dimitris Mourtzis, Greece
 Emiliano Mucchi, Italy
 Josefa Mula, Spain
 Jose J. Muñoz, Spain

Giuseppe Muscolino, Italy
Marco Mussetta, Italy
Hakim Naceur, France
Alessandro Naddeo, Italy
Hassane Naji, France
Mariko Nakano-Miyatake, Mexico
Keivan Navaie, UK
AMA Neves, Portugal
Luís C. Neves, UK
Dong Ngoduy, New Zealand
Nhon Nguyen-Thanh, Singapore
Tatsushi Nishi, Japan
Xesús Nogueira, Spain
Ben T. Nohara, Japan
Mohammed Nouari, France
Mustapha Nourelfath, Canada
Włodzimierz Ogryczak, Poland
Roger Ohayon, France
Krzysztof Okarma, Poland
Mitsuhiro Okayasu, Japan
Alberto Olivares, Spain
Enrique Onieva, Spain
Calogero Orlando, Italy
Alejandro Ortega-Moñux, Spain
Sergio Ortobelli, Italy
Naohisa Otsuka, Japan
Erika Ottaviano, Italy
Pawel Packo, Poland
Arturo Pagano, Italy
Alkis S. Paipetis, Greece
Roberto Palma, Spain
Alessandro Palmeri, UK
Pasquale Palumbo, Italy
Jürgen Pannek, Germany
Elena Panteley, France
Achille Paolone, Italy
George A. Papakostas, Greece
Xosé M. Pardo, Spain
Vicente Parra-Vega, Mexico
Manuel Pastor, Spain
Petr Páta, Czech Republic
Pubudu N. Pathirana, Australia
Surajit Kumar Paul, India
Sitek Paweł, Poland
Luis Payá, Spain
Alexander Paz, USA
Igor Pažanin, Croatia
Libor Pekař, Czech Republic
Francesco Pellicano, Italy
Marcello Pellicciari, Italy
Haipeng Peng, China
Mingshu Peng, China
Zhengbiao Peng, Australia
Zhi-ke Peng, China
Marzio Pennisi, Italy
Maria Patrizia Pera, Italy
Matjaz Perc, Slovenia
A. M. Bastos Pereira, Portugal
Ricardo Perera, Spain
Francesco Pesavento, Italy
Ivo Petras, Slovakia
Francesco Petrini, Italy
Lukasz Pieczonka, Poland
Dario Piga, Switzerland
Paulo M. Pimenta, Brazil
Antonina Pirrotta, Italy
Marco Pizzarelli, Italy
Vicent Pla, Spain
Javier Plaza, Spain
Dragan Poljak, Croatia
Jorge Pomares, Spain
Sébastien Poncet, Canada
Volodymyr Ponomaryov, Mexico
Jean-Christophe Ponsart, France
Mauro Pontani, Italy
Cornelio Posadas-Castillo, Mexico
Francesc Pozo, Spain
Christopher Pretty, New Zealand
Luca Pugi, Italy
Krzysztof Puszynski, Poland
Giuseppe Quaranta, Italy
Vitomir Racic, Italy
Jose Ragot, France
Carlo Rainieri, Italy
K. Ramamani Rajagopal, USA
Ali Ramazani, USA
Higinio Ramos, Spain
Alain Rassineux, France
S.S. Ravindran, USA
Alessandro Reali, Italy
Jose A. Reinoso, Spain
Oscar Reinoso, Spain
Fabrizio Renno, Italy
Nidhal Rezg, France
Ricardo Riaza, Spain
Francesco Riganti-Fulginei, Italy
Gerasimos Rigatos, Greece
Francesco Ripamonti, Italy
Jorge Rivera, Mexico
Eugenio Roanes-Lozano, Spain
Bruno G. M. Robert, France
Ana Maria A. C. Rocha, Portugal
José Rodellar, Spain
Luigi Rodino, Italy
Rosana Rodríguez López, Spain
Ignacio Rojas, Spain
Alessandra Romolo, Italy
Debasish Roy, India
Gianluigi Rozza, Italy
Rubén Ruiz, Spain
Antonio Ruiz-Cortes, Spain
Ivan D. Rukhlenko, Australia
Mazen Saad, France
Kishin Sadarangani, Spain
Andrés Sáez, Spain
Mehrddad Saif, Canada
John S. Sakellariou, Greece
Salvatore Salamone, USA
Vicente Salas, Spain
Jose V. Salcedo, Spain
Nunzio Salerno, Italy
Miguel A. Salido, Spain
Roque J. Saltarén, Spain
Alessandro Salvini, Italy
Sylwester Samborski, Poland
Ramon Sancibrian, Spain
Giuseppe Sanfilippo, Italy
Miguel A. F. Sanjuan, Spain
Vittorio Sansalone, France
José A. Sanz-Herrera, Spain
Nickolas S. Sapidis, Greece
Evangelos J. Sapountzakis, Greece
Luis Saucedo-Mora, Spain
Marcelo A. Savi, Brazil
Andrey V. Savkin, Australia
Roberta Sburlati, Italy
Gustavo Scaglia, Argentina
Thomas Schuster, Germany
Oliver Schütze, Mexico
Lotfi Senhadji, France
Junwon Seo, USA

Joan Serra-Sagrsta, Spain
Gerardo Severino, Italy
Ruben Sevilla, UK
Stefano Sfarra, Italy
Mohamed Shaat, Egypt
Mostafa S. Shadloo, France
Leonid Shaikhet, Israel
Hassan M. Shanechi, USA
Bo Shen, Germany
Suzanne M. Shontz, USA
Babak Shotorban, USA
Zhan Shu, UK
Nuno Simões, Portugal
Christos H. Skiadas, Greece
Konstantina Skouri, Greece
Neale R. Smith, Mexico
Bogdan Smolka, Poland
Delfim Soares Jr., Brazil
Alba Sofi, Italy
Giovanni Solari, Italy
Francesco Soldovieri, Italy
Raffaele Solimene, Italy
Jussi Sopanen, Finland
Marco Spadini, Italy
Bernardo Spagnolo, Italy
Paolo Spagnolo, Italy
Ruben Specogna, Italy
Vasilios Spitas, Greece
Sri Sridharan, USA
Ivanka Stamova, USA
Rafał Stanisławski, Poland
Florin Stoican, Romania
Salvatore Strano, Italy
Yakov Strelniker, Israel
Guang-Yong Sun, China
Sergey A. Suslov, Australia
Thomas Svensson, Sweden
Andrzej Swierniak, Poland
Andras Szekrenyes, Hungary
Kumar K. Tamma, USA
Yang Tang, Germany
Hafez Tari, USA
Alessandro Tasora, Italy
Sergio Teggi, Italy
Ana C. Teodoro, Portugal

Tai Thai, Australia
Alexander Timokha, Norway
Gisella Tomasini, Italy
Francesco Tornabene, Italy
Antonio Tornambe, Italy
Javier Martinez Torres, Spain
Mariano Torrisi, Italy
George Tsiatas, Greece
Antonios Tsourdos, UK
Federica Tubino, Italy
Nerio Tullini, Italy
Andrea Tundis, Italy
Emilio Turco, Italy
Vladimir Turetsky, Israel
Mustafa Tutar, Spain
Ilhan Tuzcu, USA
Efstratios Tzirtzilakis, Greece
Filippo Ubertini, Italy
Francesco Ubertini, Italy
Mohammad Uddin, Australia
Hassan Ugail, UK
Giuseppe Vairo, Italy
Eusebio Valero, Spain
Pandian Vasant, Malaysia
Marcello Vasta, Italy
Carlos-Renato Vázquez, Mexico
Miguel E. Vázquez-Méndez, Spain
Josep Vehi, Spain
Martin Velasco Villa, Mexico
K. C. Veluvolu, Republic of Korea
Fons J. Verbeek, Netherlands
Franck J. Vernerey, USA
Georgios Veronis, USA
Vincenzo Vespri, Italy
Renato Vidoni, Italy
V. Vijayaraghavan, Australia
Anna Vila, Spain
Rafael J. Villanueva, Spain
Francisco R. Villatoro, Spain
Uchechukwu E. Vincent, UK
Gareth A. Vio, Australia
Francesca Vipiana, Italy
Stanislav Vítek, Czech Republic
Thuc P. Vo, UK
Jan Vorel, Czech Republic

Michael Vynnycky, Sweden
Hao Wang, USA
Liliang Wang, UK
Shuming Wang, China
Yongqi Wang, Germany
Roman Wan-Wendner, Austria
Jaroslaw Wąs, Poland
P.H. Wen, UK
Waldemar T. Wójcik, Poland
Changzhi Wu, Australia
Desheng D. Wu, Sweden
Hong-Yu Wu, USA
Yuqiang Wu, China
Michalis Xenos, Greece
Guangming Xie, China
Xue-Jun Xie, China
Gen Q. Xu, China
Hang Xu, China
Joseph J. Yame, France
Xinggang Yan, UK
Mijia Yang, USA
Yongheng Yang, Denmark
Luis J. Yebra, Spain
Peng-Yeng Yin, Taiwan
Qin Yuming, China
Elena Zaitseva, Slovakia
Arkadiusz Żak, Poland
Daniel Zaldivar, Mexico
Francesco Zammori, Italy
Vittorio Zampoli, Italy
Rafał Zdunek, Poland
Ibrahim Zeid, USA
Huaguang Zhang, China
Kai Zhang, China
Qingling Zhang, China
Xian-Ming Zhang, Australia
Xuping Zhang, Denmark
Zhao Zhang, China
Yifan Zhao, UK
Jian G. Zhou, UK
Quanxin Zhu, China
Mustapha Zidi, France
Gaetano Zizzo, Italy

Contents

Advanced Control Methods for Systems with Fast-Varying Disturbances and Applications

Ton Duc Do , Hancheol Cho, Hamed Jabbari Asl, and Tran Hoai Linh
Editorial (1 page), Article ID 7219513, Volume 2018 (2018)

Enhanced Nonlinear Robust Control for TCSC in Power System

Chao Zhang , Xing Wang, Zhengfeng Ming , and Zhuang Cai
Research Article (11 pages), Article ID 1416059, Volume 2018 (2018)

An Order Effect of Neighborhood Structures in Variable Neighborhood Search Algorithm for Minimizing the Makespan in an Identical Parallel Machine Scheduling

Ibrahim Alharkan, Khaled Bamatraf, Mohammed A. Noman , Husam Kaid , Emad S. Abouel Nasr, and Abdulaziz M. El-Tamimi
Research Article (8 pages), Article ID 3586731, Volume 2018 (2018)

A New Hybrid PSS Optimization Method Based on Improved Active Set Algorithm

Xiang-Yu Liu, Yu-Ling He , and Jian Yao
Research Article (9 pages), Article ID 4348257, Volume 2018 (2018)

The Research on Second-Order ADRC Algorithm of Using Wind Turbine Virtual Inertia to Participate in Primary Frequency Regulation in a Small Stand-Alone Microgrid

Wang Yi , Jiang Hanhong, and Xing Pengxiang
Research Article (13 pages), Article ID 4752728, Volume 2018 (2018)

Asynchronous Communication under Reliable and Unreliable Network Topologies in Distributed Multiagent Systems: A Robust Technique for Computing Average Consensus

Ali Mustafa , Muhammad Najam ul Islam, Salman Ahmed, and Muhammad Ahsan Tufail
Research Article (13 pages), Article ID 4635701, Volume 2018 (2018)

Lateral Stability Control of Four-Wheel Independent Drive Electric Vehicles Based on Model Predictive Control

Bin Huang , Sen Wu, Song Huang, and Xiang Fu 
Research Article (15 pages), Article ID 6080763, Volume 2018 (2018)

Parameter Identification and Hybrid Synchronization in an Array of Coupled Chaotic Systems with Ring Connection: An Adaptive Integral Sliding Mode Approach

Nazam Siddique  and Fazal ur Rehman 
Research Article (15 pages), Article ID 6581493, Volume 2018 (2018)

Fixed-Time Stability of the Hydraulic Turbine Governing System

Caoyuan Ma, Chuangzhen Liu , Xuezi Zhang, Yongzheng Sun , Wenbei Wu , and Jin Xie
Research Article (10 pages), Article ID 1352725, Volume 2018 (2018)

Adaptive Backstepping Based MTPA Sensorless Control of PM-Assisted SynRM with Fully Uncertain Parameters

Yang Yu , Da Chang, Xiaoming Zheng, Zengqiang Mi, Xiaolong Li, and Chenjun Sun
Research Article (14 pages), Article ID 8405847, Volume 2018 (2018)



Time-Varying Noise Statistic Estimator Based Adaptive Simplex Cubature Kalman Filter

Zhaoming Li, Wenge Yang, and Dan Ding

Research Article (8 pages), Article ID 5349879, Volume 2017 (2018)

Editorial

Advanced Control Methods for Systems with Fast-Varying Disturbances and Applications

Ton Duc Do ¹, **Hancheol Cho**,² **Hamed Jabbari Asl**,³ and **Tran Hoai Linh**⁴

¹*Nazarbayev University, Astana, Kazakhstan*

²*University of Liège, Belgium*

³*Toyota Technological Institute, Japan*

⁴*Hanoi University of Science and Technology, Vietnam*

Correspondence should be addressed to Ton Duc Do; doduc.ton@nu.edu.kz

Received 22 May 2018; Accepted 22 May 2018; Published 10 June 2018

Copyright © 2018 Ton Duc Do et al. This is an open access article distributed under the Creative Commons Attribution License, which permits unrestricted use, distribution, and reproduction in any medium, provided the original work is properly cited.

In most real applications, disturbances and uncertainties, which affect stability and performance of the controlled system, are unavoidable. Unfortunately, disturbances are not measurable or too expensive to measure. A typical approach is first to estimate the disturbances and then design an advanced control law based on this estimation. Although this approach has attracted much attention of numerous researchers in various fields of study, most estimation techniques rely on the assumption that the disturbance is slowly varying or its time derivative is zero. Note that the disturbances do not arise only from external environments; uncertainties such as modelling errors and parameter perturbations can also be considered as disturbances. Also, for the objects with unknown components and noises, a good approach is to use the system with learning capability to adapt its parameters to the samples measured from the given objects.

From 36 submissions, 10 papers are accepted for publication in this special issue. Each paper was reviewed by at least one reviewer and revised according to review comments. The papers cover the following topics: time-varying noise estimation, search algorithm for minimizing the makespan, robust control for thyristor controlled series compensator (TCSC), robust technique for computing average consensus, sensorless control of uncertain PM-assisted SynRM, wind turbine frequency control in microgrid, optimization of power system stabilizer (PSS), adaptive sliding mode control (SMC) for hybrid synchronization of chaotic systems, model

predictive control (MPC) for electric vehicles, and control of hydraulic turbine governing system.

*Ton Duc Do
Hancheol Cho
Hamed Jabbari Asl
Tran Hoai Linh*

Research Article

Enhanced Nonlinear Robust Control for TCSC in Power System

Chao Zhang ¹, Xing Wang,¹ Zhengfeng Ming ¹ and Zhuang Cai²

¹*School of Mechano-Electronic Engineering, Xidian University, Xi'an 710071, China*

²*Shaanxi Electronic Information Group, Xi'an 710071, China*

Correspondence should be addressed to Zhengfeng Ming; zfmiming@xidian.edu.cn

Received 9 September 2017; Revised 6 February 2018; Accepted 15 March 2018; Published 6 May 2018

Academic Editor: Tran H. Linh

Copyright © 2018 Chao Zhang et al. This is an open access article distributed under the Creative Commons Attribution License, which permits unrestricted use, distribution, and reproduction in any medium, provided the original work is properly cited.

This paper proposes an enhanced robust control method, which is for thyristor controlled series compensator (TCSC) in presences of time-delay nonlinearity, uncertain parameter, and external disturbances. Unlike conventional adaptive control methods, the uncertain parameter is estimated by using system immersion and manifold invariant (I&I) adaptive control. Thus, the oscillation of states caused by the coupling between parameter estimator and system states can be avoided. In addition, in order to overcome the influences of time-delay nonlinearity and external disturbances, backstepping sliding mode control is adopted to design control law recursively. Furthermore, robustness of TCSC control subsystem is achievable provided that dissipation inequality is satisfied in each step. Effectiveness and efficiencies of the proposed control method are verified by simulations. Compared with adaptive backstepping sliding mode control and adaptive backstepping control, the time of reaching steady state is shortened by at least 11% and the oscillation amplitudes of transient responses are reduced by at most 50%.

1. Introduction

In modern electrical power industry, security and stability of power system are under constant threat due to increasing power grid capacity, high-voltage transmission lines, and highly complex network configuration. Thyristor controlled series compensator (TCSC) system is often used to improve the stability and transfer capability of power system by scheduling power flow, decreasing voltage asymmetry and net loss, providing voltage support, and damping power oscillation [1–3]. However, some problems generally exist in TCSC system. TCSC shows the characteristics of time-delay nonlinearity due to the time-delay between triggering time and turn-on time of its thyristor controller [4, 5]. As uncertain parameter, damping coefficient is difficult to measure accurately in practice; external disturbances can be mainly caused by interference on generator rotor windings and the fluctuation on susceptance. These problems often deteriorate the performance and increase the difficulty in the design of TCSC robust controller significantly.

The proportional-integral-derivative (PID) control is commonly used to control nonlinear systems based on feedback linearization [6, 7]. PID was applied for TCSC

controller design by assuming that accurate system models are available [8]. However, feedback linearization not only linearizes the useful nonlinearities but also requires an accurate model which is difficult to obtain. Therefore, when the operating conditions of the system fluctuate widely, the transient stability of the TCSC system cannot be guaranteed if models are not obtained precisely.

Recently, adaptive backstepping is an optional method to mitigate the effects of nonlinearities and external disturbances on the system performance without linearization [9, 10]. The core concept of the adaptive backstepping is to design a controller recursively by considering some of the state variables as “virtual controls” and designing intermediate control laws for these variables [11–14]. Some TCSC control methods are proposed on the basis of adaptive backstepping [15, 16]. Nonetheless, this method is flawed with certain shortcomings. The transient stability of a closed-loop system cannot be guaranteed when the parameter estimator is fixed to its limit value and the system running time approaches infinity [17]. In other words, if the estimator is fixed, the estimation error will be accumulated in constructing control Lyapunov function (CLF) and the coupling terms between states and estimation error will be also accumulated as

running time increase. Thus, the transient stability of the close-loop system cannot be guaranteed.

To avoid this oscillation, a new method named system immersion and manifold invariant (I&I) adaptive control can provide a mean of shaping the dynamic response of the estimation error even if estimators reach the limit of its capacity [18, 19]. Unlike conventional adaptive control schemes relying on certainty equivalence principle, I&I adaptive control provides an alternative approach which avoids the cancellation of terms in the derivative of the Lyapunov function [20]. This method was used for SVC of a SMIB system to enhance the stability and improve the transient response [14]. However, I&I adaptive control has not been adopted in estimation of uncertain parameter in nonlinear systems with time-delay nonlinearity and external disturbances.

Sliding mode control can combine with backstepping to design the control law of nonlinear TCSC system, which is insensitive to nonlinearity and external disturbances with matching condition [21–23]. There are two processes in sliding mode motion: making the orbit approach sliding mode and keeping the orbit in sliding mode surface. As the orbit in sliding mode is achieved, the robustness of control system can be guaranteed on account of the advantage of sliding mode control which is insensitive to parameter perturbation and external disturbances, whereas the robustness of control system cannot be guaranteed before the motion orbit reach to sliding mode surface. By combining the advantages of both robust control and sliding control, robust sliding control method was developed to address this problem and achieve good performance in [24, 25]. However, the robust sliding mode control has not been adopted for nonlinear TCSC system when time-delay is involved.

In this paper, an enhanced robust control method is proposed to improve stability and robustness of TCSC system by simultaneously addressing the problems involving the existing nonlinear time-delay, uncertain parameter, and external disturbances. This proposed controller consists of the design of adaptive law and control law. As for adaptive law, the I&I adaptive control is first adopted to estimate uncertain parameter in TCSC system and it achieves excellent result in avoiding the oscillation of states caused by the coupling between parameter estimator and system state. With regard to control law, the influences of time-delay nonlinearity and external disturbances are solved by constructing the control law based on backstepping sliding mode control. Simulation results show that better performance in transient and steady state response is achieved compared with adaptive backstepping sliding mode control and adaptive backstepping control.

2. TCSC System Model and Control Objective

Figure 1 shows the single-machine infinite-bus system with TCSC.

The dynamic model of the TCSC system is expressed by the following nonlinear differential equations [5, 26, 27]:

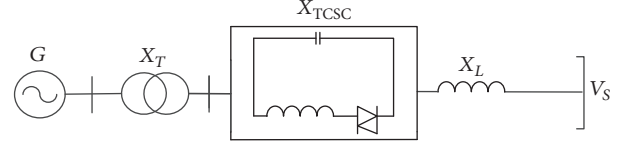


FIGURE 1: Single-machine infinite-bus power system with TCSC.

$$\dot{\delta} = \omega - \omega_0,$$

$$\dot{\omega} = \frac{\omega_0}{H} (P_m - E'_q V_s B_{TCSC} \sin \delta) - \frac{D}{H} (\omega - \omega_0) + \varepsilon_1, \quad (1)$$

$$\dot{B}_{TCSC} = \frac{1}{T_{TCSC}} (-B_{TCSC} (t - d) + B_{TCSC0} + u_B) + \varepsilon_2,$$

where δ , ω , and B_{TCSC} are state variables denoting generator rotor angle, generator rotor angular speed, and equivalent susceptance, respectively. The physical significance of parameters in (1) is shown in Physical Significance of Parameters.

In Physical Significance of Parameters, time-delay d is caused by the differences between triggering time and turn-on time of its thyristor controller. Damping coefficient D is viewed as an uncertain parameter, and the relational expression $\theta = -D/H$ is also the uncertain parameter. u_B is the equivalence input of SVC regulator. In the equation $B_{TCSC} = 1/X_1 + X_2 - X_1 X_2 (B_L - B_C)$, B_C is the susceptance of the capacitor in the TCSC. B_L is the susceptance of the inductor of the TCR. $X_1 = x'_d + X_T + X_{L1}$ is the total impedance from the generator to the injection of the SVC device with x'_d being the transient reactance of the generator on the direct axis and X_T being the reactance of the transformer. X_2 is the total impedance from the injection of the SVC device to the infinite bus. The two external disturbances are as follows: ε_1 is defined as the interference on generator rotor windings and ε_2 is the fluctuation on susceptance, respectively [14, 27]. As a result, the controlled TCSC is an uncertain and nonlinear system involving time-delay nonlinearity, uncertain parameter, and external disturbances.

To simplify (1), three state variables are redefined as $x_1 = \delta - \delta_0$, $x_2 = \omega - \omega_0$, and $x_3 = B_{TCSC} - B_{TCSC0}$, respectively, and we have

$$\dot{x}_1 = x_2,$$

$$\dot{x}_2 = \theta x_2 + k_1 P_m - k_2 (x_3 + B_{TCSC0}) \sin (x_1 + \delta_0) + \varepsilon_1, \quad (2)$$

$$\dot{x}_3 = k_3 (-x_3 (t - d) + u_B) + \varepsilon_2,$$

$$k_1 = \frac{\omega_0}{H},$$

$$k_2 = \frac{\omega_0 E'_q V_s}{H},$$

$$k_3 = \frac{1}{T_{TCSC}},$$

$$\theta = \frac{-D}{H}.$$

(3)

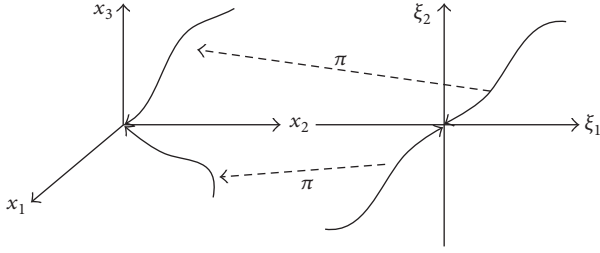


FIGURE 2: Geometric description of immersion and invariance.

The output of TCSC system is expressed as $\mathbf{y} = [\mathbf{q}_1 \mathbf{x}_1 \quad \mathbf{q}_2 \mathbf{x}_2]^T$, where q_1 and q_2 are nonnegative weighted coefficients which represent the weighted proportions of the state variables x_1 and x_2 in output.

The proposed method involves an adaptive law ($\hat{\theta}$) and a control law (u_B). The objective of designing TCSC robust controller is to guarantee that all the state variables can attain stability and eventually converge to equilibrium points in the nonlinear TCSC system. In addition, by using the proposed robust controller, the robustness of the TCSC robust controller is guaranteed, the performance and speed of transient responses is improved, and the time of reaching steady state is reduced.

3. Design of Robust Controller for Nonlinear TCSC

It divided three sections to introduce our proposed method in designing robust controller. In Section 3.1, I&I adaptive control is adopted for adaptive law $\hat{\theta}$ design, which can ensure that the estimation error of $\hat{\theta} - \theta$ gradually converged to zero. In Section 3.2, backstepping sliding mode control is used for control law u_B design recursively. The dissipation inequality is constructed in each step for guaranteeing the robustness of the subsystem. In Section 3.3, the stability and robustness of the TCSC control system are verified.

3.1. Adaptive Law Design. Figure 2 shows the mapping between the trajectories of the controlled and target system based on the notions of system immersion and manifold invariance.

The purpose of I&I methodology is to achieve stabilization by immersing the plant dynamics into a stable (lower-order) target system [20, 28]. The I&I adaptive control proposes an alternative approach avoiding the cancellation of terms in the derivative of the Lyapunov function and provides a mean of shaping the dynamic response of the estimation error [29].

Define a manifold

$$Z_e = \hat{\theta} - \theta + \varphi(x_1, x_2) = 0, \quad (4)$$

where θ is an uncertain parameter, $\hat{\theta}$ is the estimation value of θ , and Z_e is an estimation error function. $\varphi(x_1, x_2)$ is a

continuous function. The dynamics of (4) along with system (2) are

$$\begin{aligned} \dot{Z}_e = \dot{\hat{\theta}} + \sum_{k=1}^2 \frac{\partial \varphi}{\partial x_k} \times \dot{x}_k = \dot{\hat{\theta}} + \frac{\partial \varphi}{\partial x_1} x_2 + \frac{\partial \varphi}{\partial x_2} (\theta x_2 \\ + k_1 P_m - k_2 (x_3 + B_{\text{TCSC}0}) \sin(x_1 + \delta_0) + \varepsilon_1), \end{aligned} \quad (5)$$

where ε_1 is a bounded function denoting the interference on generator rotor windings.

By cancelling out all the parameter-independent terms, an adaptive law $\hat{\theta}$ is designed as

$$\begin{aligned} \dot{\hat{\theta}} = -\frac{\partial \varphi}{\partial x_1} x_2 - \frac{\partial \varphi}{\partial x_2} ((\hat{\theta} + \varphi) x_2 + k_1 P_m \\ - k_2 (x_3 + B_{\text{TCSC}0}) \sin(x_1 + \delta_0)). \end{aligned} \quad (6)$$

Substituting (6) into (5), we have

$$\dot{Z}_e = -\frac{\partial \varphi}{\partial x_2} Z_e x_2 + \frac{\partial \varphi}{\partial x_2} \varepsilon_1. \quad (7)$$

Design a CLF as

$$V = \frac{1}{2} Z_e^2 + \frac{1}{4} \rho h_1^2 (h_2 - x_2), \quad (8)$$

where h_1 is the least upper bound of external disturbance ε_1 , that is, $h_1 \geq |\varepsilon_1|$, due to the physical significance of external disturbance on generator rotor windings [14, 27, 30]; h_2 is the least upper bound of generator rotor angular x_2 due to the limitation of generator rotor, that is, $h_2 \geq |x_2|$.

Let $\varphi(x_1, x_2) = (1/2)\rho x_2^2$ with $\rho > 0$, and the dynamics of (8) is

$$\begin{aligned} \dot{V} = Z_e \left(-\frac{\partial \varphi}{\partial x_2} Z_e x_2 + \frac{\partial \varphi}{\partial x_2} \varepsilon_1 \right) - \frac{1}{4} \rho h_1^2 \\ = -\rho Z_e^2 x_2^2 + \rho Z_e x_2 \varepsilon_1 - \frac{1}{4} \rho h_1^2. \end{aligned} \quad (9)$$

Since $h_1 \geq |\varepsilon_1|$, we can obtain $-(1/4)\rho h_1^2 \leq -(1/4)\rho \varepsilon_1^2$ and then have

$$\begin{aligned} \dot{V} = -\rho Z_e^2 x_2^2 + \rho Z_e x_2 \varepsilon_1 - \frac{1}{4} \rho h_1^2 \\ \leq -\rho Z_e^2 x_2^2 + \rho Z_e x_2 \varepsilon_1 - \frac{1}{4} \rho \varepsilon_1^2 \\ = -\rho \left(Z_e x_2 - \frac{1}{2} \varepsilon_1 \right)^2 \leq 0. \end{aligned} \quad (10)$$

According to Lyapunov stability theorem, the proposed adaptive law $\hat{\theta}$ and the selected continuous function $\varphi(x_1, x_2) = (1/2)\rho x_2^2$ can ensure that Z_e converges to zero in finite time.

Remark 1. Unlike the conventional adaptive control based on certainty equivalency principle, the proposed adaptive law can introduce a continuous function $\varphi(x_1, x_2)$ to compensate

the residual estimation error $\hat{\theta} - \theta$. Furthermore, by requiring the estimation error to converge to zero, the stability and convergence of system (7) are guaranteed based on the proposed adaptive law and the selected continuous function. Therefore, the error accumulation of the coupling terms is avoided even if the parameter estimates are fixed.

Remark 2. Theoretically, there is a large flexibility in selecting $\varphi(x_1, x_2)$ which can guarantee that $\lim_{t \rightarrow \infty} Z_e(t) = 0$. For simplicity, we let $\varphi(x_1, x_2) = (1/2)\rho x_2^2$, which is the lowest order and simplest form of $\varphi(x_1, x_2)$.

Remark 3. The selected $\varphi(x_1, x_2)$ and the designed adaptive law are not only guarantee that the estimation error Z_e converges to zero but also ensure that the parametric manifold $I_e = \{(x, \hat{\theta}) \in R^3 \times R^1 \mid \hat{\theta} - \theta + \varphi(x_1, x_2) = 0\}$ is invariant and attractive [28, 29].

3.2. Control Law Design. In this section, the control law is designed by using backstepping sliding mode control method in TCSC system with time-delay nonlinearity and external disturbances. Three steps are constructed to design the control law recursively. In each step, the dissipation inequality is satisfied to guarantee the robustness of TCSC control system.

Based on dissipation theory, an inequation external disturbances is constructed as

$$V(x(T)) - V(x(0)) \leq \int_0^T s(\Delta) dt; \quad (11)$$

$V(x)$ is an energy storage function. $s(\Delta) = \gamma \|\Delta\|^2 - \|y\|^2$ is an energy supply function, where $\Delta = (\varepsilon_1, \varepsilon_2)^T$ is external disturbance, γ is a nonnegative constant, and $y = [q_1 x_1 \ q_2 x_2]^T$ is the output of the TCSC system. From (11), the dissipation inequality is achievable provided that the L_2 gain from the disturbance to the output of the system is smaller than or equal to γ , where γ is disturbance attenuation constant.

According to the definitions above, the control law is designed as follows.

Define error state variables z_i ($i = 1, 2, 3$)

$$\begin{aligned} z_1 &= x_1, \\ z_2 &= x_2 - x_2^*, \\ z_3 &= x_3 - x_3^*, \end{aligned} \quad (12)$$

where x_2^* and x_3^* are virtual control law. The derivative of z_1 along with (2) is

$$\dot{z}_1 = x_2 = z_2 + x_2^*. \quad (13)$$

Step 1. The first CLF is

$$V_1 = \frac{1}{2} z_1^2, \quad (14)$$

and the derivative of V_1 along with (13) is

$$\dot{V}_1 = z_1 z_2 + z_1 x_2^*. \quad (15)$$

To satisfy Lyapunov stability theorem, the virtual control law x_2^* is

$$x_2^* = -c_1 z_1, \quad (16)$$

where c_1 is a positive constant. Substituting (16) into (15), it can be seen clearly that $\dot{V}_1 \leq 0$ when $z_2 = 0$. However, when $z_2 \neq 0$, we can construct the second CLF in Step 2.

Step 2. The second CLF is

$$V_2 = V_1 + \frac{1}{2} z_2^2, \quad (17)$$

and the derivative of V_2 along with (15) is

$$\dot{V}_2 = \dot{V}_1 + z_2 \dot{z}_2. \quad (18)$$

Define a function M_1 as

$$M_1 = \dot{V}_2 + \frac{1}{2} (\|y\|^2 - \gamma^2 \|\varepsilon_1\|^2). \quad (19)$$

Substituting $y = [q_1 x_1 \ q_2 x_2]^T$ into (19), (19) can be rewritten as

$$\begin{aligned} M_1 &= -\alpha z_1^2 - \left(\frac{\gamma \varepsilon_1}{2} - \frac{z_2}{\gamma} \right)^2 - \frac{1}{4} \gamma^2 \varepsilon_1^2 + z_2 [\eta_1 x_1 \\ &+ \eta_2 x_2 + \theta x_2 + k_1 P_m \\ &- k_2 (x_3 + B_{\text{TCSC0}}) \sin(x_1 + \delta_0)], \end{aligned} \quad (20)$$

where

$$\begin{aligned} \alpha &= c_1 - \frac{1}{2} q_1^2 - \frac{1}{2} q_2^2 c_1^2, \\ \eta_1 &= \frac{c_1}{\gamma^2} - \frac{c_1}{2} q_2^2 + 1, \\ \eta_2 &= \frac{1}{\gamma^2} + \frac{1}{2} q_2^2 - c_1. \end{aligned} \quad (21)$$

To guarantee that $M_1 \leq 0$, x_3^* is

$$x_3^* = \frac{\eta_1 x_1 + \eta_2 x_2 + (\hat{\theta} + \varphi) x_2 + k_1 P_m}{k_2 \sin(x_1 + \delta_0)} - B_{\text{TCSC0}}, \quad (22)$$

substituting $x_3 = x_3^* + z_3$ and (22) into (20), we have

$$\begin{aligned} M_1 &= -\alpha z_1^2 - \left(\frac{\gamma}{2} \varepsilon_1 - \frac{z_2}{\gamma} \right)^2 - \frac{1}{4} \gamma^2 \varepsilon_1^2 - z_2 x_2 Z_e \\ &- k_2 \sin(x_1 + \delta_0) z_2 z_3. \end{aligned} \quad (23)$$

According to Remark 3, we can obtain $M_1 \leq 0$ when $z_3 = 0$. But, when $z_3 \neq 0$, we can get into Step 3.

Step 3. Design sliding surface $s = \lambda_1 z_1 + \lambda_2 z_2 + z_3 = 0$, where λ_1 and λ_2 are designed parameters. To ensure the

whole TCSC system is globally asymptotically stable, the third CLF is

$$V_3 = \frac{1}{2}z_1^2 + \frac{1}{2}z_2^2 + \frac{1}{2}s^2 + \int_{t-d}^t q(x(\tau)) d\tau, \quad (24)$$

where $q(x(\tau))$ is a nonnegative function. The derivative of V_3 is

$$\dot{V}_3 = z_1\dot{z}_1 + z_2\dot{z}_2 + s\dot{s} + q(x(t)) - q(x(t-d)); \quad (25)$$

M_2 is designed as

$$M_2 = \dot{V}_3 + \frac{1}{2}(\|y\|^2 - \gamma^2\|\varepsilon_1\|^2 - \gamma^2\|\varepsilon_2\|^2). \quad (26)$$

Substituting the control output and (25) into (26), we obtain

$$\begin{aligned} M_2 = & \dot{V}_3 + \frac{1}{2}(\|y\|^2 - \gamma^2\|\varepsilon_1\|^2 - \gamma^2\|\varepsilon_2\|^2) = -\alpha z_1^2 \\ & - \left(\frac{\gamma}{2}\varepsilon_1 - \frac{z_2}{\gamma}\right)^2 - \frac{1}{4}\gamma^2\varepsilon_1^2 - z_2x_2Z_e - \frac{1}{2}\gamma^2\varepsilon_2^2 - k_2 \\ & \cdot \sin(x_1 + \delta_0)z_2z_3 + s(\lambda_1x_2 + \lambda_2\dot{x}_2 + \lambda_2c_1x_2 \\ & + k_3(-x_3(t-d) + u_B) + \varepsilon_2 - \dot{x}_3^*) + q(x(t)) \\ & - q(x(t-d)). \end{aligned} \quad (27)$$

Let $z_3 = s - \lambda_1z_1 - \lambda_2z_2$; (27) is rewritten as

$$\begin{aligned} M_2 = & -(\alpha - \lambda_1^2)z_1^2 - \left(\frac{\gamma}{2}\varepsilon_1 - \frac{z_2}{\gamma}\right)^2 - \left[\lambda_2k_2 \right. \\ & \cdot \sin(x_1 + \delta_0) - \frac{1}{4}k_2^2\sin^2(x_1 + \delta_0)]z_2^2 - \left[\lambda_1z_1 \right. \\ & - \frac{1}{2}k_2\sin(x_1 + \delta_0)z_2] \left. - \left[\frac{\gamma}{2}\varepsilon_1 - \frac{s}{\gamma}\left(\lambda_2 \right. \right. \right. \\ & \left. \left. - \frac{\eta_2 + \hat{\theta} + \varphi}{k_2\sin(x_1 + \delta_0)}\right)\right]^2 - \frac{1}{2}\left(\gamma\varepsilon_2 - \frac{s}{\gamma}\right)^2 - z_2Z_ex_2 \\ & + s \left\{ \frac{s}{\gamma^2}\left(\lambda_2 - \frac{\eta_2 + \hat{\theta} + \varphi}{k_2\sin(x_1 + \delta_0)}\right)^2 - k_2 \right. \\ & \cdot \sin(x_1 + \delta_0)z_2 + (\lambda_1 + \lambda_2\hat{\theta} + \lambda_2c_1)x_2 - \lambda_2k_2 \\ & \cdot \sin(x_1 + \delta_0)(B_{\text{TCSC0}} + x_3) + \frac{s}{2\gamma^2} + \lambda_2k_1P_m \\ & - k_3x_3(t-d) + k_3u_B - \frac{1}{k_2\sin(x_1 + \delta_0)} \left[\eta_1x_2 \right. \\ & + (\hat{\theta} + \dot{\varphi})x_2(\hat{\theta} + \varphi + \eta_2) \\ & \left. \left. \left. \cdot (\hat{\theta}x_2 + k_1P_m - k_2\sin(x_1 + \delta_0)(x_3 + B_{\text{TCSC0}})) \right] \right\} \end{aligned}$$

$$\begin{aligned} & + \frac{\cos(x_1 + \delta_0)x_2}{k_2\sin^2(x_1 + \delta_0)}(\eta_1x_1 + \eta_2x_2 + (\hat{\theta} + \varphi)x_2 \\ & + k_1P_m) \left. \right\} + q(x(t)) - q(x(t-d)). \end{aligned} \quad (28)$$

Define a nonnegative function $q(x(t)) = |k_3sx_3(t)|$, and then we can obtain $q(x(t-d)) = |k_3sx_3(t-d)|$. An inequation is established as

$$-|k_3sx_3(t-d)| \leq k_3sx_3(t-d). \quad (29)$$

Moreover, to ensure the robustness and stability of the nonlinear TCSC control system, the control law is then designed as

$$\begin{aligned} u_B = & -\frac{1}{k_3} \left\{ \frac{s}{\gamma^2} \left(\lambda_2 - \frac{\eta_2 + \hat{\theta} + \varphi}{k_2\sin(x_1 + \delta_0)} \right)^2 - k_2 \right. \\ & \cdot \sin(x_1 + \delta_0)z_2 + (\lambda_1 + \lambda_2\hat{\theta} + \lambda_2c_1)x_2 - \lambda_2k_2 \\ & \cdot \sin(x_1 + \delta_0)(B_{\text{TCSC0}} + x_3) + \frac{s}{2\gamma^2} + \lambda_2k_1P_m \\ & - \frac{1}{k_2\sin(x_1 + \delta_0)} \left[\eta_1x_2 + (\hat{\theta} + \dot{\varphi})x_2 \right. \\ & + (\hat{\theta} + \varphi + \eta_2) \\ & \left. \left. \left. \cdot (\hat{\theta}x_2 + k_1P_m - k_2\sin(x_1 + \delta_0)(x_3 + B_{\text{TCSC0}})) \right] \right\} \\ & + \frac{\cos(x_1 + \delta_0)x_2}{k_2\sin^2(x_1 + \delta_0)}(\eta_1x_1 + \eta_2x_2 + (\hat{\theta} + \varphi)x_2 \\ & + k_1P_m) - \mu|k_3x_3(t)| + \sigma s \left. \right\}, \end{aligned} \quad (30)$$

where σ is a nonnegative sliding mode observer gain and μ is a sign function, which is defined as $\mu = -1$ when $s \rightarrow 0^+$ and $\mu = 1$ when $s \rightarrow 0^-$.

Substituting $q(x(t)) = |k_3sx_3(t)|$, $q(x(t-d)) = |k_3sx_3(t-d)|$, (29), and (30) into (28), (28) is rewritten as

$$\begin{aligned} M_2 & \leq -(\alpha - \lambda_1^2)z_1^2 - \left(\frac{\gamma}{2}\varepsilon_1 - \frac{z_2}{\gamma}\right)^2 \\ & - \left[\lambda_2k_2\sin(x_1 + \delta_0) - \frac{1}{4}k_2^2\sin^2(x_1 + \delta_0)\right]z_2^2 \\ & - \left[\lambda_1z_1 - \frac{1}{2}k_2\sin(x_1 + \delta_0)z_2\right]^2 \\ & - \left[\frac{\gamma}{2}\varepsilon_1 - \frac{s}{\gamma}\left(\lambda_2 + \frac{\eta_2 + \hat{\theta} + \varphi}{k_2\sin(x_1 + \delta_0)}\right)\right]^2 \\ & - \frac{1}{2}\left(\gamma\varepsilon_2 - \frac{s}{\gamma}\right)^2 - z_2Z_ex_2 - \sigma s^2 \leq 0. \end{aligned} \quad (31)$$

To guarantee $\lambda_2 k_2 \sin(x_1 + \delta_0) - (1/4)k_2^2 \sin^2(x_1 + \delta_0) \geq 0$ with $k_2 \geq 0$, we can get $\lambda_2 \geq (1/4)k_2$ if $\sin(x_1 + \delta_0) \geq 0$ and $\lambda_2 < -(1/4)k_2$ if $\sin(x_1 + \delta_0) < 0$. Furthermore, the parameters λ_1 , λ_2 , k_2 , and c_1 are selected to ensure that $\alpha - \lambda_1^2 \geq 0$ and $\lambda_2 k_2 \sin(x_1 + \delta_0) - (1/4)k_2^2 \sin^2(x_1 + \delta_0) \geq 0$. Therefore, according to Remark 3, we can obtain $M_2 \leq 0$ as time approaches to infinity.

3.3. Proof of System Stability. The dynamics of closed-loop error system are expressed as

$$\begin{aligned}\dot{z}_1 &= \dot{x}_1, \\ \dot{z}_2 &= \dot{x}_2 - \dot{x}_2^*, \\ \dot{z}_3 &= \dot{x}_3 - \dot{x}_3^*.\end{aligned}\quad (32)$$

Substituting virtual control input x_2^* and x_3^* into (32), we can obtain

$$\begin{aligned}\dot{z}_1 &= \dot{x}_1 = z_2 - c_1 z_1, \\ \dot{z}_2 &= \dot{x}_2 - \dot{x}_2^* \\ &= \theta x_2 + k_1 P_m - k_2 (x_3 + B_{\text{TCSC0}}) \sin(\delta_0 + x_1) + \varepsilon_1 \\ &\quad + c_1 z_2 - c_1^2 z_1, \\ \dot{z}_3 &= \dot{x}_3 - \dot{x}_3^* = k_3 (-x_3(t-d) + u_B) + \varepsilon_2 - \dot{x}_3^*.\end{aligned}\quad (33)$$

The asymptotic stability of the closed-loop error system (33) is discussed in two different conditions.

Firstly, when the external disturbances $\varepsilon_1 \neq 0$ and $\varepsilon_2 \neq 0$, a relationship according to (26) and (31) is constructed as

$$\begin{aligned}M_2 &= \dot{V}_3 + \frac{1}{2} (\|y\|^2 - \gamma^2 \|\varepsilon_1\|^2 - \gamma^2 \|\varepsilon_2\|^2) \\ &\leq -(\alpha - \lambda_1^2) z_1^2 - \left(\frac{\gamma}{2} \varepsilon_1 - \frac{z_2}{\gamma}\right)^2 \\ &\quad - \left[\lambda_2 k_2 \sin(x_1 + \delta_0) - \frac{1}{4} k_2^2 \sin^2(x_1 + \delta_0)\right] z_2^2 \\ &\quad - \left[\lambda_1 z_1 - \frac{1}{2} k_2 \sin(x_1 + \delta_0) z_2\right]^2 \\ &\quad - \left[\frac{\gamma}{2} \varepsilon_1 - \frac{s}{\gamma} \left(\lambda_2 + \frac{\eta_2 + \hat{\theta} + \varphi}{k_2 \sin(x_1 + \delta_0)}\right)\right]^2 \\ &\quad - \frac{1}{2} \left(\gamma \varepsilon_2 - \frac{s}{\gamma}\right)^2 - z_2 Z_e x_2 - \sigma s^2 \leq 0.\end{aligned}\quad (34)$$

Let $V(x) = 2V_3(x)$; an inequation with regard to \dot{V}_3 is expressed as

$$\dot{V} = 2\dot{V}_3 \leq \gamma^2 \|\varepsilon_1\|^2 + \gamma^2 \|\varepsilon_2\|^2 - \|y\|^2. \quad (35)$$

By integrating both sides of (35), the dissipation inequality is

$$\begin{aligned}V(x(t)) - V(x(0)) \\ \leq \int_0^T (\gamma^2 \|\varepsilon_1\|^2 + \gamma^2 \|\varepsilon_2\|^2 - \|y\|^2) dt.\end{aligned}\quad (36)$$

The dissipation inequality (34) is satisfied and the robustness of TCSC controller is guaranteed by using the proposed method. This implies that all the increased energy of the system from $t = 0$ to T is always equal to or less than the ones from outside. Therefore, the energy of power systems has been decreasing. Obviously, the proposed method consisting of the designed law u_B and the adaptive law $\hat{\theta}$ can guarantee that the closed-loop error system is globally asymptotically stable.

Secondly, when the external disturbances are not involved, we can construct Lemma 4 and prove it as below.

Lemma 4. *Based on the above derivations, one can conclude that the dynamics of closed-loop error system are asymptotically stable when $\varepsilon_1 = 0$ and $\varepsilon_2 = 0$.*

Proof. Substituting $\varepsilon_1 = 0$ and $\varepsilon_2 = 0$ into (34), we have

$$\begin{aligned}\dot{V}_3 + \frac{1}{2} \|y\|^2 \\ \leq -(\alpha - \lambda_1^2) z_1^2 - \left(\frac{z_2}{\gamma}\right)^2 \\ - \left[\lambda_2 k_2 \sin(x_1 + \delta_0) - \frac{1}{4} k_2^2 \sin^2(x_1 + \delta_0)\right] z_2^2 \\ - \left[\lambda_1 z_1 - \frac{1}{2} k_2 \sin(x_1 + \delta_0) z_2\right]^2 \\ - \left[\frac{s}{\gamma} \left(\lambda_2 - \frac{\eta_2 + \hat{\theta} + \varphi}{k_2 \sin(x_1 + \delta_0)}\right)\right]^2 - \frac{1}{2} \left(\frac{s}{\gamma}\right)^2 \\ - \sigma s^2 \leq 0.\end{aligned}\quad (37)$$

According to $\dot{V}_3 + (1/2)\|y\|^2 \leq 0$ and $(1/2)\|y\|^2 = (1/2)(q_1^2 x_1^2 + q_2^2 x_2^2) > 0$, we can obtain $\dot{V}_3 \leq 0$ and have

$$V_3(t) \leq V_3(0), \quad (38)$$

where $t \geq 0$. Furthermore, according to $V_3 = (1/2)z_1^2 + (1/2)z_2^2 + (1/2)s^2 + \int_{t-d}^t q(x(\tau))d\tau$ with $q(x(t)) = |k_3 s x_3(t)|$, we have $V_3(t) \geq 0$.

Since $V_3(0)$ is bounded, $V_3(t) \geq 0$, and $\dot{V}_3(t) \leq 0$, then we know that $V_3(t)$ is nonincreasingly bounded and z_1 , z_2 , s , x_1 , and x_2 are all bounded.

Define $Q(t) = \dot{V}_3(t)$, and the integral of $Q(t)$ is

$$\int_0^t Q(\tau) d\tau = V_3(t) - V_3(0). \quad (39)$$

According to $V_3(t)$ which is nonincreasingly bounded, $\dot{V}_3(t) \leq 0$, and $V_3(t) \geq 0$, we obtain the fact that $\lim_{t \rightarrow \infty} \int_0^t Q(\tau) d\tau$ exists. Finally, $\lim_{t \rightarrow \infty} \dot{V}_3(t) = 0$ is achievable due to Barbalat's Lemma (Barbalat, 1959).

Moreover, due to $\lim_{t \rightarrow \infty} \dot{V}_3(t) = 0$ and z_1 , z_2 , x_2 , x_1 , and s , which are all bounded, $V_3 \geq 0$, we have $z_1 \rightarrow 0$, $z_2 \rightarrow 0$, $x_1 \rightarrow 0$, $x_2 \rightarrow 0$, and $s \rightarrow 0$ when $t \rightarrow \infty$. In addition, the sliding surface is defined as $s = \lambda_1 z_1 + \lambda_2 z_2 + z_3$, and then we can get $z_3 = s - \lambda_1 z_1 - \lambda_2 z_2$. Obviously, it is obtained that $z_3 \rightarrow 0$ as $t \rightarrow \infty$. Lemma 4 holds. \square

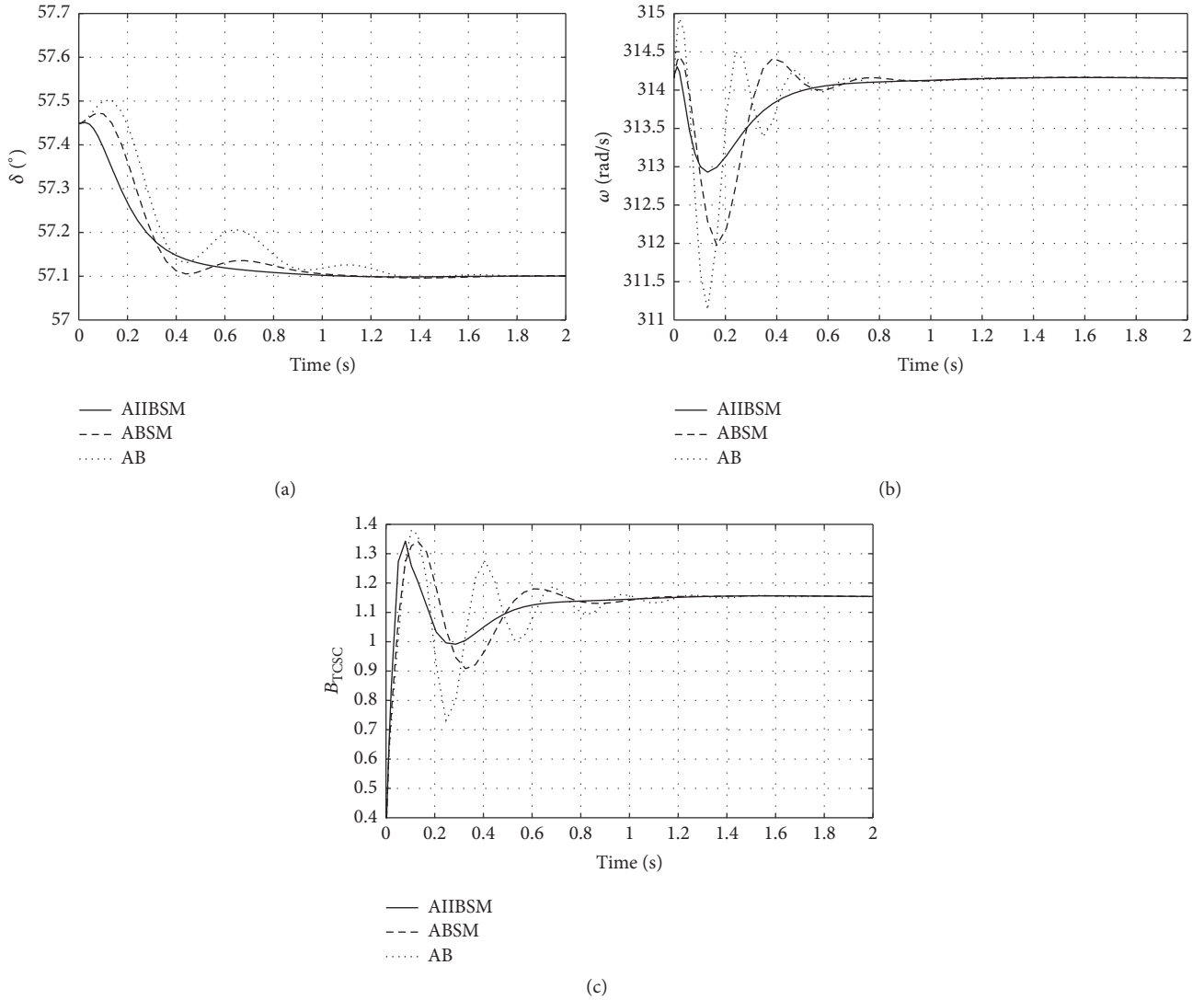


FIGURE 3: Transient responses in case 1: (a) transient responses of rotor angle; (b) transient responses of rotor angular speed; (c) transient responses of equivalent susceptance.

As a result, the control objective is achieved by using the designed law u_B and the adaptive law $\hat{\theta}$. This implies that all the responses of state variables attain stability and eventually converge to equilibrium points.

4. Simulations

The MATLAB software is performed in TCSC simulations. According to operating characteristics of TCSC system, the time-delay between the triggering time and turn-on time is equal to or less than 0.04 s. The damping coefficient is viewed as the uncertain parameter. The external disturbances in the system are $\varepsilon_1 = e^{-2t} \sin(5t)$ and the unknown fluctuation on susceptance is $\varepsilon_2 = e^{-2t} \cos(5t)$, respectively [14, 27]. The parameters used in the simulation are given in Table 1.

The generator rotor angle δ , generator rotor angular speed ω , and equivalent susceptance B_{TCSC} are the state variables whose transient response trajectories are tracked. The initial

operating values are $\delta_0 = 57.1^\circ$, $\omega_0 = 314.159$ rad/s, and $B_{TCSC0} = 0.4$ pu.

Four case studies are performed to simulate the nonlinear TCSC systems with different delay times d or attenuation coefficient γ . Cases 1–3 aim to compare the stability and robustness of TCSC control systems designed by the proposed adaptive immersion and invariance backstepping sliding mode (AIIBSM) method, adaptive backstepping sliding mode (ABSM) method, and adaptive backstepping method (AB). d and γ are set to 0.01 s and 2 in case 1, 0.02 s and 2 in case 2, and 0.04 s and 2 in case 3. In case 4, simulations of our designed TCSC system with $d_4 = 0.02$ s are performed at $\gamma_1 = 2$ and $\gamma_2 = 5$, respectively.

Figure 3 shows the comparisons between the proposed method and the two existing methods in case 1, where $d_1 = 0.01$ and $\gamma_1 = 2$. The transient responses of three state variables, that is, rotor angle, rotor angular speed, and equivalent susceptance, are investigated, respectively. It can

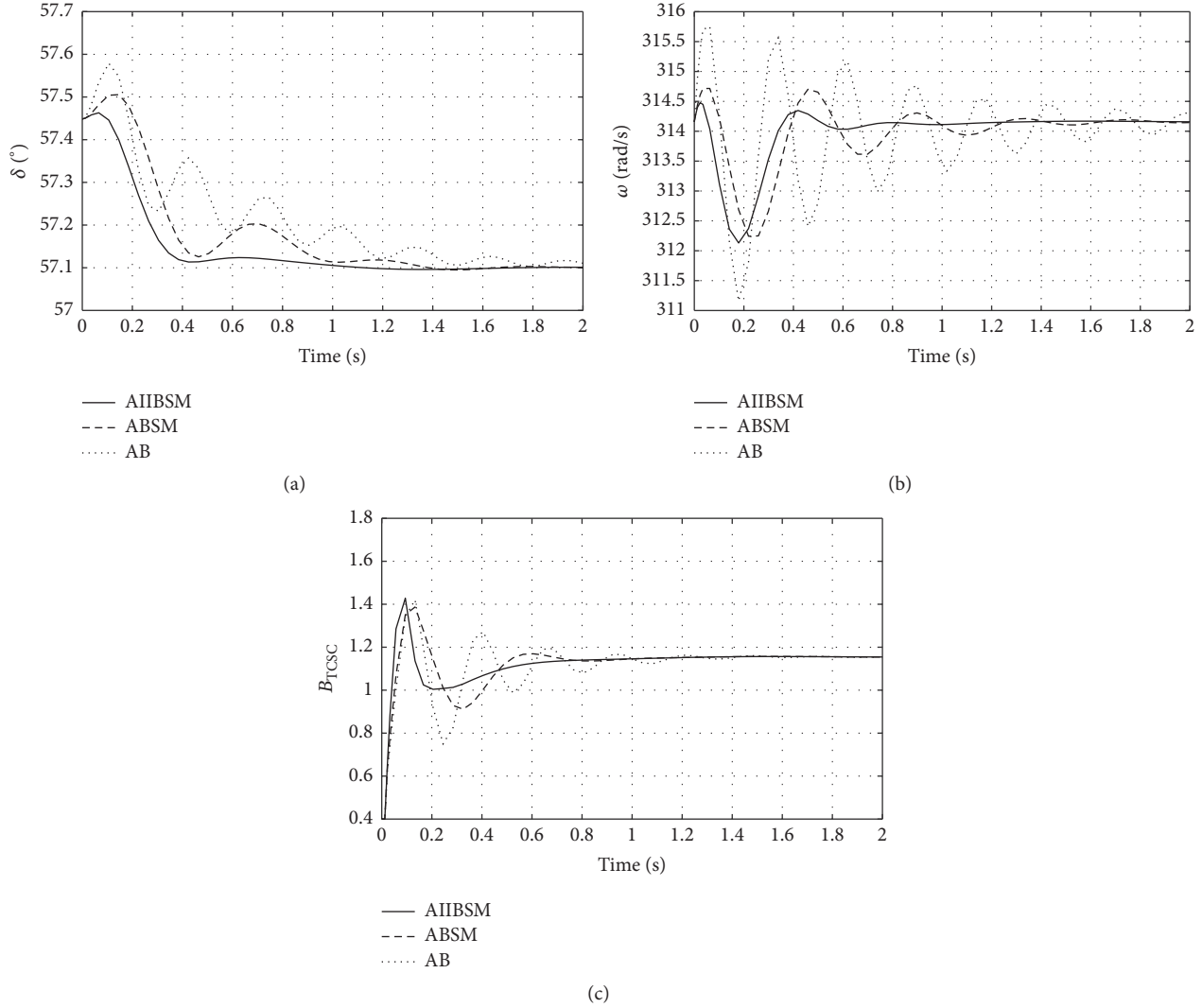


FIGURE 4: Transient responses in case 2: (a) transient responses of rotor angle; (b) transient responses of rotor angular speed; (c) transient responses of equivalent susceptance.

TABLE 1: Parameters for nonlinear TCSC system simulations.

System parameters	Values and units
Generator	$H = 8$ (p.u.); $V_s = 1.0$ (p.u.); $E'_q = 1.08$ (p.u.); $P_m = 1.0$ (p.u.);
Transmission line	$X_1 = 0.84$ (p.u.); $X_2 = 0.52$ (p.u.);
TCSC	$B_{TCSC0} = 0.814$ (p.u.); $B_L + B_C = 0.3$ (p.u.); $T_{TCSC} = 0.02$ (s);
Output weighted coefficient	$q_1 = 0.4$; $q_2 = 0.6$;
Sliding mode gain	$\lambda_1 = 1$; $\lambda_2 = 1$; $\sigma = 100$;
Unfixed parameter	$d = 0.01, 0.02, 0.04$; $\gamma = 2, 5$;

be seen that the transient responses of the state variables of the AIIBSM controller are faster and the AIIBSM system tends to attain stability more rapidly, whereas the transient responses of the ABSM and AB controllers fluctuate faster

and the ABSM and AB systems tend to reach stability in a longer finite time. Especially, three state variables cannot achieve the steady state in finite time.

Figure 4 shows the transient responses of the three state variables in case 2, where $d_2 = 0.02$ s and $\gamma_1 = 2$. The transient trajectories of the AIIBSM controller fluctuate less strongly and quickly converge to steady state than compared to those of the ABSM and AB controllers in finite time, suggesting that the proposed AIIBSM method results in better system performance.

Figure 5 shows the transient responses of the three state variables in case 3, where $d_3 = 0.04$ and $\gamma_1 = 2$. The result of case 3 reveals that the proposed method can guarantee that the state variables of the nonlinear TCSC system are globally bounded and transient responses will eventually converge to a stable value regardless of what delay time is considered. A comparison of the transient responses of the AIIBSM controller in the three cases shows that the transient

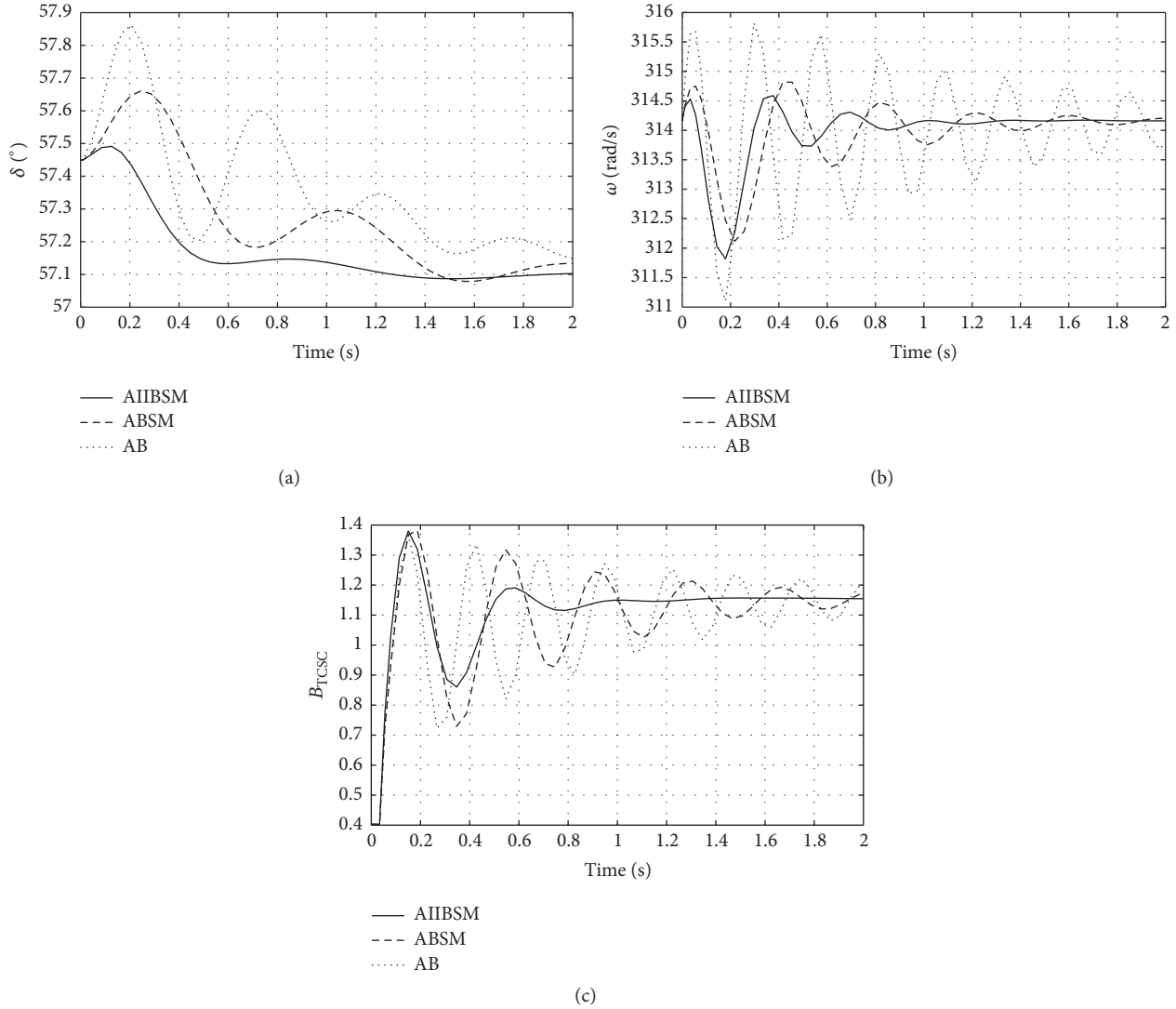


FIGURE 5: Transient responses in case 3: (a) transient responses of rotor angle; (b) transient responses of rotor angular speed; (c) transient responses of equivalent susceptance.

responses in case 3 converge more slowly and the system stability is attained in a longer finite time. Similar comparative results are obtained for the ABSM and AB controllers.

Figure 6 shows transient responses of the three state variables in case 4. The simulation results are compared to investigate the effect of the attenuation coefficient γ on the stability and robustness of TCSC control systems. It can be seen that the AIIBSM controller attains more rapid speed responses and stronger robustness at $\gamma_1 = 2$ than at $\gamma_2 = 5$. Therefore, the delay time d is a crucial nonlinear factor impacting the transient and steady performance of the TCSC system. A smaller d can lead to better transient stability and stronger robustness. Furthermore, the attenuation coefficient γ is also a key factor impacting the performance of the control system. A smaller γ tends to result in stronger robustness and smaller oscillation. This result is consistent with the theoretical analysis.

5. Conclusions

This paper investigates the problems involving time-delay nonlinearity, uncertain parameter, and external disturbances in the controller design of TCSC system. An uncertain parameter is estimated in the adaptive law design based on I&I adaptive control. The oscillation of states caused by the coupling between parameter estimator and system states is avoided, due to the fact that the errors of parameter estimation can gradually converge to zero by using the designed adaptive law. In addition, backstepping sliding mode control is adopted to solve the problems caused by time-delay nonlinearity and external disturbances in the control law design. Moreover, by satisfying the dissipation inequality, the robustness of the proposed TCSC control system is achieved. Simulation results have confirmed that, by using the proposed method, all state variables are globally

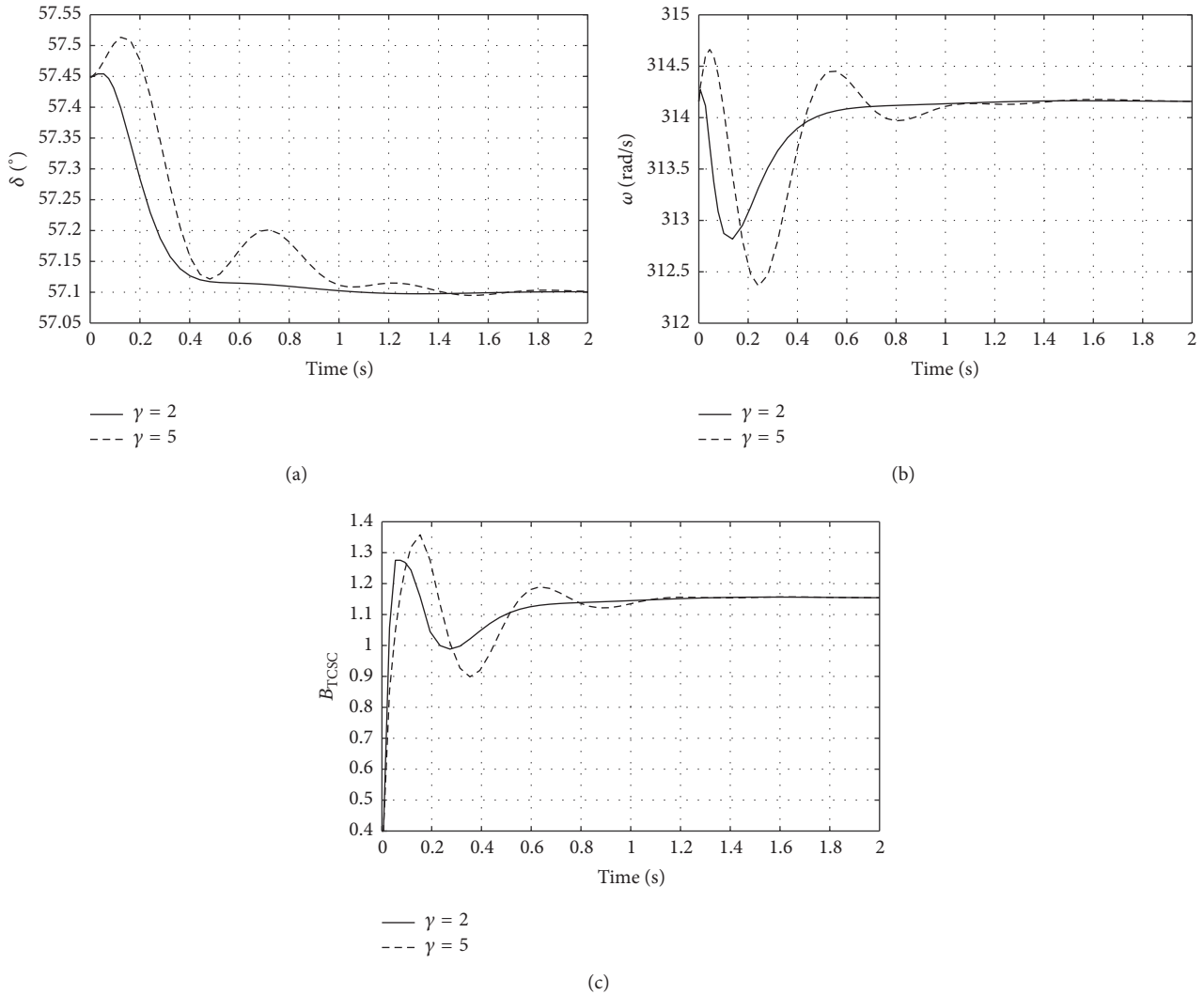


FIGURE 6: Transient responses in case 3: (a) transient responses of rotor angle (b); transient responses of rotor angular speed; (c) transient responses of equivalent susceptance.

bounded and transient responses eventually converge to equilibrium points regardless of time-delay.

Physical Significance of Parameters

- δ : Generator rotor angle
- H : Inertia constant
- P_m : Mechanical power
- d : Time-delay
- T_{TCS} : Time constant
- $\epsilon_{1,2}$: External disturbances
- ω : Generator rotor angular speed
- E'_q : Transient electromotive force
- D : Damping coefficient
- B_{TCS} : Equivalent susceptance
- V_s : Infinite bus voltage
- u_B : Equivalence input.

Conflicts of Interest

The authors declare that they have no conflicts of interest.

Acknowledgments

This work was supported in part by the NSF of China under Grant 51707140, in part by the Fundamental Research Funds for the Central Universities under Grant JBX170416, JB160415, and XJS16020, in part by the Natural Science Basic Research Plan, in Shaanxi Province of China (2017JQ5119), and in part by China Postdoctoral Science Foundation (2017M613066).

References

- [1] P. Kundur, *Power System Stability and Control*, 2014.
- [2] K. Zare, M. T. Hagh, and J. Morsali, "Effective oscillation damping of an interconnected multi-source power system with

- automatic generation control and TCSC,” *International Journal of Electrical Power & Energy Systems*, vol. 65, pp. 220–230, 2015.
- [3] G. Shahgholian, A. Movahedi, and J. Faiz, “Coordinated design of TCSC and PSS controllers using VURPSO and Genetic algorithms for multi-machine power system stability,” *International Journal of Control, Automation, and Systems*, vol. 13, no. 2, pp. 398–409, 2015.
 - [4] M. Bakhshi, M. H. Holakooie, and A. Rabiee, “Fuzzy based damping controller for TCSC using local measurements to enhance transient stability of power systems,” *International Journal of Electrical Power & Energy Systems*, vol. 85, pp. 12–21, 2017.
 - [5] C. Zhang, A. Zhang, H. Zhang, Y. Geng, and Y. Bai, “Research on improved adaptive control for static synchronous compensator in power system,” *Mathematical Problems in Engineering*, vol. 2015, Article ID 746903, 9 pages, 2015.
 - [6] H. Bevrani, T. Hiyama, and H. Bevrani, “Robust PID based power system stabiliser: Design and real-time implementation,” *International Journal of Electrical Power & Energy Systems*, vol. 33, no. 2, pp. 179–188, 2011.
 - [7] K.-H. Kim, Y.-C. Jeung, D.-C. Lee, and H.-G. Kim, “LVRT scheme of PMSG wind power systems based on feedback linearization,” *IEEE Transactions on Power Electronics*, vol. 27, no. 5, pp. 2376–2384, 2012.
 - [8] R. Vikal and G. Goyal, “TCSC Controller design using global optimization for stability analysis of single machine infinite-bus power system,” in *Proceedings of the 2009 15th International Conference on Intelligent System Applications to Power Systems, ISAP '09*, Curitiba, Brazil, November 2009.
 - [9] J. Li and D. Zhang, “Backstepping and Sliding-Mode Techniques Applied to Distributed Secondary Control of Islanded Microgrids,” *Asian Journal of Control*, 2018.
 - [10] H. Li, L. Wang, and H. Du, “Adaptive fuzzy backstepping tracking control for strict-feedback systems with input delay,” *IEEE Transactions on Fuzzy Systems*, vol. 25, no. 3, pp. 642–652, 2017.
 - [11] B. Yang, T. Yu, H. Shu, J. Dong, and L. Jiang, “Robust sliding-mode control of wind energy conversion systems for optimal power extraction via nonlinear perturbation observers,” *Applied Energy*, vol. 210, pp. 711–723, 2017.
 - [12] L. Sun, W. Huo, and Z. Jiao, “Adaptive Backstepping Control of Spacecraft Rendezvous and Proximity Operations with Input Saturation and Full-State Constraint,” *IEEE Transactions on Industrial Electronics*, vol. 64, no. 1, pp. 480–492, 2017.
 - [13] J. Zhou, C. Wen, and W. Wang, “Adaptive backstepping control of uncertain systems with unknown input time-delay,” *Automatica*, vol. 45, no. 6, pp. 1415–1422, 2009.
 - [14] L. Zhang, A. Zhang, Z. Ren, G. Li, C. Zhang, and J. Han, “Hybrid adaptive robust control of static var compensator in power systems,” *International Journal of Robust and Nonlinear Control*, vol. 24, no. 12, pp. 1707–1723, 2014.
 - [15] L. Sun, “Adaptive sliding mode control of generator excitation system with output constraints,” *Mathematical Problems in Engineering*, vol. 2016, Article ID 4247068, 6 pages, 2016.
 - [16] N. Abdelhamid and O. Abdelkhalek, “Active power flow control using a TCSC based backstepping controller in multimachine power system,” *World Academy of Science, Engineering and Technology, International Journal of Electrical, Computer, Energetic, Electronic and Communication Engineering*, vol. 8, no. 6, pp. 860–864, 2014.
 - [17] C. Zhang, A. Zhang, Y. Cui, and T. Wen, “An Advanced Control and Extensible Configuration for Static Var Generator,” *Mathematical Problems in Engineering*, vol. 2016, Article ID 2095973, 9 pages, 2016.
 - [18] A. Astolfi, D. Karagiannis, and R. Ortega, “Towards applied nonlinear adaptive control,” *Annual Reviews in Control*, vol. 32, no. 2, pp. 136–148, 2008.
 - [19] D. Karagiannis and A. Astolfi, “Nonlinear adaptive control of systems in feedback form: an alternative to adaptive backstepping,” *Systems & Control Letters*, vol. 57, no. 9, pp. 733–739, 2008.
 - [20] D. Karagiannis, D. Carnevale, and A. Astolfi, “Invariant manifold based reduced-order observer design for nonlinear systems,” *Institute of Electrical and Electronics Engineers Transactions on Automatic Control*, vol. 53, no. 11, pp. 2602–2614, 2008.
 - [21] C. Zhang, H. Zhang, J. Li, Y. Bai, Y. Geng, and A. Zhang, “Backstepping sliding-mode control of nonlinear TCSC system based on adaptive observer,” *Journal of Discrete Mathematical Sciences & Cryptography*, vol. 18, no. 1-2, pp. 157–175, 2015.
 - [22] K. Saoudi, M. N. Harmas, and Z. Bouchama, “Design of a robust and indirect adaptive fuzzy sliding mode power system stabilizer using particle swarm optimization,” *Energy Sources, Part A: Recovery, Utilization, and Environmental Effects*, vol. 36, no. 15, pp. 1670–1680, 2014.
 - [23] Z. Dai and W. Lin, “Adaptive estimation of three-phase grid voltage parameters under unbalanced faults and harmonic disturbances,” *IEEE Transactions on Power Electronics*, vol. 32, no. 7, pp. 5613–5627, 2017.
 - [24] H. Li, P. Shi, D. Yao, and L. Wu, “Observer-based adaptive sliding mode control for nonlinear Markovian jump systems,” *Automatica*, vol. 64, pp. 133–142, 2016.
 - [25] D. Chwa, “Sliding-Mode-Control-Based Robust Finite-Time Antisway Tracking Control of 3-D Overhead Cranes,” *IEEE Transactions on Industrial Electronics*, vol. 64, no. 8, pp. 6775–6784, 2017.
 - [26] L. A. S. Pilotto, A. Bianco, W. F. Long, and A.-A. Edris, “Impact of TCSC control methodologies on subsynchronous oscillations,” *IEEE Transactions on Power Delivery*, vol. 18, no. 1, pp. 243–252, 2003.
 - [27] L.-Y. Sun, S. Tong, and Y. Liu, “Adaptive backstepping sliding mode H_∞ control of static var compensator,” *IEEE Transactions on Control Systems Technology*, vol. 19, no. 5, pp. 1178–1185, 2011.
 - [28] A. Astolfi and R. Ortega, “Immersion and invariance: a new tool for stabilization and adaptive control of nonlinear systems,” *Institute of Electrical and Electronics Engineers Transactions on Automatic Control*, vol. 48, no. 4, pp. 590–606, 2003.
 - [29] A. Astolfi, R. Ortega, and A. Venkatraman, “A globally exponentially convergent immersion and invariance speed observer for n degrees of freedom mechanical systems,” in *Proceedings of the 48th IEEE Conference on Decision and Control held jointly with 2009 28th Chinese Control Conference, CDC/CCC 2009*, pp. 6508–6513, Shanghai, China, December 2009.
 - [30] G. Scarciotti and A. Astolfi, “Model reduction of neutral linear and nonlinear time-invariant time-delay systems with discrete and distributed delays,” *Institute of Electrical and Electronics Engineers Transactions on Automatic Control*, vol. 61, no. 6, pp. 1438–1451, 2016.

Research Article

An Order Effect of Neighborhood Structures in Variable Neighborhood Search Algorithm for Minimizing the Makespan in an Identical Parallel Machine Scheduling

Ibrahim Alharkan,¹ Khaled Bamatraf,¹ Mohammed A. Noman ,¹ Husam Kaid ,¹
Emad S. Abouel Nasr,^{1,2} and Abdulaziz M. El-Tamimi¹

¹Industrial Engineering Department, College of Engineering, King Saud University, P.O. Box 800, Riyadh 11421, Saudi Arabia

²Faculty of Engineering, Mechanical Engineering Department, Helwan University, Cairo 11732, Egypt

Correspondence should be addressed to Mohammed A. Noman; mmohammed1@ksu.edu.sa

Received 11 September 2017; Revised 6 February 2018; Accepted 27 February 2018; Published 22 April 2018

Academic Editor: Ton D. Do

Copyright © 2018 Ibrahim Alharkan et al. This is an open access article distributed under the Creative Commons Attribution License, which permits unrestricted use, distribution, and reproduction in any medium, provided the original work is properly cited.

Variable neighborhood search (VNS) algorithm is proposed for scheduling identical parallel machine. The objective is to study the effect of adding a new neighborhood structure and changing the order of the neighborhood structures on minimizing the makespan. To enhance the quality of the final solution, a machine based encoding method and five neighborhood structures are used in VNS. Two initial solution methods which were used in two versions of improved VNS (IVNS) are employed, namely, longest processing time (LPT) initial solution, denoted as HIVNS, and random initial solution, denoted as RIVNS. The proposed versions are compared with LPT, simulated annealing (SA), genetic algorithm (GA), modified variable neighborhood search (MVNS), and improved variable neighborhood search (IVNS) algorithms from the literature. Computational results show that changing the order of neighborhood structures and adding a new neighborhood structure can yield a better solution in terms of average makespan.

1. Introduction

Identical parallel machine scheduling (IPMS) with the objective of minimizing the makespan is one of the combinatorial optimization problems. It is known to be NP-hard by Garey and Johnson [1] since it does not have a polynomial time algorithm. Exact algorithms such as branch and bound [2] and cutting plane algorithms [3] solve this type of IPM and find optimal solution for small size instances. As the problem size increases, the exact algorithms are inefficient and take much time to get a solution.

That disadvantages bring a need for heuristics and meta-heuristics that give optimal or near optimal solution within a reasonable amount of time. Longest Processing Time Rule (LPT) proposed by Mokotoff [4] is the first heuristic applied in IPMS which has a tight worst case performance of bound of $4/3-1/3m$, where m is the number of parallel machines. LPT is based on distributing jobs on machines according to maximum processing time and the remaining jobs go one by

one to the least loaded machine until assigning all the jobs to the machines. The LPT heuristic performs well for makespan criteria but the solution obtained is often local optima. Later, Coffman et al. [5] proposed MULTIFIT algorithm that is based on techniques from bin-packing. Blackstone Jr. and Phillips [6] proposed a simple heuristic for improving LPT sequence by exchange jobs between processors to reduce makespan. Lee and Massey [7] combine two heuristics, LPT and MULTIFIT, to form a new one. The heuristic uses LPT heuristic as an initial solution for the MULTIFIT heuristic. The performance of the combined heuristic is better than LPT and the error bound is not worse than the MULTIFIT. Yue [8] proved the bound for MULTIFIT to be 13/11. Lee and Massey [9] extend the MULTIFIT algorithm and show that the error bound of implementing the algorithm is only 1/10. Garey and Johnson [1] proposed that 3-phase composite heuristic consists of constructive phase and two improvement phases with no preliminary sort of processing times. They showed that their proposed heuristic is quicker than LPT. Ho and

Wong [10] introduce Two-Machine Optimal Scheduling which uses lexicographic search. Their method performs better than LPT, MULTIFIT, and MULTIFIT extension algorithm and it takes less amount of CPU time than MULTIFIT and MULTIFIT extension algorithms.

Riera et al. [11] proposed two approximate algorithms that use LPT as an initial solution and compare them with dynamic programming and MULTIFIT algorithms. Algorithm 1 uses exchange between two jobs to improve the makespan. Algorithm 2 schedules a job such that the completion time and process time of the selected job are near the bound. Their second algorithm is compared with MULTIFIT algorithms and results showed similarity to the MULTIFIT algorithm, but their algorithm reduces CPU time with respect to MULTIFIT heuristic. Cheng and Gen [12] applied memetic algorithm to minimize the maximum weighted absolute lateness on PMS and showed that it outperforms genetic algorithm and the conventional heuristics. Ghomi and Ghazvini [13] proposed a pairwise interchange algorithm, and it gave near optimal solution in a short period of time. Min and Cheng [14] proposed a genetic algorithm GA using machine code. They showed that GA outperforms LPT and SA and is suitable for large scale IPMS problems. Gupta and Ruiz-Torres [15] proposed a LISTFIT heuristic based on bin-backing and list scheduling. The LISTFIT generate an optimal or near optimal solution and outperforms LPT, MULTIFIT, and COMBINE heuristics. Costa et al. [16] proposed algorithm inspired by the immune systems of vertebrate animals. Lee et al. [17] proposed a simulated annealing (SA) approach for makespan minimization on IPMS. It chooses LPT as an initial solution. Computational results showed that the SA heuristic outperforms the LISTFIT and pairwise interchange (PI) algorithms. Moreover, it is efficient for large scale problems. Tang and Luo [18] propose a new ILS algorithm combining with a variable number of cyclic exchanges. Experiments show that the algorithm is efficient for $Pm \parallel C_{\max}$. Akyol and Bayhan [19] proposed a dynamical neural network that employs parameters of time varying penalty. The simulation results showed that the proposed algorithm generated feasible solutions and it found better makespan when compared to LPT. Kashan and Karimi [20] presented discrete particle swarm optimization (DPSO) algorithm for makespan minimization. Computational results showed that hybridized DPSO (HDPSO) algorithm outperforms both SA and DPSO algorithms. Sevkli and Uysal [21] proposed modified variable neighborhood search (MVNS) which is based on exchange and move neighborhood structures. Computational results demonstrated that the proposed algorithm outperforms both GA and LPT algorithms. Min and Cheng [14] proposed a harmony search (HS) algorithm with dynamic subpopulation (DSHS). Results show that DSHS algorithm outperforms SA and HDPSO for many instances. Moreover, the execution time is less than 1 sec. for all computations. Chen et al. [22] proposed discrete harmony search (DHS) algorithm that uses discrete encoding scheme to initialize the harmony memory (HM), then the improvisation scheme for generating new harmony is redefined for suitability for solving the combinational optimization problem. In addition, the study made hybridizing a

local search method with DHS to increase the speed of local search. Computational results show that the DHS algorithm is very competitive when compared with other heuristics in the literature. Jing and Jun-qing [23] proposed efficient variable neighborhood search that uses four neighborhood structures and has two versions. One version uses LPT sequence as an initial solution. The other version uses random sequence as an initial solution. A computational result demonstrates that EVNS is efficient in searching global or near global optimum. M. Sevkli and A. Z. Sevkli [24] proposed stochastically perturbed particle swarm optimization algorithm (SPPSO). The algorithm compared two recent PSO algorithms. It is concluded that SPPSO algorithm has produced better results than DPSO and PSOPsv in terms of the optimal solutions number. Laha [25] proposed an improved simulated annealing (SA) heuristic. Computational results show that the proposed heuristic is better than that produced by the best-known heuristic in the literature. Other advantages of it are the ease of implementation. In this paper, the proposed algorithm of Jing and Jun-qing [23] in their paper "efficient variable neighborhood search for identical parallel machines scheduling" is used with some changes on it. One of the changes is changing in the order of the neighborhood structures and the other change is adding another neighborhood structure to get five neighborhood structures in our proposed algorithm.

The remaining sections of this paper are organized as follows. In Section 2, a brief description of IPMS problem is mentioned. In Section 3, the steps of proposed algorithm are described in detail and the neighborhood structures of this proposed algorithm are explained. In Section 4, computational results are discussed. Conclusion is made in Section 5.

2. Problem Description

The identical parallel machine scheduling (IPMS) problem can be described as follows.

A set n of an independent jobs $J = \{J_1, J_2, \dots, J_n\}$ to be processed on m identical parallel machines $M = \{M_1, M_2, \dots, M_m\}$ with the processing time of job i on any identical machine is given by p_i .

A job can only be processed on one machine simultaneously and a machine cannot process more than one job at a time. Priority and precedence constraints are not allowed. There is no job cancellation and a job completes its processing on a machine without interruption.

The objective is to minimize the total completion time "the makespan" of scheduling jobs on the machines.

This scheduling problem can be described by a triple $\alpha \mid \beta \mid \gamma$ as follows:

$$Pm \parallel C_{\max}, \quad (1)$$

where P indicates parallel machine environment, m indicates number of machines, β indicates no constraints in this problem, and C_{\max} indicates that the objective is to minimize the makespan.

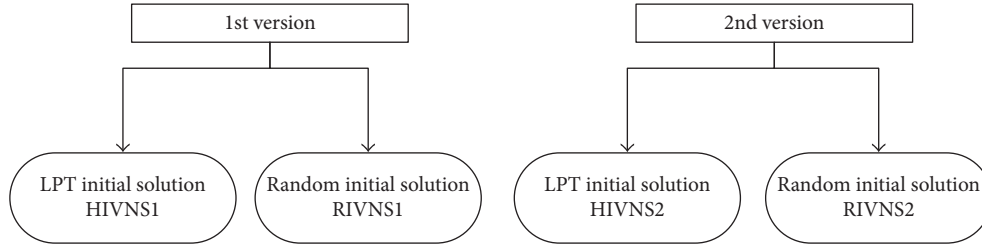


FIGURE 1: The two versions of the proposed algorithms.

This problem is interesting because minimizing the makespan has the effect of balancing the load over the various machines, which is an important goal in practice.

3. Development of the Proposed (IVNS) Algorithm

3.1. Basic VNS. Variable neighborhood search (VNS) is a metaheuristic proposed by Mladenović and Hansen [26] to enhance the solution quality by systematic neighborhoods changes. The main VNS algorithm steps can be summarized as follows: Initialization: choose the neighborhood structures set (NK^l) , $k = 1, 2, \dots, k'_{\max}$, obtain an initial solution, and select a stopping condition. Repeat the next steps until the stopping condition is satisfied:

- (1) Set $k \leftarrow 1$.
- (2) Repeat the following steps until $k = k'_{\max}$:
 - (a) Shaking: generate a point x' at random from the k th neighborhood of x ($x' \in N_k(x)$).
 - (b) Local search: apply some local search method with x' as initial solution; denote with x'' the so obtained local optimum.
 - (c) Move or not: if the local optimum x'' is better than the incumbent x , move there ($x \leftarrow x''$), and continue the search with $N1$ ($k \leftarrow 1$); otherwise, set $k \leftarrow k + 1$, improved variable neighborhood search (IVNS) algorithm.

As we mentioned earlier, the proposed algorithm is an addition of the proposed algorithm of Jing and Jun-qing [23].

The proposed algorithms have two versions and two types for each version as shown in Figure 1. In the first version, a new neighborhood structure was added to the four neighborhood structures which are proposed by Jing and Jun-qing [23] while in the second version the order of these neighborhood structures was changed. Both versions use LPT [20] and random initial solutions and are referred to as “HIVNS” and “RIVNS,” respectively. All these versions of the proposed algorithm use the same five neighborhood structures. These neighborhood structures will be discussed in the following section.

3.2. Neighborhood Structures. Determining the neighborhood structures is critical in the VNS algorithm. To enhance

the local searching abilities, five different kinds of neighborhoods are utilized to find better solutions on a given schedule in the proposed algorithm, which are designed based on such an idea that a given solution can be improved by moving or swapping jobs between the problem machines (the machines with their finished time equal to the makespan of the solution) and any other nonproblem machines (the machines with their finished time less than the makespan of the solution).

The five neighborhood structures are illustrated as follows:

- (1) Move: move a job J_i from M_p to M_{np} if condition $(C_{M_p} - C_{M_{np}} > p_i)$ is satisfied.
- (2) Exchange 1: exchange a job J_i selected from M_p with another job J_j selected from M_{np} if $(p_i - p_j > 0)$ and $(C_{M_p} - C_{M_{np}} > p_i - p_j)$.
- (3) Exchange 2: exchange two jobs, J_i and J_j , selected from M_p with one job J_k selected from M_{np} if $(p_i + p_j - p_k > 0)$ and $(C_{M_p} - C_{M_{np}} > p_i + p_j - p_k)$.
- (4) Exchange 3: exchange two jobs, J_i and J_j , selected from M_p with two jobs, J_k and J_t , selected from M_{np} if $(p_i + p_j - (p_k + p_t) > 0)$ and $(C_{M_p} - C_{M_{np}} > p_i + p_j - (p_k + p_t))$.
- (5) Exchange 4: exchange one job J_i , selected from M_p with two jobs, J_i and J_k , selected from M_{np} if $(p_i - (p_j + p_k) > 0)$ and $(C_{M_p} - C_{M_{np}} > p_i - (p_j + p_k))$.

The orders assigned to the types proposed of the algorithm are as follows:

- (1) The order of “HIVNS1” and “RIVNS1” is “move, exchange 1, exchange 2, exchange 3, and exchange 4.”
- (2) The order of “HIVNS2” and “RIVNS2” is “exchange 3, exchange 1, move, exchange 2, and exchange 4”. Improved VNS (IVNS) flow chart is shown as Figure 2.

3.3. Steps of IVNS. The steps of IVNS for “HIVNS1” and “RIVNS1” are shown as follows.

Step 1. Generate initial schedule X (generated randomly or obtain from the LPT rule), $\text{MaxIterNum} = 100$, $i = 0$, and $k_{\max} = 5$.

Step 2. Compute lower bound: $\text{LB}(C_{\max}) = \max\{[(1/m) \sum_{i=1}^n p_i]; \max_i\{p_i\}\}$.

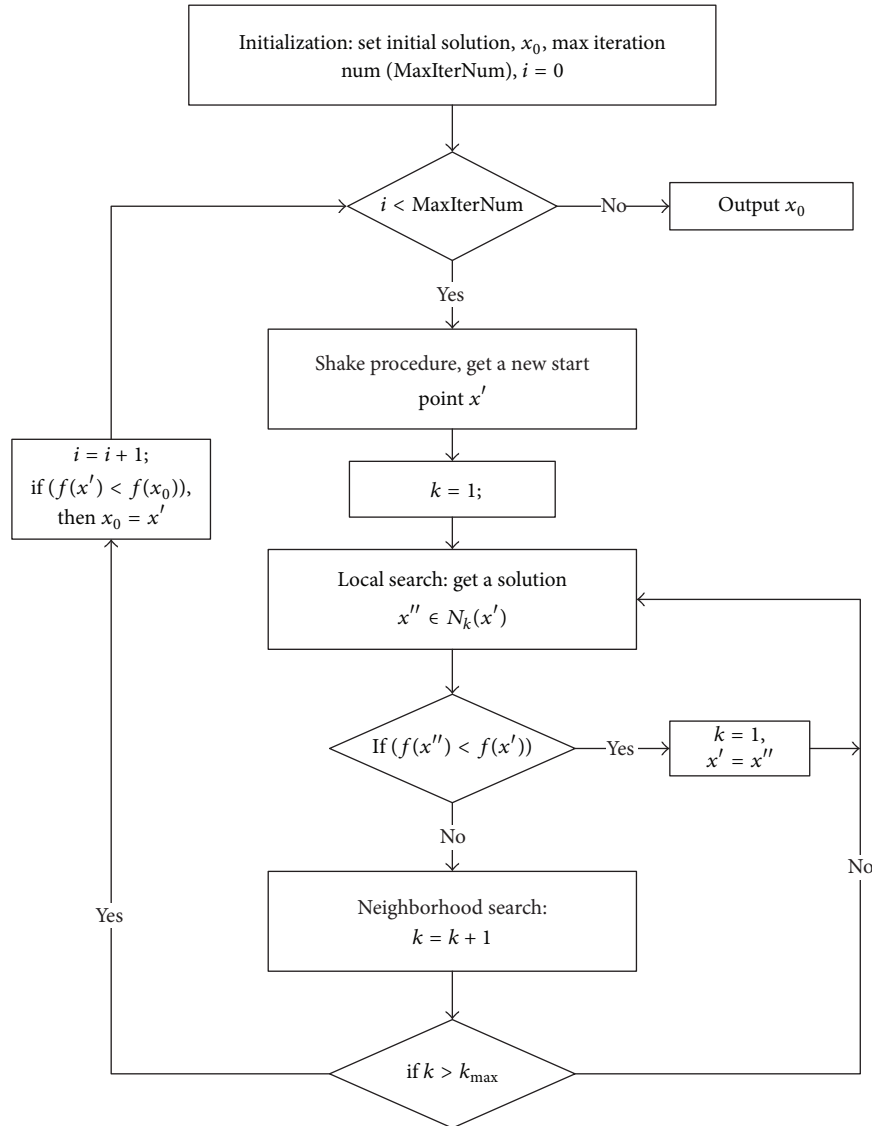


FIGURE 2: Flow chart of the basic VNS algorithm.

Step 3. Repeat until $f(X)$ (makespan of X) is equal to LB or $i > \text{MaxIterNum}$.

Step 3.1. For schedule X , distinguish the problem machine set (S_{pm}) and the nonproblem machine set (S_{npm}).

Step 3.2. For each machine M_p in S_{pm} do.

Step 3.2.1. For each machine M_{np} in S_{npm} do.

Step 3.2.1.1. Set $K = 1$, finish = false.

Step 3.2.1.2

Repeat

Switch (K) {

$K = 1$: $X' = \text{Move}(M_p, M_{np}, X)$; break;

$K = 2$: $X' = \text{Exchange } 1(M_p, M_{np}, X)$; break;

$K = 3$: $X' = \text{Exchange } 2(M_p, M_{np}, X)$; break;

$K = 4$: $X' = \text{Exchange } 3(M_p, M_{np}, X)$; break;

$K = 5$: $X' = \text{Exchange } 4(M_p, M_{np}, X)$; }

if ($f(X') < f(X)$) then set $X = X'$, finish = true, go to Step 3; otherwise, set $k = k + 1$, until $k = k_{\text{max}}$.

Step 3.3. If finish = false then $i = i + 1$.

Step 4. Output the best solution X found so far.

The steps of IVNS for “HIVNS2” and “RIVNS2” are shown as follows.

Step 1. Generate initial schedule X (generated randomly or obtain from the LPT rule), $\text{MaxIterNum} = 100$, $i = 0$, and $k_{\text{max}} = 5$.

TABLE 1: Number of machines and jobs.

Number of machines	2	5	10	20
Number of jobs	20, 50, 100, 200	20, 50, 100, 200	20, 50, 100, 200	50, 100, 200

Step 2. Compute lower bound: $LB(C_{\max}) = \max\{[(1/m) \sum_{i=1}^n pi]; \max_i\{pi\}\}$.

Step 3. Repeat until $f(X)$ (makespan of X) is equal to LB or $i > \text{MaxIterNum}$.

Step 3.1. For schedule X , distinguish the problem machine set (S_{pm}) and the nonproblem machine set (S_{npm}).

Step 3.2. For each machine M_p in S_{pm} do.

Step 3.2.1. For each machine M_{np} in S_{npm} do.

Step 3.2.1.1. Set $K = 1$, finish = false.

Step 3.2.1.2

Repeat

Switch (K) {

$K = 1$: $X' = \text{Exchange } 3(M_p, M_{np}, X)$;
break;

$K = 2$: $X' = \text{Exchange } 1(M_p, M_{np}, X)$;
break;

$K = 3$: $X' = \text{Move}(M_p, M_{np}, X)$; break;

$K = 4$: $X' = \text{Exchange } 2(M_p, M_{np}, X)$;
break;

$K = 5$: $X' = \text{Exchange } 4(M_p, M_{np}, X)$;

}

if ($f(X') < f(X)$) then set $X = X'$, finish = true, go to Step 3; otherwise, set $k = k + 1$,

until $k = k_{\max}$.

Step 3.3. If finish = false then $i = i + 1$.

Step 4. Output the best solution X found so far.

4. Computational Results and Comparison

In this section, the results of two versions of the proposed algorithm were compared with LPT [1], SA [17], GA [14], MVNS [21], and IVNS [23] algorithms from the literature. The two versions of the improved variable neighborhood search algorithms “HIVNS1 and RIVNS1” and “HIVNS2 and RIVNS2” were coded in MATLAB R2012a and executed on i5 CPU 5 GHz with 6 GB of RAM. All of them were stopped after getting the lower bound or running for 100 iterations for RIVNS1 and RIVNS2. The number of machines and number of jobs are shown in Table 1.

The processing time of the jobs is the same as Jing and Jun-qing [23]. As a result, 15 instances were conducted and each instance was conducted with 10 generations of different processing times. The total is 150 instances. The

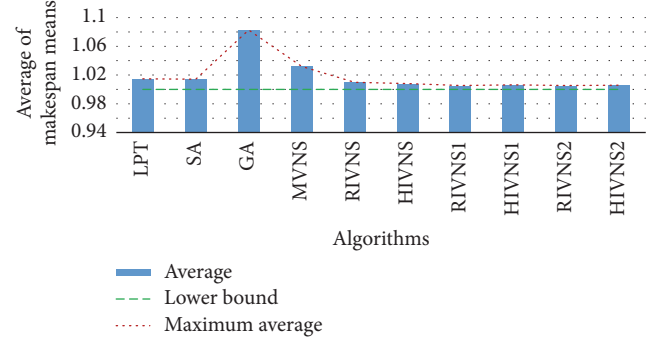


FIGURE 3: Histogram of averages of makespan means.

performance of the algorithms is measured with respect to the average makespan (mean) and average CPU time (Avg. time in second). The “mean” performance is a relative quality measure of solutions computed by C/LB , where C is the average makespan obtained for each instance with 10 generations given by the algorithm and LB is the lower bound of the instance, calculated in equation that mentioned in Section 3.3, Step 2. The “Avg. time” refers to the total time it takes for the algorithm to finish the solution. Table 2 presents the results of the previous algorithms from the literature while Table 3 presents the results from the proposed algorithms. By comparing the results of the average means of the makespan. It is obvious that the proposed algorithms outperform all the algorithms in Table 2 from the literature. It is worth noting that for each instance the proposed algorithms obtain no worse than algorithms in Table 2 except at 10 machines and 20 jobs instance in only HIVNS algorithm and that is due to the difficulty facing the proposed algorithms to get a lower bound when the difference between the number of machines and the number of jobs is relatively small. In addition, by comparing the two proposed algorithms, we can see that the versions have the same average means of the makespan in case of random initial solution while as the 2nd version outperforms the 1st version in case of LPT initial solution in both average means of makespan and average CPU time.

Figure 3 shows the averages of makespan mean the maximum averages for each algorithm and the lower bound. It can be observed that the two proposed versions algorithms have makespan means averages, which closed to the lower bound, especially in RIVNS1 and RIVNS2 that have the same average (1.0054).

Figure 4 shows the averages of Avg. time means for all algorithms. We can see that RIVNS1 and RIVNS2 have the smallest Avg. time, which are 0.008 and 0.007, respectively. Moreover, it can be observed that the Avg. time of HIVNS1 and HIVNS2 is much higher than HIVNS, because in this paper, Matlab is used to construct the code of HIVNS1 and

TABLE 2: The makespan results before the changing order of the neighborhood structures [23].

Instance number	m	n	SA			GA			MVNS			RIVNS			HIVNS		
			LPT	Mean	Avg. time												
1		20	1.0033	1.0006	1.0149	1.0000	0.2215	1.0000	0.0106	1.0000	0.0009	1.0000	0.0006	1.0000	0.0006	1.0000	0.0006
2	2	50	1.0001	1.0000	1.0738	1.0000	0.5131	1.0000	0.0226	1.0000	0.0016	1.0000	0.0003	1.0000	0.0003	1.0000	0.0003
3		100	1.0000	1.0000	1.9382	1.0000	2.7948	1.0000	0.0445	1.0000	0.0031	1.0000	0.0005	1.0000	0.0005	1.0000	0.0005
4		200	1.0000	1.0000	0.9218	1.0000	2.3145	1.0000	0.0905	1.0000	0.0059	1.0000	0.0003	1.0000	0.0003	1.0000	0.0003
5		20	1.0315	1.0264	1.3614	1.0356	0.3412	1.0127	0.0124	1.0045	0.0083	1.0043	0.0073	1.0043	0.0073	1.0043	0.0073
6	5	50	1.0053	1.0045	2.5502	1.0312	0.6935	1.0050	0.0283	1.0012	0.0027	1.0009	0.0022	1.0009	0.0022	1.0009	0.0022
7		100	1.0005	1.0005	4.2271	1.0242	1.3862	1.0052	0.0534	1.0002	0.0042	1.0000	0.0015	1.0000	0.0015	1.0000	0.0015
8		200	1.0003	1.0003	14.4302	1.0168	2.6560	1.0084	0.1064	1.0001	0.0075	1.0000	0.0035	1.0000	0.0035	1.0000	0.0035
9		20	1.0794	1.0792	1.9328	1.1336	0.3575	1.0987	0.0131	1.0799	0.0402	1.0590	0.0384	1.0590	0.0384	1.0590	0.0384
10	10	50	1.0207	1.0207	4.1428	1.1169	1.6303	1.0315	0.0315	1.0078	0.0075	1.0036	0.0067	1.0036	0.0067	1.0036	0.0067
11		100	1.0110	1.0110	20.1301	1.1421	1.4547	1.0181	0.0647	1.0031	0.0061	1.0011	0.0043	1.0011	0.0043	1.0011	0.0043
12		200	1.0007	1.0007	1.0165	1.0611	3.3761	1.0127	0.1561	1.0004	0.0117	1.0002	0.0034	1.0002	0.0034	1.0002	0.0034
13		50	1.0510	1.0510	2.4803	1.3167	0.9728	1.1671	0.0441	1.0312	0.1389	1.0304	0.1392	1.0304	0.1392	1.0304	0.1392
14	20	100	1.0123	1.0123	4.2799	1.2270	1.8111	1.0857	0.0905	1.0087	0.0179	1.0046	0.0087	1.0046	0.0087	1.0046	0.0087
15		200	1.0063	1.0063	14.6684	1.1353	3.4492	1.0415	0.1840	1.0039	0.0163	1.0024	0.0113	1.0024	0.0113	1.0024	0.0113
<i>Average</i>				1.0148	1.0142	5.0779	1.0827	1.5982	1.0319	0.0635	1.0095	0.0182	0.0152	1.0071	0.0152	1.0071	0.0152

TABLE 3: The makespan results after the effect of the changing order of the neighborhood structures.

Instance number	m	n	RIVNS1		HIVNS1		RIVNS2		HIVNS2	
			Mean	Avg. time						
1	2	20	1.0000	0.0005	1.0000	0.0004	1.0000	0.0008	1.0000	0.0005
2		50	1.0000	0.0002	1.0000	0.0002	1.0000	0.0002	1.0000	0.0002
3		100	1.0000	0.0004	1.0000	0.0005	1.0000	0.0004	1.0000	0.0083
4		200	1.0000	0.0002	1.0000	0.0004	1.0000	0.0002	1.0000	0.7030
5	5	20	1.0005	0.0014	1.0000	0.0025	1.0005	0.0014	1.0000	0.0016
6		50	1.0000	0.0005	1.0000	0.0028	1.0000	0.0008	1.0000	0.0175
7		100	1.0000	0.0235	1.0000	0.1104	1.0000	0.0258	1.0000	0.1705
8		200	1.0000	0.0002	1.0000	2.5874	1.0000	0.0002	1.0000	2.5057
9	10	20	1.0625	0.0016	1.0682	0.0040	1.0625	0.0015	1.0602	0.0040
10		50	1.0004	0.0103	1.0000	0.0156	1.0000	0.0064	1.0000	0.0580
11		100	1.0000	0.0052	1.0000	0.1122	1.0000	0.0054	1.0000	0.0713
12		200	1.0000	0.0238	1.0000	1.8051	1.0000	0.0207	1.0000	1.556
13	20	50	1.0175	0.0158	1.0256	0.0542	1.0175	0.0153	1.0263	0.0672
14		100	1.0003	0.0288	1.0000	0.2312	1.0003	0.0270	1.0000	0.0222
15		200	1.0000	0.0004	1.0000	1.0538	1.0000	0.0004	1.0000	0.7414
<i>Average</i>			1.0054	0.0075	1.0063	0.3987	1.0054	0.0071	1.0058	0.3951

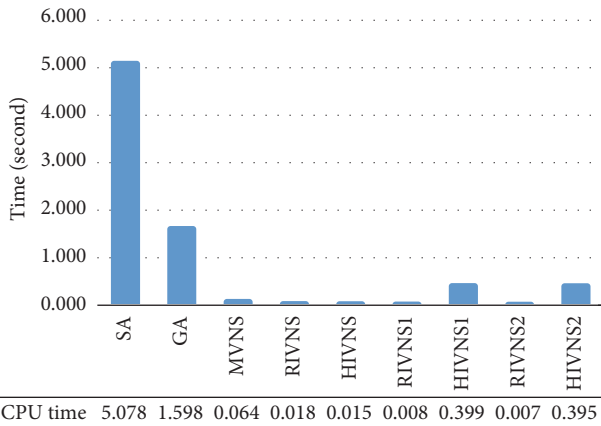


FIGURE 4: Histogram of averages of Avg. time means.

HIVNS2, and the authors of [23] used C++ to construct HIVNS. Thus, the benefits of Avg. time offered by C++ far outweigh the simplicity of Matlab. Avg. time is especially important when dealing with algorithms, since many calculations involve immense optimization with complex equations and algorithms or calculations with a large number of iterations. As the amount of data increases, the computation time (Avg. time) for Matlab code increases significantly; therefore, Matlab code takes more time for those calculations; for example, in Table 3 the cases of $m = 2, 5, 10, 20, n = 200$ are need to large number of iterations. C++ is the way to go for algorithms calculations because of its speed and versatility.

5. Conclusion

In this paper, two versions of improved variable neighborhood search (IVNS) algorithms are proposed for scheduling

identical parallel machines IPM with the objective of studying the effect of adding a new neighborhood structure and changing the order of neighborhood structures on minimizing the makespan C_{max} . In the proposed algorithms, a machine based encoding method and five neighborhood structures are used to enhance the quality of the final solution. Computational results showed that the proposed algorithms outperform all the algorithms in the literature and obtain no worse than algorithms except when the number of machines and the number of jobs are relatively small which is due to the difficulty facing the proposed algorithms to get a lower bound in that case. In addition, we concluded that the second version outperforms the first version in case of LPT initial solution and therefore changing the order of neighborhood structures has an effect on minimizing the makespan. Further research is to implement the proposed algorithms in scheduling of unrelated parallel machines.

Conflicts of Interest

The authors declare that there are no conflicts of interest regarding the publication of this paper.

Acknowledgments

The authors extend their appreciation to the Deanship of Scientific Research at King Saud University for funding this work through Research Group no. RG-1439-009.

References

[1] M. R. Gary and D. S. Johnson, *Computers and Intractability: A Guide to the Theory of NP-completeness*, WH Freeman and Company, New York, NY, USA, 1979.

- [2] R. L. Graham, "Bounds on multiprocessing timing anomalies," *SIAM Journal on Applied Mathematics*, vol. 17, pp. 416–429, 1969.
- [3] S. L. van de Velde, "Duality-based algorithms for scheduling unrelated parallel machines," *ORSA Journal on Computing*, vol. 5, no. 2, pp. 192–205, 1993.
- [4] E. Mokotoff, "An exact algorithm for the identical parallel machine scheduling problem," *European Journal of Operational Research*, vol. 152, no. 3, pp. 758–769, 2004.
- [5] J. Coffman, M. R. Garey, and D. S. Johnson, "An application of bin-packing to multiprocessor scheduling," *SIAM Journal on Computing*, vol. 7, no. 1, pp. 1–17, 1978.
- [6] J. H. Blackstone Jr. and D. T. Phillips, "An improved heuristic for minimizing makespan among m identical parallel processors," *Computers & Industrial Engineering*, vol. 5, no. 4, pp. 279–287, 1981.
- [7] C.-Y. Lee and J. D. Massey, "Multiprocessor scheduling: combining LPT and MULTIFIT," *Discrete Applied Mathematics*, vol. 20, no. 3, pp. 233–242, 1988.
- [8] M. Y. Yue, "On the exact upper bound for the multifit processor scheduling algorithm," *Annals of Operations Research*, vol. 24, no. 1–4, pp. 233–259, 1990.
- [9] C.-Y. Lee and J. D. Massey, "Multiprocessor scheduling: An extension of the MULTIFIT algorithm," *Journal of Manufacturing Systems*, vol. 7, no. 1, pp. 25–32, 1988.
- [10] J. C. Ho and J. S. Wong, "Makespan minimization for m parallel identical processors," *Naval Research Logistics (NRL)*, vol. 42, no. 6, pp. 935–948, 1995.
- [11] J. Riera, D. Alcaide, and J. Sicilia, "Approximate algorithms for the $P \parallel C_{\max}$ problem," *TOP*, vol. 4, no. 2, pp. 345–359, 1996.
- [12] R. Cheng and M. Gen, "Parallel machine scheduling problems using memetic algorithms," *Computers & Industrial Engineering*, vol. 33, no. 3–4, pp. 761–764, 1997.
- [13] S. F. Ghomi and F. J. Ghazvini, "A pairwise interchange algorithm for parallel machine scheduling," *Production Planning & Control*, vol. 9, pp. 685–689, 1998.
- [14] L. Min and W. Cheng, "A genetic algorithm for minimizing the makespan in the case of scheduling identical parallel machines," *Artificial Intelligence in Engineering*, vol. 13, no. 4, pp. 399–403, 1999.
- [15] J. N. D. Gupta and J. Ruiz-Torres, "A LISTFIT heuristic for minimizing makespan on identical parallel machines," *Production Planning and Control*, vol. 12, no. 1, pp. 28–36, 2001.
- [16] A. M. Costa, P. A. Vargas, F. J. Von Zuben, and P. M. Franca, "Makespan minimization on parallel processors: An immune-based approach," in *Proceedings of the 2002 Congress on Evolutionary Computation (CEC '02)*, pp. 920–925, IEEE, May 2002.
- [17] W.-C. Lee, C.-C. Wu, and P. Chen, "A simulated annealing approach to makespan minimization on identical parallel machines," *The International Journal of Advanced Manufacturing Technology*, vol. 31, no. 3–4, pp. 328–334, 2006.
- [18] L. Tang and J. Luo, "A new ILS algorithm for parallel machine scheduling problems," *Journal of Intelligent Manufacturing*, vol. 17, no. 5, pp. 609–619, 2006.
- [19] D. E. Akyol and G. M. Bayhan, "Minimizing makespan on identical parallel machines using neural networks," in *Proceedings of the International Conference on Neural Information Processing*, vol. 4234 of *Lecture Notes in Computer Science*, pp. 553–562, Springer, 2006.
- [20] A. H. Kashan and B. Karimi, "A discrete particle swarm optimization algorithm for scheduling parallel machines," *Computers & Industrial Engineering*, vol. 56, no. 1, pp. 216–223, 2009.
- [21] M. Sevkli and H. Uysal, "A modified variable neighborhood search for minimizing the makespan on identical parallel machines," in *Proceedings of the 2009 International Conference on Computers and Industrial Engineering (CIE '09)*, pp. 108–111, IEEE, July 2009.
- [22] J. Chen, Q.-K. Pan, and H. Li, "Harmony search algorithm with dynamic subpopulations for scheduling identical parallel machines," in *Proceedings of the 2010 6th International Conference on Natural Computation (ICNC '10)*, pp. 2369–2373, IEEE, August 2010.
- [23] C. Jing and L. Jun-qing, "Efficient variable neighborhood search for identical parallel machines scheduling," in *Proceedings of the Control Conference (CCC '12)*, pp. 7228–7232, IEEE, 2012.
- [24] M. Sevkli and A. Z. Sevkli, *A Stochastically Perturbed Particle Swarm Optimization for Identical Parallel Machine Scheduling Problems*, INTECH Open Access Publisher, 2012.
- [25] D. Laha, "A simulated annealing heuristic for minimizing makespan in parallel machine scheduling," in *Proceedings of the International Conference on Swarm, Evolutionary, and Memetic Computing*, pp. 198–205, Springer, 2012.
- [26] N. Mladenović and P. Hansen, "Variable neighborhood search," *Computers & Operations Research*, vol. 24, no. 11, pp. 1097–1100, 1997.

Research Article

A New Hybrid PSS Optimization Method Based on Improved Active Set Algorithm

Xiang-Yu Liu,¹ Yu-Ling He ,² and Jian Yao³

¹State Grid Hebei Electric Power Research Institute, Shijiazhuang 050021, China

²Institute of Equipment Fault Diagnosis and Testing Technology, North China Electric Power University, Baoding 071003, China

³Jiangsu Lianneng Electric Power Research Institute, Nanjing 210018, China

Correspondence should be addressed to Yu-Ling He; heyuling1@163.com

Received 28 July 2017; Revised 26 January 2018; Accepted 26 February 2018; Published 3 April 2018

Academic Editor: Ton D. Do

Copyright © 2018 Xiang-Yu Liu et al. This is an open access article distributed under the Creative Commons Attribution License, which permits unrestricted use, distribution, and reproduction in any medium, provided the original work is properly cited.

This paper proposes a new hybrid optimization method for the phase-frequency characteristics of the double input power system stabilizer (PSS) based on the improved active set algorithm. This method takes the effect of the filtering section optimization on the parameter improvement into account, and the optimized model focuses on the minimum residual sum of squares between the actual and the target phase-frequency characteristics. The result shows that the improved parameters obtained from the proposed method provide much better phase-frequency characteristics than the widely used engineering parameters. The comparison between the proposed method and the typical commercial software indicates the universal superiority of the proposed method. And the studies on the impact of considering the filter section optimization on the phase-frequency improvement show that taking the filter section optimization into account will be beneficial for the phase-frequency improvement, though in application to the PSS2A model and the PSS2B model there are some differences. The achievements obtained in this paper provide a significant reference for the practical PSS parameter modification and improvement.

1. Introduction

With the fast development of the ultrahigh voltage grid, the high-capacity power transmission among different districts becomes more and more popular, resulting in the significant change of the low-frequency oscillation mode of the regional power grids [1, 2]. Generally, two kinds of low-frequency oscillation modes at the range of 0.1 Hz-2 Hz, that is, the partial mode and the regional mode, will be caused due to the low damping [3].

In recent years, the enlargement of the power grid has gradually reduced the natural frequency of the system and meanwhile caused the low-frequency oscillation accident to be more serious [4]. Correspondingly, most of the generators whose capacities are more than 300 MW in China have installed a PSS. However, many parameters need to be modified accordingly to make PSS perform more efficiently and robustly. How to optimize the PSS parameters is the significant problem to provide the system with the best damping and the partial and regional grids with the better reliability and strength.

In the multigenerator system, there are generally two kinds of PSS parameter design methods [5]. The first kind is to calculate the PSS parameters according to the predefined indexes such as the damping ration and the pole locations, specifically aiming at a certain performing condition. This kind of method is advantaged in the strict theory and the accurate calculation, while actually it is weak in the robustness and the convergence [6]. The other kind is to make the PSS parameters satisfy the wide variety of the performing conditions. This kind of method, which is generally based on the phase compensation and focuses on the robustness, has been widely used [7]. By far, most of the practical PSS types are of PSS2A and PSS2B, for which scholars have developed different methods [5–13] to improve their properties. Typically, for the phase-frequency characteristics compensation, researchers have proposed various optimization studies [5, 6, 8, 9] and have founded a fine basis for the practical application.

However, most of the proposed work only focused on the phase shifters, while the practicability has not yet been

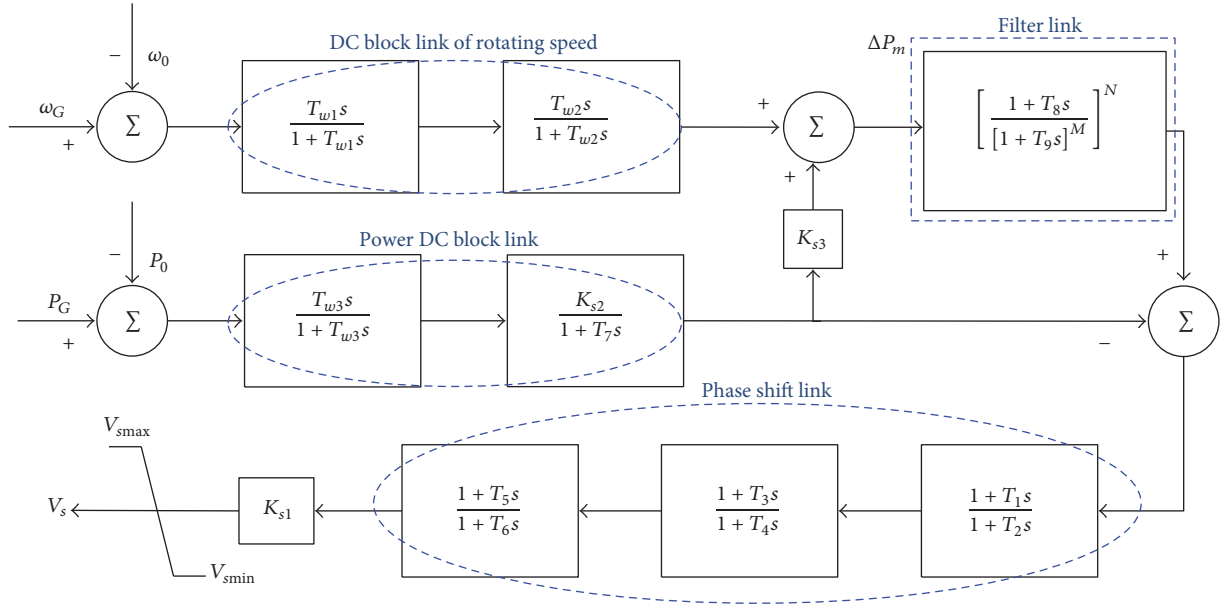


FIGURE 1: The block diagram of double input PSS2B model.

well verified. Although scholars have also developed a new improved PSS model with the double-signal input to optimize the low-frequency and high-frequency features [7, 10], the new model is still in the theory demonstration period and relatively lacks implement basis. To make an improvement, researchers presented parameter optimization methods for PSS4B and have verified the effectiveness by simulations and experiments [11–13]. However, since PSS4B is based on a parallel connected mode and is much more complex [7, 13], it has not yet been widely used in the practical engineering.

This paper proposes a new hybrid optimization method for the phase-frequency characteristic improvement based on Active Set Algorithm and Chaos Algorithm. This method not only improves the phase shifters, but also optimizes the DC blockers. The application effect comparison between the proposed method and the commonly used commercial software both for PSS2A and for PSS2B verifies the effectiveness and the advantages of the method.

2. Engineering Phase-Frequency Characteristic Improvement of Double Input PSS

2.1. Double Input PSS. Due to the suppression effect on the inverse reactive adjustment based on the compound of the power input branch and the rotating speed input branch [5], the double input PSS, especially the PSS2A type, has been widely used in the power systems. Typically, the PSS2B model is illustrated in Figure 1, where the rotating-speed DC blocker and the power DC blocker are used to filter the DC components, the filter section is used to filter the noises and the torsional oscillation signals in the frequency-deviation series, and the phase shifter is used to modify the frequency characteristics. When T_5 equals T_6 , the third phase shifter will be invalid. In this case, the PSS2B model is equivalent to the PSS2A model which has only two phase shifters.

Currently, the technique standard [14] primarily considers the phase-frequency characteristic improvement, while ignoring the amplitude-frequency characteristic optimization. It is mainly because the amplitude-frequency characteristic will be affected little by the parameter variation but mostly influenced by the model structures (the practical PSS has a certain model structure) [7, 10]. Limited by the unit security request and the calculation complexity constraint, no matter in the theory study [11, 12] or the practical application [5, 6, 8, 15], most optimization methods primarily focus on the parameter improvement of the phase shifters, while specific attention has been rarely paid to the DC blockers.

Objectively, both the system oscillation and the active mechanical torsion adjustment will cause power variations to the generator. And the power variation will further make the PSS modify the reactive power output of the generator through the exciting system. However, the reactive power modification caused by the active mechanical torsion adjustment, which is usually called reactive power inverse-modification problem, will be harmful to the generator. To solve this very problem, the composite additive signal of the rotating speed and the power, namely, ΔP_m , is employed as the input of the torsional filter link. Its basic scheme is to make the additive signal ΔP_m indicated in Figure 1 near zero, so that the reactive power inverse-modification effect can be mostly restrained. Therefore, theoretically, the parameter modification of the filter section will not affect the damping effect of the whole PSS [16]. This means the filter section can be ignored during the analysis on the key transfer function of the system. Only taking the power input branch into account, the transfer function of PSS can be written as

$$G(s) = K_{s1} \frac{T_{w3}s}{1+T_{w3}s} \cdot \frac{K_{s2}}{1+T_7s} \cdot \frac{1+T_1s}{1+T_2s} \cdot \frac{1+T_3s}{1+T_4s} \cdot \frac{1+T_5s}{1+T_6s} \quad (1)$$

TABLE 1: Parameters for engineering application in Dingzhou power plant.

Parameters	T_1	T_2	T_3	T_4	T_5	T_6	T_{W3}	T_7
Values	0.2	0.03	0.2	0.02	0	0	5	5

and the phase-frequency expression of the PSS2B model based on (1) is

$$\begin{aligned} \phi_p = & \frac{\pi}{2} - \arctan(\omega T_{w3}) - \arctan(\omega T_7) \\ & + \arctan(\omega T_1) - \arctan(\omega T_2) + \arctan(\omega T_3) \\ & - \arctan(\omega T_4) + \arctan(\omega T_5) - \arctan(\omega T_6). \end{aligned} \quad (2)$$

Setting T_5 equivalent to T_6 , the phase-frequency characteristic formula of the PSS2A model can be obtained:

$$\begin{aligned} \phi_p = & \frac{\pi}{2} - \arctan(\omega T_{w3}) - \arctan(\omega T_7) \\ & + \arctan(\omega T_1) - \arctan(\omega T_2) + \arctan(\omega T_3) \\ & - \arctan(\omega T_4). \end{aligned} \quad (3)$$

When the DC blockers are not taken into optimization, the parameters T_{w3} and T_7 in (2) and (3) will be usually set as constants.

2.2. Phase-Frequency Characteristic Improvement in Engineering. The phase-frequency improvement is usually performed based on the operators' practical experiences and the commercial software. For instance, the practical engineering method is to use engineers' professional experiences to set the PSS parameters in the commercial software firstly and then verify the parameters according to the technical standards required in [14].

Taking 1# generator unit in Dingzhou power plant, Hebei Province, China, as an example, the detailed parameters are shown in Table 1 [15]. It can be found from Table 1 that the third-phase shifter is ignored and the model is actually a PSS2A type. The phase-frequency characteristic curves with compensation and without compensation, respectively, are indicated in Figure 2.

3. PSS Phase-Frequency Optimization Based on Improved Active Set Algorithm

3.1. Optimization Target and Restraint. The relation between the input signal and the phase compensation is indicated in Figure 3, where M_{adv} and M_{lag} are the lower and the upper thresholds of M , respectively. The phase compensation is to make the angle between the damper torque M and the rotating difference $\Delta\omega$ zero by modifying the PSS parameters. When the frequency lies in $[0.2, 2]$, M_{adv} is usually set as 20° and M_{lag} is set as -45° . However, when the frequency lies in $[0, 0.2)$, M_{adv} is set as 40° and M_{lag} is still set as -45° [14]. Usually, $-\Delta P$ is taken as the reference of the delay angle. Then the range between M_{adv} and M_{lag} is transferred to $[-70^\circ, -135^\circ]$.

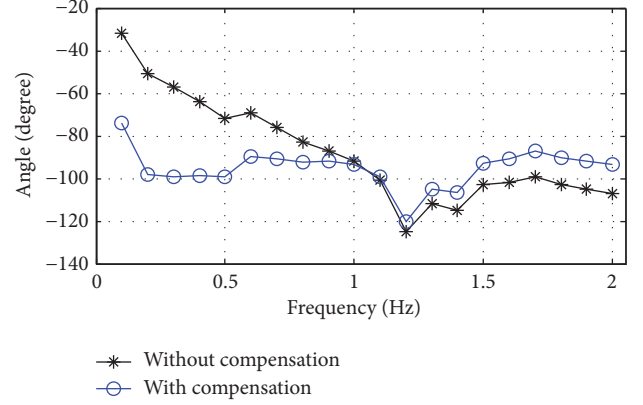


FIGURE 2: Phase-frequency characteristic of the PSS set by practical tuning method.

The ideal phase characteristic is to be consistent with $\Delta\omega$. This means the purpose of phase-frequency optimization is to set the phase angle at each frequency point to be -90° via properly modifying the PSS parameters. Commonly, the minimum residual sum of squares between the actual and the target phase-frequency curves is taken as the optimization objective which can be expressed as

$$\min \left(\sum_{j=1}^m (\varphi_0(f_j) + \varphi_p(f_j) + 90) ^2 \right), \quad (4)$$

where m is the number of the sampling frequency points from 0 to 2 Hz. In engineering, there are usually 20 frequency points, with the intervals of 0.1 Hz. $\varphi_p(f_j)$ stands for the compensation phase angle produced by PSS at f_j , which depends on the detailed PSS parameters and can be written as (3) for the PSS2A model, while $\varphi_0(f_j)$ stands for the delayed phase angle of the generator set without compensation at f_j . Technically, to test $\varphi_0(f_j)$, the periodic frequency-modification signal which includes the sine waves from 0 to 2 Hz is set as the input of the automatic voltage regulator (instead of the PSS signal). Then the magnitude of the input signal will be amplified until the output voltage of the generator has a slight fluctuation. Finally, the phase angle between the input signal and the output voltage of the generator is detected. This angle is the delayed angle of the generator. More details can be found in the Chinese national standard; see [14].

According to [17], only the phase shifter is taken as the optimization object, and the parameters of T_{W3} and T_7 are set as Table 1, while the parameters of $T_1 \sim T_4$ are set within the range of $[0.01, 1]$.

3.2. Improved Active Set Algorithm. The solution of the nonlinear parametric optimization problem should consider both the efficiency and the initial values. Unreasonable initial values often lead to the local poles and the loss of the global optimal solution. Since the chaotic system has the characteristics of randomness and ergodic regularity, it can travel more evenly in the range of the variables without a repetition. In addition, it can effectively avoid the local

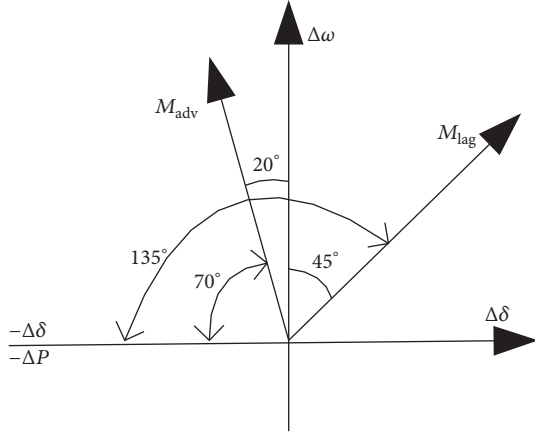


FIGURE 3: Diagram between input signal and phase compensation.

optimal values of the calculated parameters. However, chaos algorithm will be unsatisfactory when the search space is large [18]. The Active Set Algorithm, which is an effective tool to solve the boundary restricted problems [19, 20], is combined with the chaos algorithm in this paper to solve the boundary optimization problem shown in

$$\begin{aligned} \min \quad & f(x) \\ \text{s.t.} \quad & l \leq x \leq u. \end{aligned} \quad (5)$$

3.2.1. Initial Value Calculation Based on Chaos Algorithm. Typically, the classical logistic map which indicates the one-dimensional chaotic system can be written as

$$x_{n+1} = \mu x_n (1 - x_n), \quad (6)$$

where the control parameter $\mu = 4$, $0 \leq x_i \leq 1$, and $n = 0, 1, 2, 3, \dots$

Obviously, the system indicated in (6) is in the state of chaos and sensitive to the initial values. By giving i initial values, the system can be assigned with i subtle different chaotic variables. Introducing the chaotic variables into the optimization, the chaotic motion range will be expanded to the scope of the optimized variable ranges. The specific steps are as follows.

Step 1. Respectively, assign i subtle different initial values to x_i , and obtain i different chaotic variables $x_{i,n+1}$.

Step 2. The ranges of chaotic variables are, respectively, mapped to the optimized variable ranges by

$$x'_{i,n+1} = c_i + d_i x_{i,n+1}, \quad (7)$$

where c_i and d_i are the constant mobile coefficients and the amplification coefficients, respectively.

Step 3. Calculate $f(x'_{i,n+1})$ based on the iteration search of the chaotic variables and meanwhile make a record for both the parameters and $f(x'_{i,n+1})$.

TABLE 2: Parameter optimization results of two phase shifters.

Parameters	T_1	T_2	T_3	T_4
Optimization results	0.22	0.03	0.23	0.02

Step 4. If the optimal performance indicators remain constant after several iterations as Step 3, then set the values as the initial solutions.

3.2.2. Solutions by Active Set Algorithm. In the boundary restricted problem shown in (5), $f(x)$ is a real-number function, $x \in R^n$ is the n -order real value vector, and l and u are the boundary vectors, respectively. Since the upper and the lower boundaries of the parameters are also the restraint conditions of (5), this equation is a boundary restricted optimization problem. The active set at the point x^* is defined as

$$I(x^*) = L(x^*) \cup U(x^*), \quad (8)$$

where $L(x^*) = \{i : x_i^* = l_i\}$ and $U(x^*) = \{i : x_i^* = u_i\}$.

Assuming that (5) is the active set of the optimized answers, the problem can be transferred to an equality constraint optimization question, so that the solving difficulty is greatly reduced. However, since the optimal solving result x^* is unknown, the active set $I(x^*)$ is also unknown and requires an estimation performance.

The key thought of the active set algorithm is to begin with the initial value x^0 and keep generating an estimated active set $A(x^p)$ for each iteration until obtaining an optimized solving result. Therefore, the key point to solve the problem is to select a proper active set strategy [21]. In this paper, we employ the approximate active set strategy proposed by Ni and Yuan [22] to solve the problem. The approximate active set A and the inactive set B can be written as

$$\begin{aligned} A(x) &= \{i : l_i \leq x_i \leq l_i + \varepsilon_b\} \cup \{i : u_i - \varepsilon_b \leq x_i \leq u_i\} \\ B(x) &= \{1, \dots, n\} \setminus A(x) = \{i : l_i + \varepsilon_b \leq x_i \leq u_i - \varepsilon_b\}, \end{aligned} \quad (9)$$

where $0 < \varepsilon_b < \min_i [(u_i - l_i)/3]$. During the calculation, the algorithm divides the search directions into three ones, that is, the quasi-Newton direction in the subspace expanded with the invalid parameters, the gradient direction, and the modified gradient direction in the subspace expanded with the valid parameters. The invalid parameters are updated by the limited internal storage quasi-Newton method, while the valid parameters are updated by the projection gradient method.

3.3. Optimization Result and Discussion of Two Phase Shifters.

Taking the modified parameters shown in Table 1 as the initial values of PSS, the optimized results for the phase-frequency characteristics indicated in (4) based on the Active Set Algorithm mentioned in Section 3.2 are shown in Table 2. And the phase-frequency characteristic curves of PSS after optimization of the two phase shifters are indicated in Figure 4.

As indicated in Figure 4, it is obvious that the phase-frequency characteristic curve optimized with two phase

TABLE 3: Key information of the oscillation mode.

Method	Frequency	Damping ratio
Without PSS	1.33	0.0576
PSS performed with the practical engineering method	1.39	0.2167
PSS performed with the two-phase-shifter optimized method	1.35	0.2665

TABLE 4: Robustness verification under different disturbance degrees.

Step amplitude variation percentage of the exciting voltage	22%	44%	66%
Damping ratio obtained from commercial software	0.1705	0.1687	0.1659
Damping ratio obtained from this paper	0.2336	0.2285	0.2218

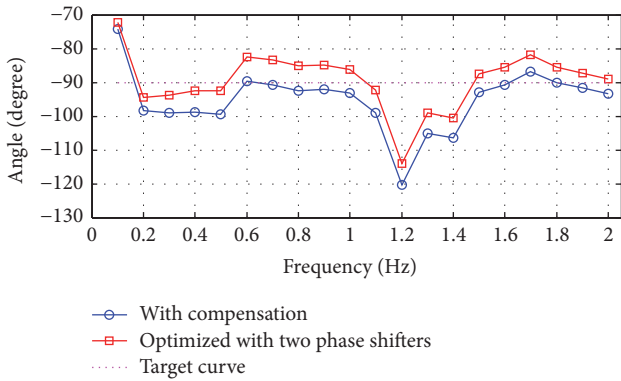


FIGURE 4: Phase-frequency characteristic curves before and after optimizations of the two phase shifters.

shifters is closer to the target curve. The sampling points beyond $[-80^\circ, -100^\circ]$ are reduced from 4 to 2, and the max phase angle deviation at 1.2 Hz is also changed from -120.4° to -114° .

Taking the least squares calculation value between the phase-frequency characteristic curve and the target curve as the evaluation index (the smaller, the better), the index value after optimization is 1433, which is reduced by 32.5% compared to the index value of 2122 before optimization.

3.4. Simulating Verification of Optimized Result. To further verify the practical effect, the actual offline data is employed for the simulating calculation. The result is obtained through the Prony analysis method by means of loading a step excitation and a transient fault disturbance. Keeping the gain coefficient K_{s1} (see Figure 1) stable in different cases, the responses are illustrated in Figure 5, and the key information about the oscillation mode is shown in Table 3.

It is suggested from Figure 5 that, by loading the same disturbance, PSS has an obvious inhibiting effect on the power oscillation. Without PSS, it needs more than 5 cycles to quiet down the oscillation, while with PSS it needs only 3 oscillation cycles. Employing the PSS of which the two phase shifters are optimized by the proposed method in this paper, it only needs two cycles to remove the oscillation. Moreover, the oscillation magnitudes are apparently smaller. As indicated in Table 3, the damping ratio after optimization is 0.2665, which is

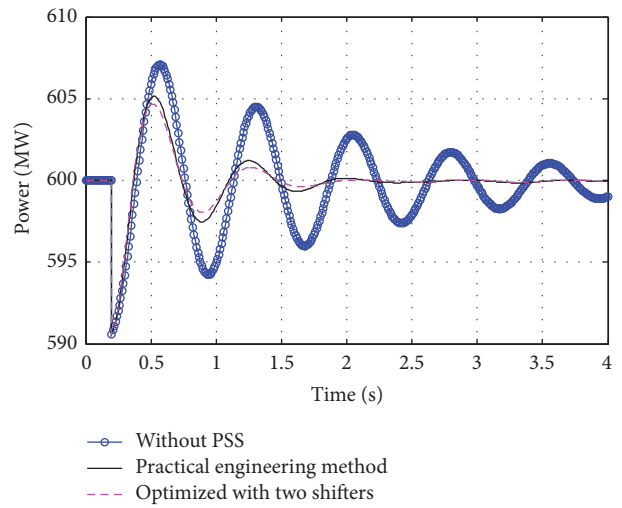


FIGURE 5: Power oscillation responses for a transient disturbance.

increased by 23% compared to the practical engineering method.

In addition to the effectiveness of the optimization method, the robustness is also a key point. To verify the robustness of the proposed method, a comparison between the proposed method and the commercial software (*PSS Parameter Calculation Program* developed by China Electric Power Research Institute) is taken. The step amplitude variation percentage of the exciting voltage is used as a disturbance, and the damping ratios obtained from the commercial software and the proposed method are indicated in Table 4. It is shown that the proposed method has a better damping ratio, suggesting the better robustness of the proposed method.

4. Effect Comparisons with Commercial Software

Employing the commercial software *PSS Parameter Calculation Program* which is widely used in China and the proposed method in this paper, respectively, to calculate the optimization parameters of 1# generator set in Dingzhou Power Plant, the results are shown in Table 5, and the phase-frequency

TABLE 5: Optimized parameter obtained by commercial software.

Parameter	T_1	T_2	T_3	T_4
Optimized value	0.16	0.02	0.3	0.03

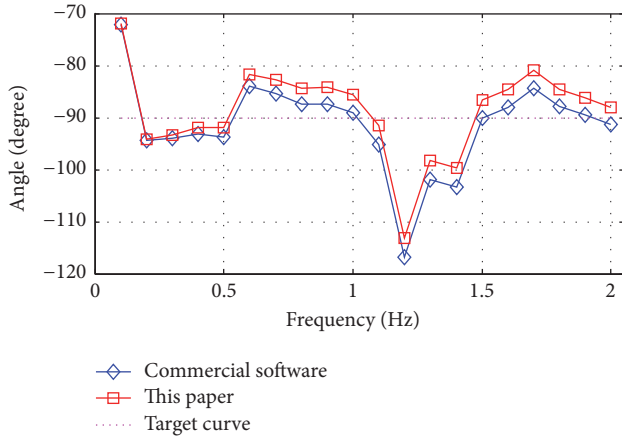


FIGURE 6: Phase-frequency characteristic curves obtained by the commercial software and the proposed method.

characteristic curves are indicated in Figure 6. The index value for the commercial software is 1556 (the smaller the better), while the index value of the proposed method is 1433. It is shown that the proposed method is 8% superior to the widely used commercial software.

Objectively, we also employ another 4 actual generator sets of PSS2A type to make a further verification. The phase-frequency characteristic curves are indicated in Figure 7, while the optimized parameters and the evaluation index values are indicated in Table 6.

As indicated in Figure 7, the phase-frequency characteristic curves optimized by the proposed method are closer to the target curve than those obtained from the commercial software. The evaluation index values for the 4 optimized generator sets are reduced by 37.9%, 27.6%, 22.3%, and 24.9%, respectively, showing that the proposed method is universal and has a generally better optimized effect.

5. Expanded Optimization of Phase-Frequency Characteristics

5.1. Parameter Optimization in Two Phase Shifters and DC Blockers. The primary difference between the PSS2A model and the PSS2B model is the number of the phase shifters. The PSS2B model has three phase shifters, while the PSS2A model has only two phase shifters (see Section 2.1).

For the PSS2A model, the initial values of the PSS parameters are set as Table 1 to study the improved effect of optimizing the DC blockers and the two phase shifters at the same time. The improved phase-frequency characteristics are calculated by the method mentioned in Section 3.2 based on (4). The detailed expression of $\varphi_p(f_j)$ is indicated as (3), where $T_1 \sim T_4$, T_{W3} , and T_7 are the optimization parameters. According to [17], the values of T_{W3} and T_7 are in the range of [4, 6], while the values of $T_1 \sim T_4$ are in the range of [0.01, 1].

The optimized parameters obtained from the proposed method are shown in Table 7, and the optimized phase-frequency curves obtained from the proposed method and the practical engineering method, respectively, are indicated in Figure 8.

According to Table 7, the evaluation index value of the optimized parameters is 1313, which is 38.1% superior to the practical engineering method. Comparing with the two-phase-shifter optimization case, the expanded optimization method improves the effect by 8.4%. As illustrated in Figure 8, although the improved extent is not very large, the proposed hybrid optimization method is still worth to be carried out to furthest obtain the best phase-frequency characteristics.

5.2. Parameter Optimization in Three Phase Shifters and DC Blockers. For the PSS2B model, the optimization work acts on the DC blockers and the three phase shifters at the same time. The initial values of the PSS parameters are set as Table 1, and the improved phase-frequency characteristics are calculated by the method mentioned in Section 3.2 based on (4). The detailed expression of $\varphi_p(f_j)$ is as (2). $T_1 \sim T_6$, T_{W3} , and T_7 are the optimization parameters. According to [17], the value of T_{W3} and T_7 is in the range of [4, 6], while the value of $T_1 \sim T_6$ is in the range of [0.01, 1].

The improved parameters obtained by the proposed hybrid optimization method are shown in Table 8, and the optimized phase-frequency curves obtained by the proposed method and the practical engineering method are indicated in Figure 9.

According to Table 8, the evaluation index value of the hybrid optimized parameters is 1243, which is 41.4% superior to the practical engineering method and 5.3% superior to the two-phase-shifter optimization case. Moreover, the hybrid optimization method has the best improving effect both at the frequency point 0.1 Hz and at the frequency band from 1.2 to 1.4 Hz (these frequency points have been paid much attention by scholars). This means the hybrid optimization method has a better effect on the phase-frequency characteristic improvement at the extreme points.

Since the PSS2A model is less complex than PSS2B and has fewer parameters to modify, the PSS2A model which has qualified accuracy is more widely used in the engineering application. The PSS2B model is usually only used for the generators whose phase-frequency characteristics are obviously weak.

6. Conclusions

This paper proposes a new hybrid optimization method for the double input PSS. The comparing results show that this method is able to significantly improve the phase-frequency characteristics for both the PSS2A model and the PSS2B model. The primary conclusions drawn from the study are as follows.

(1) The practical engineering method and the commonly used commercial method only take the phase shifter optimization into account, while ignoring the DC blocker improvement. Actually, it is better to optimize the phase shifters and the DC blockers at the same time.

TABLE 6: Optimized parameters and evaluation index values obtained by the commercial software and the proposed method.

Parameters	T_1	T_2	T_3	T_4	Index value	
Generator set 1	Commercial software	0.30	0.03	0.30	0.03	3389
	This paper	0.13	0.01	0.33	0.01	2103
Generator set 2	Commercial software	0.15	0.02	0.30	0.03	1977
	This paper	0.24	0.01	0.12	0.01	1432
Generator set 3	Commercial software	0.19	0.02	0.2	0.03	1768
	This paper	0.17	0.01	0.16	0.01	1373
Generator set 4	Commercial software	0.19	0.02	0.2	0.03	5677
	This paper	0.17	0.01	0.16	0.01	4261

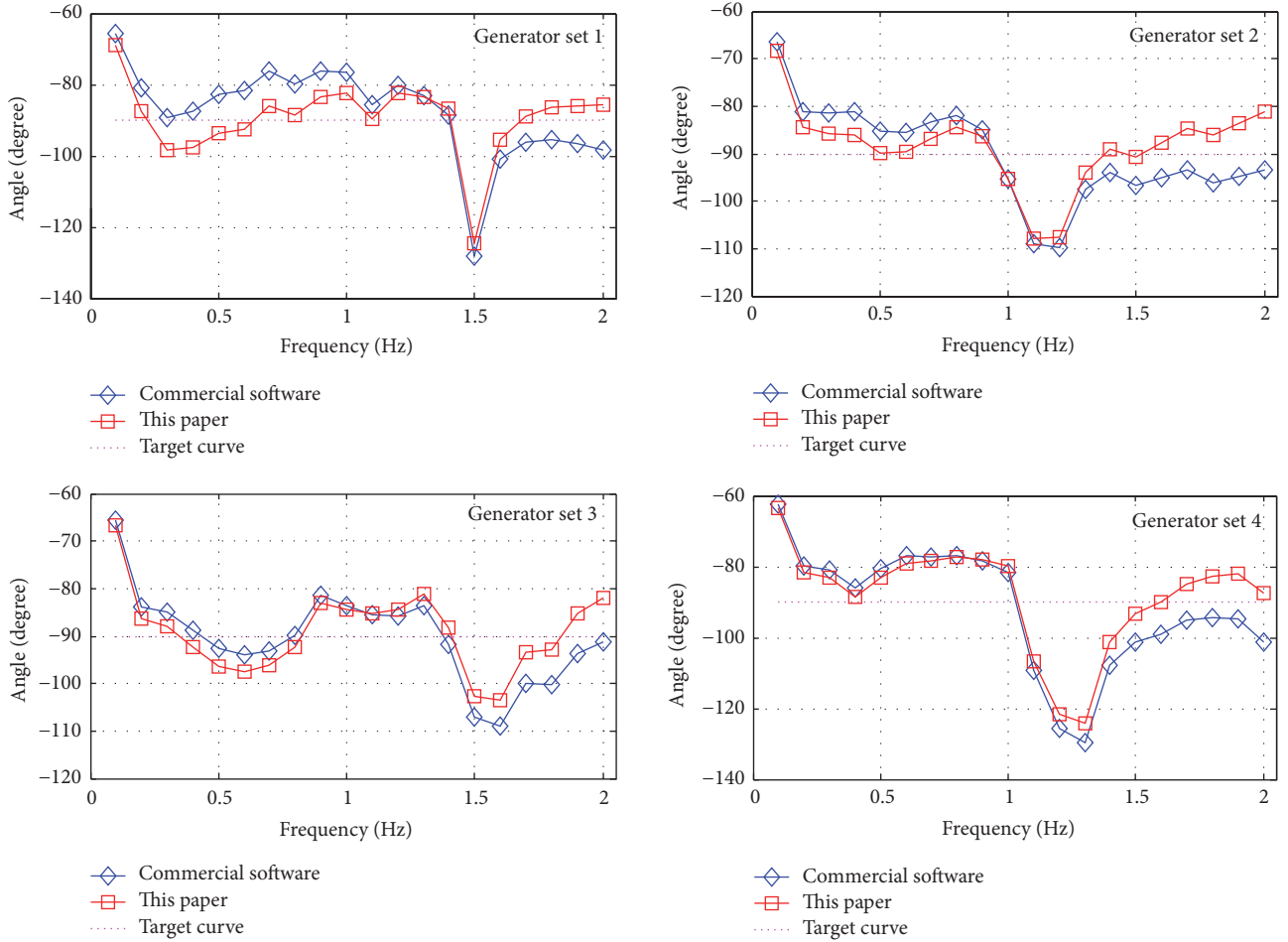


FIGURE 7: Phase-frequency characteristic comparison between the commercial software and the proposed method.

TABLE 7: Optimized parameters of the DC blockers and the two phase shifters.

Parameters	T_1	T_2	T_3	T_4	T_{W3}	T_7
Optimized value	0.23	0.02	0.23	0.03	6	6

TABLE 8: Optimized parameters of the DC blockers and the three phase shifters.

Parameters	T_1	T_2	T_3	T_4	T_5	T_6	T_{W3}	T_7
Optimized results	0.18	0.05	0.19	0.05	0.18	0.05	6	6

(2) This paper proposes a new hybrid optimization method based on Chaos Algorithm and Active Set Algorithm to improve the PSS parameters. The Prony simulating calculation and the actual offline data verification have confirmed

the effectiveness of the proposed method. Moreover, this algorithm does not need manually specified initial values.

(3) The comparing result shows that the optimized effect of the proposed method is superior to the practical engineering method and the commercial software.

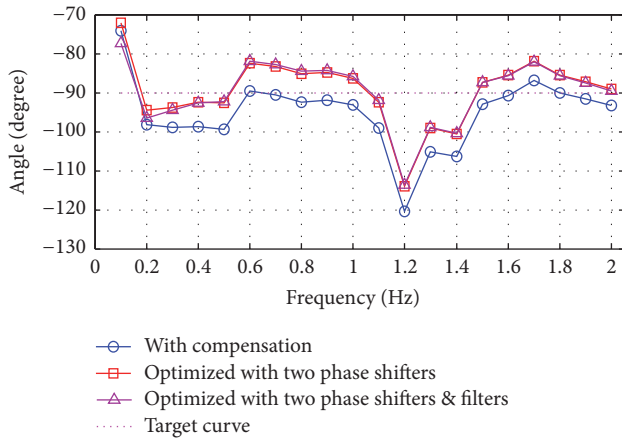


FIGURE 8: Optimized phase-frequency characteristic curves.

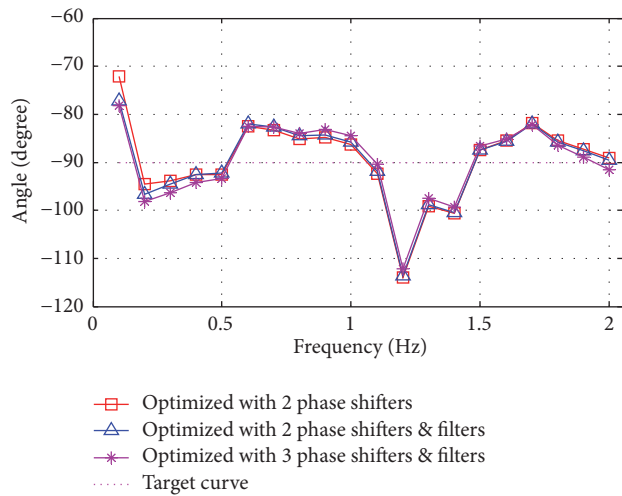


FIGURE 9: Optimized phase-frequency characteristics obtained by different methods.

Conflicts of Interest

The authors declare that they have no conflicts of interest.

Acknowledgments

This work is in part supported by National Natural Science Foundation of China (51307058, 51777074), Natural Science Foundation of Hebei Province, China (E2015502013), and Chinese Fundamental Research Funds for the Central Universities (2018YQ03).

References

- [1] J. Zhang, C. Y. Chung, and Y. Han, "A novel modal decomposition control and its application to PSS design for damping interarea oscillations in power systems," *IEEE Transactions on Power Systems*, vol. 27, no. 4, pp. 2015–2025, 2012.
- [2] S. Kamalasan and G. D. Swann, "A novel system-centric intelligent adaptive control architecture for damping interarea mode oscillations in power system," *IEEE Transactions on Industry Applications*, vol. 47, no. 3, pp. 1487–1497, 2011.
- [3] M. Xiao-Ming, Z. Yao, G. Lin, and W. Xiao-Chen, "Coordinated control of interarea oscillation in the China Southern power grid," *IEEE Transactions on Power Systems*, vol. 21, no. 2, pp. 845–852, 2006.
- [4] J. He, C. Lu, X. Wu, P. Li, and J. Wu, "Design and experiment of wide area HVDC supplementary damping controller considering time delay in china southern power grid," *IET Generation, Transmission & Distribution*, vol. 3, no. 1, pp. 17–25, 2009.
- [5] J. Ma, H. J. Wang, and K. L. Lo, "Clarification on power system stabiliser design," *IET Generation, Transmission and Distribution*, vol. 7, no. 9, pp. 973–981, 2013.
- [6] A. Kumar, "Power system stabilizers design for multimachine power systems using local measurements," *IEEE Transactions on Power Systems*, vol. 31, no. 3, pp. 2163–2171, 2016.
- [7] W. Kuayu, L. Cencen, L. Long et al., "A new PSS with double-signal input and its simulation research," *Power System Technology*, vol. 40, no. 5, pp. 1462–1468, 2016.
- [8] F. S. Al-Ismael, M. A. Hassan, and M. A. Abido, "RTDS implementation of STATCOM-based power system stabilizers," *Canadian Journal of Electrical and Computer Engineering*, vol. 37, no. 1, Article ID 6823225, pp. 48–56, 2014.
- [9] J. Zhang, C. Y. Chung, S. Zhang, and Y. Han, "Practical wide area damping controller design based on ambient signal analysis," *IEEE Transactions on Power Systems*, vol. 28, no. 2, pp. 1687–1696, 2013.
- [10] S. Zhang and F. L. Luo, "An improved simple adaptive control applied to power system stabilizer," *IEEE Transactions on Power Electronics*, vol. 24, no. 2, pp. 369–375, 2009.
- [11] D. Rimorov, I. Kamwa, and G. Joós, "Model-based tuning approach for multi-band power system stabilisers PSS4B using an improved modal performance index," *IET Generation, Transmission & Distribution*, vol. 9, no. 15, pp. 2135–2143, 2015.
- [12] A. Yaghooti, M. Oloomi Buygi, and M. H. M. Shanechi, "Designing coordinated power system stabilizers: a reference model based controller design," *IEEE Transactions on Power Systems*, vol. 31, no. 4, pp. 2914–2924, 2016.
- [13] I. Kamwa, R. Grondin, and G. Trudel, "IEEE PSS2B versus PSS4B: the limits of performance of modern power system stabilizers," *IEEE Transactions on Power Systems*, vol. 20, no. 2, pp. 903–915, 2005.
- [14] National Energy Bureau, *DL/T 1231-2013 Experiment Principles of PSS Setting*, China Electric Power Press, Beijing, China, 2013.
- [15] Y. Chang, *PSS Experiment of 1# Generator Set in Guohua Dingzhou Power Generation Co., Ltd*, Report in State Grid Hebei Electric Power Research Institute, Shijiazhuang, China, 2015.
- [16] M. A. Masrob, M. A. Rahman, and G. H. George, "Design of a neural network based power system stabilizer in reduced order power system," in *Proceedings of the 30th IEEE Canadian Conference on Electrical and Computer Engineering, CCECE '17*, pp. 1–6, 2017.
- [17] Y. Liu, Q. H. Wu, H. Kang, and X. Zhou, "Switching power system stabilizer and its coordination for enhancement of multi-machine power system stability," *CSEE Journal of Power and Energy Systems*, vol. 2, no. 2, pp. 98–106, 2016.
- [18] C.-H. Huang, C.-H. Lin, and C.-L. Kuo, "Chaos synchronization-based detector for power-quality disturbances classification in a power system," *IEEE Transactions on Power Delivery*, vol. 26, no. 2, pp. 944–953, 2011.

- [19] Q. Fan, Y. Jiao, and X. Lu, "A primal dual active set algorithm with continuation for compressed sensing," *IEEE Transactions on Signal Processing*, vol. 62, no. 23, pp. 6276–6285, 2014.
- [20] D. R. Musicant and A. Feinberg, "Active set support vector regression," *IEEE Transactions on Neural Networks and Learning Systems*, vol. 15, no. 2, pp. 268–275, 2004.
- [21] H. Chung, E. Polak, and S. Sastry, "An external active-set strategy for solving optimal control problems," *Institute of Electrical and Electronics Engineers Transactions on Automatic Control*, vol. 54, no. 5, pp. 1129–1133, 2009.
- [22] Q. Ni and Y. Yuan, "A subspace limited memory quasi-Newton algorithm for large-scale nonlinear bound constrained optimization," *Mathematics of Computation*, vol. 66, no. 220, pp. 1509–1520, 1997.

Research Article

The Research on Second-Order ADRC Algorithm of Using Wind Turbine Virtual Inertia to Participate in Primary Frequency Regulation in a Small Stand-Alone Microgrid

Wang Yi ¹, Jiang Hanhong¹ and Xing Pengxiang²

¹National Key Laboratory of Science and Technology on Vessel Integrated Power System, Naval University of Engineering, Wuhan 430033, China

²School of Electrical Engineering, Wuhan University, Wuhan 430072, China

Correspondence should be addressed to Wang Yi; wangyi500500@163.com

Received 19 August 2017; Accepted 31 October 2017; Published 15 March 2018

Academic Editor: Ton D. Do

Copyright © 2018 Wang Yi et al. This is an open access article distributed under the Creative Commons Attribution License, which permits unrestricted use, distribution, and reproduction in any medium, provided the original work is properly cited.

In order to improve the transient stability of frequency in a small stand-alone microgrid (SSM), this paper takes a SSM composed of a direct-drive permanent magnet synchronous generator (D-PMSG) and a micro gas turbine (MGT) as the background and uses wind turbine generator (WTG) virtual inertia (VI) to participate in the primary (short-term) system frequency regulation. First of all, this paper constructs a grid-connected model composed of a WTG and a MGT, analyzes the WTG virtual inertia frequency regulation mechanism, and explains the principle of proportional-differentiation (PD) virtual inertia control (VIC) and its shortcomings. Secondly, the paper introduces the structure principle of n -order active disturbance rejection control (ADRC) and deduces the design process of second-order ADRC-VIC. Finally, through the simulation and experimental verification, comparing the frequency perturbation of without-VIC, PD-VIC, and ADRC-VIC, it is concluded that PD-VIC and ADRC-VIC both can use the WTG virtual inertia to participate in the primary frequency regulation. The frequency regulation effect of ADRC-VIC is better than PD-VIC, ADRC-VIC can extend the rotor speed recovery time and avoid overshoot, and its frequency fluctuation amplitude and settling time are obviously improved, and ADRC-VIC can effectively avoid the overshoot phenomenon of the MGT output power.

1. Introduction

The small stand-alone microgrid (SSM) is an effective way to solve the power supply in the mountains, islands, and remote areas. The principle is to use the collected wind energy, solar energy, and other renewable energy to connect with the traditional synchronous generator (SG), thus building a power supply system independent of the large power grid [1–3]. With the progress of wind power technology, its application in the stand-alone microgrid is more and more extensive. Direct-drive permanent magnet synchronous generator (D-PMSG) has the advantages of flexible control, good reliability, and high power generation efficiency, and it has good application prospect [4]. Micro gas turbine (MGT) has the advantages of low emissions, high efficiency, good fuel adaptability, and flexible control, and it is widely used in distributed power generation technology [5].

In this paper, a SSM constructed by a D-PMSG and MGT is used as the research object to analyze the problem of the transient stability of frequency. The master-control power supply of the SSM is MGT, so the stability of frequency mainly relies on MGT. On the one hand, due to economic reasons, the design capacity of microgrid and the demand of load are matched, resulting in the fact that the microgrid capacity is limited and the system inertia is small. On the other hand, due to technical reasons, the system inertia can only damp the system frequency changes, but it can not completely prevent the system frequency changes [6–8]. Therefore, the system requires the WTG to actively participate in the frequency response, so as to improve the transient stability of system frequency. In general, WTG participates in system frequency regulation in two ways [9–11]. One is called deloaded operation of WTG; when the system frequency has a deviation,

the WTG releases the standby power to participate in the system frequency regulation. This process takes a long time, but it is at the expense of wind energy utilization and the operating economy of WTG, and it is difficult to promote the application. The other is virtual inertia control (VIC) [12]; since the WTG itself has mechanical inertia, it has available rotor kinetic energy in operation. The rotor kinetic energy can transform into electromagnetic power through the control algorithm, to provide support for the system frequency, and this process takes a short time and “zero power consumption” [13, 14]. In addition, the permeability of wind power is often larger due to the limited capacity of SSM, which ensures the effectiveness of WTG participating in the system transient frequency regulation [15–17]. Many scholars have started the research on how to use the virtual inertia of WTG in the system frequency regulation and improve the transient stability of frequency.

The paper [12] gives smart microgrid hierarchical frequency control ancillary service provision based on virtual inertia concept, both the static and dynamic frequency securities of an islanded microgrid are provided in primary and secondary control levels. In [10, 11], frequency-based VIC is realized based on the rate of change of frequency (ROCOF) df/dt or frequency deviation Δf from the nominal value or a combination of both. The proportional (P) term with Δf makes the WTG respond to frequency changes and the differential (D) term with df/dt emulates the inertia. The paper [13] introduces a method of PD-VIC to improve the primary frequency contribution of grid-connected variable speed WTG; by adjusting the droop of the WTG in response to wind velocities, the system primary frequency response is significantly improved. In [14], it is concluded that WTG can provide an extra active power production from its stored kinetic energy; the amount of extra injected power is determined according to the frequency deviation Δf and/or the rate of change of frequency df/dt .

The above literatures illustrate the feasibility of using virtual inertia to participate in system frequency regulation and PD-VIC has a certain practicality. However, the PD algorithm has its inherent limitations, such as the fact that it is difficult to determine the optimal control parameters and likely to cause an overshoot, and the robustness of the controller is poor.

This paper attempts to design a controller from the view of suppressing the system frequency disturbance, which has strong robustness and can avoid overshoot. In [18], the performance superiority of WTG with the proposed linear ADRC approach over that with the traditional proportional integral and fuzzy-proportional integral-based controllers is validated by the simulation results. The simulation results indicate that the performance of the LADRC-based controller is much better than PI and Fuzzy-PI-based controllers. The result also shows that the proposed LADRC-based controller has an excellent robustness and a good capability of disturbance rejection. The authors of [19, 20] have presented the ADRC for the doubly fed induction generator (DFIG) used in wind energy conversion systems, the proposed control has demonstrated its effectiveness under wind variation, and both generated power and rotational speed are kept in their safety region.

Based on the above research, this paper studies the PD-VIC and second-order ADRC-VIC algorithms, and it analyzes the frequency regulation mechanism of the two algorithms. Under the premise of not exceeding WTG virtual inertia frequency regulation capability, the characteristics of the two algorithms are compared and analyzed by simulation and experiment.

The remainder of this paper is given as follows. Section 2 gives a single WTG grid-connected structure and the mechanism of VIC. In Section 3, the structure of n -order ADRC is described first, and then the second-order ADRC is designed according to the frequency dynamic response equation. Simulation analysis and experiment verification are given in Sections 4 and 5, respectively. Finally, conclusions are drawn in Section 6.

2. A WTG Grid-Connected Structure and the Mechanism of VIC

2.1. A WTG Grid-Connected Structure. After a WTG combined to the grid, the system structure is shown in Figure 1. The WTG includes wind wheel, D-PMSG, full-power converter, and its control system.

The wind turbine (WT) is used to capture the wind energy through the wind wheel to drive the D-PMSG to generate electricity. The motion equation of the WTG rotor is

$$2H_w \frac{d\omega_w}{dt} = P_{\text{wind}} - P_w, \quad (1)$$

where H_w denotes the inertia time constant of D-PMSG, ω_w the rotor speed of wind wheel, P_{wind} the mechanical power captured by wind turbine, and P_w the electromagnetic power of the WTG.

The expression of P_{wind} is [21]

$$P_{\text{wind}} = 0.5\rho\pi R^2 v^3 C_p(\lambda, \theta), \quad (2)$$

where ρ denotes the air density, R the radius of the wind wheel, v the wind speed, $C_p(\lambda, \theta)$ the power coefficient of WTG, θ the pitch angle, and λ the tip speed ratio. The expression of $C_p(\lambda, \theta)$ is as follows:

$$C_p(\lambda, \theta) = 0.22 \left(\frac{116}{\sigma} - 0.4\theta - 5 \right) e^{-12.5/\sigma} \quad (3)$$

$$\sigma = \frac{1}{(1/(\lambda + 0.08\theta) - 0.035/(\theta^3 + 1))}$$

$$\lambda = \frac{\omega_w R}{v}.$$

When the pitch angle θ is constant, $C_p(\lambda, \theta)$ is a function of λ . $C_p(\lambda, \theta)$ can reach the maximum value $C_{p\text{max}}(\lambda, \theta)$ by adjusting the rotor speed ω_w and λ reaches the optimal value λ_{opt} at the same time, as shown in Figure 2(a). At this point, it can be seen from (2) that P_{wind} corresponds to only one maximum point ($P_{\text{max}}, \omega_{\text{wopt}}$) at different wind speeds v and rotor speed ω_w , and these maximum points are connected to a line, which is the maximum power point tracking (MPPT) curve, as shown in Figure 2(b).

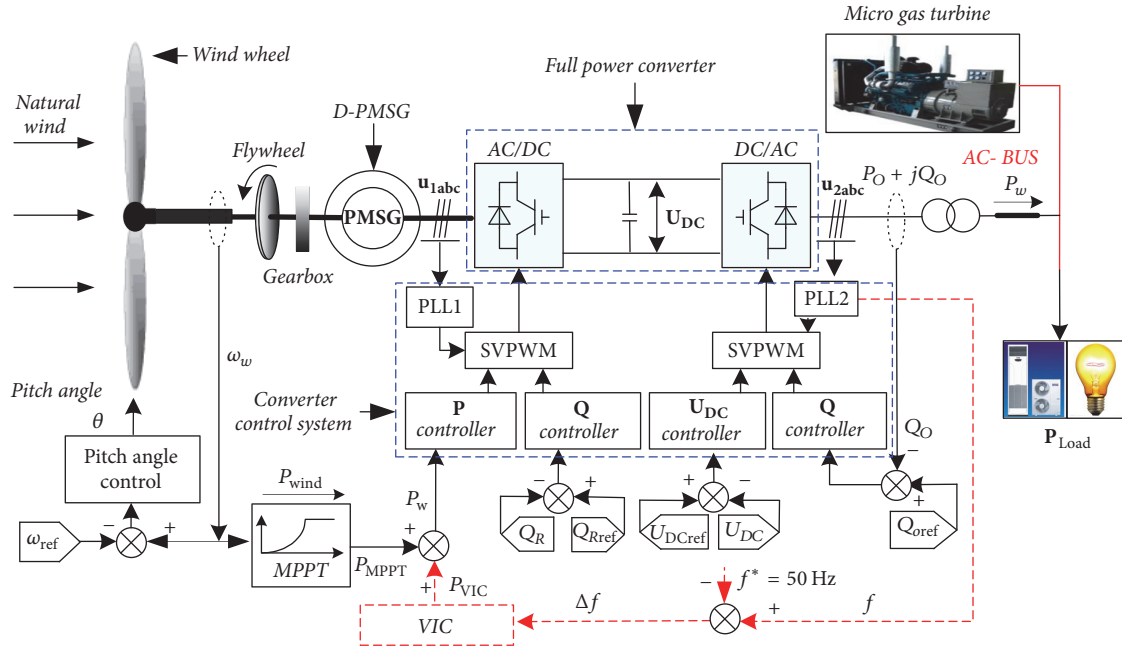


FIGURE 1: A wind turbine system structure after the grid-connection.

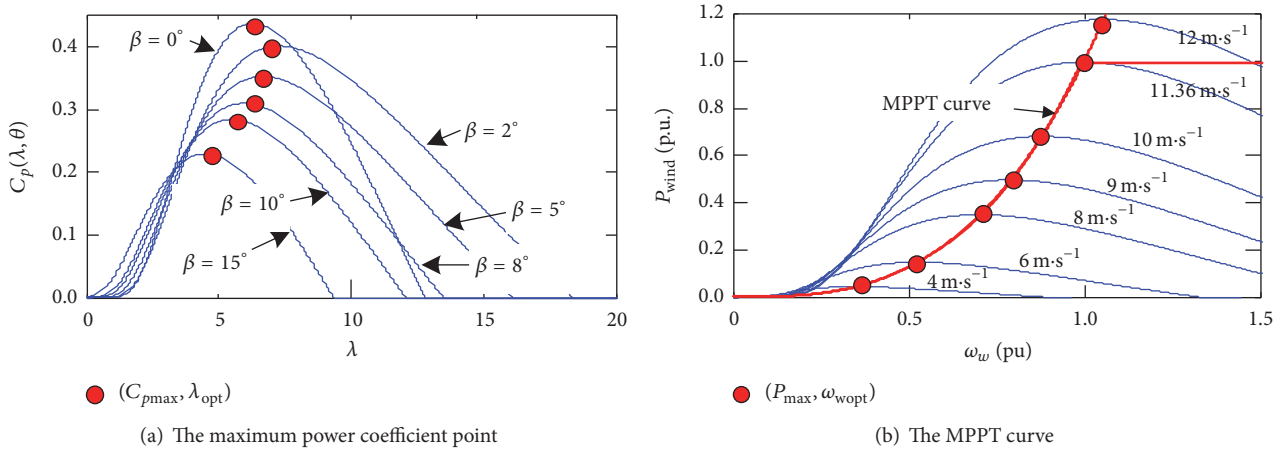


FIGURE 2: The MPPT control of WTG.

When the WTG runs according to the MPPT curve, the wind energy obtained by WTG is

$$P_{\text{MPPT}} = k_{\text{max}} \omega_w^3, \quad (4)$$

where k_{max} is the coefficient that makes WTG obtain the maximum wind energy, and its expression is $k_{\text{max}} = 0.5\rho\pi R^5 C_{p\text{max}}(\lambda, \theta) / \lambda_{\text{opt}}^3$. When the VIC is introduced into the microgrid, as shown by the red dotted line in Figure 1, the expression of P_w is

$$P_w = P_{\text{MPPT}} + P_{\text{VIC}}, \quad (5)$$

where P_{MPPT} is the output power of the MPPT control and P_{VIC} is the auxiliary frequency regulation power of VIC output. As shown in Figure 1, the input of VIC is the system

frequency deviation Δf , and $\Delta f = f - f^*$, f is the system frequency obtained by the grid-side phase-locked loop (PLL), and f^* is the reference frequency 50 Hz. P_{VIC} is calculated by the frequency deviation Δf . When the system is in steady-state operation, that is, $|\Delta f| = 0$, $P_{\text{VIC}} = 0$, the WTG runs in the state of MPPT control, and virtual inertia does not participate in the system frequency regulation. When the system frequency is disturbed, that is, $|\Delta f| > 0$, $P_{\text{VIC}} \neq 0$, the WTG adjust the generator rotating speed and output power through the full-power converter to use virtual inertia in the system frequency regulation.

2.2. The Response Mechanism of VIC. The operation process of WTG includes MPPT and VIC. Figure 3 shows the characteristic curves of WTG in the processes of MPPT and VIC.

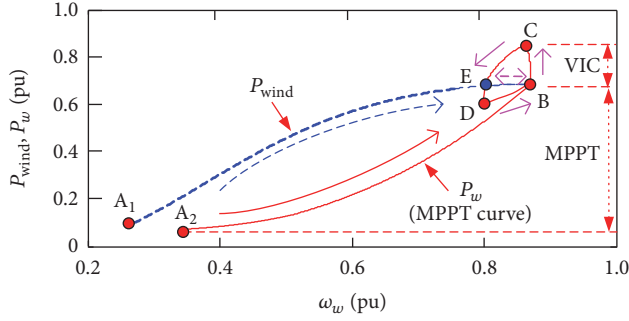


FIGURE 3: The WTG response processes of MPPT and VIC.

The wind speed v keeps constant $7 \text{ m}\cdot\text{s}^{-1}$, and the system load is increased by 15% after WTG reached the MPPT point (B). P_{wind} and P_w denote the mechanical power and the electromagnetic power, respectively.

The Process of MPPT ($A_i \rightarrow B$). The process by which WTG changes from point A_i ($i = 1, 2$) to point B is the MPPT process under the constant wind speed. In this process, P_w changes along the curve of MPPT, and P_{wind} of WTG changes along its characteristic curve. As P_{wind} is greater than P_w , ω_w is constantly rising, and the system is stable at point B ultimately. As can be seen from the curve of P_w in Figure 3, point B is the maximum power point of WTG at this wind speed.

The Process of VIC ($B \rightarrow C \rightarrow D \rightarrow B$). When the system frequency falls due to the sudden increase in load, the VIC of WTG makes P_w climb from points B to C quickly. In this process, due to the inertia of WTG, ω_w does not change immediately, so P_{wind} remains at point B. At this time, since P_{wind} is less than P_w , ω_w starts to decrease. During the decrease process of ω_w , P_{wind} changes along the curve $B \rightarrow E$, and P_w runs along the curve $C \rightarrow D$, when the system finally runs to point D, and then ω_w reaches the minimum value. At this time, P_{wind} is greater than P_w , ω_w starts to increase, P_{wind} of WTG change along the curve $E \rightarrow B$, P_w run along the curve $D \rightarrow B$, the system is back to point B finally, the mechanical power P_{wind} and the electromagnetic power P_w are balanced again, and the rotor speed ω_w is stabilized at the optimal speed of point B.

In the process of VIC, the principle of auxiliary frequency regulation is mainly to change the power of WTG to reduce the impact of the system load disturbance on the MGT, thereby reducing the changing rate and amplitude of the system frequency.

2.3. The Rotor Speed Recovery and Overshoot. As shown in Figure 4, when the system frequency drops, VIC can quickly reduce the rotor speed and release the rotor kinetic energy. WTG delivers active power to the system for a short period of time to provide support for the system frequency. The inherent drawback of this process is that, at the rapid recovery of the rotor speed, on the one hand, this causes the oscillation and overshoot phenomenon of the WTG output power and

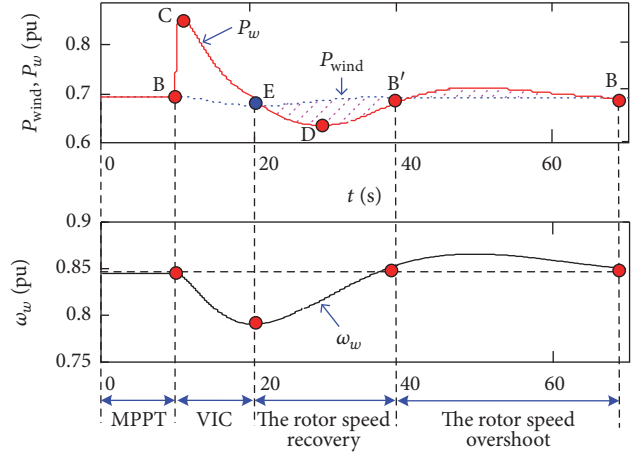


FIGURE 4: The recovery and overshoot of the rotor speed.

the rotor speed (the shadow portion of the $E \rightarrow B$ time period); on the other hand, during the rotor speed recovery process, the WTG absorbs energy from the grid (the shadow portion of the $E \rightarrow B'$ time period), resulting in a smaller power supply to the microgrid, which is not conducive to frequency recovery stability.

In fact, the rotor speed recovery process is carried out when the frequency is not stable, this process is to reduce the WTG output power and increase the system load, which has played a “superposition effect” in the decline process of the frequency, making the frequency response characteristics deteriorate, and in severe cases can cause the system frequency to fall twice.

In Figure 4, $B \rightarrow E$ is the time period of VIC. $E \rightarrow B$ is the time period of the rotor speed recovery and overshoot, which is the time of the rapid decline in frequency regulation capacity, through extending this time period to slow down the speed recovery rate, so as to reduce the rapid decline of frequency regulation capacity and reduce the system frequency deviation.

3. Second-Order ADRC-VIC

ADRC is proposed by Han [22], which is based on the error feedback control theory of traditional PID and the development of modern control theory [23, 24]. ADRC is less dependent on the accuracy of the mathematical model of the controlled object, and the main idea is to estimate the system real-time disturbance by using the extended state observer (ESO) [25] and compensate it. ADRC has the characteristics of fast response, robustness, and adaptability [26]. In this paper, the second-order ADRC is designed according to the frequency dynamic response equation of the microgrid.

MGT is the main control power supply, which can be equivalent to conventional synchronous generator model for analysis, and the system voltage fluctuations caused by the load switching will not be taken into account. Thus, the constant E'_q of the synchronous generator model (in p.u.) is as follows:

$$\begin{aligned}
u_d &= x_q i_q - r_s i_d \\
u_q &= E'_q - x'_d i_d - r_s i_q \\
2H\dot{\omega} &= T_m - E'_q i_q + (x'_d - x_q) i_d i_q - D\omega,
\end{aligned} \tag{6}$$

where u_d , u_q , i_d , and i_q are d -axis voltage, q -axis voltage, d -axis current, and q -axis current of the generator, respectively. x'_d and x_q are the d -axis transient reactance and q -axis reactance, respectively. r_s denotes the stator resistance. ω is the rotor speed. H and D are the rotational inertia and the damping coefficient, respectively. T_m is the mechanical torque.

Laplace transformation of (7) can be expressed as

$$\begin{aligned}
u_d &= x_q i_q - r_s i_d \\
u_q &= E'_q - x'_d i_d - r_s i_q \\
2Hs\omega &= T_m - E'_q i_q + (x'_d - x_q) i_d i_q - D\omega.
\end{aligned} \tag{7}$$

The speed governor model of the synchronous generator can be expressed as

$$\begin{aligned}
T_m &= k_1 \Delta\omega + k_2 \frac{\Delta\omega}{s} \\
\Delta\omega &= \omega_{\text{ref}} - \omega,
\end{aligned} \tag{8}$$

where k_1 and k_2 are the proportional and integral coefficients of PI controller, respectively. ω_{ref} is the reference value of the synchronous generator speed. The active power P_{MGT} of the microgrid synchronous generator can be expressed as

$$P_{\text{MGT}} = u_d i_d + u_q i_q. \tag{9}$$

Substituting (8), (9), and $i^2 = i_d^2 + i_q^2$ into (8) leads to

$$P_{\text{MGT}} = k_1 \Delta\omega + k_2 \frac{\Delta\omega}{s} - D\omega - 2Hs\omega - r_s i^2. \tag{10}$$

It is known from (10) that the VIC system frequency response dynamic equation is

$$2Hs\Delta f = P_{\text{MPPT}} + P_{\text{MGT}} - P_L - D\Delta f + P_{\text{VIC}}. \tag{11}$$

Substituting (10) into (11) leads to

$$\begin{aligned}
2Hs\Delta f + D\Delta f &= k_1 \Delta\omega + k_2 \frac{\Delta\omega}{s} - D\omega - 2Hs\omega + P_A \\
&+ P_{\text{VIC}},
\end{aligned} \tag{12}$$

where $P_A = P_{\text{MPPT}} - P_L - r_s i^2$.

The relationship between the system frequency (p.u.) and the generator rotor speed (p.u.) is expressed as

$$\begin{aligned}
f &= \omega \\
\Delta f &= \Delta\omega.
\end{aligned} \tag{13}$$

Substituting (13) into (12) leads to

$$\begin{aligned}
(2Hs + D)\Delta f &= \left(k_1 + \frac{k_2}{s}\right)\Delta f - (D + 2Hs)f + P_A \\
&+ P_{\text{VIC}}.
\end{aligned} \tag{14}$$

Both sides of the equation are multiplied by s , and then

$$\begin{aligned}
(2Hs^2 + Ds - k_1s + k_2)\Delta f \\
= -(D + 2Hs)sf + s(P_A + P_{\text{VIC}}).
\end{aligned} \tag{15}$$

Namely,

$$\begin{aligned}
2H\Delta\ddot{f} + (D - k_1)\Delta\dot{f} + k_2\Delta f \\
= -D\dot{f} - 2H\ddot{f} + \dot{P}_A + \dot{P}_{\text{VIC}}.
\end{aligned} \tag{16}$$

Substituting $\dot{f} = \Delta\dot{f}$ into (16) leads to

$$4H\Delta\ddot{f} + (2D - k_1)\Delta\dot{f} + k_2\Delta f = \dot{P}_A + \dot{P}_{\text{VIC}}. \tag{17}$$

The second-order differential equation of the power system frequency deviation Δf is expressed as

$$\Delta\ddot{f} = \frac{1}{4H} \left((k_1 - 2D)\Delta\dot{f} - k_2\Delta f + \dot{P}_A \right) + \frac{\dot{P}_{\text{VIC}}}{4H}, \tag{18}$$

where the uncertain items of the controlled object can be defined as the sum of internal and external disturbance as follows:

$$\begin{aligned}
f(x_1, x_2, t, w(t)) \\
= \frac{1}{4H} \left((k_1 - 2D)\Delta\dot{f} - k_2\Delta f - \dot{P}_A \right).
\end{aligned} \tag{19}$$

The differential equation of Δf and P_{VIC} in (18) indicates that when the ADRC is substituted for the conventional PD controller, the output of the controlled object is the same as that of the conventional PD controller, which is the value of the system frequency deviation Δf . The block diagram of the second-order ADRC is based on (18), as shown in Figure 5.

In Figure 5, z_1 is the estimated value of the system frequency deviation value Δf , z_2 is the estimated value of $\Delta\dot{f}$, and z_3 is the estimated value of the system uncertain item $(1/4H) * ((k_1 - 2D)\Delta\dot{f} - k_2\Delta f + \dot{P}_A)$. a denotes the compensation coefficient of the estimated values z_3 and z_2 . In this paper, $a = 4H$ and $b = 1/4H$. Since the purpose of the ADRC is to suppress fluctuations in system frequency, the reference values Δf^* and $\Delta\dot{f}^*$ of variation in status can be directly set to 0, respectively. Thus, the design of TD shown in Figure 5 is left out.

In practical engineering applications, there is a need to discretize the algorithm of each module for the ADRC [22, 23]. The discretized form of the nonlinear ESO can be expressed as

$$\begin{aligned}
e(k) &= z_1(k) - x_1(k) \\
z_1(k+1) &= z_1(k) + h(z_2(k) - \beta_1 e(k)) \\
z_2(k+1) &= z_2(k) + h(z_3(k) - \beta_2 \text{fal}(e(k), \alpha_1, h) + bu(k)) \\
z_3(k+1) &= z_3(k) + h(-\beta_3 \text{fal}(e(k), \alpha_2, h)),
\end{aligned} \tag{20}$$

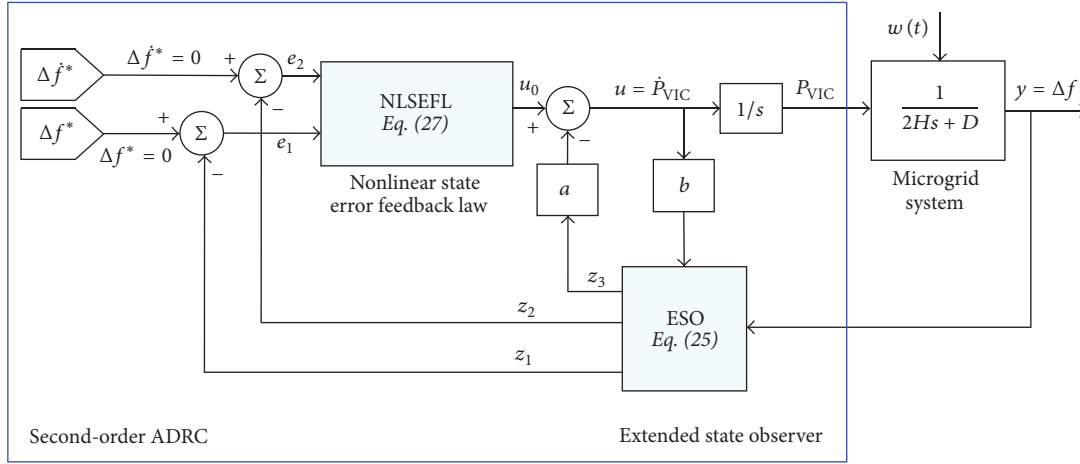


FIGURE 5: Diagram of second-order ADRC controller.

where h is the sampling step size and β_1, β_2 , and β_3 are the observer parameters needed to be determined. According to the characteristics of inherent parameters of the ADRC, $\beta_1 = 1/h$, $\beta_2 = 1/3h^2$, and $\beta_3 = 1/32h^3$, which are used in this paper. In order to avoid the chattering, the saturation function $\text{fal}(e, a, \delta)$ is expressed as

$$\text{fal}(e, a, \delta) = \begin{cases} \frac{e}{\delta^{\alpha-1}} & |e| \leq \delta \\ |e|^\alpha \text{sgn}(e) & |e| > \delta, \end{cases} \quad (21)$$

where δ is the linear interval length and $\text{sgn}(\cdot)$ is the symbolic function and a denotes the saturation function factor. When the absolute value of the error e is relatively large, its gain will decrease to prevent the overshoot. When the absolute value of the error e is relatively small, its gain will increase to speed up the convergence process.

The NLSEF and the discrete control amount produced by disturbance compensation are expressed as

$$\begin{aligned} e_1(k) &= \Delta f^* - z_1(k) \\ e_2(k) &= \Delta \dot{f}^* - z_2(k) \\ u_0(k) &= \beta_{01} \text{fal}(e_1(k), a_{01}, \delta_0) \\ &\quad + \beta_{02} \text{fal}(e_2(k), a_{02}, \delta_0) \\ u(k) &= u_0(k) - az_3(k), \end{aligned} \quad (22)$$

where β_{01} and β_{02} are the output correction coefficients and the parameters $0 < a_{01} < 1 < a_{02}$ are used to mediate the nonlinearity of the $\text{fal}(e, a, \delta)$ function. The ADRC designed in this paper has the following advantages over the conventional PD controller: (1) due to its observation and compensation of power disturbance, its better dynamic characteristic of suppressing the frequency disturbance; (2) increasing the error tracking efficiency by designing the optimized NLSEF and using saturation function to achieve the objective of “small error and large gain, large error and small gain”; (3) its better applicability and robustness because of adopting ESO

for the estimation and compensation of the system parameter disturbance.

Although the parameters of ADRC are much more than PD, the advantages of ADRC over PD are as follows. On the one hand, in order to release more WTG virtual inertia, the PD is achieved by increasing the proportional factor k_p and differential factor k_d , but this causes the WTG speed overshoot phenomenon, when the overshoot is serious which will cause the system frequency secondary drop. On the other hand, as more WTG virtual inertia was released, ADRC will not cause the WTG rotor speed overshoot, and its ability to adjust the system frequency will be further improved. And ADRC has a certain ability to resist parameter disturbance. The following is through simulation and experiment to illustrate this.

4. Simulation Analysis

In this paper, a SSM simulation model composed of a WGT and a MGT is built in MATLAB/Simulink. The main parameters of the simulation model are shown in Appendix A. First of all, the estimation effect of ESO and the robustness of antiparameter perturbation of ADRC are verified by simulation.

4.1. The Simulation of ESO Observation Effect. Figure 6 shows the estimated effect of ESO when the load $P_{\text{Load}1}$ is switched. The red solid line is the p.u. value of the actual system power perturbation, $\Delta P = f(x_1, x_2, t, w(t)) \times 4H$. The blue dotted line is the ESO estimate value. z_3 is the estimate amount of $f(x_1, x_2, t, w(t))$. It can be seen from the figure that ESO can realize the accurate tracking and estimation of the system load disturbance, which provides a reliable basis for the compensation and suppression of the system frequency disturbance.

During the operation of the system, the inertia time constant H of the system is in the process of change due to the random fluctuation of the wind resource and the load disturbance. Therefore, it is necessary to examine the impact

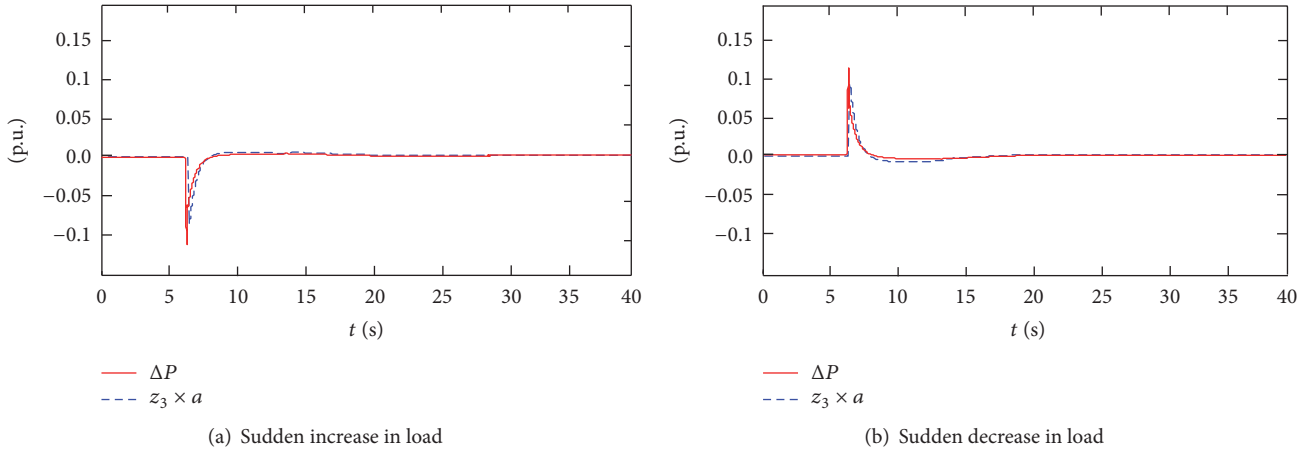


FIGURE 6: Observations of ESO during load switching.

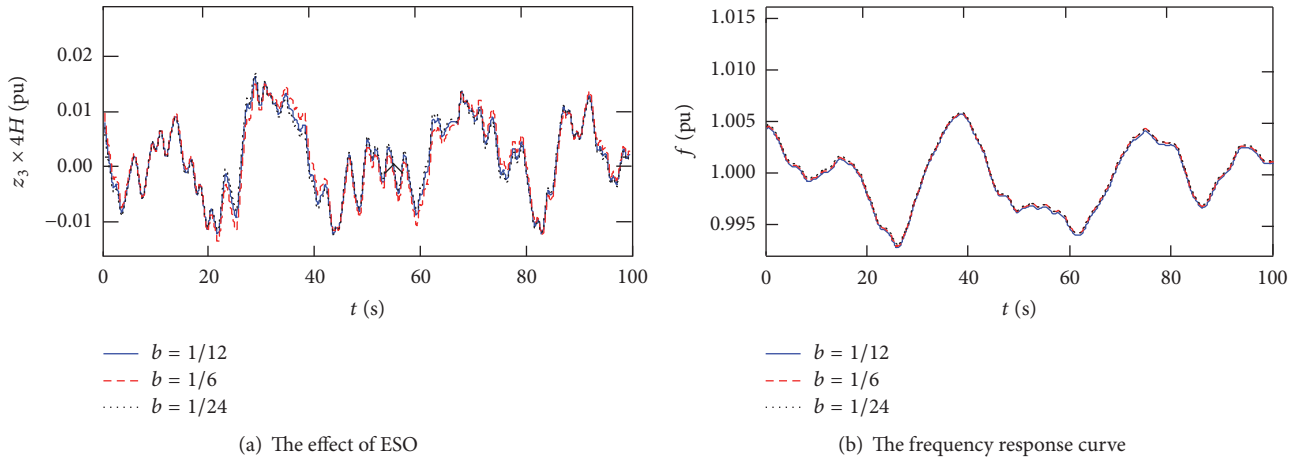


FIGURE 7: The influences of control parameter variation on ADRC performance.

of parameter b on control algorithm performance. When the wind speed fluctuates randomly and b takes 1/12, 1/6, or 1/24, respectively, the ADRC control characteristic is shown in Figure 7.

Figures 7(a) and 7(b) are the estimated effect curves and system frequency response curves of ESO, respectively. As can be seen from Figure 7(b), the frequency response curves of the system are completely coincident with different parameters b . The ESO of ADRC has strong robustness, which is inherent in ESO performance. When the parameter b is disturbed within a certain range, the ADRC control performance is not affected, which is determined by its robustness. Therefore, the change of the value of b will not affect the ESO accurate estimation of the system power disturbance; that is, it will not affect the control effect of ADRC on the system frequency. This shows that ADRC has a certain ability to resist system parameters perturbation, which reduces the ADRC dependence on grid parameters.

4.2. The Simulation of PD-VIC and Second-Order ADRC-VIC. In order to compare the effects of the PD-VIC and second-order ADRC-VIC to suppress the frequency disturbance, the

microgrid frequency disturbance is caused by sudden increase load. Figure 8 is the waveforms of simulation during the sudden increase in load, and wind speed v is 7 m/s.

The design of simulation scenario: at $t = 0$ s, a WTG and MGT are connected to bear the fixed load $P_{load0} = 10$ kW together, the output power of WTG is $P_{WGT} = 3$ kW, the rotor speed of WTG is $\omega_w = 14$ rad/s, and the output power of MGT is $P_{MGT} = 7$ kW. At $t = 5$ s, the sudden increase in load is $P_{load1} = 5$ kW.

In Figure 8, blue dotted lines are without-VIC simulation waveforms. At $t = 5$ s, P_{load1} is put into the system. MGT independently bears the load disturbance, and WTG does not participate in frequency regulation. The frequency nadir is 49.55 Hz and the setting time is at $t = 20$ s after two oscillation periods. $P_{WGT} = 3$ kW and $\omega_w = 14$ rad/s remain unchanged. Since the load disturbance is only borne by MGT, P_{MGT} increases 12 kW by step.

The red long-dotted lines are PD-VIC simulation waveforms. At $t = 5$ s, the WTG uses virtual inertia to participate in frequency regulation. The lowest point f drops to is 49.7 Hz and the setting time is at $t = 18$ s after one oscillation period. During the sudden increase in load, P_{WGT} increases

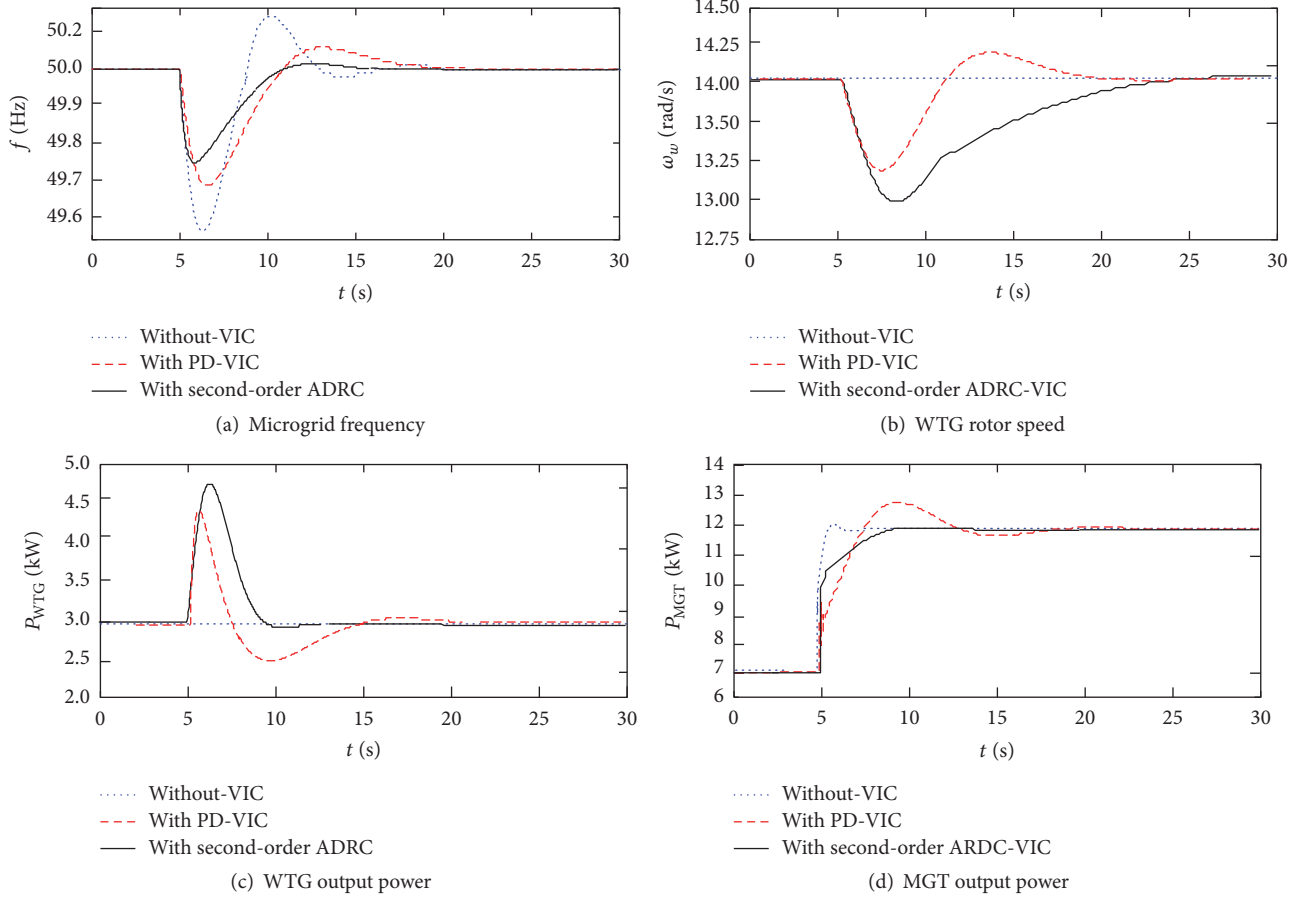


FIGURE 8: The simulation waveforms of sudden increase load.

to the maximum value 4 kW and then returns to 3 kW, ω_w falls to 13.25 rad/s and then returns to 14 rad/s, and P_{WTG} and ω_w have the phenomenon of oscillation and overshoot. P_{MGT} increases to 12 kW after a certain distortion and appears overshoot phenomenon which is higher than 12 kW.

The black solid lines are the second-order ADRC-VIC simulation waveforms. The lowest point f drops to is 49.85 Hz and the setting time is at $t = 16$ s. During the sudden increase in load, P_{WTG} increases to a maximum point 4.5 kW and then returns to 3 kW, ω_w falls to 13 rad/s and then returns to 14 rad/s, and P_{WTG} and ω_w have no phenomenon of oscillation and overshoot. The recovery time of ω_w is longer than PD-VIC. Compared with that in PD-VIC, P_{MGT} does not appear overshoot phenomenon, P_{MGT} can be more smooth added to 12 kW, and second-order ADRC-VIC reduces the impact of load disturbance on MGT.

Based on the above conclusions, when the wind speed is constant, PD-VIC and second-order ADRC-VIC both can use the WTG virtual inertia to participate in the short-term frequency regulation and effectively reduce the transient fluctuations of the system frequency. Compared with PD-VIC, second-order ADRC-VIC can extend the recovery time of ω_w and avoid overshoot, reduce the amplitude of the frequency Δf_{\max} by 0.15 Hz and the settling time Δt by 2 s, and make P_{MGT} more smooth transition during load disturbances.

When the wind speed fluctuates randomly and the system load is constant, the system frequency disturbance is mainly caused by the fluctuation of WTG output power. The effects of different VIC algorithms on suppressing frequency perturbation are compared by simulation in Figure 9. Compared with without-VIC and PD-VIC, second-order ADRC-VIC (blue dash-dotted line) frequency disturbance is significantly smaller. As WTG uses second-order ADRC-VIC to increase the intensity of participating in the frequency regulation, the disturbance range of the rotor speed ω_w becomes larger, which indicates that WTG virtual inertia can be more fully released.

5. Experimental Verification

5.1. The Design of Simulative Experiment Platform. In order to further verify the effectiveness and feasibility of the above algorithms, a set of simulative WTG grid-connected experimental systems with capacity of 275 kVA is built, which includes a simulative WTG and a virtual synchronous generator (VSG) simulated by a full-power converter. The full-power converter simulates the MGT frequency characteristics according to the algorithm in [27]. Figures 10 and 11 are the schematic diagram of the simulative experiment system and the field of the simulative experimental platform, respectively.

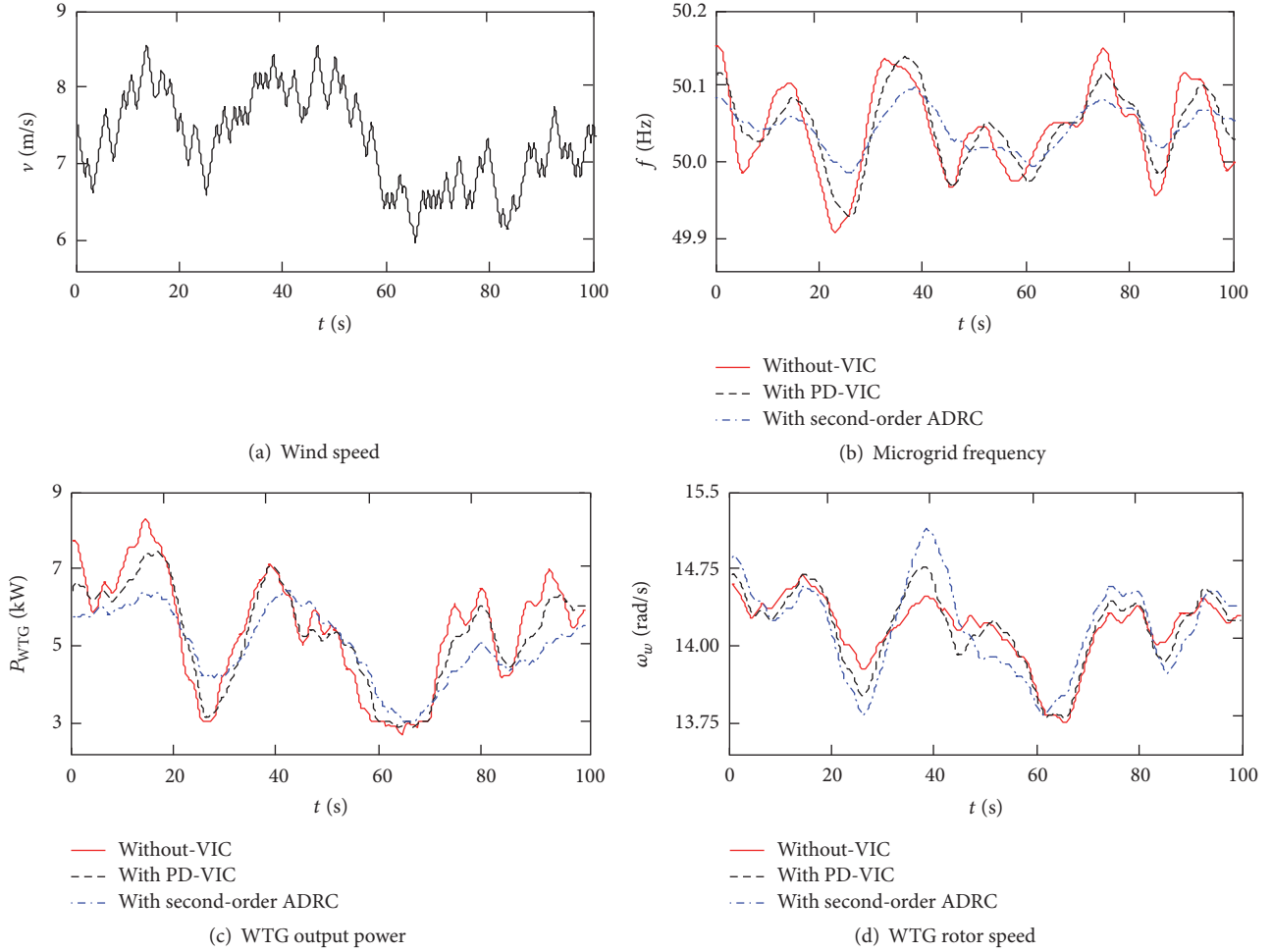


FIGURE 9: Simulation waveforms of random wind speed.

In the experimental system, the rated power of the simulative WTG is $P'_{wn} = 7.5$ kW, the rated rotor speed is $\omega'_{wn} = 18.8$ rad/s, the radius of the wind turbine is $R = 3.4$ m, and the rated wind speed is 10 m/s. The rated capacity of simulative MGT is $P'_{MGTh} = 20$ kW and inertia time constant is $T'_{CH} = 10$ s. The fixed load is $P'_{load0} = 10$ kW, and the switchable load is $P'_{load1} = 5$ kW. The controller chips of simulative WTG and MGT are DSP F2812 of TI company, the controllers exchange data with LabWindows/CVI of host computers through the RS485 communication protocol.

The design of experimental scenario: at $t = 0$, the WTG and MGT are grid-connected, $P_{WTG} = 2.5$ kW, and $P_{MGT} = 7.5$ kW. At $t = 7.5$ s, the system load was increased by 5 kW. Three groups of experiment are carried out in the order of without-VIC, PD-VIC, and ADRC-VIC. Since the focus of this paper is on the VIC algorithm of the short-time frequency regulation, the wind speed is set to a constant 6.5 m/s during this period.

5.2. The Analysis of Experimental Results. Figure 12 is the experimental waveforms of without-VIC, PD-VIC, and second-order ADRC-VIC during the load increase, respectively.

The analysis of without-VIC experimental waveforms: at $t = 7.5$ s, with sudden increase of the load P'_{load1} , the simulative MGT independently bears the load disturbance, and the fluctuation characteristic of frequency is similar to the actual MGT. As shown in Figure 12(a), the maximum frequency excursion is about $\Delta f_{max} = 1.25$ Hz, the stabilization time of frequency is about $t = 19.5$ s after three cycles of oscillation, and $\Delta t = 12$ s. In Figures 12(b) and 12(c), the output power of WTG $P_{WTG} = 2.5$ kW and the rotor speed $\omega_w = 14$ rad/s remain unchanged. In Figure 12(d), the P_{MGT} increases 5 kW by step.

The analysis of PD-VIC experimental waveforms: compared with that in without-VIC, the fluctuation amplitude of f is decreased, $\Delta f_{max} = 0.9$ Hz, the settling time is about $t = 15$ s after two cycles of oscillation, and $\Delta t = 7.5$. In Figure 12(c), the increased auxiliary power of P_{WTG} is the use of virtual inertia to participate in frequency regulation, the extreme value is $\Delta P_{VICmax} = 1.25$ kW, and P_{WTG} and ω_w have the phenomenon of oscillation and overshoot. P_{MGT} is increased 5 kW with the load increasing, but the WTG participates in the system frequency regulation with virtual inertia at this time, resulting in a distortion and overshoot phenomenon of P_{MGT} .

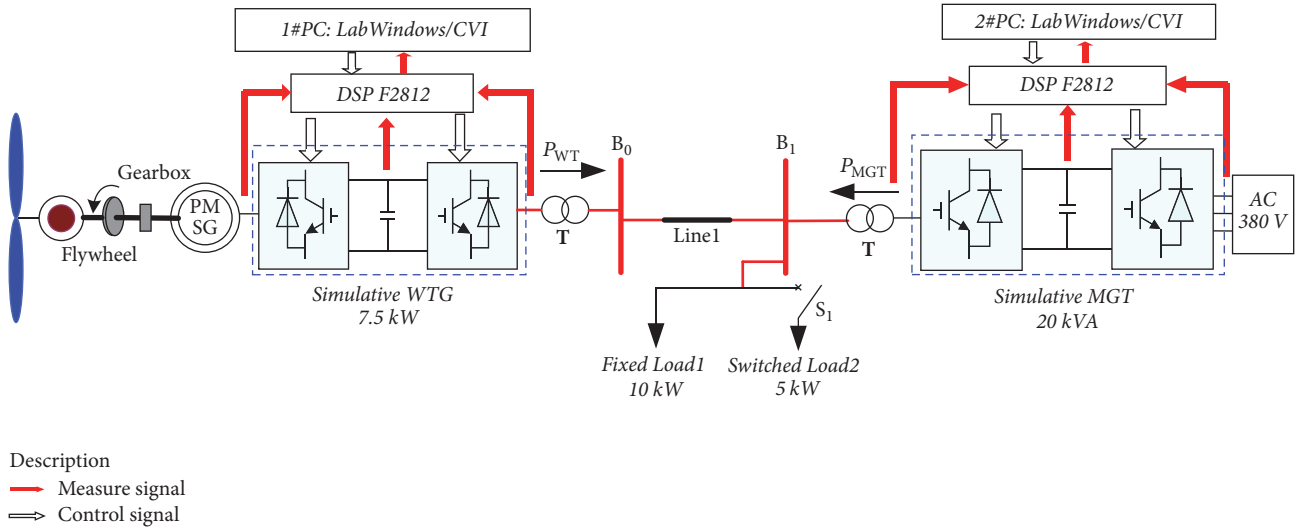


FIGURE 10: The schematic diagram of the simulative experiment system.

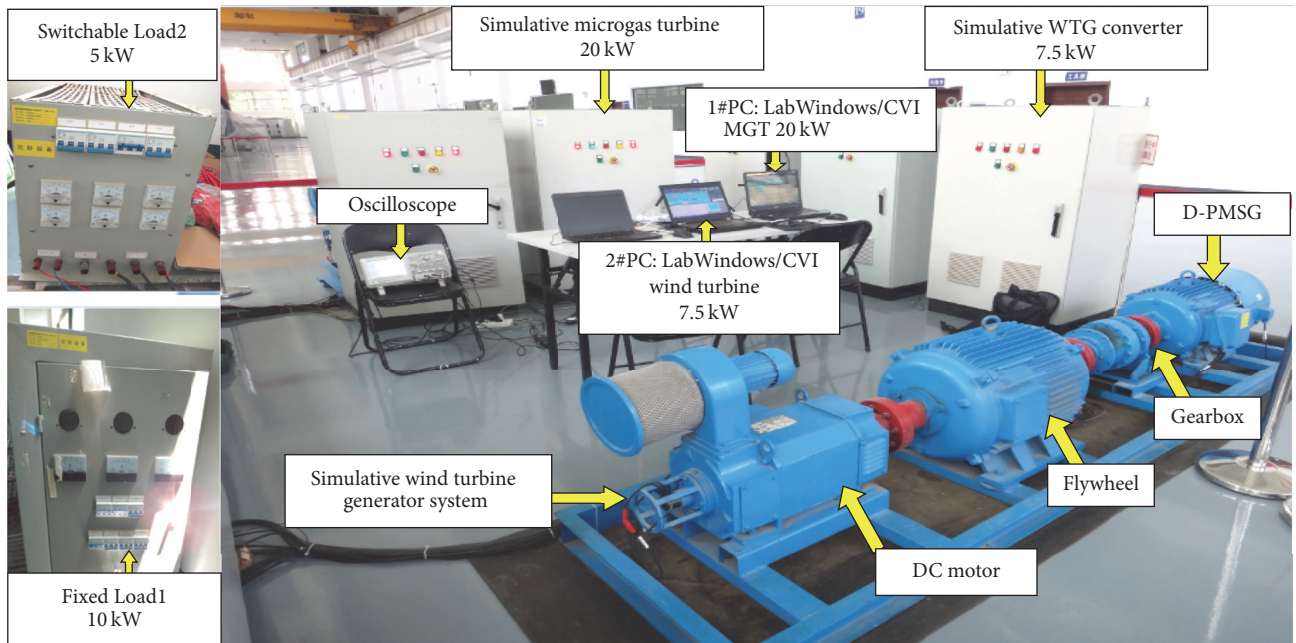


FIGURE 11: The field of the simulative experimental platform.

The analysis of second-order ADRC-VIC experimental waveforms: compared with that in without-VIC, the fluctuation amplitude of frequency is obviously reduced, the maximum deviation of the frequency is about $\Delta f_{\max} = 0.7$ Hz, the settling time is at $t = 13.5$ s or so, and $\Delta t = 5$ s. The extreme of auxiliary power is $\Delta P_{\text{VICmax}} = 2$ kW. P_{WTG} and ω_w have no phenomenon of oscillation and overshoot. Second-order ADRC-VIC makes ω_w recovery time Δt_1 longer and avoids overshoot, so that the WTG virtual inertia is released more fully. P_{MGT} appears to be no overshoot phenomenon.

Therefore, the PD-VIC and the second-order ADRC-VIC both can effectively improve the transient stability of the system frequency in the same experimental environment.

Compared with the PD-VIC, the ADRC-VIC can effectively extend the ω_w recovery time and avoid overshoot, and second-order ADRC-VIC reduces the microgrid frequency fluctuation amplitude value Δf_{\max} by 0.2 Hz, the time of stabilization Δt is reduced by about 1.5 s, and the overshoot phenomenon in P_{MGT} can be avoided.

6. Conclusions and Future Works

6.1. The Conclusions of This Paper. Based on the background of a SSM, this paper studies the algorithm of primary frequency regulation by using WTG virtual inertia and focuses on the algorithms of PD-VIC and second-order ADRC-VIC.

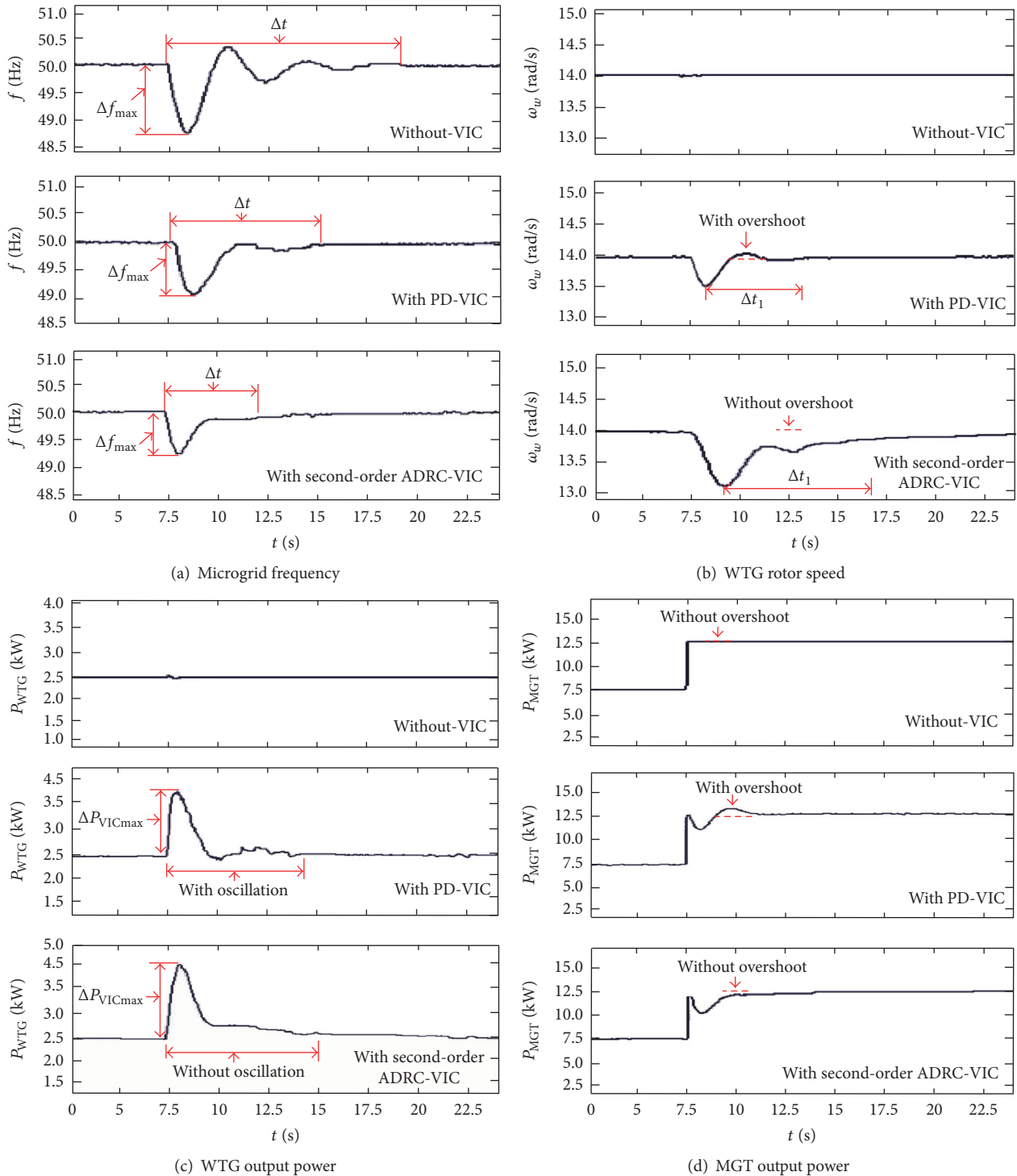


FIGURE 12: The experiment waveforms of without-VIC, PD-VIC, and second-order ADRC-VIC.

The paper shows that the PD-VIC is clear in physical meaning and easy to implement, but there is a problem that the setting of the optimal parameter is difficult and it is easy to cause overshoot. ADRC is a controller designed to suppress the system frequency disturbance. This paper presents the design and implementation of the second-order ADRC-VIC.

Through the verification of simulation and experiment, PD-VIC and second-order ADRC-VIC both can effectively use the WTG virtual inertia to participate in the system primary frequency regulation. Compared with PD-VIC, the second-order ADRC-VIC can effectively extend the ω_w recovery time and avoid overshoot, and the simulation

shows that second-order ADRC-VIC reduces the maximum deviation and the settling time of frequency by 0.15 Hz and 2 s, respectively, the experiment shows that ADRC reduces the maximum deviation and the settling time of frequency by 0.2 Hz and 1.5 s, respectively, and ADRC can avoid the overshoot of the MGT output power. Therefore, ADRC makes WTG virtual inertia release more full, and the frequency regulation effect of second-order ADRC-VIC is better.

6.2. The Future Works. This paper only studies the algorithm of the WTG virtual inertial control but does not fully consider the WTG frequency regulation capability. How to fully release the WTG virtual inertia to participate in frequency regulation is a research that needs to be done in the future. In this paper, a single WTG participating in the frequency regulation is studied only, and multiple WTGs in coordinate frequency regulation are the next research to be carried out.

Appendix

A. Parameters of Simulation Model

MGT rate power P_{MGTn} : 50 kW
 MGT inertia time constant T_{ch} : 8 s
 MGT line-to-line voltage U_n : 380 V
 a WTG rate power P_{WGTn} : 20 kW
 Microgrid steady frequency f_n : 50 Hz
 Fixed load P_{Load0} : 10 kW
 Switchable load P_{Load1} : 5 kW
 PD coefficients k_{pf} , k_{df} : 2×10^3 , 1.5×10^3
 Sampling step size h : 0.001 s
 ESO parameters β_1 , β_2 , and β_3 : 1000, 334, and 332
 ESO parameters a_1 , a_2 , δ , and b : 0.5, 0.8, 1, and 1/24
 NLSFE parameters β_{01} , β_{02} : 70, 10
 NLSFE parameters a_{01} , a_{02} , δ_0 , and a : 0.5, 2, 1, and 24

B. Parameters of Experimental System

MGT rate power P'_{MGTn} : 20 kW
 MGT inertia time constant T'_{ch} : 10 s
 MGT line-to-line voltage U'_n : 380 V
 a WTG rate power P'_{MGTn} : 7.5 kW
 Fixed load P'_{load0} : 10 kW
 Switchable load P'_{load1} : 5 kW
 PD coefficients k'_{pf} , k'_{df} : 1.2×10^3 , 1.1×10^3
 Sampling step size h' : 0.01 s
 ESO parameters β'_1 , β'_2 , and β'_3 : 100, 34, and 31
 ESO parameters a'_1 , a'_2 , δ' , and b' : 0.7, 0.9, 1, and 1/40
 NLSFE parameters β'_{01} , β'_{02} : 90, 30
 NLSFE parameters a'_{01} , a'_{02} , δ'_0 , and a' : 0.7, 5, 3, and 40

Conflicts of Interest

The authors declare that there are no conflicts of interest regarding the publication of this article.

Acknowledgments

This work is supported by the National Natural Science Foundation of China (Grant no. 51377167) and the National Basic Research Program (973 Program) of China (2012GB215103).

References

- [1] N. Bizon, "Load-following mode control of a standalone renewable/fuel cell hybrid power source," *Energy Conversion and Management*, vol. 77, pp. 763–772, 2014.
- [2] E. Rakhshani and J. Sadeh, "Practical viewpoints on load frequency control problem in a deregulated power system," *Energy Conversion and Management*, vol. 51, no. 6, pp. 1148–1156, 2010.
- [3] H. Bevrani, F. Habibi, P. Babahajyani, M. Watanabe, and Y. Mitani, "Intelligent frequency control in an AC microgrid: Online PSO-based fuzzy tuning approach," *IEEE Transactions on Smart Grid*, vol. 3, no. 4, pp. 1935–1944, 2012.
- [4] F. Khater and A. Omar, "A Review of Direct Driven PMSG for Wind Energy Systems," *Journal of Energy and Power Engineering*, vol. 7, pp. 1592–1603, 2013.
- [5] F. Sircilli, S. J. P. Retief, L. B. Magalhães et al., "Measurements of a micro gas turbine plume and data reduction for the purpose of infrared signature modeling," *IEEE Transactions on Aerospace and Electronic Systems*, vol. 51, no. 4, pp. 3282–3293, 2015.
- [6] T. S. Bhatti, A. A. F. Al-Ademi, and N. K. Bansal, "Load frequency control of isolated wind diesel hybrid power systems," *Energy Conversion and Management*, vol. 38, no. 9, pp. 829–837, 1997.
- [7] F. Díaz-González, M. Hau, A. Sumper, and O. Gomis-Bellmunt, "Coordinated operation of wind turbines and flywheel storage for primary frequency control support," *International Journal of Electrical Power & Energy Systems*, vol. 68, pp. 313–326, 2015.
- [8] W. Tan, "Decentralized load frequency controller analysis and tuning for multi-area power systems," *Energy Conversion and Management*, vol. 52, no. 5, pp. 2015–2023, 2011.
- [9] T. Malakar, S. K. Goswami, and A. K. Sinha, "Impact of load management on the energy management strategy of a wind-short hydro hybrid system in frequency based pricing," *Energy Conversion and Management*, vol. 79, pp. 200–212, 2014.
- [10] U. N. Rahmat, T. Thiringer, and D. Karlsson, "Temporary primary frequency control support by variable speed wind turbines potential and applications. IEEE Trans. Power Syst," in *IEEE Trans. Power Syst*, vol. 23, pp. 601–612, 2008.
- [11] J. Morren, S. W. H. de Haan, W. L. Kling, and J. A. Ferreira, "Wind turbines emulating inertia and supporting primary frequency control," *IEEE Transactions on Power Systems*, vol. 21, no. 1, pp. 433–434, 2006.
- [12] N. Rezaei and M. Kalantar, "Smart microgrid hierarchical frequency control ancillary service provision based on virtual inertia concept: An integrated demand response and droop controlled distributed generation framework," *Energy Conversion and Management*, vol. 92, pp. 287–301, 2015.
- [13] K. V. Vidyandandan and N. Senroy, "Primary frequency regulation by deloaded wind turbines using variable droop," *IEEE Transactions on Power Systems*, vol. 28, no. 2, pp. 837–846, 2013.

- [14] M. Akbari and S. M. Madani, "Analytical evaluation of control strategies for participation of doubly fed induction generator-based wind farms in power system short-term frequency regulation," *IET Renewable Power Generation*, vol. 8, no. 3, pp. 324–333, 2014.
- [15] R. Ponciroli, A. Cammi, S. Lorenzi, and L. Luzzi, "Control approach to the load frequency regulation of a Generation IV Lead-cooled Fast Reactor," *Energy Conversion and Management*, vol. 103, pp. 43–56, 2015.
- [16] V. Ravikumar Pandi, A. Al-Hinai, and A. Feliachi, "Coordinated control of distributed energy resources to support load frequency control," *Energy Conversion and Management*, vol. 105, pp. 918–928, 2015.
- [17] M. Shiroei and A. M. Ranjbar, "Supervisory predictive control of power system load frequency control," *International Journal of Electrical Power & Energy Systems*, vol. 61, pp. 70–80, 2014.
- [18] Y. Tang, Y. Bai, C. Huang, and B. Du, "Linear active disturbance rejection-based load frequency control concerning high penetration of wind energy," *Energy Conversion and Management*, vol. 95, pp. 259–271, 2015.
- [19] A. Boukhriss, A. Essadki, A. Bouallouch, and T. Nasser, "Maximization of generated power from wind energy conversion systems using a doubly fed induction generator with active disturbance rejection control," in *Proceedings of the 2nd World Conference on Complex Systems, WCCS 2014*, pp. 330–335, November 2014.
- [20] A. Boukhriss, T. Nasser, and A. Essadki, "A linear active disturbance rejection control applied for DFIG based wind energy conversion system," *Int J Comput Sci Iss*, vol. 10, pp. 391–399, 2013.
- [21] F. Akel, T. Ghennam, E. M. Berkouk, and M. Laour, "An improved sensorless decoupled power control scheme of grid connected variable speed wind turbine generator," *Energy Conversion and Management*, vol. 78, pp. 584–594, 2014.
- [22] J. Q. Han, "From PID to active disturbance rejection control," *IEEE Transactions on Industrial Electronics*, vol. 56, no. 3, pp. 900–906, 2009.
- [23] D. Sun, "Comments on active disturbance rejection control," *IEEE Transactions on Industrial Electronics*, vol. 54, no. 6, pp. 3428–3429, 2007.
- [24] C.-Z. Huang and Q. Zheng, "Frequency response analysis of linear active disturbance rejection control," *Sensors and Transducers*, vol. 157, no. 10, pp. 346–354, 2013.
- [25] B.-Z. Guo and Z.-L. Zhao, "On convergence of non-linear extended state observer for multi-input multi-output systems with uncertainty," *IET Control Theory & Applications*, vol. 6, no. 15, pp. 2375–2386, 2012.
- [26] R. Yang, M. Sun, and Z. Chen, "Active disturbance rejection control on first-order plant," *Journal of Systems Engineering and Electronics*, vol. 22, no. 1, pp. 95–102, 2011.
- [27] H. Bevrani, T. Ise, and Y. Miura, "Virtual synchronous generators: A survey and new perspectives," *International Journal of Electrical Power and Energy Systems*, vol. 54, pp. 244–254, 2014.

Research Article

Asynchronous Communication under Reliable and Unreliable Network Topologies in Distributed Multiagent Systems: A Robust Technique for Computing Average Consensus

Ali Mustafa ^{1,2}, Muhammad Najam ul Islam,¹
Salman Ahmed,³ and Muhammad Ahsan Tufail²

¹Department of Electrical Engineering, Bahria University, Islamabad, Pakistan

²Department of Electrical Engineering, COMSATS Institute of IT, Attock, Pakistan

³Department of Computer Systems Engineering, University of Engineering and Technology, Peshawar, Pakistan

Correspondence should be addressed to Ali Mustafa; ali.mustafa@ciit-attok.edu.pk

Received 8 September 2017; Accepted 31 January 2018; Published 11 March 2018

Academic Editor: Ton D. Do

Copyright © 2018 Ali Mustafa et al. This is an open access article distributed under the Creative Commons Attribution License, which permits unrestricted use, distribution, and reproduction in any medium, provided the original work is properly cited.

Nearly all applications in multiagent systems demand precision, robustness, consistency, and rapid convergence in designing of distributed consensus algorithms. Keeping this thing in our sight, this research suggests a robust consensus protocol for distributed multiagent networks, continuing asynchronous communications, where agent's states values are updated at diverse interval of time. This paper presents an asynchronous communication for both reliable and unreliable network topologies. The primary goal is to delineate local control inputs to attain time synchronization by processing the update information received by the agents associated in a communication topology. Additionally in order to accomplish the robust convergence, modelling of convergence analysis is conceded by commissioning the basic principles of graph and matrix theory alongside the suitable lemmas. Moreover, statistical examples presenting four diverse scenarios are provided in the end; produced results are the recognisable indicator to authenticate the robust effectiveness of the proposed algorithm. Likewise, a simulation comparison of the projected algorithm with the other existing approaches is conducted, considering different performance parameters are being carried out to support our claim.

1. Introduction

Multiagent systems can be defined as a system that is distributed in nature; multiple agents in a network communicate with each other with their limited resources to achieve their local and global goal in a cooperative manner. It is important to mention here that agents are intelligent nodes and have some degree of independence to take their decisions to achieve their desired goals. Such coordination in multiagent system is referred to as a consensus, and it is considered as one the fundamental research activities in distributed control strategy. Study of multiagent systems attracted scientists and researchers from diverse fields of control theory, applied mathematical modelling, computer sciences, engineering, and so on to study the significance of distributed control of agents in a network, as distributed multiagents systems gain a lot of significance in various real time applications

such as flocking [1–4], wireless sensor networks (WSN) [5, 6], coordination control of robots [7, 8], underwater vehicles, unmanned aerial vehicles [9, 10], intelligent transportation systems [11], robotics [12], formation control [13, 14], balancing of load in parallel computers [15], and intelligent decentralized mechanism for smart grids [16, 17].

Consensus problem was first investigated in late 1960s in the modelling of statistical theory and management science [18]. Moreover in the fields of control system theory, consensus problem was initially discussed by [19]. Computer sciences problem focusing on animal aggregation through consensus control is studied by the author in [20]. In latest research horizons of consensus control is pioneered by Olfati-Saber and Murray; they utilize the concepts of graph and matrix theories along with the different network topologies with directed and undirected graph connectivity [21, 22]. Later on authors in [23] implement the consensus control

for dynamically changing topologies. Moreover, consensus in switching network topologies is addressed by [24, 25], filter designing for consensus is addressed by [26], optimized solution for large scale industry using distributed consensus algorithm is proposed by the authors in [27], and Kalman filtering design for distributed consensus approach is initially addressed in [28]. Impulsive control as an important mechanism is highlighted in [29]. Time synchronized algorithms for various application are discussed by authors in [30–32]. Likewise, concept of asynchronous consensus under different network environments is presented by authors in [33, 34].

After concisely discussing various theories and the existing approaches, we are suggesting a new control mechanism for attaining robust average consensus for asynchronous communication in distributed multiagent network centred on discrete time information sharing among the neighbours within the communication network. Practically such networks may suffer communication delays, information loss, broken communication links, unreliable switching network topology, and limitation in channel capacity. So in our proposed solution, we are considering resource constrained intelligent agents with limited communication abilities and also simulated the proposed network control mechanism under both reliable and unreliable random network topologies. Most importantly as mentioned above it is asynchronous in nature, which means that each agent communicating in a network is adjusting its dynamics independently with respect to other neighbouring agents. In proposed scheme starting time of each agent is common but the update time of each agent in a network is assigned randomly; in other words we can say update time of each agent is asynchronous and depending on upper and lower bound of the time. For designing of the proposed control algorithm we used the key concepts from the theory of graph and nonnegative matrix along with state space model to prove the convergence conditions. Proposed algorithm is compared with other existing protocols with a synchronous communication in four different scenarios under reliable and unreliable network topologies and results are compared it a tabular form consisting of various performance parameters. Structure of the paper is organised as follows. Key concepts from the matrix theory and algebraic graph theory are presented in Section 2, convergence analysis is proved in Section 3, and Section 4 is enriched with the proposed control algorithm. Numerical simulation and comparison analysis of performance parameters are presented in Section 5. Section 6 is devoted for concluding remarks.

2. Preliminaries from Algebraic Graph and Matrix Theory

Algebraic graph theory and nonnegative matrix theory are considered as a preliminary tool for designing and convergence analysis in distributed algorithms in multiagent systems. In this segment significant fundamental concepts are concisely deliberated to enhance the understanding of the projected investigation.

In algebraic graph theory, graph is fundamentally a group of linked agents communicating with each other through

communication links. Mathematically it can be represented as $G = (V, E)$. Agents set in a graph are called vertex set and they can be written as $V = v_1, v_2, \dots, v_n$, where $1, 2, n$ are the number of agents in a graph. Moreover, connection links between vertices are referred to as an edge set $\mathcal{E} = (i, j)$. Graph can be classified into two types, directed graph and undirected graph. In directed communication between the agents is one way (i, j) demonstrating data flowing from j th vertex to i th and vice versa. Similarly in undirected graph the communication between vertices is bidirectional. Furthermore, edge set consists of order pairs of vertices representing the information flow. Directly connected vertices which are directly communicating with each other through edges are known as neighbour and algebraically notated as \mathcal{N}_i for agent i . In graph theory connectivity of the agents in a network is represented by $n * n$ matrix, known as adjacency matrix $A = [a_{ij}]$. Degree matrix $D = [d_{ij}]$ delivers the information about the total neighbours connected with any agent in a communication network. Additionally if one vertex in a network has the direct path to all the vertices in a network, then the connectivity graph is supposed to procedure a spanning tree. Spanning tree is considered as one vital convergence condition for consensus in reliable communication but not considerably enough for the systems with time varying delays [35]. If edges in a graph have weights then the matrix is called weighted matrix and summation of the weights coming towards the vertex is called in-degree and alike sum of outward weight is said to be out-degree [36, 37]. Few other matrices which are considered to be of prime importance in convergence analysis for the distributed consensus algorithms are named Laplacian matrix $L = D - A$, rank 1 matrix, stochastic matrix P , and SIA matrix [38].

Furthermore, when designing the weighting matrix β to validate the convergence condition towards a targeted value, then there are multiple approaches available to design such matrices. Local degree weight matrix is one of the popular methodologies, which states that the highest out-degree of any two incident agents is assigned as weight on each edge [39]. It is significant to mention here that it is compulsory that each agent in a network must possess the knowledge of out-degrees of all of its neighbors. Mathematically we can express

$$\beta_{ij}(t_k^i) = \begin{cases} \frac{1}{((\max(d_i(t_k^i), d_j(t_k^i))))} & i \neq j \\ 0 & \text{otherwise.} \end{cases} \quad (1)$$

Similarly one of the popular techniques is for designing weigh matrix as metropolis hasting weights. It can be defined as the fact that all agents must know the out-degree of all of its neighbors but it is essential to mention here that the graph topology is changing at all instants of time. It can be algebraically expressed as [40, 41]

$$\beta_{ij}(t_k^i) = \begin{cases} \frac{1}{((\max(d_i(t_k^i), d_j(t_k^i)))) + 1} & i \neq j \\ 0 & \text{otherwise.} \end{cases} \quad (2)$$

Moreover, while in designing process of distributed consensus algorithm, some useful lemmas and facts from the theory of controls play a very significant role to produce desire results to achieve convergence.

Lemma 1. Assume a collection of stochastic matrices Z_1, Z_2, \dots, Z_n . The final graph which is produced after performing the union operation of all the graphs in matrices set $\mathcal{G}(Z_1), \mathcal{G}(Z_2), \dots, \mathcal{G}(Z_n)$ must possess the spanning tree; afterwards the produced matrix outcome $Z_n Z_{n-1} \dots Z_1$ is called a SIA matrix [23].

Lemma 2. Stochastic matrix Z is supposed to be a SIA, if and only if a spanning tree in $\mathcal{G}(Z)$ is present [42].

3. Convergence Condition

This section will deal with the convergence analysis of the proposed algorithm based on the given below distributed iteration:

$$z_i(t_k^i + 1) = \beta_{ii}(t_k^i) z_i(t_k^i) + \sum_{j \in N_i} \beta_{ij}(t_k^i) z_j(t_k^i); \quad (3)$$

where i ranges between $i = 1, 2, 3, \dots, n$, and similarly $t_k^i = 0, 1, 2, \dots$

β_{ij} is the weight on z_j at agent i , where $\beta_{ii} = (1 - \sum_{j \in N_i} \beta_{ij})$. By assigning $\beta_{ij} = 0$ for $j \in N_i$, we can write (3) in a vector form as

$$Z(t_k^i + 1) = \beta(t_k^i) Z(t_k^i) \quad (4)$$

by utilizing the concept of a t -step transition matrix, we can state that

$$\beta(t_k^i) = \beta(t - 1) \dots \beta(1) \beta(0), \quad (5)$$

where in (4)

$$Z(t_k^i + 1) = \begin{bmatrix} Z_1(t_k^1 + 1) \\ Z_2(t_k^2 + 1) \\ \dots \\ \dots \\ Z_n(t_k^n + 1) \end{bmatrix} \quad (6)$$

$$Z(t_k^i) = \begin{bmatrix} Z_1(t_k^1) \\ Z_2(t_k^2) \\ \dots \\ \dots \\ Z_n(t_k^n) \end{bmatrix}$$

$\beta \in \psi$ represents the sparsity design of the matrix β with restraint, where

$$\psi = \{\beta \in R^{n \times n} \mid \beta_{ij} = 0 \text{ if } \{i, j\} \notin \mathcal{E}, i \neq j\} \quad (7)$$

After defining the sparsity pattern of the matrix, we can now transform (4) as

$$Z(t_k^i) = \left(\prod_{i=0}^{t_k^i-1} \beta(t_k^i) \right) Z(0). \quad (8)$$

Here it is important to highlight that (8) is valid for all t_k^i :

$$Z(t_k^i) = \beta(t_k^i) Z(0). \quad (9)$$

Now the primary goal is to achieve a consensus and to select a weighting matrix in such a way that the convergence condition is satisfied and $Z(t_k^i)$ converge to the average vector, with any initial value $Z(0)$:

$$\lim_{t_k^i \rightarrow \infty} Z(t_k^i) = \left(\frac{1}{n} \right) 11^T Z(0), \quad (10)$$

where n represents the number of participating agents in communication network and a 1 is a vector of ones:

$$\lim_{t_k^i \rightarrow \infty} Z(t_k^i) = \lim_{t_k^i \rightarrow \infty} \beta(t_k^i) Z(0). \quad (11)$$

If we now compare (10) with (11), we will attain

$$\lim_{t_k^i \rightarrow \infty} \beta(t_k^i) Z(0) = \left(\frac{1}{n} \right) 11^T Z(0). \quad (12)$$

Here we compare the terms in (12), and we will come up with

$$\lim_{t_k^i \rightarrow \infty} \beta(t_k^i) = \left(\frac{1}{n} \right) 11^T. \quad (13)$$

From (13) we can compute the equations for different performance parameters for convergence analysis; the asymptotic convergence factor [26] is calculated as

$$r_{\text{asym}}(\beta(t_k^i)) = \sup_{z(0) \neq \dot{z}} \left(\frac{\|z(t_k^i) - \dot{z}\|_2}{\|z(0) - \dot{z}\|_2} \right)^{1/t_k^i}, \quad (14)$$

where $\dot{z} = \lim_{t \rightarrow \infty} z(t_k^i)$.

Generally convergence is mentioned as a degree of error reduction with refinement towards zero for finite elements with grid spacing. Similarly asymptotic convergence is defined as a convergence behaviour of the system when grid arrangement is considered very trivial in a matrix and error between two states ranges towards zero.

From (14), the convergence time can be computed as

$$\tau_{\text{asym}} = \frac{1}{\log(1/r_{\text{asym}}(\beta(t_k^i)))}. \quad (15)$$

Convergence time of any system is defined as a computation time, exactly how speedily different agents in a network touch a state of consistent convergence. It is considered to be one of the foremost goals and vital performance indicators in designing of distributed algorithms.

One of the other important performance indicators used for network convergence is matrix spectral radius and it is denoted by $\rho(\cdot)$. It is a biggest absolute value of its eigenvalues in the matrix spectrum. Mathematically it can be expressed as

$$r_{\text{asym}}(\beta) = \rho\left(\beta - \frac{11^T}{n}\right). \quad (16)$$

4. Proposed Algorithm

In the field of distributed multiagent systems, its primary impression that consensus algorithms enforce the network agents communicating in a network towards a common value by information exchange by their neighbourhood if the communication is reliable; network topology is considered fixed. But achieving consensus for the cases in which network connectivity is unreliable, communication is asynchronous and update time for the network agents varying time to time is really challenging.

In this section we are proposing a consensus algorithm for distributed network consisting of n autonomous agents (i.e., $1, 2, \dots, n$), whose directed graph topology is considered as a fixed (reliable) and for switching topology (unreliable). Agents are sharing a common state space \mathbb{R} with asynchronous communication in terms of different update time for each agent. Initial start time for all agent is considered the same but later on each agent adjusts its current state value, depending on the information received from other set of defined neighbors $N(t, i)$ at a particular instance of time. Let $z_i(t_k^i) \in \mathbb{R}$ represents the initial state of an agent i and let $Z = [z_1, z_2, \dots, z_n]^T$. We can represent designed discrete time multiagent system as $z(t_k^i + 1) = f(t_k^i, u(t_k^i))$, where $u(t_k^i)$ is a state feedback controller which needs to be designed as well with the help of weighting matrix. If we suppose $z(t_k^i)$ as an initial value and it converges to a stable value z , in such away that $\dot{z}_i = \dot{z}_j$ for all i, j as $t \rightarrow \infty$, then it is said to achieve consensus. If agent i receives the state information of its neighbors at t_k^i , then agent i is assumed to take the following dynamics in time interval (t_k^i, t_{k+1}^i) :

$$\dot{z}_i(t) = z_i(t) + \sum_{j \in N(t_k^i, i)} \beta_{ij}(t_k^i) (z_j(t_k^i) - z_i(t)) \quad (17)$$

if $N(t_k^i, i) \neq \phi$,

where $t \in [t_k^i, t_{k+1}^i)$.

We assume that agent i receives its neighbors states at update times $t_0^i, t_1^i, \dots, t_k^i, \dots$ which can be denoted as $\{t_k^i\}$. In proposed model we are considering the following condition, which presumed to be essentially contented by $\{t_k^i\}$.

Condition. For any $k \in \mathbb{Z}_+$, $0 < \tilde{T}_u \leq t_{k+1}^i \leq \widehat{T}_u$, where $\tilde{T}_u, \widehat{T}_u$.

The core intention behind the update times is to acquire an information of neighbours state value by an agent i to apprise its dynamic consequently. Two time bounds are presented in the proposed algorithm, upper bound \widehat{T}_u and lower

bound \tilde{T}_u . Both have their own importance and significance in convergence analysis under asynchronous time update communication. Lower bound \tilde{T}_u of time interval among any two consecutive update time offers assurance to the authentication of the consensus algorithm, while on the other hand upper bound \widehat{T}_u ; of $t_{k+1}^i - t_k^i$ supports the dissimilar states of an agents to assemble themselves on a common value.

While designing a proposed algorithm, primary goals are to achieve quick convergence, reduce the iterations for bounded convergence, and also meet the best of performance indicators as mentioned in the previous section.

Proposed algorithm can be mathematically expressed as

$$z_i(t_{k+1}^i) = z_i(t_k^i) + \sum_{j \in N(t_k^i, i)} \beta_{ij}(t_k^i) (z_j(t_k^i) - z_i(t_k^i)) \quad (18)$$

we can write

$$\beta_{ij}(t_k^i) = \begin{cases} \frac{(d_i(t_k^i) + d_j(t_k^i))}{(2d_i(t_k^i) * d_j(t_k^i))} & i \neq j \\ 0 & \text{otherwise.} \end{cases} \quad (19)$$

In the above equation d_i is the degree of agent i or we can say the total neighbors of an agent i .

Proof of an Algorithm. Suppose

$$Z(t_k^i) = \begin{bmatrix} Z_1(t_k^1) \\ Z_2(t_k^2) \\ \dots \\ \dots \\ Z_n(t_k^n) \end{bmatrix}, \quad (20)$$

$$U(t_k^i) = \begin{bmatrix} u_1(t_k^1) \\ u_2(t_k^2) \\ \dots \\ \dots \\ u_n(t_k^n) \end{bmatrix}.$$

Similarly

$$Z(t_k^i + 1) = \begin{bmatrix} z_1(t_k^1 + 1) \\ z_2(t_k^2 + 1) \\ \dots \\ \dots \\ z_n(t_k^n + 1) \end{bmatrix}. \quad (21)$$

At this point it is significant to articulate a global state equation for a system, which is intended for average convergence in the given form as

$$Z(t_k^i + 1) = Z(t_k^i) + U(t_k^i). \quad (22)$$

Global input vector can be formulated as

$$U(t_k^i) = \beta_{ij}(t_k^i) [A - D] Z(t_k^i). \quad (23)$$

For unreliable network topology the weighting matrix β is not fixed, so for the particular case we used the following symbolization $\beta_{ij}(t_k^i)$ in (23). After deputizing (23) in (22), we will get

$$Z(t_k^i + 1) = Z(t_k^i) + \beta_{ij}(t_k^i) [A - D] Z(t_k^i). \quad (24)$$

We can additionally write the following after applying the concept of Laplacian matrix:

$$Z(t_k^i + 1) = Z(t_k^i) - L\beta_{ij}(t_k^i) Z(t_k^i), \quad (25)$$

$$Z(t_k^i + 1) = [I - L\beta_{ij}(t_k^i)] Z(t_k^i). \quad (26)$$

Distributed linear iteration in (26) designates for $t_k^i = 0, 1, 2, \dots$:

$$Z(t_k^i) = [I - L\beta_{ij}(t_k^i)] Z(0), \quad (27)$$

$$\lim_{t_k^i \rightarrow \infty} Z(t_k^i) = \lim_{t_k^i \rightarrow \infty} (I - \beta_{ij}(t_k^i) L) Z(0). \quad (28)$$

Now equating (11) and (28),

$$\lim_{t_k^i \rightarrow \infty} \beta(t_k^i) = \lim_{t_k^i \rightarrow \infty} (I - \beta_{ij}(t_k^i) L). \quad (29)$$

Now referring to (13)

$$\lim_{t_k^i \rightarrow \infty} \beta(t_k^i) = \left(\frac{1}{n}\right) 11^T. \quad (30)$$

Therefore,

$$\lim_{t_k^i \rightarrow \infty} (I - \beta_{ij}(t_k^i) L) = \left(\frac{1}{n}\right) 11^T. \quad (31)$$

If we consider a system, with infinite number of agents, that is, $n \rightarrow \infty$, then we can write

$$\lim_{t_k^i \rightarrow \infty} (I - \beta_{ij}(t_k^i) L) = 0. \quad (32)$$

The concluding outcome of (32) will develop as

$$\beta_{ij}(t_k^i) = \begin{cases} \frac{(d_i(t_k^i) + d_j(t_k^i))}{(2d_i(t_k^i) * d_j(t_k^i))} & i \neq j \\ 0 & \text{otherwise.} \end{cases} \quad (33)$$

□

5. Numerical Examples and Simulation Results

In this section stimulation results are presented for various numerical examples. All examples are simulated in Matlab environment for generating results. This section also validate the efficiency of projected algorithm in four different scenarios for asynchronous time update communication

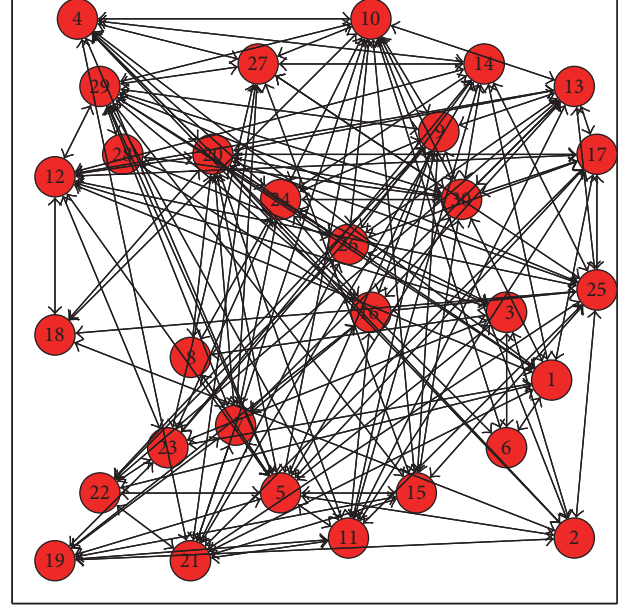


FIGURE 1: Network topology considered in Example 1.

under reliable and unreliable communication. To compare the benchmarks of proposed algorithm, a detailed simulation comparison with other existing approaches is performed. For that particular purpose four different performance parameters, that is, total number of iterations, CPU time, asymptotic convergence factor, and convergence time, have been considered to compute the results for each scenario. Total number of iterations is basically the iteration count in which the consensus is achieved using Matlab software and similarly CPU time is the processing time of the machine on which all the simulation are carried out with same computational resources. Error graphs of proposed method and other existing approaches are also produced in this section for better understanding. Initial values are assigned to agents as $x_n(0) = 1$ and $x_i(0) = 0$, $\forall i = 1, 2, 3, \dots, n-1$ in all four numerical examples. For any $i \in I_n$, $t_{k+1}^i - t_k^i$ is evenly distributed between 0.2 and 0.6, lower time bound is $\tilde{T}_u = 0.2$, and upper time bound is $\widehat{T}_u = 0.6$. Additionally error tolerance considered is $e = 10^{-15}$, in which the total number of iterations is represented by NI, where

$$e_i(k) = \sum_{j \in N_i} |x_i(k) - x_j(k)|, \quad i = 1, 2, \dots, n. \quad (34)$$

Example 1 (fixed network topology with asynchronous time update). In this example, a case of reliable communication among multiagents with asynchronous time update is considered (Figure 1). Communication topology remains fixed throughout the simulation but the update times of agents are diverse and independent of each others. Each agent can get all of its neighbour states only at its update times. For any $i \in I_n$, $t_{k+1}^i - t_k^i$ is evenly distributed between 0.2 and 0.6. A network of 30 agents is considered which are communicating with each other under reliable conditions. All agents have to develop an average consensus on the value of 0.0333. To

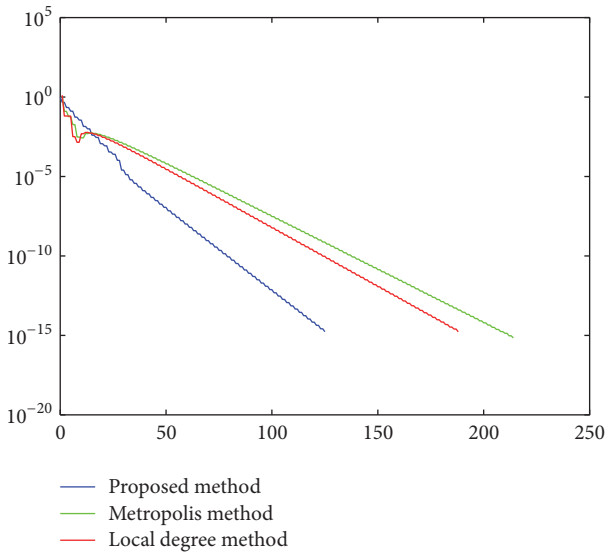


FIGURE 2: Plot of error graph generated for Example 1.

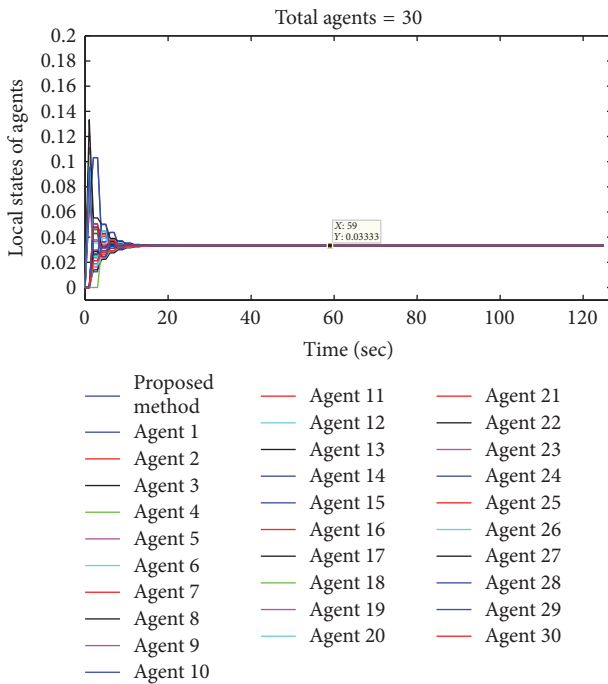


FIGURE 3: Agents approaching to a consensus value using proposed algorithm in Example 1.

evaluate the performance of proposed algorithm, the comparison results of Example 1, simulated by proposed and existing methods are shown in Table 1. An error graph is generated in Figure 2, which evaluates how fast a method converges to its consensus value. It also helps us to graphically evaluate the performance of different methods. The consensus graphs of proposed method, Metropolis method, and local degree method are shown in Figures 3, 4, and 5 respectively.

Example 2 (unreliable switching network topology with asynchronous time update). The second case is on unreliable

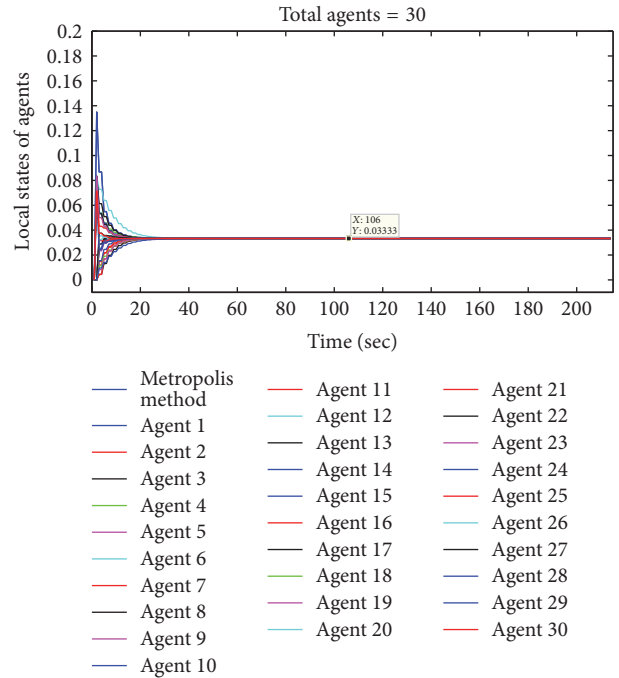


FIGURE 4: Agents approaching to a consensus value using Metropolis method in Example 1.

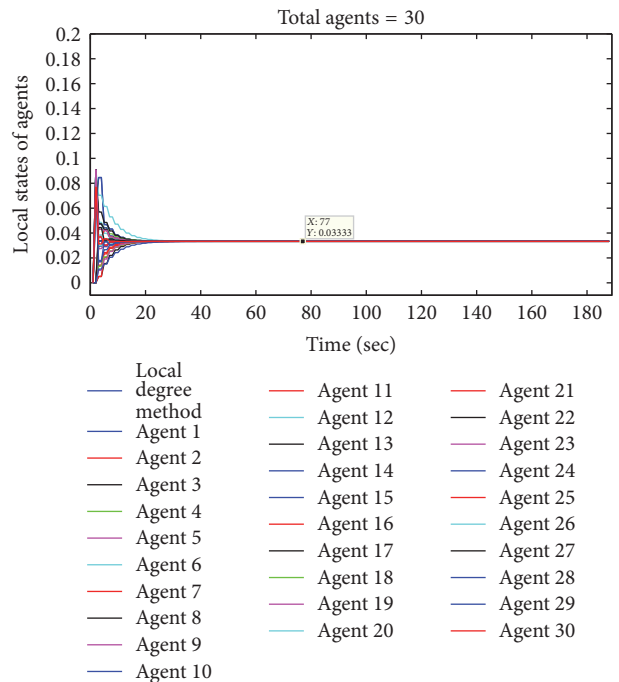


FIGURE 5: Agents approaching to a consensus value using local degree method in Example 1.

switching topologies with asynchronous update time. In this example two major challenges in cooperative control are highlighted, that is, unreliable communication among agents and asynchronous behavior in update times. When the communication topology is changing dynamically and

TABLE 1: Comparison results of Example 1 for different performance parameters.

Methods	NI	CPU _{Min}	$\rho(W - 11^T/n)$	τ_{asym}
Proposed method	127	0.342	0.7518	3.505
Metropolis method	215	0.3972	0.8461	6.003
Local degree method	189	0.3617	0.8284	5.3131

TABLE 2: Comparison results of Example 2 for different parameters.

Methods	NI	CPU _{Min}	$\rho(W - 11^T/n)$	τ_{asym}
Proposed method	163	0.2092	0.7998	4.778
Metropolis method	245	0.2868	0.8635	6.8173
Local degree method	215	0.2540	0.8456	5.9660

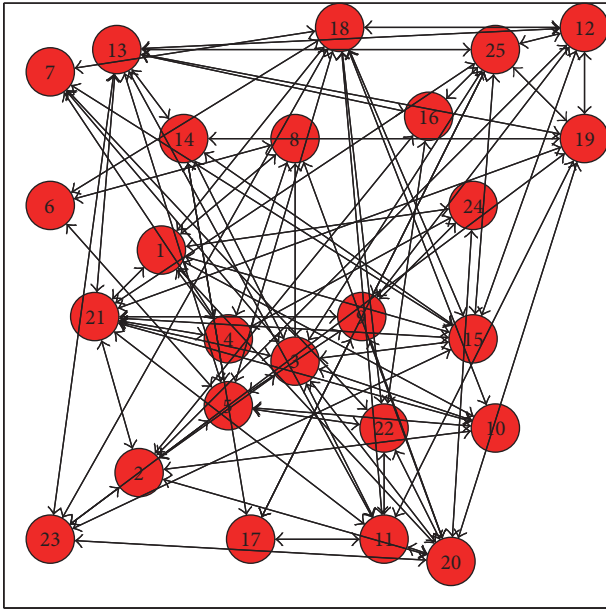


FIGURE 6: Network topology considered in Example 2.

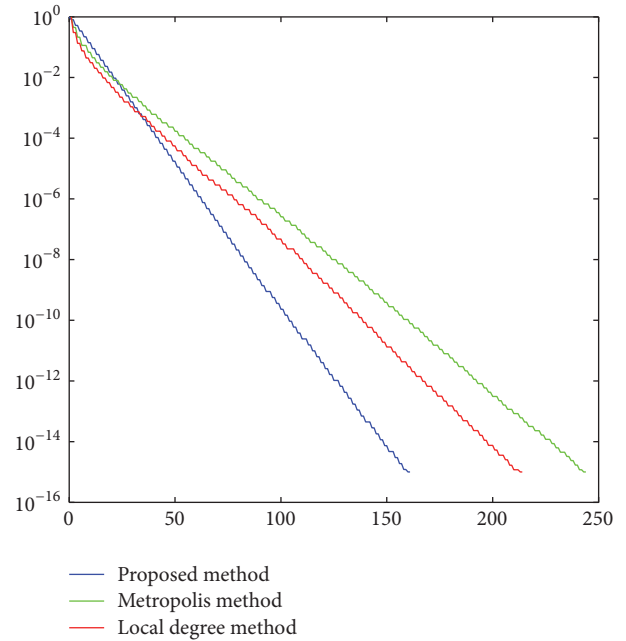


FIGURE 7: Plot of an error graph for Example 2.

additionally the update times are also varying and independent of each other, it becomes more challenging for agents to make consensus on a single value. These kinds of problems are really helpful to compare the performance of consensus methods. The numerical results of case 2 are shown in Table 2. The graphical comparison of consensus methods and the network topology are shown in Figures 7 and 6, respectively. The consensus graphs of proposed method, Metropolis method, and local degree method are shown in Figures 8, 9, and 10, respectively, which are the evidence of perfectness of proposed method.

Example 3 (addition of agents in reliable network topology at any time instant). This example is the continuity case of Example 1 and is called forced consensus problem. As in Example 1, some agents are selected randomly with fixed topology with asynchronous time updates, and finally they develop a consensus on a single value. Similarly in this example, some agents are randomly added in the network at any

time instant and now they have to develop consensus on some new unique value. This means that at any time instant, the agents are forced from one value to another consensus value. In this example, 10 agents are added at some time interval; that is, $t = 50$ ms; the total number of agents becomes 40 and they have to develop consensus on value 0.025 with utilizing the asynchronous time updates; that is, it is fixed between 0.2 and 0.6. The numerical results of Example 3 are produced in Table 3. The network topology considered for this example is shown in Figure 11. In Figure 12, error is plotted for the proposed method, metropolis, and local degree method, respectively. Consensus graphs for this case are presented in Figures 13, 14, and 15.

Example 4 (addition of agents in unreliable network topology with asynchronous time update at any instant of time). This example is the second problem of forced consensus and is the continuity of case in Example 2. As in Example 2, some agents are selected randomly with dynamically changing interaction

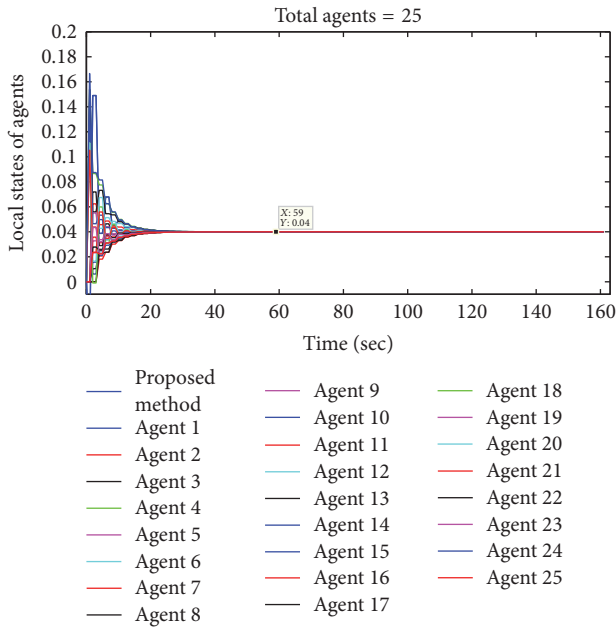


FIGURE 8: Agents approaching to a consensus value using proposed algorithm in Example 2.

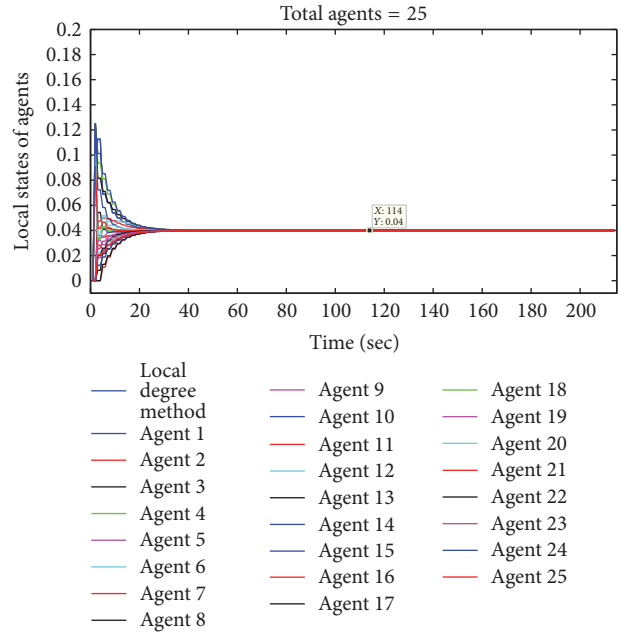


FIGURE 10: Agents approaching to a consensus value using local degree method in Example 2.

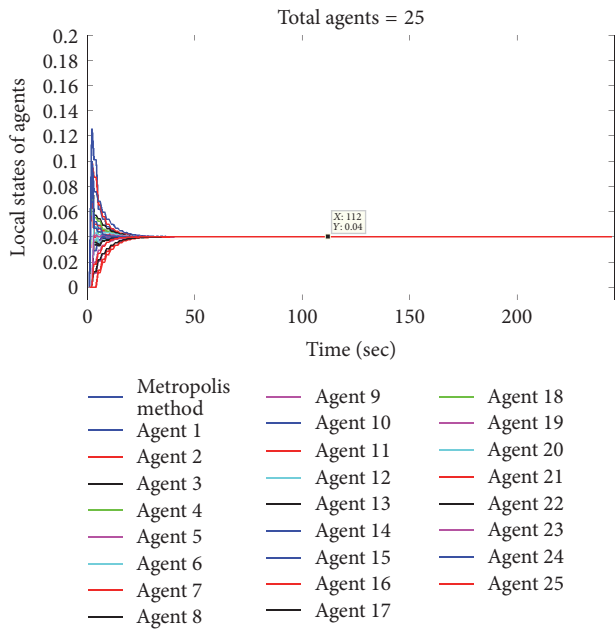


FIGURE 9: Agents approaching to a consensus value using Metropolis method in Example 2.

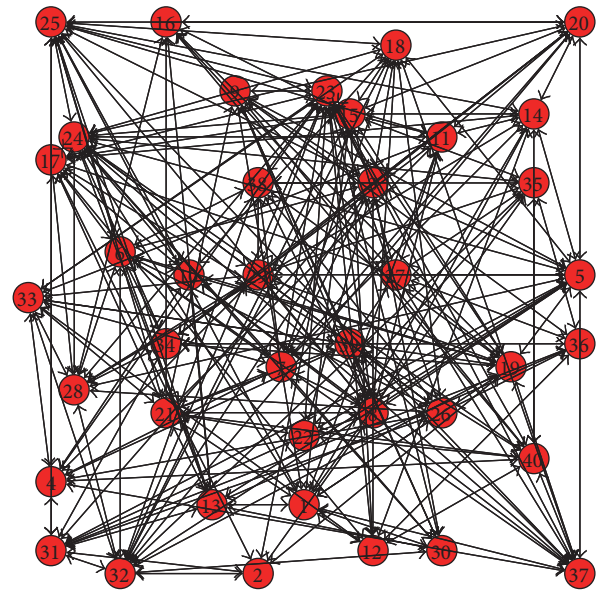


FIGURE 11: Communication topology considered in Example 3.

topology and asynchronous time updates; they developed consensus on a single value. In this example some agents are randomly added in the system at any time instant. Addition of agents disturbs the performance of consensus methods as the communication strategy is unreliable and changing randomly and also the time updates are asynchronous, so it becomes difficult for the agents to develop agreement on a single value but with proposed method it reaches to the consensus value in a less convergence time as compared to

other techniques. The numerical results of Example 4 are shown in Table 4. The network topology considered for this example is given in Figure 16. In Figure 17 error is plotted for the proposed method, metropolis, and local degree method, respectively. Consensus graphs for this case are shown in Figures 18, 19, and 20. From the numerical and graphical analysis of different consensus techniques, it is observed that the proposed method converges faster to consensus value than other well-known consensus methods.

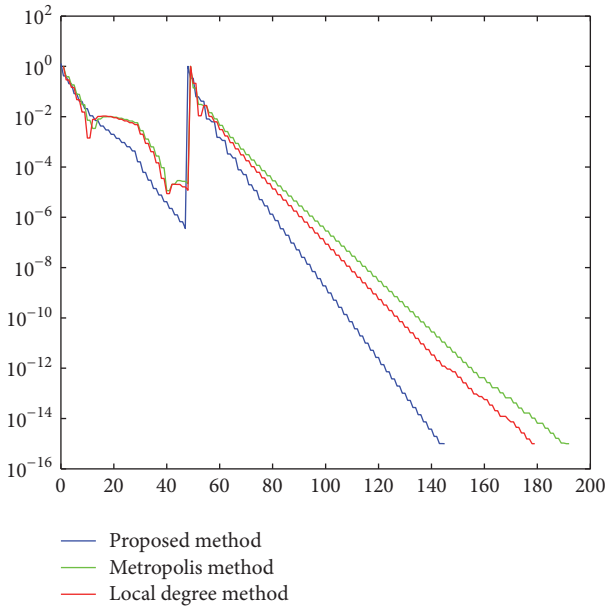


FIGURE 12: Plot of error graph generated for Example 3.

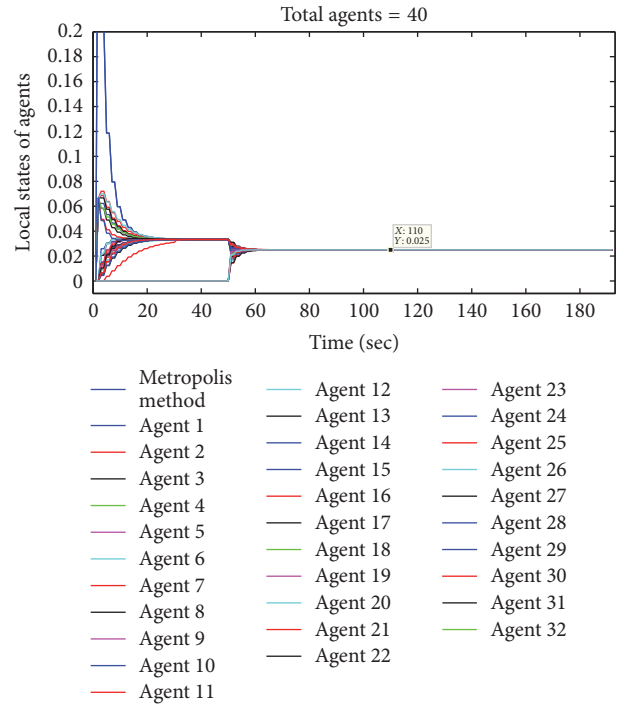


FIGURE 14: Agents approaching to a consensus value using Metropolis method in Example 3.

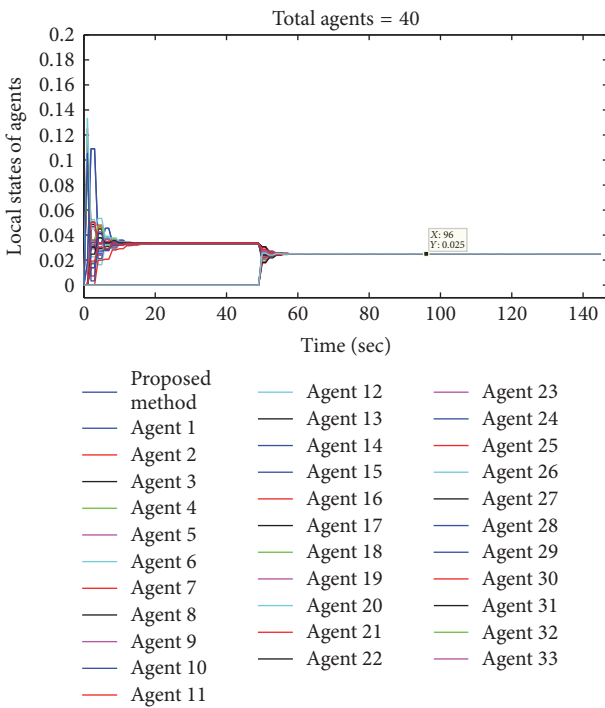


FIGURE 13: Agents approaching to a consensus value using proposed algorithm in Example 3.

6. Conclusion

This paper proposed a new convergence algorithm for distributed multiagent systems. A unique approach of asynchronous time updates under reliable and unreliable network topology is implemented to produce better results in terms of different performance indicators, such as number of iterations and computational cost, and, capable of operability

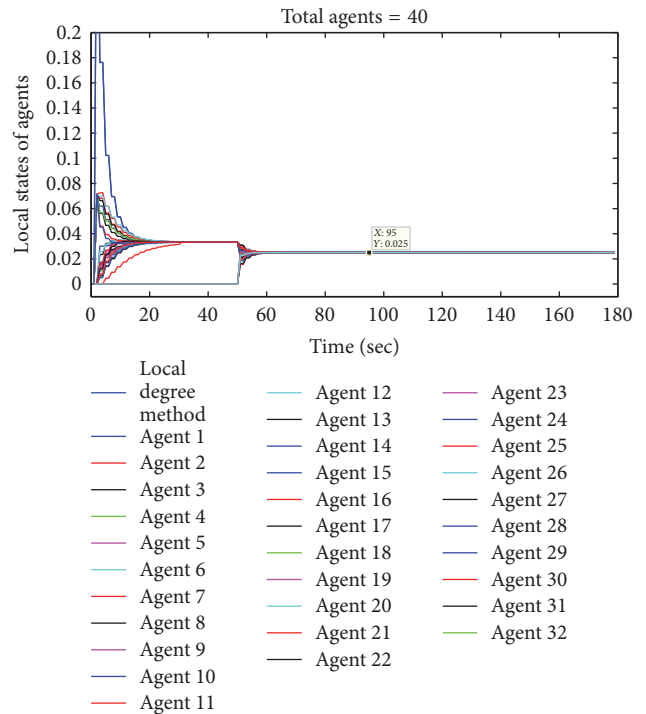


FIGURE 15: Agents approaching to a consensus value using local degree method in Example 3.

in large dynamic networks with unreliable communication, CPU processing time, asymptotic convergence factor, and

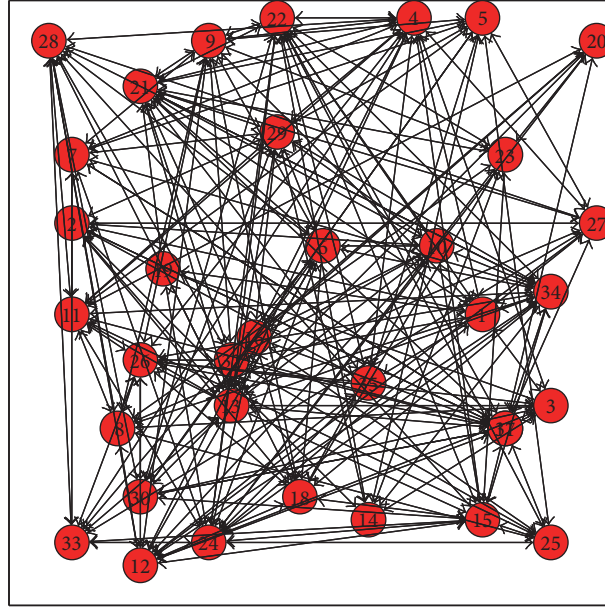


FIGURE 16: Network topology considered in Example 4.

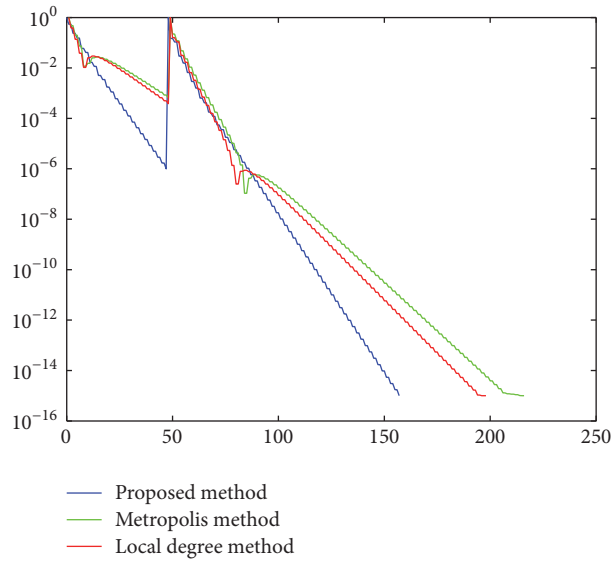


FIGURE 17: Plot of an error graph for Example 4.

TABLE 3: Comparison results of Example 3 for different parameters.

Methods	NI	CPU _{Min}	$\rho(W - 11^T/n)$	τ_{asym}
Proposed method	147	0.3515	0.7743	3.909
Metropolis method	193	0.4013	0.8216	5.089
Local degree method	180	0.3961	0.8070	4.663

TABLE 4: Comparison results of Example 4 for different parameters.

Methods	NI	CPU _{Min}	$\rho(W - 11^T/n)$	τ_{asym}
Proposed method	159	0.4571	0.7950	4.359
Metropolis method	217	0.4767	0.8494	6.1297
Local degree method	199	0.4654	0.8370	5.6231

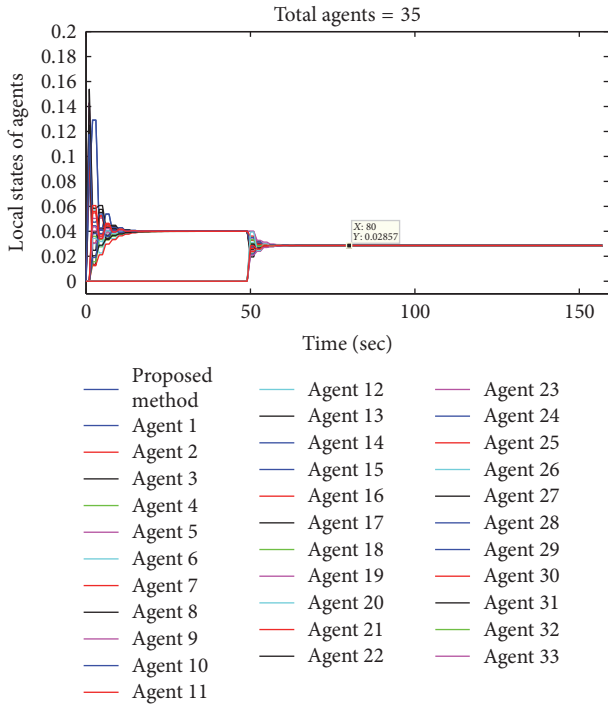


FIGURE 18: Agents approaching to a consensus value using proposed algorithm in Example 4.

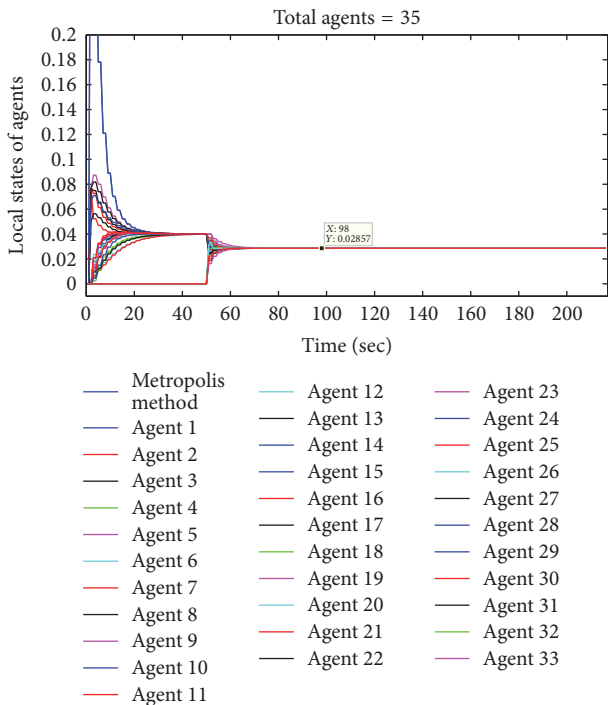


FIGURE 19: Agents approaching to a consensus value using Metropolis method in Example 4.

convergence time have been considered. A detailed comparison is produced with each example with different operational scenario, as an effective evidence to prove the efficiency of the proposed algorithm. In future we will extend our

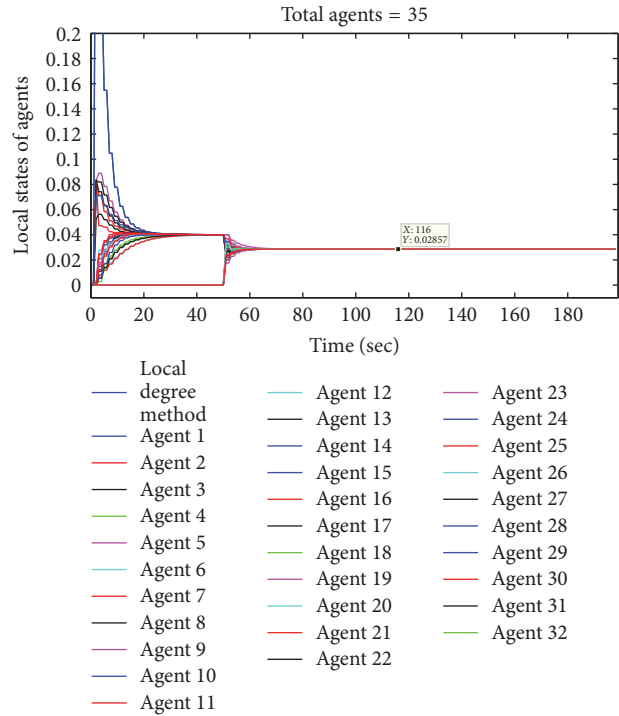


FIGURE 20: Agents approaching to a consensus value using local degree method in Example 4.

research for systems experiencing time varying delays under asynchronous communication to study their performance.

Conflicts of Interest

The authors declare that there are no conflicts of interest regarding the publication of this paper.

References

- [1] Q. Zhang, P. Li, Z. Yang, and Z. Chen, “Distance constrained based adaptive flocking control for multiagent networks with time delay,” *Article ID*, Article ID 901282, 2014.
- [2] R. Olfati-Saber, “Flocking for multi-agent dynamic systems: algorithms and theory,” *Institute of Electrical and Electronics Engineers Transactions on Automatic Control*, vol. 51, no. 3, pp. 401–420, 2006.
- [3] J. Zhu, J. Lu, and X. Yu, “Flocking of multi-agent non-holonomic systems with proximity graphs,” *IEEE Transactions on Circuits and Systems I: Regular Papers*, vol. 60, no. 1, pp. 199–210, 2013.
- [4] M. M. Zavlanos, A. Jadbabaie, and G. J. Pappas, “Flocking while preserving network connectivity,” in *Proceedings of the 46th IEEE Conference on Decision and Control*, pp. 2919–2924, December 2007.
- [5] M. Khan, G. Pandurangan, and V. S. A. Kumar, “Distributed algorithms for constructing approximate minimum spanning trees in wireless sensor networks,” *IEEE Transactions on Parallel and Distributed Systems*, vol. 20, no. 1, pp. 124–139, 2009.
- [6] B. K. N. Trigoni and B. Krishnamachari, “Sensor network algorithms and applications,” *Philosophical Transactions of the Royal Society A: Mathematical, Physical & Engineering Sciences*, vol. 370, no. 1958, pp. 5–10, 2012.

- [7] J. Dai, A. Benini, H. Lin, P. J. Antsaklis, M. J. Rutherford, and K. P. Valavanis, "Learning-based formal synthesis of cooperative multi-agent systems with an application to robotic coordination," in *Proceedings of the 24th Mediterranean Conference on Control and Automation, MED 2016*, pp. 1008–1013, Greece, June 2016.
- [8] M. F. Ge, Z. H. Guan, B. Hu, D. X. He, and R. Q. Liao, "Distributed controller-estimator for target tracking of networked robotic systems under sampled interaction," *Automatica*, vol. 69, pp. 410–417, 2016.
- [9] J. Barreiro-Gomez, I. Mas, C. Ocampo-Martinez, R. Sanchez-Pena, and N. Quijano, "Distributed formation control of multiple unmanned aerial vehicles over time-varying graphs using population games," in *Proceedings of the 55th IEEE Conference on Decision and Control, CDC 2016*, pp. 5245–5250, USA, December 2016.
- [10] R. W. Beard, J. Lawton, and F. Y. Hadaegh, "A coordination architecture for spacecraft formation control," *IEEE Transactions on Control Systems Technology*, vol. 9, no. 6, pp. 777–790, 2001.
- [11] R. Toyot and T. Namerikawa, "Formation control of multi-agent system considering obstacle avoidance," in *Proceedings of the 2017 56th Annual Conference of the Society of Instrument and Control Engineers of Japan (SICE)*, pp. 446–451, Kanazawa, September 2017.
- [12] D. E. Soltero, M. Schwager, and D. Rus, "Decentralized path planning for coverage tasks using gradient descent adaptive control," *International Journal of Robotics Research*, vol. 33, no. 3, pp. 401–425, 2014.
- [13] T. Han, Z. H. Guan, M. Chi, B. Hu, T. Li, and X. H. Zhang, "Multi-formation control of nonlinear leader-following multi-agent systems," *ISA Transactions*, vol. 69, pp. 140–147, 2017.
- [14] J. A. Fax and R. M. Murray, "Information flow and cooperative control of vehicle formations," *Institute of Electrical and Electronics Engineers Transactions on Automatic Control*, vol. 49, no. 9, pp. 1465–1476, 2004.
- [15] A. Kashyap, T. Başar, and R. Srikant, "Quantized consensus," *Automatica*, vol. 43, no. 7, pp. 1192–1203, 2007.
- [16] X. Hu, H. Zhou, Z. Liu, X. Yu, and C. Li, "Hierarchical Distributed Scheme for Demand Estimation and Power Reallocation in a Future Power Grid," *IEEE Transactions on Industrial Informatics*, vol. 13, no. 5, pp. 2279–2290, 2017.
- [17] C. Li, X. Yu, W. Yu, T. Huang, and Z.-W. Liu, "Distributed event-triggered scheme for economic dispatch in smart grids," *IEEE Transactions on Industrial Informatics*, vol. 12, no. 5, pp. 1775–1785, 2016.
- [18] J. Wolfowitz, "Products of indecomposable, aperiodic, stochastic matrices," *Proceedings of the American Mathematical Society*, vol. 14, pp. 733–737, 1963.
- [19] V. Borkar and P. P. Varaiya, "Asymptotic agreement in distributed estimation," *Institute of Electrical and Electronics Engineers Transactions on Automatic Control*, vol. 27, no. 3, pp. 650–655, 1982.
- [20] C. W. Reynolds, "Flocks, herds, and schools: a distributed behavioral model," *Computer Graphics*, vol. 21, no. 4, pp. 25–34, 1987.
- [21] R. Olfati-Saber and R. M. Murray, "Consensus problems in networks of agents with switching topology and time-delays," *Institute of Electrical and Electronics Engineers Transactions on Automatic Control*, vol. 49, no. 9, pp. 1520–1533, 2004.
- [22] R. Olfati-Saber, J. A. Fax, and R. M. Murray, "Consensus and cooperation in networked multi-agent systems," *Proceedings of the IEEE*, vol. 95, no. 1, pp. 215–233, 2007.
- [23] W. Ren and R. W. Beard, "Consensus seeking in multiagent systems under dynamically changing interaction topologies," *Institute of Electrical and Electronics Engineers Transactions on Automatic Control*, vol. 50, no. 5, pp. 655–661, 2005.
- [24] L. Moreau, "Stability of multiagent systems with time-dependent communication links," *Institute of Electrical and Electronics Engineers Transactions on Automatic Control*, vol. 50, no. 2, pp. 169–182, 2005.
- [25] L. Moreau, "Stability of continuous-time distributed consensus algorithms," in *Proceedings of the 43rd IEEE Conference on Decision and Control (CDC '04)*, pp. 3998–4003, December 2004.
- [26] E. Kokopoulou and P. Frossard, "Polynomial filtering for fast convergence in distributed consensus," *IEEE Transactions on Signal Processing*, vol. 57, no. 1, pp. 342–354, 2009.
- [27] D. Yuan, D. W. C. Ho, and S. Xu, "Regularized Primal-Dual Sub-gradient Method for Distributed Constrained Optimization," *IEEE Transactions on Cybernetics*, vol. 46, no. 9, pp. 2109–2118, 2016.
- [28] W. Li, G. Wei, F. Han, and Y. Liu, "Weighted average consensus-based unscented Kalman filtering," *IEEE Transactions on Cybernetics*, 2015.
- [29] Z. H. Guan, D. J. Hill, and X. Shen, "On hybrid impulsive and switching systems and application to nonlinear control," *Institute of Electrical and Electronics Engineers Transactions on Automatic Control*, vol. 50, no. 7, pp. 1058–1062, 2005.
- [30] Y. Wu, H. Su, P. Shi, Z. Shu, and Z. Wu, "Consensus of multi-agent systems using aperiodic sampled-data control," *IEEE Transactions on Cybernetics*, vol. 46, no. 9, pp. 2132–2143, 2016.
- [31] G. S. Han, Z. H. Guan, J. Li, R. Q. Liao, and X. M. Cheng, "Multi-consensus of multi-agent networks via a rectangular impulsive approach," *Systems Control Letters*, vol. 76, pp. 28–34, 2015.
- [32] W. Yu, L. Zhou, X. Yu, J. Lu, and R. Lu, "Consensus in multi-agent systems with second-order dynamics and sampled data," *IEEE Transactions on Industrial Informatics*, vol. 9, no. 4, pp. 2137–2146, 2013.
- [33] M. T. Hale, A. Nedi, and M. Egerstedt, "Asynchronous multi-agent primal-dual optimization," *Institute of Electrical and Electronics Engineers Transactions on Automatic Control*, vol. 62, no. 9, pp. 4421–4435, 2017.
- [34] Z. Liu, "Asynchronous impulsive consensus of multi-agent systems," in *Proceedings of the 2017 Eighth International Conference on Intelligent Control and Information Processing (ICICIP)*, pp. 278–281, Hangzhou, November 2017.
- [35] X. Wang, Z. Zeng, and Y. Cong, "Multi-agent distributed coordination control: developments and directions via graph viewpoint," *Neurocomputing*, vol. 199, pp. 204–218, 2016.
- [36] V. K. Yanumula, I. Kar, and S. Majhi, "Consensus of second-order multi-agents with actuator saturation and asynchronous timedelays," *IET Control Theory Applications*, pp. 3201–3210, 2017.
- [37] S. Bolognani, R. Carli, E. Lovisari, and S. Zampieri, "A randomized linear algorithm for clock synchronization in multi-agent systems," *Institute of Electrical and Electronics Engineers Transactions on Automatic Control*, vol. 61, no. 7, pp. 1711–1726, 2016.
- [38] Y. Feng, S. Xu, and B. Zhang, "Group consensus control for double-integrator dynamic multiagent systems with fixed

- communication topology,” *International Journal of Robust and Nonlinear Control*, vol. 24, no. 3, pp. 532–547, 2014.
- [39] L. Xiao and S. Boyd, “Fast linear iterations for distributed averaging,” in *Proceedings of the 42nd IEEE International Conference on Decision and Control*, pp. 4997–5002, Maui, HI, USA.
- [40] W. K. Hastings, “Monte Carlo sampling methods using Markov chains and their applications,” *Biometrika*, vol. 57, no. 1, pp. 97–109, 1970.
- [41] N. Metropolis, A. W. Rosenbluth, M. N. Rosenbluth, A. H. Teller, and E. Teller, “Equation of state calculations by fast computing machines,” *The Journal of Chemical Physics*, vol. 21, no. 6, pp. 1087–1092, 1953.
- [42] F. Xiao and L. Wang, “State consensus for multi-agent systems with switching topologies and time-varying delays,” *International Journal of Control*, vol. 79, no. 10, pp. 1277–1284, 2006.

Research Article

Lateral Stability Control of Four-Wheel Independent Drive Electric Vehicles Based on Model Predictive Control

Bin Huang , Sen Wu, Song Huang, and Xiang Fu 

Hubei Key Laboratory of Advanced Technology of Automobile Parts, School of Automotive Engineering,
Wuhan University of Technology, Wuhan 430070, China

Correspondence should be addressed to Xiang Fu; fuxiang@whut.edu.cn

Received 8 July 2017; Revised 9 November 2017; Accepted 13 December 2017; Published 7 February 2018

Academic Editor: Tran H. Linh

Copyright © 2018 Bin Huang et al. This is an open access article distributed under the Creative Commons Attribution License, which permits unrestricted use, distribution, and reproduction in any medium, provided the original work is properly cited.

Four-wheel independent drive electric vehicle was used as the research object to discuss the lateral stability control algorithm, thus improving vehicle stability under limit conditions. After establishing hierarchical integrated control structure, we designed the yaw moment decision controller based on model predictive control (MPC) theory. Meanwhile, the wheel torque was assigned by minimizing the sum of consumption rates of adhesion coefficients of four tires according to the tire friction ellipse theory. The integrated simulation platform of Carsim and Simulink was established for simulation verification of yaw/rollover stability control algorithm. Then, we finished road experiment verification of real vehicle by integrated control algorithm. The result showed that this control method can achieve the expectation of effective vehicle tracking, significantly improving the lateral stability of vehicle.

1. Introduction

With independent controllable drive/brake moment, rapid moment response, and measurable torque and speed, four-wheel independent drive electric vehicle has advantages in improving vehicle stability. When the vehicle has the risk of instability or has lost stability, it is difficult for the ground to maintain vehicle tracking and attitude adjustment with sufficient lateral force. Meanwhile, the vehicle based on active steering has little effect on driving direction control [1, 2]. In differential braking/driving process, the longitudinal force of the tire is adjusted to control yaw stability. It still has significant control effect even when the vehicle yaw movement loses stability. Differential braking is integrated with differential driving to broaden the range of active yaw moment, thus reducing the decrease in vehicle speed and keeping the vehicle in a stable running state.

Domestic and foreign scholars have made lots of researches on yaw stability control based on distributed structure electric vehicle. The developed control strategy can be divided into yaw moment decision and wheel torque distribution control layers. References [3–5] focus on achieving direct yaw control by distributing the rear wheel driving or braking

force. However, a single wheel produces limited yaw response with limited adhesion during the process of steering instability. Effective use of the adhesion of multiple wheels can greatly enhance the stability. In [6], the concept of additional yaw torque control is proposed. Based on independent control of braking force, the in-wheel motor is integrated with the rear wheel drive force control. Relying on the yaw control of driving and braking forces, the yaw response decreases at least 10% of the delay, and the lateral acceleration rises by up to 40%. In [7–11], the yaw moment decision is completed by adaptive control, fuzzy logic, and so on. Braking and driving coordination control can be used to achieve faster yaw response. However, these researches only apply simple method for hierarchical control. Only controlling the current state makes the existence of improved space for system robustness and accuracy. In [12], the classical sliding mode control theory is used to calculate the yaw moment required for dynamic control of in-wheel motor driving vehicle. The sliding surface is formed by the yaw rate error and the error change rate. The torque outputs of the motors are coordinated to achieve the above yaw moment value. When the system parameters are uncertain, this control method has good robustness. However, the high-frequency switching of sliding mode controller introduces a certain degree of “chattering”

phenomenon, which affects the control precision of vehicle dynamics.

For the vehicles with high centroid, when they run on the high adhesion road with high speed, the emergency avoidance operation can easily cause the risk of rollover because of large lateral acceleration. The rollover stability control (RSC) is as important as the yaw stability control (YSC). Fujimoto and Hori's team of University of Tokyo have done a lot of related research on their developed small test vehicle. In [13, 14], RSC and YSC are designed by utilizing two-degree-of-freedom (2-DOF) control based on disturbance observer (DOB); the tracking capability and robustness for lateral acceleration disturbance against such as side blast are realized by the proposed DOB. And they further propose electronic stability program based on DOB, which achieves integrated three dimensional vehicle motion control [15]. The DOB is based on the model following control; it works very well if the velocity is constant and not so high. But, at high speed, the control effect is reduced. The purpose of this paper is to propose integrated yaw/rollover stability control; MPC-based four-wheel braking/driving torque coordinated control strategy was proposed to improve the driving stability of four-wheel independent electric drive off-road vehicle. The proposed MPC, which is independent of exact mathematical model, compared with the DOB can also overcome the influence of modeling errors and environmental uncertainties. MPC controls the current vehicle state while predicting the states in sampling periods. The current input is corrected to obtain more prominent control accuracy, stability and robustness. Therefore, it is suitable for solving nonlinear, multiple input, and output problems [16].

In the work, MPC-based four-wheel braking/driving torque coordinated control strategy was proposed to improve the driving stability of four-wheel independent electric drive off-road vehicle. According to MPC system structure, we established predictive control-oriented vehicle dynamics model. After that, the work improved vehicle yaw and rollover stability under limit conditions by taking driver's input as the reference and road adhesion as constraint. Vehicle braking/driving force was allocated by MPC to minimize rollover index LTR, the deviations of yaw rate and side slip angle. Then, we used Carsim and Simulink joint simulation platform including professional vehicle and road models for yaw stability control under low adhesion coefficient and double lane-change conditions as well as rollover stability control algorithm validation under high adhesion coefficient and hook conditions. At last, real vehicle test verification was performed under high speed double lane-change condition.

2. Lateral Stability Control Strategy

The control goal of lateral stability control strategy enables the vehicle to run in the control of the driver without the risk of rollover, achieving convenient operation and stable driving. The lateral stability of the vehicle includes both the yaw and the roll stabilities. Scholars take linear yaw characteristic deduced from two-degree-of-freedom vehicle model as the ideal characteristic of the vehicle. In the work, we also select it as the control target of ideal yaw stability of

the vehicle. For rollover stability, it is impossible to obtain the ideal rollover characteristic by establishing a simplified vehicle model. The current rollover condition of the vehicle is characterized only by selecting the appropriate rollover index. Besides, a suitable predicted value is selected to measure the possibility of rollover. In the rollover stability control, the expected rollover possibility should be as small as possible.

2.1. Yaw Stability Control Analysis. The yaw stability is characterized by state variables including side slip angle and yaw rate. Therefore, we determine the yaw stability of vehicle, and whether to carry out yaw stability control according to the two state variables.

When the side slip angle of vehicle satisfies the following equation, the vehicle is in a stable zone; otherwise, it is in an unstable zone, and the stability control must be added.

$$|\beta + B_1\dot{\beta}| \leq B_2, \quad (1)$$

where B_1 and B_2 are the parameters relevant to vehicle characteristics and driving state. In the work, we refer to the method of determining the boundary values of side slip angle by vehicle speed and pavement friction coefficient in [17]. Then, the relation between B_1 and B_2 is obtained by fitting.

$$\begin{aligned} |\dot{\beta} + B_1\beta| &\leq B_2, \\ B_1(\mu) &= 15.62\mu^2 - 34.37\mu - 6.719, \\ B_2(V, \mu) &= |0.0002343\mu^2V^2 - 0.000516\mu V^2 - 0.7498\mu^2 + 1.650\mu|, \end{aligned} \quad (2)$$

where μ is the tire-road friction coefficient and V is the travel speed. Equation (2) is used to determine the stability boundary of side slip angle. After that, we obtain the estimated values of side slip angle and its derivative through the state estimation procedure which has been developed and validated by the authors in [18], thus deriving actual state point of the vehicle. The driving state of vehicle can be determined and expressed as (3) according to the distance between actual state point and stable boundary.

$$\Delta D = |\beta + B_1\dot{\beta}| - B_2. \quad (3)$$

According to (1)–(3), we obtain the vehicle stability judgment phase diagram based on the side slip angle (see Figure 1).

If the side slip angle and yaw rate of the vehicle satisfy the following equation, then the vehicle is in a stable state; otherwise, the vehicle is in an unstable state.

$$\begin{aligned} |\gamma - \gamma^*| &\leq \gamma_{th}, \\ |\beta + B_1\dot{\beta}| - B_2 &\leq 0, \end{aligned} \quad (4)$$

where γ_{th} is the threshold of yaw rate determined by the change rate of steering angle.

In order to prevent the control system from frequent operation, the yaw stability control module is activated only

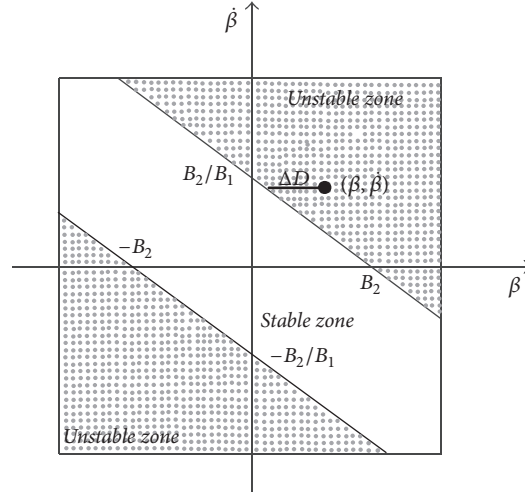


FIGURE 1: Vehicle stability judgment phase diagram based on the side slip angle.

when the deviation reaches a certain value. The control threshold is subtracted to determine effective deviation of additional yaw moment.

$$e_\gamma = \begin{cases} \Delta\gamma - \Delta\gamma_+ & \Delta\gamma > \Delta\gamma_+ \\ \Delta\gamma - \Delta\gamma_- & \Delta\gamma < \Delta\gamma_- \\ 0 & \text{others,} \end{cases} \quad (5)$$

$$e_\beta = \begin{cases} \Delta\beta - \Delta\beta_+ & \Delta\beta > \Delta\beta_+ \\ \Delta\beta - \Delta\beta_- & \Delta\beta < \Delta\beta_- \\ 0 & \text{others.} \end{cases}$$

2.2. Rollover Stability Control Analysis. When the off-road vehicle with high centroid runs in the high adhesion road with high speed, the emergency avoidance operation can easily cause the risk of rollover because of large lateral acceleration. The tire load transfer rate is the most direct indicator to describe vehicle rollover condition, which can be expressed by

$$\text{LTR} = \frac{F_{z0} - F_{zi}}{F_{z0} + F_{zi}}, \quad (6)$$

where F_{z0} , F_{zi} are outside and inside wheel vertical load.

The vehicle rollover state identified by the LTR value reflects the current vehicle state. For the driver, the vehicle rollover is possible to happen before the controller identifies the wheel off the ground by calculating $\text{LTR} = 1$. In the vehicle rollover stability analysis, it is important to predict the rollover state in the coming time.

The system warns the driver in advance to take an efficient operation within sufficient time or enables the rollover control system to take appropriate action by a command, effectively improving the rollover stability of vehicle [19].

In 2001, Bo-Chiuan Chen from University of Michigan firstly proposed the concept of Time-To-Rollover (TTR), which characterizes the time interval from the current

moment to the rollover time [15]. TTR is a good index to measure the risk degree of vehicle rollover. The TTR is calculated as follows. The vehicle prediction model can predict vehicle movement state within the longest N steps (T_s represents a step) according to the current vehicle state parameter and the steering wheel angle input. If LTR does not exceed its threshold within N steps, then $\text{TTR} = \text{TTR}_{\text{th}}$ (TTR_{th} represents the threshold), indicating that there is no risk of rollover in prediction time; if LTR exceeds the threshold in the n th step ($n < N$), then $\text{TTR} = n \cdot T_s$, indicating that there is a certain risk of rollover. The closer the TTR is to 0, the greater the risk of rollover is. At this moment, the prediction model stops the forecast and takes TTR value as the output. Meanwhile, the rollover warning system issues a warning and commands the rollover control system to intervene. Figure 2 shows the specific process.

Wherein, the rollover prediction model takes the current vehicle speed, the steering wheel angle, the additional yaw moment calculated at the previous time, and the vehicle sensor measurement value or the vehicle state estimation value as input. During the prediction process, it is assumed that the vehicle speed, steering wheel angle, and additional yaw moment remain unchanged.

The problem of vehicle yaw stability can occur in the road surface with any adhesion condition, and the rollover stability problem mainly occurs in the high adhesion road. Therefore, the yaw stability control takes effect in low adhesion road. In the high adhesion road, both yaw and rollover stability controls are possibly triggered synchronously or asynchronously.

2.3. Yaw Moment Decision Controller Based on MPC. The integrated controller determines the total driving/braking torque demand based on the throttle/brake pedal opening or the difference between the target and actual vehicle speed. YSC yaw moment decision module calculates the required yaw moment ensuring vehicle yaw stability by taking the difference between the actual and ideal values of centroid slip/yaw angle velocity as the input. RSC yaw moment decision module calculates the required yaw moment for

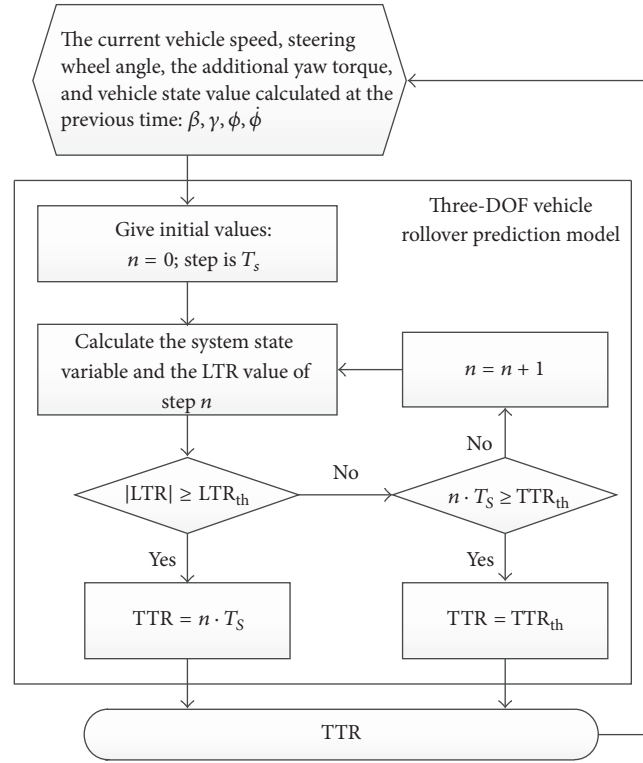


FIGURE 2: TTR rollover warning algorithm.

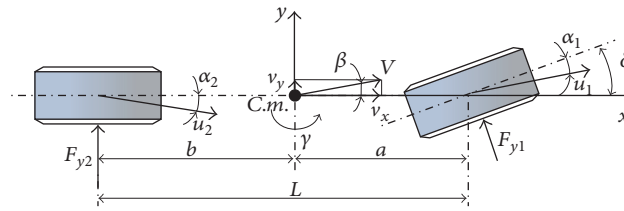


FIGURE 3: Linear two-DOF vehicle model.

rollover stabilization control by taking the LTR value output by the rollover prediction system as the input. The integrated control module of yaw/rollover stability finally determines the total yaw moment based on yaw and rollover state. When the sum of four-wheel target driving/braking torque is equal to the total demand torque, then the total demand torque is assigned to each wheel according to a certain distribution rule. Thus, the longitudinal forces of wheels produce the desired yaw moments. Wherein, the model prediction theory is used for YSC and RSC yaw moment decision modules.

2.3.1. Vehicle Reference Model. With little computation and good real-time control, the linear two-DOF vehicle model can better describe the driver's driving intention. The two degrees of freedom contain lateral and yaw directions. Figure 3 shows the specific reference vehicle model.

In Figure 3, β is the side slip angle; γ is the yaw rate; δ is the front wheel rotor angle; V is the centroid velocity; α_1 and α_2 are the slip angles of front and rear wheels; v_x and v_y are

the components of centroid velocity in axes x and y ; u_1 and u_2 are the velocities at the midpoints of front and rear axles; F_{y1} and F_{y2} are the slip forces of front and rear wheels.

$$\begin{aligned} F_{y1} &= k_1 \alpha_1, \\ F_{y2} &= k_2 \alpha_2, \end{aligned} \quad (7)$$

where k_1 and k_2 are the equivalent cornering stiffness of front and rear axles. According to the provisions of the tire coordinate system, the slip angles of front and rear wheels are expressed as follows:

$$\begin{aligned} \alpha_1 &= \beta + \frac{a\gamma}{v_x} - \delta, \\ \alpha_2 &= \beta - \frac{b\gamma}{v_x}, \end{aligned} \quad (8)$$

where a , b are the distance from centroid to front and rear axle.

The differential equations of motion in lateral and yaw directions are expressed as follows:

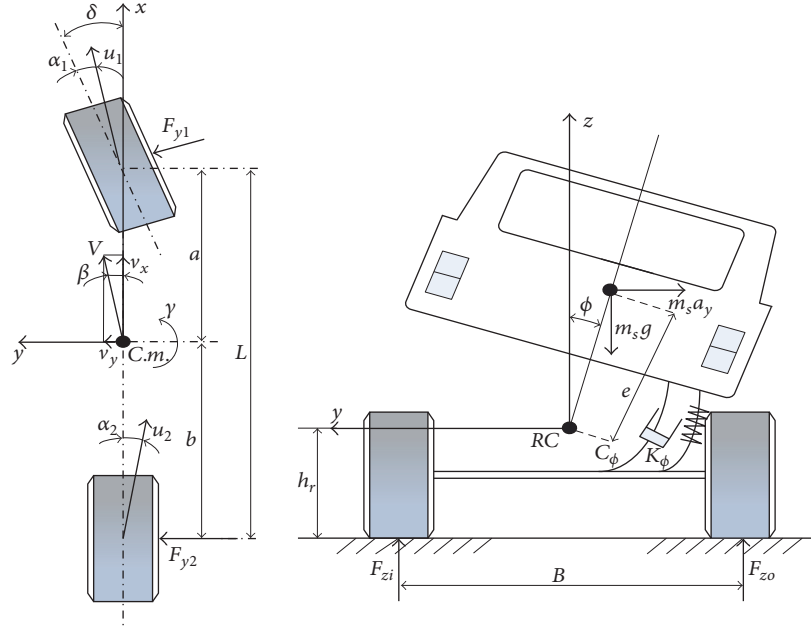


FIGURE 4: Three-DOF vehicle model.

$$(k_1 + k_2) \beta + \frac{ak_1 - bk_2}{v_x} \gamma - k_1 \delta = m(\dot{v}_y + v_x \gamma), \quad (9)$$

$$(ak_1 - bk_2) \beta + \frac{a^2 k_1 + b^2 k_2}{v_x} \gamma - ak_1 \delta = I_z \dot{\gamma}.$$

In stable state, the yaw angle velocity of vehicle is fixed. Here, $\dot{\gamma} = 0$; $v_y = 0$. Equation (9) is used to obtain the reference values of centroid slip and yaw angle velocities.

$$\beta_d = \left[\frac{b}{(1 + Kv_x^2)L} + \frac{amv_x^2}{(1 + Kv_x^2)k_2 L^2} \right] \delta, \quad (10)$$

$$\gamma_d = \frac{v_x/L}{1 + Kv_x^2} \delta,$$

where L is the wheelbase, K is the stability factor, and $K = m(a/k_2 - b/k_1)/L^2$.

It is assumed that the tire of linear two-DOF vehicle model is linear. When the vehicle is in the limit state, the steady-state response of reference model is not suitable as a reference value. Therefore, the reference value is replaced by boundary value [20]. Equations (11) and (12) show the boundary values of the side slip angle and yaw rate.

The boundary values of the side slip angle are as follows:

$$|\beta_{d,b}| = \arctan(0.02\mu g). \quad (11)$$

The boundary values of the yaw rate are as follows:

$$|\gamma_{d,b}| = \frac{0.85\mu g}{v_x}, \quad (12)$$

where μ is the pavement friction coefficient.

2.3.2. Vehicle Prediction Model. In Figure 4, m is the mass of the vehicle; m_s is the sprung mass; v_x, v_y are the component of the centroid velocity on the x - and y -axes; γ is the yaw rate; ϕ_v is the roll angle of the vehicle; ϕ_r is the lateral slope of the road; δ is the front wheel angle; a_y is the lateral acceleration of the vehicle; e is the distance from the center of mass to the roll axis; K_ϕ is the roll stiffness of the suspension; C_ϕ is the roll damping of the suspension; I_x, I_z are the rotational inertia of the axle around the x - and z -axes of the vehicle; I_{xeq} is the moment of inertia of the sprung mass around the roll axis: $I_{xeq} = I_x + m_s e^2$.

In general, the more accurate prediction model leads to better control effect of the controller. However, the precise model weakens the real-time performance of controller. At present, most controllers in real vehicle use two or three-DOF model [21]. Therefore, we established a three-DOF vehicle model with additional yaw moment M_z for prediction (see Figure 4). The dynamic equations in lateral, yaw, and roll directions are expressed as follows:

$$mv_x(\dot{\beta} + \gamma) - m_s e \ddot{\phi} = F_{y1} + F_{y2},$$

$$I_z \dot{\gamma} = aF_{y1} - bF_{y2} + M_z, \quad (13)$$

$$I_{xeq} \ddot{\phi} = m_s e(g\phi + a_y) - K_\phi \phi - C_\phi \dot{\phi}.$$

According to $\dot{\phi} = \dot{\phi}$, (7), (8), and (13), the differential equation of three-DOF vehicle model can be rewritten into a matrix form:

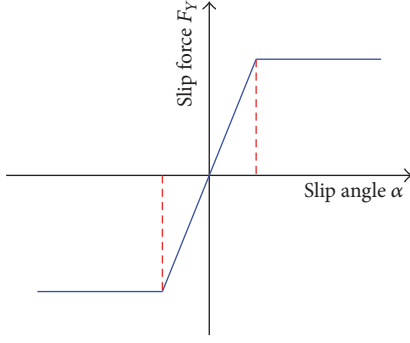


FIGURE 5: Two-stage fold line tire model.

$$\begin{aligned}
 & \begin{bmatrix} mv_x & 0 & 0 & -m_s e \\ 0 & I_z & 0 & 0 \\ -m_s e v_x & 0 & 0 & I_{xeq} \\ 0 & 0 & 1 & 0 \end{bmatrix} \begin{bmatrix} \dot{\beta} \\ \dot{\gamma} \\ \dot{\phi} \\ \ddot{\phi} \end{bmatrix} \\
 &= \begin{bmatrix} C \frac{D}{v_x} - mv_x & 0 & 0 \\ D & \frac{E}{v_x} & 0 \\ 0 & m_s e v_x & m_s e g - K_\phi & -C_\phi \\ 0 & 0 & 0 & 1 \end{bmatrix} \begin{bmatrix} \beta \\ \gamma \\ \phi \\ \dot{\phi} \end{bmatrix} \quad (14) \\
 &+ \begin{bmatrix} 0 \\ 1 \\ 0 \\ 0 \end{bmatrix} M_z + \begin{bmatrix} -k_1 \\ -ak_1 \\ 0 \\ 0 \end{bmatrix} \delta,
 \end{aligned}$$

where $C = k_1 + k_2$; $D = ak_1 - bk_2$; $E = a^2k_1 + b^2k_2$. $x(t) = [\beta \ \gamma \ \phi \ \dot{\phi}]^T$ is selected as the state vector; $u(t) = M_z$ is the control input; $w(t) = \delta$ is the disturbance variable. Equation (14) can also be expressed as

$$F\dot{x}(t) = Gx(t) + Pu(t) + Qw(t). \quad (15)$$

The nonlinear equation (14) is linearized by Taylor series expansion and simplifies the system design by reducing the higher-order derivative as a small amount. Equation (16) is the state space equation after linearization.

$$\begin{aligned}
 \dot{x}(t) &= Ax(t) + B_1u(t) + B_2w(t), \\
 y(t) &= Cx(t),
 \end{aligned} \quad (16)$$

where $A = F^{-1}G$; $B_1 = F^{-1}P$; $B_2 = F^{-1}Q$; $C = I_4$. I_4 is the four-order unit matrix.

The two-stage fold line tire model is used for vehicle prediction (see Figure 5). When the tire works in the linear region, the cornering stiffness can be linear. After the tire enters the nonlinear region, the side angle increases. However, the concerning force remains unchanged; namely, the slope of the curve F_y - α is zero.

2.3.3. Design of MPC Control Algorithm. MPC belongs to a discrete control. The state equation of (16) cannot be used directly as a prediction model. It needs to be transformed into incremental form by discretization.

First, (16) can be transformed into

$$\begin{aligned}
 \frac{x(t+1) - x(t)}{\Delta t} &= Ax(t) + B_1u(t) + B_2w(t), \\
 y(t) &= Cx(t).
 \end{aligned} \quad (17)$$

Then,

$$\begin{aligned}
 x(t+1) &= A_c x(t) + B_{1c}u(t) + B_{2c}w(t), \\
 y(t) &= Cx(t),
 \end{aligned} \quad (18)$$

where Δt is sampling time, $A_c = \Delta t \cdot A + I_4$; $B_{1c} = \Delta t \cdot B_1$; $B_{2c} = \Delta t \cdot B_2$

Let $t = k$, k is sampling point. Then get

$$\begin{aligned}
 x(k+1) &= A_c x(k) + B_{1c}u(k) + B_{2c}w(k), \\
 y(k) &= Cx(k).
 \end{aligned} \quad (19)$$

A_c , B_{1c} , and B_{2c} are discrete matrices, in order to reduce or eliminate static errors; (19) is rewritten as an incremental model (20).

$$\begin{aligned}
 \Delta x(k+1) &= A_c \Delta x(k) + B_{1c} \Delta u(k) + B_{2c} \Delta w(k), \\
 y(k) &= C \Delta x(k) + y(k-1),
 \end{aligned} \quad (20)$$

where $\Delta x(k) = x(k) - x(k-1)$; $\Delta u(k) = u(k) - u(k-1)$; $\Delta w(k) = w(k) - w(k-1)$.

According to the MPC theory, the most recent measured value is taken as the initial condition to predict the future dynamic based on the predictive model. We make the following assumptions in the work:

- (1) The predicted time domain is p ; the control time domain is m ; and $p \geq m$ ($m = 3$, $p = 10$).
- (2) At the current k moment, the estimated and measured values ($\hat{x}(k)$ and $y(k)$) of state vector are known.
- (3) The controlled variable remains unchanged outside of control time domain. $\Delta u(k+i) = 0$ ($i \geq m$).
- (4) The measurable disturbance variable remains unchanged after moment k . $\Delta w(k+i) = 0$ ($i \geq 1$).

Within predicted time domain p , the prediction expression for the p th step state vector at moment k is as follows:

$$\begin{aligned}
 \Delta x(k+1 | k) &= A_c \Delta \hat{x}(k) + B_{1c} \Delta u(k) + B_{2c} \Delta w(k) \\
 \Delta x(k+2 | k) &= A_c^2 \Delta \hat{x}(k) + A_c B_{1c} \Delta u(k) \\
 &\quad + B_{1c} \Delta u(k+1) + A_c B_{2c} \Delta w(k) \\
 &\quad \vdots \\
 \Delta x(k+p | k) &= A_c^p \Delta x(k) + A_c^{p-1} B_{1c} \Delta u(k) \\
 &\quad + A_c^{p-2} B_{1c} \Delta u(k+1) + \cdots + B_{1c} \Delta u(k+p-1) \\
 &\quad + A_c^{p-1} B_{2c} \Delta w(k).
 \end{aligned} \quad (21)$$

At moment k , we predict the output from $k+1$ to $k+p$ according to the predicted value of state vector in

$$\begin{aligned}
 y(k | k) &= y(k) \\
 y(k + 1 | k) &= CA_c \Delta \hat{x}(k) + CB_{1c} \Delta u(k) \\
 &\quad + CB_{2c} \Delta w(k) + y(k) \\
 y(k + 2 | k) &= (CA_c^2 + CA_c) \Delta \hat{x}(k) \\
 &\quad + (CA_c B_{1c} + CB_{1c}) \Delta u(k) + CB_{1c} \Delta u(k + 1) \\
 &\quad + (CA_c B_{2c} + CB_{2c}) \Delta w(k) + y(k) \\
 y(k + 3 | k) &= \sum_{i=1}^3 CA_c^i \Delta \hat{x}(k) + \sum_{i=1}^3 CA_c^{i-1} B_{1c} \Delta u(k) \\
 &\quad + \dots + CB_{1c} \Delta u(k + 2) + \sum_{i=1}^3 CA_c^{i-1} B_{2c} \Delta u(k) \\
 &\quad + y(k) \\
 &\quad \vdots \\
 y(k + p | k) &= \sum_{i=1}^p CA_c^i \Delta \hat{x}(k) + \sum_{i=1}^p CA_c^{i-1} B_{1c} \Delta u(k) \\
 &\quad + \dots + CB_{1c} \Delta u(k + p - 1) + \sum_{i=1}^p CA_c^{i-1} B_{2c} \Delta u(k) \\
 &\quad + y(k).
 \end{aligned} \tag{22}$$

The vectors $Y_p(k)$ and $\Delta U_m(k)$ are defined as follows:

$$\begin{aligned}
 Y_p(k) &= [y(k + 1 | k) \quad y(k + 2 | k) \quad \dots \quad y(k + p | k)]^T, \\
 \Delta U_m(k) &= [\Delta u(k) \quad \Delta u(k + 1) \quad \dots \quad \Delta u(k + m - 1)]^T.
 \end{aligned} \tag{23}$$

The p th step control output of the prediction system can be expressed as

$$Y_p(k) = S_x \Delta \hat{x}(k) + L_y y(k) + S_u \Delta U(k) + S_w \Delta w(k), \tag{24}$$

where

$$\begin{aligned}
 S_x &= \begin{bmatrix} CA_c \\ CA_c^2 + CA_c \\ \vdots \\ \sum_{i=1}^p CA_c^i \end{bmatrix}; \\
 S_w &= \begin{bmatrix} CB_{2c} \\ CA_c B_{2c} + CB_{2c} \\ \vdots \\ \sum_{i=1}^p CA_c^{i-1} B_{2c} \end{bmatrix};
 \end{aligned}$$

$$\begin{aligned}
 L_c &= \begin{bmatrix} I_4 \\ I_4 \\ \vdots \\ I_4 \end{bmatrix}, \\
 S_u &= \begin{bmatrix} CB_{1c} & 0 & 0 & \dots & 0 \\ CA_c B_{1c} & CB_{1c} & 0 & \dots & 0 \\ \vdots & \vdots & \vdots & \dots & \vdots \\ \sum_{i=1}^p CA_c^i B_{1c} & \sum_{i=1}^{p-1} CA_c^{i-1} B_{1c} & \dots & \dots & \sum_{i=1}^{p-m+1} CA_c^{i-1} B_{1c} \end{bmatrix}.
 \end{aligned} \tag{25}$$

Similarly, we can deduce the p th step predictive equation with constraint output.

MPC is an algorithm of determining control strategy by optimization. Firstly, it is necessary to determine m control increments $\Delta u(k), \Delta u(k + 1), \dots, \Delta u(k + m - 1)$ from moment k . In the next p moment, the predicted output values $y(k + 1 | k), y(k + 2 | k), \dots, y(k + p | k)$ of the controlled object can approximate to the given expected value $d(k + i)$, $i = 1, 2, \dots, p$.

In the control process, the control increment should not have sharp change. Based on this factor, soft constraints are added to optimization performance indexes. Thus, the optimization performance index of moment k can be expressed as

$$\begin{aligned}
 \min J(k) &= \sum_{i=1}^p q_i [d(k + i) - y(k + 1)] \\
 &\quad + \sum_{j=1}^m r_j \Delta u^2(k + j - 1),
 \end{aligned} \tag{26}$$

where q_i and r_j are the weighting coefficients, which represent error tracking and suppression of control increment. If the constraint is not considered, the above problem is described as follows.

Taking $\Delta U(k) = [\Delta u(k) \quad \Delta u(k + 1) \quad \dots \quad \Delta u(k + m - 1)]^T$ as optimal variable, the performance index (26) is minimized under prediction model (20). Likewise, optimal performance index (26) can also be written as the form of vector.

$$\min J(k) = \|D_p(k) - Y_p(k)\|_Q^2 + \|\Delta U_m(k)\|_R^2, \tag{27}$$

where $D_p(k) = [d(k + 1) \quad d(k + 2) \quad \dots \quad d(k + p)]^T$ is the expected output value in the optimization time domain, namely, side slip angle and yaw rate based on vehicle model output. It is assumed that the expected value is fixed in the optimization time domain; namely, $d(k + 1) = d(k + 2) = \dots = d(k + i)$; $Q = \text{diag}(q_1 \quad q_2 \quad \dots \quad q_p)$; and

$R = \text{diag}(r_1 \ r_2 \ \cdots \ r_m)$ are diagonal matrices comprised of weighting coefficients.

At the moment k , $D_p(k)$, and $Y_p(k)$ are known. In order to minimize $\Delta U_m(k)$ by $J(k)$, the optimal control sequence is obtained according to the necessary condition of the extremum: $dJ(k)/d\Delta U_m(k) = 0$.

$$\begin{aligned} \Delta U^*(k) \\ = (S_u^T Q^T Q S_u + Q^T Q)^{-1} S_u^T Q^T Q E_p(k+1 | k), \end{aligned} \quad (28)$$

where $E_p(k+1 | k)$ is control deviation, which can be calculated on line by the following equation:

$$\begin{aligned} E_p(k+1 | k) = D_p(k) - S_x \Delta \hat{x}(k) - L_y y(k) \\ - S_w \Delta w(k). \end{aligned} \quad (29)$$

In each sampling period, the first element of the derived optimal solution $\Delta U^*(k)$ is the control increment of MPC.

$$\Delta u(k) = [1 \ 0 \ 0] \Delta U^*(k), \quad (30)$$

where $u(k) = u(k-1) + \Delta u(k)$ is the additional yaw moment provided for the torque distribution layer.

The Lyapunov function $V^*(k)$ at the moment k is defined as the optimal performance index of open loop.

$$V^*(k) \stackrel{\text{def}}{=} J^*(k). \quad (31)$$

Relationship between $V^*(k)$ and $V(k+1)$ is established:

$$\begin{aligned} V^*(k) = V(k+1) + J(y^*(1 | k), u^*(0 | k), \\ \Delta u^*(0 | k)) - J(y(p | k+1), u(p-1 | k+1), \\ \Delta u(p-1 | k+1)). \end{aligned} \quad (32)$$

Since $V(k+1) \geq V^*(k+1)$, we can derive

$$\begin{aligned} V^*(k+1) - V^*(k) \leq \|y^*(p+1 | k)\|_2^2 \\ - \|y^*(1 | k)\|_2^2 \\ + \|u^*(p-1 | k)\|_2^2 \\ - \|u^*(0 | k)\|_2^2 \\ - \|\Delta u^*(0 | k)\|_2^2. \end{aligned} \quad (33)$$

As $\|y(p+1 | k)\|_2^2 \leq \|y(1 | k)\|_2^2$ and $\|u(p | k)\|_2^2 \leq \|u(0 | k)\|_2^2$, we can get

$$V^*(k+1) - V^*(k) \leq 0. \quad (34)$$

According to the Lyapunov second stability theorem, the proposed MPC closed-loop system is stable.

2.4. Wheel Torque Distribution. For the tire, lower pavement adhesion consumption rate leads to greater adhesion margin and larger distance between the tire and nonlinear

saturation zone, indirectly improving the stability of the vehicle. According to tire friction ellipse theory, the work distributes the wheel torque for the purpose of minimum sum of pavement adhesion consumption rates of four tires. Equation (35) shows the objective function.

$$\min J_\mu = \sum_{i=1}^4 C_i \frac{F_{xi}^2 + F_{yi}^2}{\mu^2 F_{zi}^2}, \quad i = 1, 2, 3, 4, \quad (35)$$

where F_{xi} is the tire longitudinal force; F_{yi} the tire lateral force; F_{zi} the vertical load on the wheel; C_i the weight coefficient within the interval $(0, 1)$. The tire longitudinal force F_{xi} can be obtained by

$$F_{xi} = \frac{T_{wi} - I_{eq} \dot{\omega}_i}{r_w}, \quad (36)$$

where T_{wi} is the drive torque on the wheel; r_w the wheel radius; $\dot{\omega}_i$ the wheel rotation angle acceleration; I_{eq} the wheel equivalent inertia of in-wheel motor and reducer inertia.

The vertical load F_{zi} of wheel consists of static load and dynamic load caused by longitudinal and lateral accelerations without considering the centroid change caused by vehicle rollover and the influence of suspension system. The vertical load of each wheel is calculated by

$$\begin{bmatrix} F_{z1} \\ F_{z2} \\ F_{z3} \\ F_{z4} \end{bmatrix} = \frac{mg}{2L} \begin{bmatrix} b \\ b \\ a \\ a \end{bmatrix} + \frac{m a_x h}{2L} \begin{bmatrix} -1 \\ -1 \\ 1 \\ 1 \end{bmatrix} + \frac{m a_y h}{BL} \begin{bmatrix} -b \\ b \\ -a \\ a \end{bmatrix}, \quad (37)$$

where a and b are the distance from the centroid to front and rear axle; L is the wheelbase; h is the height of centroid; B is the trend.

The objective function in (35) determines smallest sum of the load rates of four tires. However, it is impossible to ensure that each tire works at a low load-rate state. Therefore, the utilization factor of each tire is adjusted by the weighting factor C_i . Under different driving conditions, C_i is not a fixed value. In simulation and debugging process, it is found that the value has great relationship with tire vertical load and road adhesion condition. The following equation is selected in the work:

$$C_i = \left(\mu \frac{F_{zi}}{mg} \right)^2, \quad i = 1, 2, 3, 4. \quad (38)$$

Here, we focus on longitudinal driving torque distribution in the conventional operating conditions. It is difficult to acquire the lateral force of tire in actual driving, so the pavement adhesion consumption rate is simplified to the longitudinal adhesion consumption rate. Equation (35) can be transformed into the following equation:

$$\min J_\mu = \sum_{i=1}^4 C_i \left(\frac{F_{xi}}{\mu F_{zi}} \right)^2. \quad (39)$$

When the yaw moment control is not required, the sum of longitudinal forces of four wheels satisfies the total moment

TABLE 1: Specifications of the experimental electric vehicle.

Parameter	Value
Mass	3565 kg
Yaw moment of inertia	7016 kg·m ²
Distance from CG to front axle	1.593 m
Distance from CG to rear axle	1.707 m
Tire radius	0.435 m
Maximum motor torque	250 Nm
Maximum motor power	55.5 kW
Maximum motor speed	6000 rpm
Planetary reducer ratio	9.15

demand, which is obtained by analyzing the pedal input. Therefore, constraint equation is expressed as follows:

$$\sum_{i=1}^4 F_{xi} = f(\theta_p), \quad (40)$$

where θ_p is the accelerator pedal opening; $f(\sim)$ the pedal analysis strategy. In addition, the longitudinal force of tire is also restricted by pavement adhesion condition and motor output capacity.

$$-\mu F_{zi} \leq F_{xi} \leq \min(\mu F_{zi}, F_{\max}), \quad i = 1, 2, 3, 4, \quad (41)$$

where F_{\max} is the maximum wheel drive force provided by the motor; namely, $F_{\max} = T_{w\max}/r_w$. Therefore, the optimization problem can be expressed as follows:

$$\begin{aligned} \min \quad & J_\mu = \sum_{i=1}^4 C_i \left(\frac{F_{xi}}{\mu F_{zi}} \right)^2 \\ \text{s.t.} \quad & \sum_{i=1}^4 F_{xi} = f(\theta_p) - \mu F_{zi} \leq F_{xi} \\ & \leq \min(\mu F_{zi}, F_{\max}) (F_{x2} - F_{x1}) \frac{B}{2} \\ & + (F_{x4} - F_{x3}) \frac{B}{2} = T_z. \end{aligned} \quad (42)$$

The nonlinear constrained optimization problem is solved by numerical optimization method to obtain the longitudinal forces for four tires. Then, we derive the drive torques which should be allocated to four wheels by calculation.

3. Control Algorithm Simulation Validation

The proposed controller was simulated on a 4WID vehicle in the Carsim and MATLAB environment. The vehicle under investigation is the light-duty off-road vehicle with the specifications which are listed in Table 1.

The proposed controller (MPC) in this paper and its results are compared with the proposed controller (DOB) by [15]. Furthermore, the uncontrolled state is simulated, too.

3.1. Yaw Stability Control Algorithm Validation. When the steering wheel reaches certain rotor angle, the vehicle will

be in danger of yaw instability on low adhesion road. The effect of control algorithm on vehicle stability is verified by selecting the double lane condition on low adhesion road. The specific simulation conditions are as follows: the road adhesion coefficient is 0.3; the driving speed is 60 km/h. Figure 6(a) shows the vehicle trajectory under three different control modes. Figure 6(b) shows steering angle for the lane-change maneuver. Figures 6(c)–6(e) give the response curves of the yaw rate, sideslip angle, and lateral acceleration under the above three kinds of control modes.

From Figure 6, it is seen that without the stability control, when the steering wheel reaches a certain angle, the vehicle loses stability to cause the failure of lane-change. The yaw rate and the side slip angle of the vehicle change in a wide range, which cannot effectively track the expected value. After the MPC-based or DOB-based stability control, the yaw rate and side slip angle of vehicle can effectively track the expected value to pass through the test road according to predetermined trajectory, maintaining high speed stability. It can be well controlled under these two kinds of controllers. Moreover, the MPC-based controller can achieve the same smooth nonflutter control effect as the DOB-based controller. Figure 6(f) shows the wheel torque calculated by MPC-based stability control algorithm.

3.2. Verification of Rollover Stability Control Algorithm. The hook condition is conducted on the road with an adhesion coefficient of 0.85. The initial speed is 80 km/h, and the maximum steering angle is 180°. Figure 7(a) shows the hook condition steering wheel angle input. Figures 7(b)–7(e) give the response curves of the roll, roll rate, yaw rate, sideslip angle, and longitudinal velocity under the three kinds of control modes. Figure 7(g) shows the vehicle trajectory under three different control modes.

In hook condition, the vehicle will lose stability and roll over if there is no stability control. After MPC-based or DOB-based stability control, the vehicle does not roll over as the roll is in a reasonable range. It can be seen that the response curves of MPC-based controller are as smooth as DOB-based controller. In addition, it can also be concluded that the stability will achieve a litter better accuracy under the proposed MPC-based stability controller and keep a higher longitudinal velocity. Figure 7(h) indicates the wheel torque calculated by the MPC-based stability control algorithm.

4. Verification of Real Vehicle Test

According to ISO/FDIS 3888-1 standard, we performed double lane-change field test of light-duty off-road vehicle. The piles were arranged on the test field (see Figure 8).

The gyroscope was installed in the vehicle for real-time acquisition of the yaw rate and lateral acceleration of the vehicle. The GPS speed sensor was used to measure the longitudinal and lateral velocities. The angular velocities of four wheels were collected by in-wheel motor speed sensor. We measured the steering wheel angle by steering wheel angle sensor. The test speed of vehicle was 80 km/h (± 2 km/h).

Figures 9–11 show the double lane-change test results with MPC-based stability control, with DOB-based stability

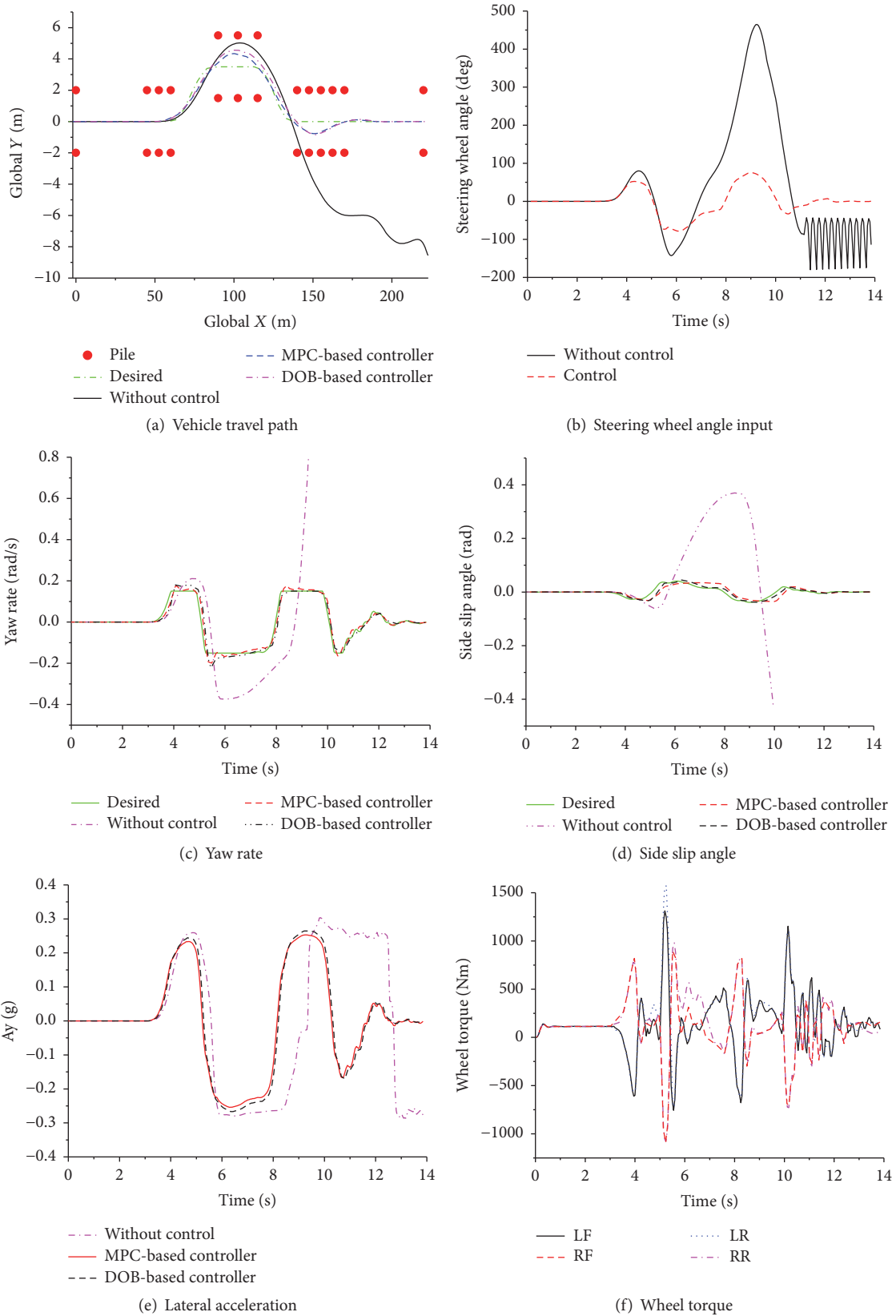


FIGURE 6: Double lane-change simulation test on low adhesion road.

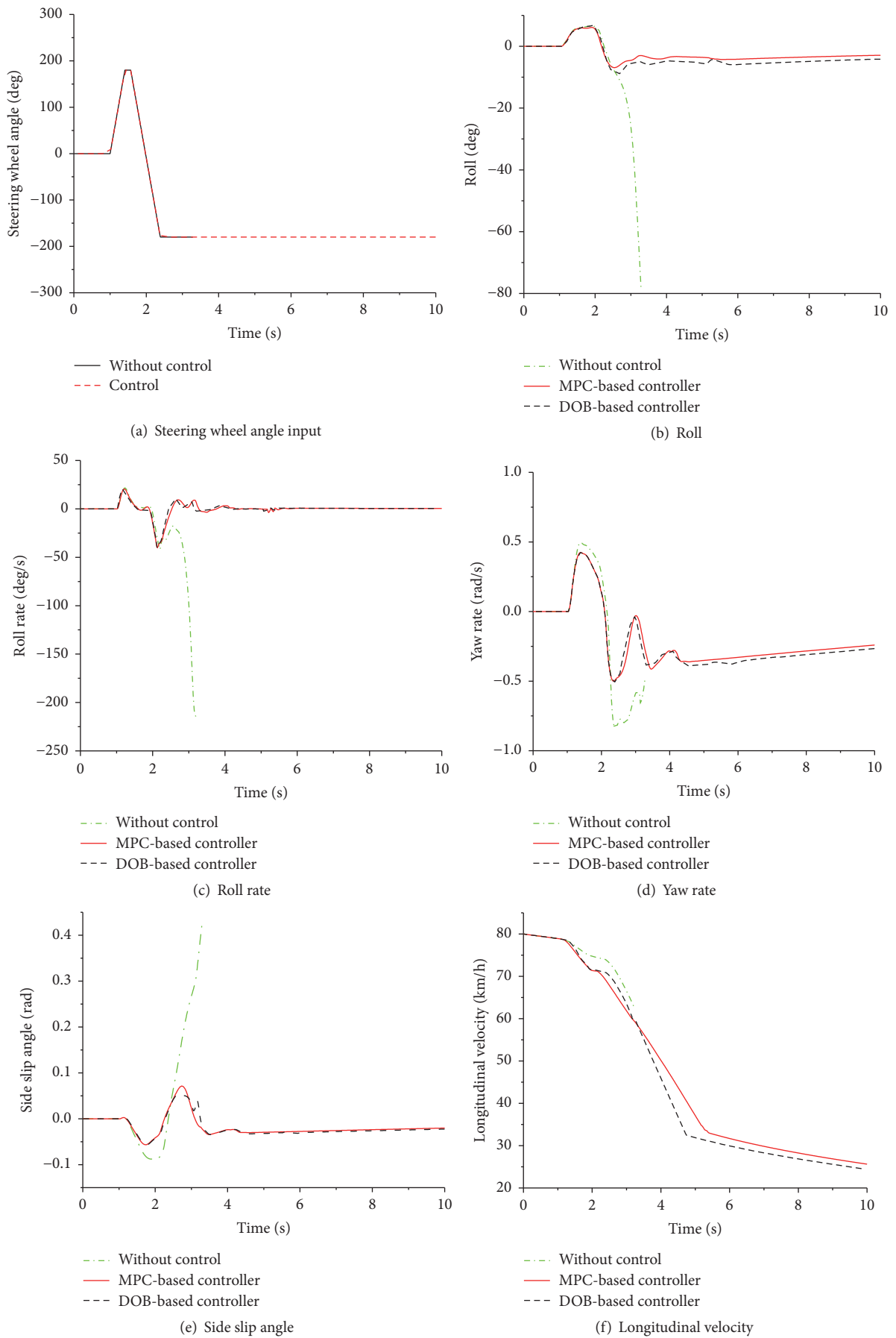


FIGURE 7: Continued.

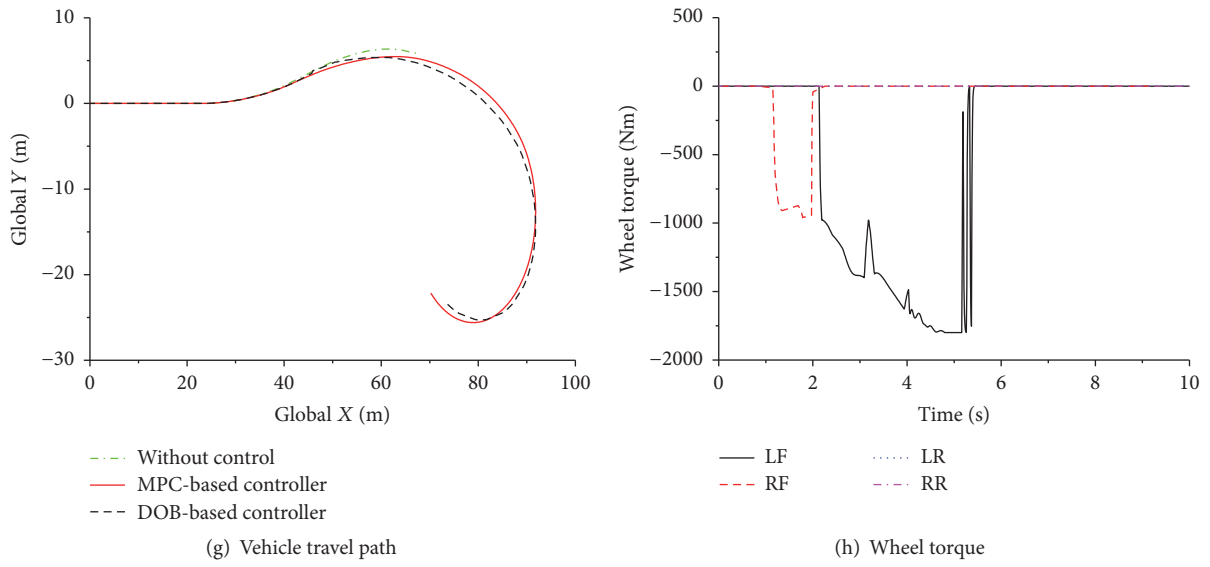


FIGURE 7: Hook condition simulation test on high adhesion road.

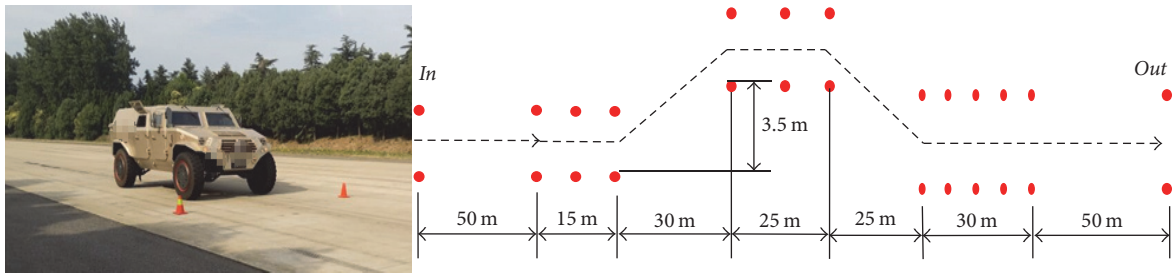


FIGURE 8: Double lane-change test.

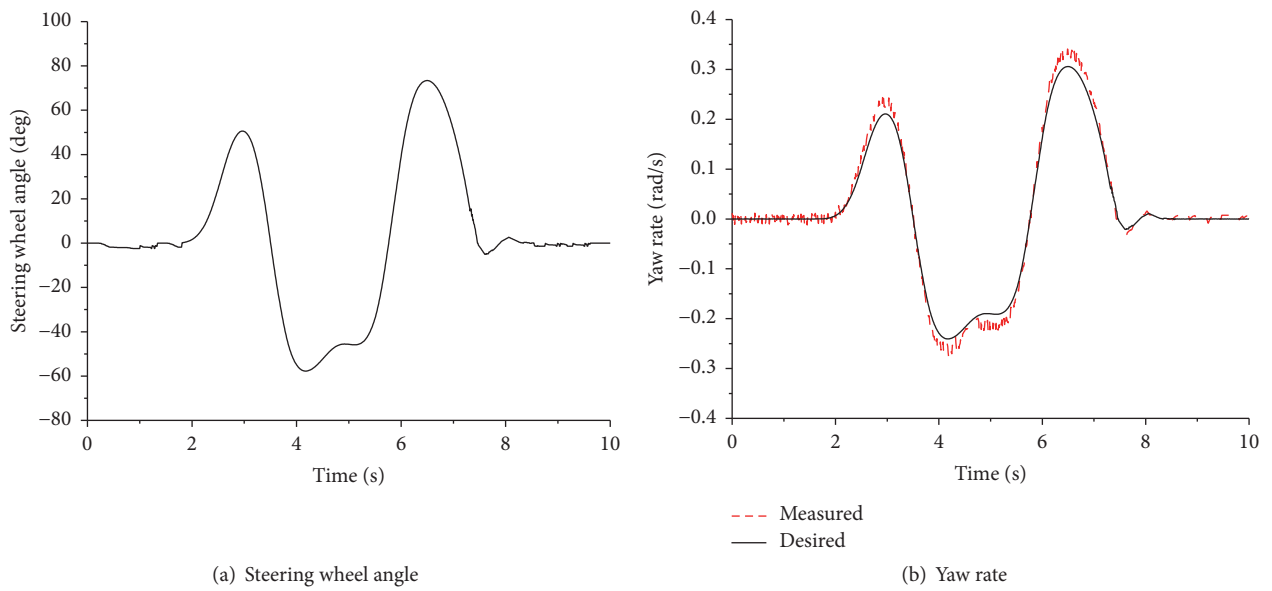


FIGURE 9: Double lane-change test results with MPC-based stability control.

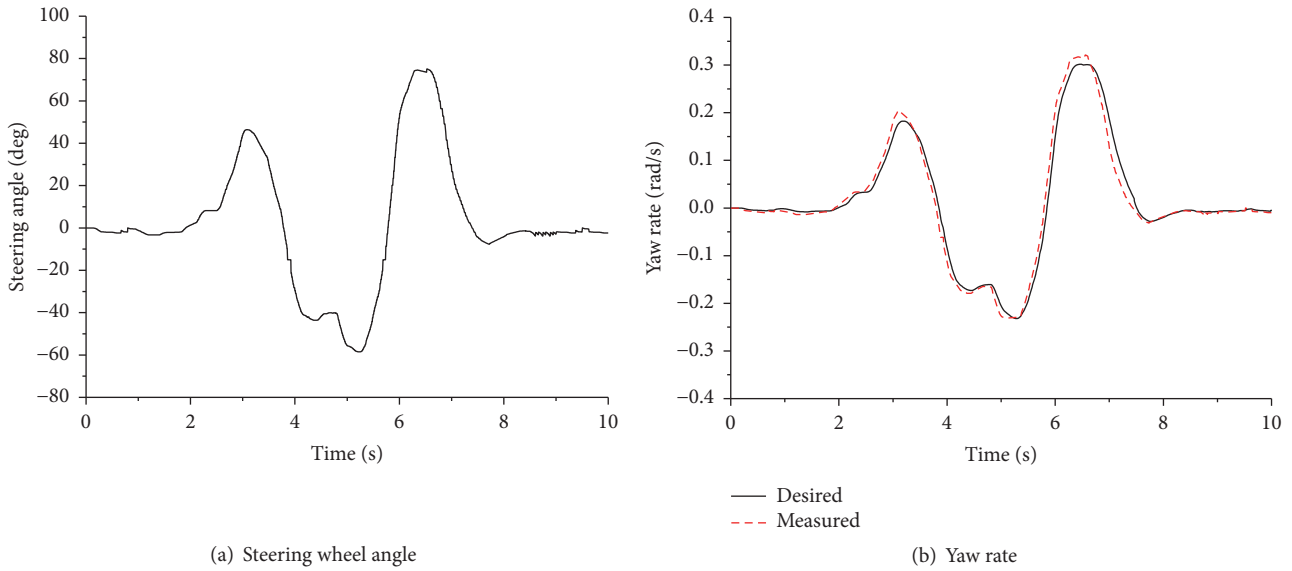


FIGURE 10: Double lane-change test results with DOB-based stability control.

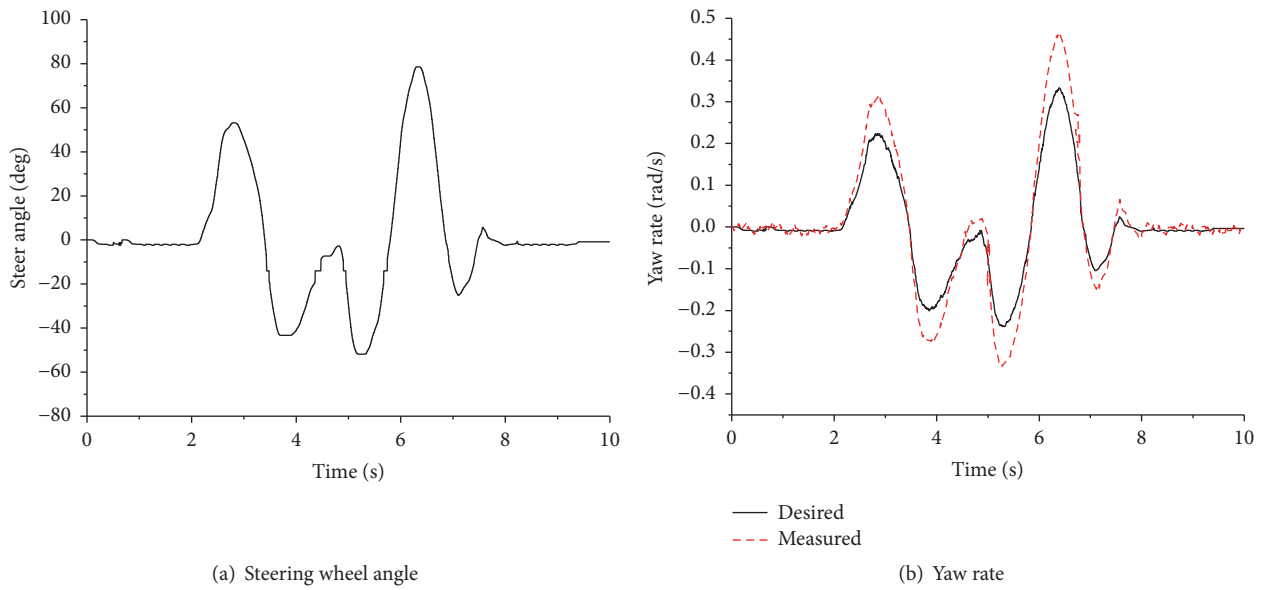


FIGURE 11: Double lane-change test results without stability control.

control, and without control, respectively. It can be seen that the vehicle without control has poor stability because of large difference between yaw rate and reference value. After MPC-based or DOB-based stability control, the difference obviously decreases to strengthen vehicle stability. Figure 12 shows double lane-change driving route. If the steering angle reaches a certain value, the vehicle without stability control will lose stability to approach the curb, thus failing to track the desired trajectory. With MPC-based or DOB-based stability control, the vehicle can pass through the test road in accordance with the desired trajectory. The control effects of the two controllers are comparable, and the MPC-based control in the direction of the moment of emergency change is relatively more stable.

5. Conclusions

In the work, we proposed the lateral stability control method of in-wheel motor drive off-road vehicle based on MPC. The multiinput and multioutput system predictive control law was designed by establishing vehicle dynamics model for predictive control. The motor braking/driving torque was directly generated to conduct yaw stability control under low adhesion coefficient and double lane-change conditions as well as rollover stability control algorithm validation under high adhesion coefficient and hook conditions. At last, real vehicle test verification was performed under high speed double lane-change condition. This paper only carries out the test under the condition of invariable road surface and

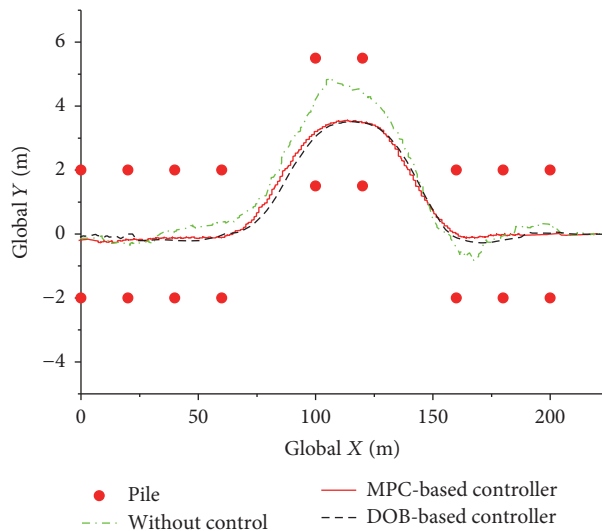


FIGURE 12: Double lane-change driving route.

constant velocity but does not verify the proposed MPC-based stability control under the condition of changing road surface and time-varying velocity. Subsequent further research, we will verify it.

Consequently, the following conclusions were obtained.

(1) Distributed electric vehicle braking/driving force coordination control made full use of multiwheel adhesion to provide vehicle with greater yaw moment and faster response, increasing vehicle stability under limit conditions.

(2) With high accuracy and good robustness, MPC was suitable for solving complex coordination problem for multiple actuators. It could also be applied in lateral stability control of distributed electric drive vehicle.

(3) Simulation result and real vehicle test showed that MPC algorithm had better effect in integrated control of yaw/rollover stability, thus greatly improving the lateral stability of vehicle.

Conflicts of Interest

The authors declare that there are no conflicts of interest regarding the publication of this paper.

Acknowledgments

The authors acknowledge that this paper has been supported by the National High Technology Research and Development Program of China (Grant no. 2011AA11A260).

References

- [1] C. Lin, Z. Xu, and R. Zhang, "A yaw stability control algorithm for four-wheel independently actuated electric ground vehicles considering control boundaries," *Mathematical Problems in Engineering*, vol. 2015, Article ID 256715, 10 pages, 2015.
- [2] N. Ando and H. Fujimoto, "Yaw-rate control for electric vehicle with active front/rear steering and driving/braking force distribution of rear wheels," in *Proceedings of the 2010 11th IEEE International Workshop on Advanced Motion Control, (AMC '10)*, pp. 726–731, March 2010.
- [3] Y. Hori, "Future vehicle driven by electricity and control: research on four-wheel-motored 'UOT Electric March II,'" *IEEE Transactions on Industrial Electronics*, vol. 51, no. 5, pp. 954–962, 2004.
- [4] K. Makoto, W. Kevin, and Y. Hiroaki, "Improvement of vehicle dynamic performance by means of in-wheel electric motors," *Mitsubishi Motor Technical Review*, 2006.
- [5] Y. Dejun, O. Manabu, S. Hiroshi, and H. Yoichi, "Active Stability Control Strategy Based on Maximum Transmissible Torque Estimation," *J Automotive Safety and Energy*, vol. 2, no. 1, pp. 34–38, 2011.
- [6] B. Jacobsen, "Potential of electric wheel motors as new chassis actuators for vehicle manoeuvring," *Proceedings of the Institution of Mechanical Engineers, Part D: Journal of Automobile Engineering*, vol. 216, no. 8, pp. 631–640, 2002.
- [7] L. Feiqiang, W. Jun, and L. Zhaodu, "Motor torque based vehicle stability control for four-wheel-drive electric vehicle," in *Proceedings of the IEEE Vehicle Power and Propulsion Conference (VPPC '09)*, pp. 1596–1601, Dearborn, Mich, USA, September 2009.
- [8] P. Yang, L. Xiong, K. Zhang, and Z. Yu, "Stability control strategy design and experiment of distributed electric drive vehicle," *Jixie Gongcheng Xuebao/Journal of Mechanical Engineering*, vol. 49, no. 24, pp. 128–143, 2013.
- [9] C. Geng, L. Mostefai, M. Denai, and Y. Hori, "Direct yaw-moment control of an in-wheel-motored electric vehicle based on body slip angle fuzzy observer," *IEEE Transactions on Industrial Electronics*, vol. 56, no. 5, pp. 1411–1419, 2009.
- [10] Z. He and X. Ji, "Nonlinear robust control of integrated vehicle dynamics," *Vehicle System Dynamics*, vol. 50, no. 2, pp. 247–280, 2012.
- [11] R. Wang, H. R. Karimi, N. Chen, G. Yin, and J. Wang, "Motion control of four-wheel independently actuated electric ground vehicles considering tire force saturations," *Mathematical Problems in Engineering*, vol. 2013, Article ID 819302, 8 pages, 2013.
- [12] J. Kim, C. Park, S. Hwang, Y. Hori, and H. Kim, "Control algorithm for an independent motor-drive vehicle," *IEEE Transactions on Vehicular Technology*, vol. 59, no. 7, pp. 3213–3222, 2010.
- [13] K. Kawashima, T. Uchida, and Y. Hori, "Rolling stability control of in-wheel electric vehicle based on two-degree-of-freedom control," in *Proceedings of the 10th International Workshop on Advanced Motion Control, (AMC '08)*, pp. 751–756, March 2008.
- [14] H. Fujimoto, A. Tsumasaka, and T. Noguchi, "Vehicle stability control of small electric vehicle on snowy road," *Review of Automotive Engineering*, vol. 27, no. 2, pp. 279–286, 2006.
- [15] K. Kawashima, T. Uchida, and Y. Hori, "Rolling stability control utilizing rollover index for in-wheel motor electric vehicle," *IEEE Transactions on Industry Applications*, vol. 130, no. 5, pp. 10–662, 2010.
- [16] P. Falcone, H. Eric Tseng, F. Borrelli, J. Asgari, and D. Hrovat, "MPC-based yaw and lateral stabilisation via active front steering and braking," *Vehicle System Dynamics*, vol. 46, no. 1, pp. 611–628, 2008.
- [17] S. Pan, Z. Chang-fu, and T. Masayoshi, "A terminal sliding mode based torque distribution control for an individual-wheel-drive vehicle," *Journal of Zhejiang University-SCIENCE A (Applied Physics & Engineering)*, vol. 15, no. 9, pp. 681–693, 2014.

- [18] B. Huang, S. Wu, X. Fu, and J. Luo, "State estimation of four-wheel independent drive electric vehicle based on adaptive unscented Kalman filter," *International Journal of Electric and Hybrid Vehicles*, vol. 9, no. 2, pp. 151–168, 2017.
- [19] J. Kang, J. Yoo, and K. Yi, "Driving control algorithm for maneuverability, lateral stability, and rollover prevention of 4WD electric vehicles with independently driven front and rear wheels," *IEEE Transactions on Vehicular Technology*, vol. 60, no. 7, pp. 2987–3001, 2011.
- [20] J. Deur, D. Pavković, G. Burgio, and D. Hrovat, "A model-based traction control strategy non-reliant on wheel slip information," *Vehicle System Dynamics*, vol. 49, no. 8, pp. 1245–1265, 2011.
- [21] R. Wang, Y. Chen, D. Feng, X. Huang, and J. Wang, "Development and performance characterization of an electric ground vehicle with independently actuated in-wheel motors," *Journal of Power Sources*, vol. 196, no. 8, pp. 3962–3971, 2011.

Research Article

Parameter Identification and Hybrid Synchronization in an Array of Coupled Chaotic Systems with Ring Connection: An Adaptive Integral Sliding Mode Approach

Nazam Siddique  and Fazal ur Rehman 

Department of Electrical Engineering, Capital University of Science and Technology, Islamabad, Pakistan

Correspondence should be addressed to Nazam Siddique; nazim.siddiq@gmail.com

Received 10 August 2017; Revised 11 October 2017; Accepted 28 November 2017; Published 30 January 2018

Academic Editor: Ton D. Do

Copyright © 2018 Nazam Siddique and Fazal ur Rehman. This is an open access article distributed under the Creative Commons Attribution License, which permits unrestricted use, distribution, and reproduction in any medium, provided the original work is properly cited.

This article presents an adaptive integral sliding mode control (SMC) design method for parameter identification and hybrid synchronization of chaotic systems connected in ring topology. To employ the adaptive integral sliding mode control, the error system is transformed into a special structure containing nominal part and some unknown terms. The unknown terms are computed adaptively. Then the error system is stabilized using integral sliding mode control. The controller of the error system is created that contains both the nominal control and the compensator control. The adapted laws and compensator controller are derived using Lyapunov stability theory. The effectiveness of the proposed technique is validated through numerical examples.

1. Introduction

Ever since the classic effort by Pecora and Carroll [1], the synchronization in chaotic systems became an active research area because of its useful applications [2–5]. Different synchronization schemes for chaotic systems were studied and investigated [6–10]. Among these schemes, hybrid synchronization [11–19] is one in which some of the chaotic systems are synchronized whereas others are antisynchronized. Due to its importance, hybrid synchronization has been the subject of many research works. These works include study of synchronization/antisynchronization for permanent magnet synchronous motors connected in ring topology [11], function projective type synchronization for complex dynamical networks [12], investigation of complete synchronization and antiphase synchronization together [13], hybrid synchronization of networks having heterogeneous systems [14], study of synchronization for fractional-order systems [15], investigation of synchronization for systems with hyperchaotic nature [16, 17], and study of synchronization for complex networks [18, 19]. Study of hybrid synchronization involves multiple chaotic systems like complete, adaptive, global, projective,

and antisynchronization systems [17, 20–27], and synchronization systems in multiple coupled complex networks [28, 29]. Currently, hybrid synchronization of several connected chaotic systems is a hot topic of research and the work includes investigation of complex network synchronization for perturbations and delays [30] and a study of neural networks for synchronization [31].

In this paper, chaotic systems connected in ring topology are considered which can be shown in Figure 1. This arrangement was studied in [32] for the known parameter case. We extend this work and consider that all the parameters of all the systems in the ring connected network are unknown. To reach hybrid synchronization in this system we use adaptive integral SMC.

SMC is a distinct nonlinear control method. The objective of the SMC method is to drive the states of the system to a specific surface, called sliding manifold. When the surface is touched, the dynamic system is required to persist on it afterward. The main disadvantage of SMC is discontinuous control law. In practice, this creeps towards an undesirable occurrence called “chattering.” The closed-loop dynamics of the system in SMC depend only on the design parameters of

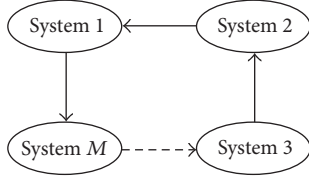


FIGURE 1: Chaotic systems connected in ring topology [32].

the switching sliding manifold. Sliding mode control also offers several benefits like simplicity, robustness to external disturbance, and parameter variation and quick response. The integral SMC, a variant of SMC, guarantees the robustness [33] because of eliminating the reaching-phase. Since reaching-phase is eradicated therefore robustness of the dynamic system can be sure all the way through the system response, beginning from initial conditions. The integral sliding mode control combines both the nominal control which steadies the nominal system and the discontinuous control which discards uncertainties.

In this research, we use adaptive integral sliding mode control technique to identify the unknown parameters and to achieve the hybrid synchronization of many chaotic systems connected in the ring topology. By using this technique, the error system is transformed into a special structure containing nominal part and some unknown terms. The unknown terms are computed adaptively. Then the error system is synthesized using integral sliding mode control. The controller of the error system is created that contains both the nominal control and the compensator control. The adaptive laws and compensator controller are derived using Lyapunov stability theory. The effectiveness of the proposed technique is validated through numerical examples.

The remainder of the paper is arranged as follows; Section 2 presents preliminaries and system description. Section 3 presents proposed control strategies for the general case of hybrid synchronization. Section 4 presents application examples. Section 5 presents discussion and simulation results and in the last section, paper is concluded.

2. System Description and Preliminaries

The structure of chaotic systems connected in ring topology is described as

$$\begin{aligned}
 \dot{x}_1 &= f_1(x_1) + F_1(x_1)\theta_1 + D_1(x_M - x_1) \\
 \dot{x}_2 &= f_2(x_2) + F_2(x_2)\theta_2 + D_2(x_1 - x_2) \\
 &\vdots \\
 \dot{x}_M &= f_M(x_M) + F_M(x_M)\theta_M + D_M(x_{M-1} - x_M),
 \end{aligned} \tag{1}$$

where x_1, x_2, \dots, x_M are vectors and $x_o = (x_{o1}, x_{o2}, \dots, x_{om})^T$, $f_o : \mathfrak{R}^m \rightarrow \mathfrak{R}^m$, $o = 1, 2, \dots, M$ are the nonlinear continuous function, and $\theta_o \in \mathfrak{R}^g$, $o = 1, 2, 3, 4, \dots, M$ are vectors of unknown parameters. $F_o(x_o) \in \mathfrak{R}^{m \times g}$, $o = 1, 2, 3, 4, \dots, M$ are matrices, $D_o = \text{diag}\{d_{o1}, d_{o2}, \dots, d_{om}\}$, $o = 1, 2, 3, 4, \dots, M$ are m dimensional diagonal matrices, and

$d_{op} \geq 0$ represent diagonal matrix parameters. When $f_o(\cdot) \neq f_p(\cdot)$, $o, p = 1, 2, 3, 4, \dots, M$, then the above arrangement has nonidentical systems.

Remark 1. In (1), all the chaotic systems are connected in ring topology [17], because the first system is connected with M th and second is connected with first; and so the final chaotic system is connected with $M - 1$ system.

So the hybrid synchronization for the above system (1) may be expressed as follows:

$$\begin{aligned}
 \dot{x}_1 &= f_1(x_1) + F_1(x_1)\theta_1 + D_1(x_M - x_1) \\
 \dot{x}_2 &= f_2(x_2) + F_2(x_2)\theta_2 + D_2(x_1 - x_2) + u_1 \\
 &\vdots \\
 \dot{x}_M &= f_M(x_M) + F_M(x_M)\theta_M + D_M(x_{M-1} - x_M) \\
 &\quad + u_{M-1}.
 \end{aligned} \tag{2}$$

Definition 2. For system (2), we define that it exhibits hybrid synchronization if controllers u_o , $o = 1, 2, 3, 4, \dots, M - 1$ exist such that all trajectories $x_1(t), x_2(t), x_3(t), x_4(t), \dots, x_M(t)$ for any initial condition $(x_1(0), x_2(0), x_3(0), x_4(0), \dots, x_M(0))$ satisfy the following:

(1) For the antisynchronization errors $e_{ro} = (e_{ro1}, e_{ro2}, \dots, e_{rom})^T$, $o = 1, 2, 3, 4, \dots, M - 1$, we have that

$$\lim_{t \rightarrow \infty} \|e_{ro}\| = \lim_{t \rightarrow \infty} \|x_o(t) + x_{o+1}(t)\| = 0, \tag{3}$$

$$o = 1, 2, 3, 4, \dots, M - 1.$$

(2) The Synchronization errors $e'_{rp} = (e'_{rp1}, e'_{rp2}, \dots, e'_{rpm})^T$ and $e'_{rq} = (e'_{rq1}, e'_{rq2}, \dots, e'_{rqm})^T$ if M ($M \geq 3$) is odd; then e'_{rp} and e'_{rq} satisfy

$$\lim_{t \rightarrow \infty} \|e'_{rp}\| = \lim_{t \rightarrow \infty} \|x_{p+2}(t) - x_p(t)\| = 0, \tag{4}$$

$$p = 1, 3, 5, 7, 9, \dots, M - 2$$

$$\lim_{t \rightarrow \infty} \|e'_{rq}\| = \lim_{t \rightarrow \infty} \|x_{q+2}(t) - x_q(t)\| = 0,$$

$$q = 2, 4, 6, 8, 10, \dots, M - 3$$

and if M ($M \geq 4$) is even, then e'_{rp} and e'_{rq} satisfy

$$\lim_{t \rightarrow \infty} \|e'_{rp}\| = \lim_{t \rightarrow \infty} \|x_{p+2}(t) - x_p(t)\| = 0, \tag{5}$$

$$p = 1, 3, 5, 7, 9, \dots, M - 3$$

$$\lim_{t \rightarrow \infty} \|e'_{rq}\| = \lim_{t \rightarrow \infty} \|x_{q+2}(t) - x_q(t)\| = 0,$$

$$q = 2, 4, 6, 8, 10, \dots, M - 2.$$

We notice from this definition that the error systems e_{ro} , e'_{rp} , and e'_{rq} are globally and asymptotically stable. This shows that, to ensure hybrid synchronization, we have to design controllers $u_o(t)$ to make e_{ro} , e'_{rp} , and e'_{rq} converge to zero.

3. Parameter Identification and Hybrid Synchronization for the General Case

For antisynchronization, the error vectors are

$$\begin{aligned} e_{r1} &= x_2 + x_1, \\ e_{r2} &= x_3 + x_2, \dots, e_{rM-1} = x_M + x_{M-1}. \end{aligned} \quad (6)$$

Let $\hat{\theta}_o$ be estimates of θ_o , $o = 1, 2, 3, 4, \dots, M$, respectively, and let $\tilde{\theta}_o = \theta_o - \hat{\theta}_o$, $o = 1, 2, 3, 4, \dots, M$ be errors while estimating the parameters θ_o , $o = 1, 2, \dots, M$, respectively. Derivative of (6) leads to the following:

$$\begin{aligned} \dot{e}_{r1} &= \dot{x}_2 + \dot{x}_1 = f_2(x_2) + F_2(x_2)\hat{\theta}_2 + F_2(x_2)\tilde{\theta}_2 \\ &\quad + D_2(x_1 - x_2) + u_1 + f_1(x_1) + F_1(x_1)\hat{\theta}_1 \\ &\quad + F_1(x_1)\tilde{\theta}_1 + D_1(x_M - x_1) \\ \dot{e}_{r2} &= \dot{x}_3 + \dot{x}_2 = f_3(x_3) + F_3(x_3)\hat{\theta}_3 + F_3(x_3)\tilde{\theta}_3 \\ &\quad + D_3(x_2 - x_3) + u_2 + f_2(x_2) + F_2(x_2)\hat{\theta}_2 \end{aligned}$$

$$\begin{aligned} &+ F_2(x_2)\tilde{\theta}_2 + D_2(x_1 - x_2) + u_1 \\ \dot{e}_{r3} &= \dot{x}_4 + \dot{x}_3 = f_4(x_4) + F_4(x_4)\hat{\theta}_4 + F_4(x_4)\tilde{\theta}_4 \\ &\quad + D_4(x_3 - x_4) + u_3 + f_3(x_3) + F_3(x_3)\hat{\theta}_3 \\ &\quad + F_3(x_3)\tilde{\theta}_3 + D_3(x_2 - x_3) + u_2 \\ &\quad \vdots \\ \dot{e}_{rM-1} &= \dot{x}_M + q\dot{x}_{M-1} = f_M(x_M) + F_M(x_M)\hat{\theta}_M \\ &\quad + F_M(x_M)\tilde{\theta}_M + D_M(x_{M-1} - x_M) + u_{M-1} \\ &\quad + f_{M-1}(x_{M-1}) + F_{M-1}(x_{M-1})\hat{\theta}_{M-1} \\ &\quad + F_{M-1}(x_{M-1})\tilde{\theta}_{M-1} + D_{M-1}(x_{M-2} - x_{M-1}) \\ &\quad + u_{M-2} \end{aligned} \quad (7)$$

which can be written as

$$\begin{aligned} &\begin{bmatrix} \dot{e}_{r1} \\ \dot{e}_{r2} \\ \vdots \\ \dot{e}_{rM-1} \end{bmatrix} \\ &= \begin{bmatrix} f_2(x_2) + f_1(x_1) + F_2(x_2)\hat{\theta}_2 + F_1(x_1)\hat{\theta}_1 + D_2(x_1 - x_2) + D_1(x_M - x_1) \\ f_3(x_3) + f_2(x_2) + F_3(x_3)\hat{\theta}_3 + F_2(x_2)\hat{\theta}_2 + D_3(x_2 - x_3) + D_2(x_1 - x_2) \\ \vdots \\ f_M(x_M) + f_{M-1}(x_{M-1}) + F_M(x_M)\hat{\theta}_M + F_{M-1}(x_{M-1})\hat{\theta}_{M-1} + D_M(x_{M-1} - x_M) + D_{M-1}(x_{M-2} - x_{M-1}) \end{bmatrix} \quad (8) \\ &+ \begin{bmatrix} F_2(x_2)\tilde{\theta}_2 + F_1(x_1)\tilde{\theta}_1 \\ F_3(x_3)\tilde{\theta}_3 + F_2(x_2)\tilde{\theta}_2 \\ \vdots \\ F_M(x_M)\tilde{\theta}_M + F_{M-1}(x_{M-1})\tilde{\theta}_{M-1} \end{bmatrix} + \begin{bmatrix} 1 & 0 & 0 & \cdots & 0 \\ 1 & 1 & 0 & \cdots & 0 \\ 0 & 1 & 1 & \cdots & 0 \\ \vdots & \vdots & \vdots & \ddots & \vdots \\ 0 & 0 & \cdots & 1 & 1 \end{bmatrix} \begin{bmatrix} u_1 \\ u_2 \\ \vdots \\ u_{M-1} \end{bmatrix}. \end{aligned}$$

By choosing

$$\begin{bmatrix} u_1 \\ u_2 \\ \vdots \\ u_{M-1} \end{bmatrix} = \begin{bmatrix} 1 & 0 & 0 & \cdots & 0 \\ 1 & 1 & 0 & \cdots & 0 \\ 0 & 1 & 1 & \cdots & 0 \\ \vdots & \vdots & \vdots & \ddots & \vdots \\ 0 & 0 & \cdots & 1 & 1 \end{bmatrix}^{-1} \left\{ \begin{bmatrix} e_{r2} \\ e_{r3} \\ \vdots \\ e_{rM-1} \\ v \end{bmatrix} - A \right\}, \quad (9)$$

where v is the new input vector and

$$A = \begin{bmatrix} f_2(x_2) + f_1(x_1) + F_2(x_2)\tilde{\theta}_2 + F_1(x_1)\tilde{\theta}_1 + D_2(x_1 - x_2) + D_1(x_M - x_1) \\ f_3(x_3) + f_2(x_2) + F_3(x_3)\tilde{\theta}_3 + F_2(x_2)\tilde{\theta}_2 + D_3(x_2 - x_3) + D_2(x_1 - x_2) \\ \vdots \\ f_M(x_M) + f_{M-1}(x_{M-1}) + F_M(x_M)\tilde{\theta}_M + F_{M-1}(x_{M-1})\tilde{\theta}_{M-1} + D_M(x_{M-1} - x_M) + D_{M-1}(x_{M-2} - x_{M-1}) \end{bmatrix} \quad (10)$$

then system (7) becomes

$$\begin{aligned} \dot{e}_{r1} &= e_{r2} + F_2(x_2)\tilde{\theta}_2 + F_1(x_1)\tilde{\theta}_1 \\ \dot{e}_{r2} &= e_{r3} + F_3(x_3)\tilde{\theta}_3 + F_2(x_2)\tilde{\theta}_2 \\ \dot{e}_{r3} &= e_{r4} + F_4(x_4)\tilde{\theta}_4 + F_3(x_3)\tilde{\theta}_3 \\ &\vdots \\ \dot{e}_{rM-2} &= e_{rM-1} + F_{M-1}(x_{M-1})\tilde{\theta}_{M-1} \\ &\quad + F_{M-2}(x_{M-2})\tilde{\theta}_{M-2} \\ \dot{e}_{rM-1} &= v + F_M(x_M)\tilde{\theta}_M + F_{M-1}(x_{M-1})\tilde{\theta}_{M-1}. \end{aligned} \quad (11)$$

To employ the integral sliding mode control, choose the nominal system for (11) as

$$\begin{aligned} \dot{e}_{r1} &= e_{r2} \\ \dot{e}_{r2} &= e_{r3} \\ \dot{e}_{r3} &= e_{r4} \\ &\vdots \\ \dot{e}_{rM-2} &= e_{rM-1} \\ \dot{e}_{rM-1} &= v_0. \end{aligned} \quad (12)$$

To stabilize the system (11), we choose the Hurwitz sliding surface for system (12) as $\sigma_0 = (1 + d/dt)^{M-2} e_{r1} = e_{r1} + c_1 e_{r2} + \dots + c_{M-3} e_{rM-2} + e_{rM-1}$, where the coefficients c_o are chosen in such a way that σ_0 becomes Hurwitz polynomial. Then $\dot{\sigma}_0 = e_{r2} + c_1 e_{r3} + c_2 e_{r4} + \dots + c_{M-3} e_{rM-1} + v_0$.

By choosing $v_0 = -e_{r2} - c_1 e_{r3} - c_2 e_{r4} - \dots - c_{M-3} e_{rM-1} - k\sigma_0 - k \text{sign}(\sigma_0)$, $k > 0$, we have $\dot{\sigma}_0 = -k \text{sign}(\sigma_0) - k\sigma_0$; therefore $\sigma_0 \rightarrow 0$, which gives $e_{r1}, e_{r2}, \dots, e_{rM-1} \rightarrow 0$. Therefore, system (12) becomes asymptotically stable.

The sliding surface for system (9) is $\sigma = \sigma_0 + z$. The term z in the sliding surface is an integral term computed later. To avoid the reaching-phase, choose $z(0)$ such that $\sigma(0) = 0$. By choosing $v = v_0 + v_s$ where v_0 is the nominal input vector

and v_s is compensator terms computed later, then the time derivative of the sliding surface becomes as

$$\begin{aligned} \dot{\sigma} &= \dot{\sigma}_0 + \dot{z} \\ &= \dot{e}_{r1} + c_1 \dot{e}_{r2} + c_2 \dot{e}_{r3} + c_3 \dot{e}_{r4} + \dots + c_{M-3} \dot{e}_{rM-2} \\ &\quad + \dot{e}_{rM-1} + \dot{z} \\ &= e_{r2} + c_1 e_{r3} + c_2 e_{r4} + \dots + c_{M-3} e_{rM-1} + v_0 + v_s + \dot{z} \\ &\quad + F_1(x_1)\tilde{\theta}_1 + (1 + c_1)F_2(x_2)\tilde{\theta}_2 \\ &\quad + (c_1 + c_2)F_3(x_3)\tilde{\theta}_3 + (c_2 + c_3)F_4(x_4)\tilde{\theta}_4 + \dots \\ &\quad + (c_{M-4} + c_{M-3})F_{M-2}(x_{M-2})\tilde{\theta}_{M-2} \\ &\quad + (c_{M-3} + 1)F_{M-1}(x_{M-1})\tilde{\theta}_{M-1} + F_M(x_M)\tilde{\theta}_M. \end{aligned} \quad (13)$$

By choosing a Lyapunov function: $V = (1/2)\{\sigma^T \sigma + \tilde{\theta}_1^T \tilde{\theta}_1 + \tilde{\theta}_2^T \tilde{\theta}_2 + \sum_{o=1}^{M-4} \tilde{\theta}_{o+2}^T \tilde{\theta}_{o+2} + \tilde{\theta}_{M-1}^T \tilde{\theta}_{M-1} + \tilde{\theta}_M^T \tilde{\theta}_M\}$, designing the adaptive laws for $\tilde{\theta}_o, \hat{\theta}_o$, $o = 1, 2, \dots, M$ and computing v_s such that $\dot{V} < 0$.

Theorem 3. Consider a Lyapunov function $V = (1/2)\{\sigma^T \sigma + \tilde{\theta}_1^T \tilde{\theta}_1 + \tilde{\theta}_2^T \tilde{\theta}_2 + \sum_{o=1}^{M-4} \tilde{\theta}_{o+2}^T \tilde{\theta}_{o+2} + \tilde{\theta}_{M-1}^T \tilde{\theta}_{M-1} + \tilde{\theta}_M^T \tilde{\theta}_M\}$. Then $\dot{V} < 0$ if the adaptive laws for $\tilde{\theta}_o, \hat{\theta}_o$, $o = 1, 2, 3, 4, \dots, M$ and the value of v_s are chosen as

$$\dot{z} = -e_{r2} - \sum_{o=3}^{M-1} c_{o-2} e_{ro} - v_0,$$

$$v_s = -k\sigma$$

$$\dot{\tilde{\theta}}_1 = -F_1^T(x_1)\sigma - k_1 \tilde{\theta}_1,$$

$$\dot{\tilde{\theta}}_1 = -\dot{\tilde{\theta}}_1$$

$$\dot{\tilde{\theta}}_2 = -(1 + c_1)F_2^T(x_2)\sigma - k_2 \tilde{\theta}_2,$$

$$\dot{\tilde{\theta}}_2 = -\dot{\tilde{\theta}}_2$$

$$\dot{\tilde{\theta}}_{o+2} = -(c_o + c_{o+1})F_{o+2}^T(x_{o+2})\sigma - k_{o+2} \tilde{\theta}_{o+2},$$

$$\dot{\tilde{\theta}}_{o+2} = -\dot{\tilde{\theta}}_{o+2},$$

$$o = 1, \dots, M - 4$$

$$\begin{aligned}\dot{\tilde{\theta}}_{M-1} &= -(c_{M-3} + 1) F_{M-1}^T(x_{M-1}) \sigma - k_{M-1} \tilde{\theta}_{M-1}, \\ \dot{\tilde{\theta}}_{M-1} &= -\dot{\tilde{\theta}}_{M-1} \\ \dot{\tilde{\theta}}_M &= -F_M^T(x_M) \sigma - k_M \tilde{\theta}_M,\end{aligned}\quad (14)$$

$$\dot{\tilde{\theta}}_M = -\dot{\tilde{\theta}}_M. \quad (15)$$

Proof. Since

$$\begin{aligned}\dot{V} &= \sigma^T \dot{\sigma} + \tilde{\theta}_1^T \dot{\tilde{\theta}}_1 + \tilde{\theta}_2^T \dot{\tilde{\theta}}_2 + \sum_{o=1}^{M-4} \tilde{\theta}_{o+2}^T \dot{\tilde{\theta}}_{o+2} + \tilde{\theta}_{M-1}^T \dot{\tilde{\theta}}_{M-1} \\ &+ \tilde{\theta}_M^T \dot{\tilde{\theta}}_M = \sigma^T \left\{ e_{r2} + \sum_{o=3}^{M-1} c_{o-2} e_{ro} + v_0 + v_s + \dot{z} \right\} \\ &+ \tilde{\theta}_1^T \left\{ \dot{\tilde{\theta}}_1 + F_1^T(x_1) \sigma \right\} + \tilde{\theta}_2^T \left\{ \dot{\tilde{\theta}}_2 \right. \\ &+ \left. (1 + c_1) F_2^T(x_2) \sigma \right\} \\ &+ \sum_{o=1}^{M-4} \tilde{\theta}_{o+2}^T \left\{ \dot{\tilde{\theta}}_{o+2} + (c_o + c_{o+1}) F_{o+2}^T(x_{o+2}) \sigma \right\} \\ &+ \tilde{\theta}_{M-1}^T \left\{ \dot{\tilde{\theta}}_{M-1} + (c_{M-3} + 1) F_{M-1}^T(x_{M-1}) \sigma \right\} \\ &+ \tilde{\theta}_M^T \left\{ \dot{\tilde{\theta}}_M + F_M^T(x_M) \sigma \right\}\end{aligned}\quad (16)$$

by using (14) we have

$$\dot{V} = -k\sigma^2 - \sum_{o=1}^M k_o \tilde{\theta}_o^T \tilde{\theta}_o. \quad (17)$$

From this we conclude that $\sigma, \tilde{\theta}_o \rightarrow 0$. Since $\sigma \rightarrow 0$, therefore $e_o \rightarrow 0$, $o = 1, 2, 3, \dots, M-1$. Thus the antisynchronization is achieved.

The controllers designed for the antisynchronization are used for the complete synchronization. For this we consider two cases:

Case 1. For odd number of systems and M ($M \geq 3$), synchronization error is expressed like

$$\begin{aligned}e'_{rp}(t) &= x_{p+2}(t) - x_p(t), \\ p &= 1, 3, 5, 7, 9, \dots, M-2 \\ e'_{rq}(t) &= x_{q+2}(t) - x_q(t), \\ q &= 2, 4, 6, 8, 10, \dots, M-3.\end{aligned}\quad (18)$$

Then

$$\begin{aligned}\lim_{t \rightarrow \infty} \|e'_{rp}\| &= \lim_{t \rightarrow \infty} \|x_{p+2}(t) - x_p(t)\| \\ \lim_{t \rightarrow \infty} \|x_{p+2}(t) + x_{p+1}(t) - x_{p+1}(t) - x_p(t)\| \\ &\leq \lim_{t \rightarrow \infty} \|x_{p+2}(t) + x_{p+1}(t)\| \\ &+ \lim_{t \rightarrow \infty} \|x_{p+1}(t) + x_p(t)\| = 0\end{aligned}\quad (19)$$

due to antisynchronization.

Thus

$$\lim_{t \rightarrow \infty} \|e'_{rp}\| = 0, \quad p = 1, 3, 5, 7, 9, \dots, M-2. \quad (20)$$

Similarly

$$\begin{aligned}\lim_{t \rightarrow \infty} \|e'_{rp}\| &= \lim_{t \rightarrow \infty} \|x_{q+2}(t) - x_q(t)\| \\ &= \lim_{t \rightarrow \infty} \|x_{q+2}(t) + x_{q+1}(t) - x_{q+1}(t) - x_q(t)\| \\ &\leq \lim_{t \rightarrow \infty} \|x_{q+2}(t) + x_{q+1}(t)\| \\ &+ \lim_{t \rightarrow \infty} \|x_{q+1}(t) + x_q(t)\| = 0\end{aligned}\quad (21)$$

$$\lim_{t \rightarrow \infty} \|e'_{rp}\| = 0, \quad q = 2, 4, 6, 8, 10, \dots, M-3.$$

Case 2. For even number of systems and M ($M \geq 4$), synchronization error is expressed like

$$\begin{aligned}e'_{rp} &= x_{p+2}(t) - x_p(t), \\ e'_{rq} &= x_{q+2}(t) - x_q(t) \\ \lim_{t \rightarrow \infty} \|e'_{rp}\| &= \lim_{t \rightarrow \infty} \|x_{p+2}(t) - x_p(t)\| \\ &= \lim_{t \rightarrow \infty} \|x_{p+2}(t) + x_{p+1}(t) - x_{p+1}(t) - x_p(t)\| \\ &\leq \lim_{t \rightarrow \infty} \|x_{p+2}(t) + x_{p+1}(t)\| \\ &+ \lim_{t \rightarrow \infty} \|x_{p+1}(t) + x_p(t)\| = 0 \\ \lim_{t \rightarrow \infty} \|e'_{rp}\| &= 0, \quad p = 1, 3, 5, 7, 9, \dots, M-3.\end{aligned}\quad (22)$$

Similarly

$$\begin{aligned}\lim_{t \rightarrow \infty} \|e'_{rq}\| &= \lim_{t \rightarrow \infty} \|x_{q+2}(t) - x_q(t)\| = 0, \\ q &= 2, 4, 6, 8, 10, \dots, M-2.\end{aligned}\quad (23)$$

So complete synchronization is too achieved. \square

4. Application Examples

To illustrate the control design procedure for reaching the hybrid synchronization behavior, we present two examples with $M = 3$ and $M = 4$.

Example 1 ($M = 3$). Chen chaotic system, Lorenz chaotic system, and Lü chaotic system, in that order, are selected for this numerical example and are expressed below:

$$\begin{aligned}
 \dot{x}_{11} &= -35x_{11} + 35x_{12} + d_{11}(x_{31} - x_{11}) \\
 \dot{x}_{12} &= -7x_{11} + 28x_{12} + x_{11}x_{13} + d_{12}(x_{32} - x_{12}) \\
 \dot{x}_{13} &= -3x_{13} + x_{11}x_{12} + d_{13}(x_{33} - x_{13}) \\
 \dot{x}_{21} &= -36x_{21} + 36x_{22} + d_{21}(x_{11} - x_{21}) + u_{11} \\
 \dot{x}_{22} &= 20x_{22} - x_{21}x_{23} + d_{22}(x_{12} - x_{22}) + u_{12} \\
 \dot{x}_{23} &= -3x_{23} + x_{21}x_{22} + d_{23}(x_{13} - x_{23}) + u_{13} \\
 \dot{x}_{31} &= -10x_{31} + 10x_{32} + d_{31}(x_{21} - x_{31}) + u_{21} \\
 \dot{x}_{32} &= 28x_{31} - x_{32} - x_{31}x_{33} + d_{32}(x_{22} - x_{32}) + u_{22} \\
 \dot{x}_{33} &= -\frac{8}{3}x_{33} + x_{31}x_{32} + d_{33}(x_{23} - x_{33}) + u_{23}.
 \end{aligned} \tag{24}$$

By assuming that the systems parameters are unknown, we write systems (24) as

$$\begin{aligned}
 \dot{x}_{11} &= a_1x_{11} + b_1x_{12} + d_{11}(x_{31} - x_{11}) \\
 \dot{x}_{12} &= c_1x_{11} + d_{12}x_{12} - x_{11}x_{13} + d_{12}(x_{32} - x_{12}) \\
 \dot{x}_{13} &= e_1x_{13} + x_{11}x_{12} + d_{13}(x_{33} - x_{13}) \\
 \dot{x}_{21} &= a_2x_{21} + b_2x_{22} + d_{21}(x_{11} - x_{21}) + u_{11} \\
 \dot{x}_{22} &= c_2x_{22} - x_{21}x_{23} + d_{22}(x_{12} - x_{22}) + u_{12} \\
 \dot{x}_{23} &= e_2x_{23} + x_{21}x_{22} + d_{23}(x_{13} - x_{23}) + u_{13} \\
 \dot{x}_{31} &= a_3x_{31} + b_3x_{32} + d_{31}(x_{21} - x_{31}) + u_{21} \\
 \dot{x}_{32} &= c_3x_{31} - x_{32} - x_{31}x_{33} + d_{32}(x_{22} - x_{32}) + u_{22} \\
 \dot{x}_{33} &= e_3x_{33} + x_{31}x_{32} + d_{33}(x_{23} - x_{33}) + u_{23}.
 \end{aligned} \tag{25}$$

Let $\hat{a}_o, \hat{b}_o, \hat{c}_o, \hat{e}_{ro}, \hat{d}_1$, $o = 1, 2, 3$ be estimates of $a_o, b_o, c_o, e_{ro}, d_1$, $o = 1, 2, 3$, respectively, and let $\tilde{a}_o = a_o - \hat{a}_o$, $\tilde{b}_o = b_o - \hat{b}_o$, $\tilde{c}_o = c_o - \hat{c}_o$, $\tilde{e}_{ro} = e_{ro} - \hat{e}_{ro}$, $\tilde{d}_1 = d_1 - \hat{d}_1$, $o = 1, 2, 3$ be errors in estimation of a_o, b_o, c_o, e_o, d_1 , $o = 1, 2, 3$, respectively.

Defining

$$\begin{aligned}
 x_1 &= \begin{bmatrix} x_{11} \\ x_{12} \\ x_{13} \end{bmatrix}, \\
 x_2 &= \begin{bmatrix} x_{21} \\ x_{22} \\ x_{23} \end{bmatrix}, \\
 x_3 &= \begin{bmatrix} x_{31} \\ x_{32} \\ x_{33} \end{bmatrix},
 \end{aligned}$$

$$u_1 = \begin{bmatrix} u_{11} \\ u_{12} \\ u_{13} \end{bmatrix},$$

$$u_2 = \begin{bmatrix} u_{21} \\ u_{22} \\ u_{23} \end{bmatrix},$$

$$\hat{\theta} = \begin{bmatrix} \hat{a} \\ \hat{b} \\ \hat{c} \\ \hat{d} \end{bmatrix},$$

$$\tilde{\theta} = \begin{bmatrix} \tilde{a} \\ \tilde{b} \\ \tilde{c} \\ \tilde{d} \end{bmatrix}$$

(26)

then the systems (25) in vector form are written as

$$\begin{aligned}
 \dot{x}_1 &= f_1(x_1) + F_1(x_1)\hat{\theta}_1 + F_1(x_1)\tilde{\theta}_1 \\
 \dot{x}_2 &= f_2(x_2) + F_2(x_2)\hat{\theta}_2 + F_2(x_2)\tilde{\theta}_2 + u_1 \\
 \dot{x}_3 &= f_3(x_3) + F_3(x_3)\hat{\theta}_3 + F_3(x_3)\tilde{\theta}_3 + u_2,
 \end{aligned} \tag{27}$$

where

$$f_1(x_1) = \begin{bmatrix} d_{11}(x_{31} - x_{11}) \\ x_{11}x_{13} + d_{12}(x_{32} - x_{12}) \\ x_{11}x_{12} + d_{13}(x_{33} - x_{13}) \end{bmatrix},$$

$$F_1(x_1) = \begin{bmatrix} x_{11} & x_{12} & 0 & 0 & 0 \\ 0 & 0 & \hat{c}_1 & \hat{d}_1 & 0 \\ 0 & 0 & 0 & 0 & x_{13} \end{bmatrix},$$

$$\hat{\theta}_1 = \begin{bmatrix} \hat{a}_1 \\ \hat{b}_1 \\ \hat{c}_1 \\ \hat{d}_1 \\ \hat{e}_1 \end{bmatrix},$$

$$\tilde{\theta}_1 = \begin{bmatrix} \tilde{a}_1 \\ \tilde{b}_1 \\ \tilde{c}_1 \\ \tilde{d}_1 \\ \tilde{e}_1 \end{bmatrix},$$

$$f_2(x_2) = \begin{bmatrix} d_{21}(x_{11} - x_{21}) \\ -x_{21}x_{23} + d_{22}(x_{12} - x_{22}) \\ x_{21}x_{22} + d_{23}(x_{13} - x_{23}) \end{bmatrix},$$

$$F_2(x_2) = \begin{bmatrix} x_{21} & x_{22} & 0 & 0 \\ 0 & 0 & x_{22} & 0 \\ 0 & 0 & 0 & x_{23} \end{bmatrix},$$

$$\hat{\theta}_2 = \begin{bmatrix} \hat{a}_2 \\ \hat{b}_2 \\ \hat{c}_2 \\ \hat{e}_2 \end{bmatrix},$$

$$\tilde{\theta}_2 = \begin{bmatrix} \tilde{a}_2 \\ \tilde{b}_2 \\ \tilde{c}_2 \\ \tilde{e}_2 \end{bmatrix},$$

$$f_3(x_3) = \begin{bmatrix} d_{31}(x_{21} - x_{31}) \\ -x_{32} - x_{31}x_{33} + d_{32}(x_{22} - x_{32}) \\ x_{31}x_{32} + d_{33}(x_{23} - x_{33}) \end{bmatrix},$$

$$F_3(x_3) = \begin{bmatrix} x_{31} & x_{32} & 0 & 0 \\ 0 & 0 & x_{31} & 0 \\ 0 & 0 & 0 & x_{33} \end{bmatrix},$$

$$\hat{\theta}_3 = \begin{bmatrix} \hat{a}_3 \\ \hat{b}_3 \\ \hat{c}_3 \\ \hat{e}_3 \end{bmatrix},$$

$$\tilde{\theta}_3 = \begin{bmatrix} \tilde{a}_3 \\ \tilde{b}_3 \\ \tilde{c}_3 \\ \tilde{e}_3 \end{bmatrix}.$$

For the antisynchronization, the errors

$$e_{r1} = \begin{bmatrix} e_{r11} \\ e_{r12} \\ e_{r13} \end{bmatrix},$$

$$e_{r2} = \begin{bmatrix} e_{r21} \\ e_{r22} \\ e_{r23} \end{bmatrix}$$

are

$$\begin{aligned} e_{r1} &= x_2 + x_1, \\ e_{r2} &= x_3 + x_2. \end{aligned} \quad (30)$$

Therefore

$$\begin{aligned} \begin{bmatrix} \dot{e}_{r1} \\ \dot{e}_{r2} \end{bmatrix} &= \begin{bmatrix} f_2(x_2) + F_2(x_2)\hat{\theta}_2 + f_1(x_1) + F_1(x_1)\hat{\theta}_1 \\ F_2(x_2)\hat{\theta}_2 + f_3(x_3) + F_3(x_3)\hat{\theta}_3 \end{bmatrix} \\ &+ \begin{bmatrix} F_1(x_1)\tilde{\theta}_1 + F_2(x_2)\tilde{\theta}_2 \\ F_2(x_2)\tilde{\theta}_2 + F_3(x_3)\tilde{\theta}_3 \end{bmatrix} + \begin{bmatrix} 1 & 0 \\ 1 & 1 \end{bmatrix} \begin{bmatrix} u_1 \\ u_2 \end{bmatrix}. \end{aligned} \quad (31)$$

By choosing

$$\begin{aligned} \begin{bmatrix} u_1 \\ u_2 \end{bmatrix} &= \begin{bmatrix} 1 & 0 \\ 1 & 1 \end{bmatrix}^{-1} \\ &\cdot \left\{ - \begin{bmatrix} f_2(x_2) + F_2(x_2)\hat{\theta}_2 + f_1(x_1) + F_1(x_1)\hat{\theta}_1 \\ f_3(x_3) + F_3(x_3)\hat{\theta}_3 + F_2(x_2)\hat{\theta}_2 \end{bmatrix} \right. \\ &\left. + \begin{bmatrix} e_{r2} \\ v \end{bmatrix} \right\}, \end{aligned} \quad (32)$$

where $v = [v_1 \ v_2 \ v_3]^T$ is the new input vector, then system (31) becomes

$$\begin{aligned} \dot{e}_{r1} &= e_2 + F_2(x_2)\tilde{\theta}_2 + F_1(x_1)\tilde{\theta}_1 \\ \dot{e}_{r2} &= v + F_3(x_3)\tilde{\theta}_3 + F_2(x_2)\tilde{\theta}_2. \end{aligned} \quad (33)$$

The nominal system for (33) is

$$\begin{aligned} \dot{e}_{r1} &= e_2 \\ \dot{e}_{r2} &= v_0, \end{aligned} \quad (34)$$

where $v_0 = [v_{01} \ v_{02} \ v_{03}]^T$ is the nominal input vector.

The sliding surface for nominal system (34) is $\sigma_0 = e_{r1} + e_{r2}$; that is,

$$\begin{bmatrix} \sigma_{01} \\ \sigma_{02} \\ \sigma_{03} \end{bmatrix} = \begin{bmatrix} e_{r11} + e_{r21} \\ e_{r12} + e_{r22} \\ e_{r13} + e_{r23} \end{bmatrix}. \quad (35)$$

(29) The nominal system (34) is asymptotically stable if $v_0 = -e_{r2} - k\sigma_0 - k \text{sign}(\sigma_0)$, $k > 0$. The sliding surface for system (33) is $\sigma = \sigma_0 + z = e_{r1} + e_{r2} + z$, where $z = [z_1 \ z_2 \ z_3]^T$ is some integral term and $z(0)$ is chosen in such a way that $\sigma(0) = 0$. Defining $v = v_0 + v_s$ where $v_0 = [v_{01} \ v_{02} \ v_{03}]^T$ is the nominal

input and $v_s = [v_{s1} \ v_{s2} \ v_{s3}]^T$ is compensator, then system (33) can be rewritten as

$$\begin{aligned}\dot{e}_{r11} &= e_{r21} + \bar{a}_2 x_{21} + \bar{b}_2 x_{22} + \bar{a}_1 x_{11} + \bar{b}_1 x_{12} \\ \dot{e}_{r12} &= e_{r22} + \bar{c}_2 x_{22} + \bar{c}_1 x_{11} + \bar{d}_1 x_{12} \\ \dot{e}_{r13} &= e_{r23} + \bar{e}_2 x_{23} + \bar{e}_1 x_{13} \\ \dot{e}_{r21} &= v_1 + \bar{a}_3 x_{31} + \bar{b}_3 x_{32} + \bar{a}_2 x_{21} + \bar{b}_2 x_{22} \\ \dot{e}_{r22} &= v_2 + \bar{c}_3 x_{31} + \bar{c}_2 x_{22} \\ \dot{e}_{r23} &= v_3 + \bar{e}_3 x_{33} + \bar{e}_2 x_{23}.\end{aligned}\quad (36)$$

Then $\dot{\sigma} = \dot{e}_{r1} + \dot{e}_{r2} + \dot{z}$ gives

$$\begin{aligned}\dot{\sigma}_1 &= e_{r21} + v_{01} + v_{s1} + \dot{z}_1 + \bar{a}_1 x_{11} + \bar{b}_1 x_{12} + 2\bar{a}_2 x_{21} \\ &\quad + 2\bar{b}_2 x_{22} + \bar{a}_3 x_{31} + \bar{b}_3 x_{32} \\ \dot{\sigma}_2 &= e_{r22} + v_{02} + v_{s2} + \dot{z}_2 + \bar{c}_1 x_{11} + \bar{d}_1 x_{12} + 2\bar{c}_2 x_{22} \\ &\quad + \bar{c}_3 x_{31} \\ \dot{\sigma}_3 &= e_{r23} + v_{03} + v_{s3} + \dot{z}_3 + 2\bar{e}_2 x_{23} + \bar{e}_1 x_{13} + \bar{e}_3 x_{33}.\end{aligned}\quad (37)$$

By choosing a Lyapunov function

$$\begin{aligned}V &= \frac{1}{2} \{ \sigma_1^2 + \sigma_2^2 + \sigma_3^2 + \bar{a}_1^2 + \bar{a}_2^2 + \bar{a}_3^2 + \bar{b}_1^2 + \bar{b}_2^2 + \bar{b}_3^2 \\ &\quad + \bar{c}_1^2 + \bar{c}_2^2 + \bar{c}_3^2 + \bar{e}_1^2 + \bar{e}_2^2 + \bar{e}_3^2 + \bar{d}_1^2 \}\end{aligned}\quad (38)$$

then $\dot{V} < 0$ if the adaptive laws for $\bar{a}_o, \hat{a}_o, \bar{b}_o, \hat{b}_o, \bar{c}_o, \hat{c}_o, \bar{e}_{ro}, \hat{e}_{ro}, \bar{d}_1, \hat{d}_1$, $o = 1, 2, 3$ and the values of v_{so} , $o = 1, 2, 3$ are chosen as

$$\begin{aligned}\dot{z}_1 &= -e_{r21} - v_{01}, \\ v_{s1} &= -k_1 s_1 \\ \dot{z}_2 &= -e_{r22} - v_{02}, \\ v_{s2} &= -k_2 s_2 \\ \dot{z}_3 &= -e_{r23} - v_{03}, \\ v_{s3} &= -k_3 s_3 \\ \dot{\bar{a}}_1 &= -\sigma_1 x_{11} - k_4 \bar{a}_1, \\ \dot{\hat{a}}_1 &= -\dot{\bar{a}}_1 \\ \dot{\bar{a}}_2 &= -2\sigma_1 x_{21} - k_5 \bar{a}_2, \\ \dot{\hat{a}}_2 &= -\dot{\bar{a}}_2 \\ \dot{\bar{a}}_3 &= -\sigma_1 x_{31} - k_6 \bar{a}_3,\end{aligned}$$

$$\begin{aligned}\dot{\bar{a}}_3 &= -\dot{\hat{a}}_3 \\ \dot{\bar{b}}_1 &= -\sigma_1 x_{12} - k_7 \bar{b}_1, \\ \dot{\hat{b}}_1 &= -\dot{\bar{b}}_1 \\ \dot{\bar{b}}_2 &= -2\sigma_1 x_{22} - k_8 \bar{b}_2, \\ \dot{\hat{b}}_2 &= -\dot{\bar{b}}_2 \\ \dot{\bar{b}}_3 &= -\sigma_1 x_{32} - k_9 \bar{b}_3, \\ \dot{\hat{b}}_3 &= -\dot{\bar{b}}_3 \\ \dot{\bar{c}}_1 &= -\sigma_2 x_{11} - k_{10} \bar{c}_1, \\ \dot{\hat{c}}_1 &= -\dot{\bar{c}}_1 \\ \dot{\bar{c}}_2 &= -2\sigma_2 x_{22} - k_{11} \bar{c}_2, \\ \dot{\hat{c}}_2 &= -\dot{\bar{c}}_2 \\ \dot{\bar{c}}_3 &= -\sigma_2 x_{31} - k_{12} \bar{c}_3, \\ \dot{\hat{c}}_3 &= -\dot{\bar{c}}_3 \\ \dot{\bar{e}}_{r1} &= -\sigma_3 x_{13} - k_{13} \bar{e}_{r1}, \\ \dot{\hat{e}}_{r1} &= -\dot{\bar{e}}_{r1} \\ \dot{\bar{e}}_{r2} &= -2\sigma_3 x_{23} - k_{14} \bar{e}_{r2}, \\ \dot{\hat{e}}_{r2} &= -\dot{\bar{e}}_{r2} \\ \dot{\bar{e}}_{r3} &= -\sigma_3 x_{33} - k_{15} \bar{e}_{r3}, \\ \dot{\hat{e}}_{r3} &= -\dot{\bar{e}}_{r3} \\ \dot{\bar{d}}_1 &= -\sigma_2 x_{12} - k_{16} \bar{d}_1, \\ \dot{\hat{d}}_1 &= -\dot{\bar{d}}_1,\end{aligned}$$

$$k_o > 0, \quad o = 1, 2, \dots, 16.$$

(39)

We have

$$\begin{aligned}\dot{V} &= -k_2 \sigma_1^2 - k_2 \sigma_2^2 - k_3 \sigma_3^2 - k_4 \bar{a}_1^2 - k_5 \bar{a}_2^2 - k_6 \bar{a}_3^2 \\ &\quad - k_7 \bar{b}_1^2 - k_8 \bar{b}_2^2 - k_9 \bar{b}_3^2 - k_{10} \bar{c}_1^2 - k_{11} \bar{c}_2^2 - k_{12} \bar{c}_3^2 \\ &\quad - k_{13} \bar{e}_{r1}^2 - k_{14} \bar{e}_{r2}^2 - k_{15} \bar{e}_{r3}^2 - k_{16} \bar{d}_1^2.\end{aligned}\quad (40)$$

From this we conclude that $\sigma_o, \bar{e}_{ro}, \bar{d}_1, \bar{a}_o, \bar{b}_o, \bar{c}_o \rightarrow 0$, $o = 1, 2, 3$. Since $\sigma_o \rightarrow 0$, $o = 1, 2, 3$, therefore $e_{r1}, e_{r2} \rightarrow 0$. Therefore, antisynchronization is realized. For complete synchronization, the error is $e'_{r1} = x_3 - x_1$, which can be written as $e'_{r1} = x_3 - x_1 = x_3 + x_2 - x_2 - x_1 = e_{r2} - e_{r1}$. As

$e_{r1}, e_{r2} \rightarrow 0$ therefore $e'_{r1} \rightarrow 0$. Thus complete synchronization is achieved. Results of simulations are depicted in Figures 2-4.

Example 2 ($M = 4$). In this example, only Lorenz systems with unknown parameters are chosen to examine the effectiveness of the proposed method.

These can be expressed as

$$\begin{aligned}
\dot{x}_{11} &= -10x_{11} + 10x_{12} + d'_{11}(x_{41} - x_{11}) \\
\dot{x}_{12} &= 28x_{11} - x_{12} - x_{11}x_{13} + d'_{12}(x_{42} - x_{12}) \\
\dot{x}_{13} &= -\frac{8}{3}x_{13} + x_{11}x_{12} + d'_{13}(x_{43} - x_{13}) \\
\dot{x}_{21} &= -10x_{21} + 10x_{22} + d'_{21}(x_{11} - x_{21}) + u'_{11} \\
\dot{x}_{22} &= 28x_{21} - x_{22} - x_{21}x_{23} + d'_{22}(x_{12} - x_{22}) + u'_{12} \\
\dot{x}_{23} &= -\frac{8}{3}x_{23} + x_{21}x_{22} + d'_{23}(x_{13} - x_{23}) + u'_{13} \\
\dot{x}_{31} &= -10x_{31} + 10x_{32} + d'_{31}(x_{21} - x_{31}) + u'_{21} \\
\dot{x}_{32} &= 28x_{31} - x_{32} - x_{31}x_{33} + d'_{32}(x_{22} - x_{32}) + u'_{22} \\
\dot{x}_{33} &= -\frac{8}{3}x_{33} + x_{31}x_{32} + d'_{33}(x_{23} - x_{33}) + u'_{23} \\
\dot{x}_{41} &= -10x_{41} + 10x_{42} + d'_{41}(x_{31} - x_{41}) + u'_{31} \\
\dot{x}_{42} &= 28x_{41} - x_{42} - x_{41}x_{43} + d'_{42}(x_{32} - x_{42}) + u'_{32} \\
\dot{x}_{43} &= -\frac{8}{3}x_{43} + x_{41}x_{42} + d'_{43}(x_{33} - x_{43}) + u'_{33}.
\end{aligned} \tag{41}$$

With unknown parameters above four systems can be represented as

$$\begin{aligned}
\dot{x}_{11} &= ax_{11} + bx_{12} + d'_{11}(x_{41} - x_{11}) \\
\dot{x}_{12} &= cx_{11} - x_{12} - x_{11}x_{13} + d'_{12}(x_{42} - x_{12})
\end{aligned} \tag{42}$$

$$\begin{aligned}
\dot{x}_{13} &= dx_{13} + x_{11}x_{12} + d'_{13}(x_{43} - x_{13}) \\
\dot{x}_{21} &= ax_{21} + bx_{22} + d'_{21}(x_{11} - x_{21}) + u'_{11} \\
\dot{x}_{22} &= cx_{21} - x_{22} - x_{21}x_{23} + d'_{22}(x_{12} - x_{22}) + u'_{12}
\end{aligned} \tag{43}$$

$$\begin{aligned}
\dot{x}_{23} &= dx_{23} + x_{21}x_{22} + d'_{23}(x_{13} - x_{23}) + u'_{13} \\
\dot{x}_{31} &= ax_{31} + bx_{32} + d'_{31}(x_{21} - x_{31}) + u'_{21} \\
\dot{x}_{32} &= cx_{31} - x_{32} - x_{31}x_{33} + d'_{32}(x_{22} - x_{32}) + u'_{22}
\end{aligned} \tag{44}$$

$$\begin{aligned}
\dot{x}_{33} &= dx_{33} + x_{31}x_{32} + d'_{33}(x_{23} - x_{33}) + u'_{23} \\
\dot{x}_{41} &= ax_{41} + bx_{42} + d'_{41}(x_{31} - x_{41}) + u'_{31} \\
\dot{x}_{42} &= cx_{41} - x_{42} - x_{41}x_{43} + d'_{42}(x_{32} - x_{42}) + u'_{32}
\end{aligned} \tag{45}$$

$$\dot{x}_{43} = dx_{43} + x_{41}x_{42} + d'_{43}(x_{33} - x_{43}) + u'_{33}.$$

Let $\hat{a}, \hat{b}, \hat{c}, \hat{d}$ be estimates of a, b, c, d , respectively, and let $\tilde{a} = a - \hat{a}$, $\tilde{b} = b - \hat{b}$, $\tilde{c} = c - \hat{c}$, $\tilde{d} = d - \hat{d}$ be the errors in estimation of a, b, c, d , respectively.

Defining

$$\begin{aligned}
x_1 &= \begin{bmatrix} x_{11} \\ x_{12} \\ x_{13} \end{bmatrix}, \\
x_2 &= \begin{bmatrix} x_{21} \\ x_{22} \\ x_{23} \end{bmatrix}, \\
x_3 &= \begin{bmatrix} x_{31} \\ x_{32} \\ x_{33} \end{bmatrix}, \\
x_4 &= \begin{bmatrix} x_{41} \\ x_{42} \\ x_{43} \end{bmatrix}, \\
u'_1 &= \begin{bmatrix} u'_{11} \\ u'_{12} \\ u'_{13} \end{bmatrix}, \\
u'_2 &= \begin{bmatrix} u'_{21} \\ u'_{22} \\ u'_{23} \end{bmatrix}, \\
u'_3 &= \begin{bmatrix} u'_{31} \\ u'_{32} \\ u'_{33} \end{bmatrix}, \\
\hat{\theta} &= \begin{bmatrix} \hat{a} \\ \hat{b} \\ \hat{c} \\ \hat{d} \end{bmatrix}, \\
\tilde{\theta} &= \begin{bmatrix} \tilde{a} \\ \tilde{b} \\ \tilde{c} \\ \tilde{d} \end{bmatrix},
\end{aligned} \tag{46}$$

systems (43)–(45) are represented as

$$\begin{aligned}
\dot{x}_1 &= f_1(x_1) + F_1(x_1)\hat{\theta} + F_1(x_1)\tilde{\theta} \\
\dot{x}_2 &= f_2(x_2) + F_2(x_2)\hat{\theta} + F_2(x_2)\tilde{\theta} + u'_1 \\
\dot{x}_3 &= f_3(x_3) + F_3(x_3)\hat{\theta} + F_3(x_3)\tilde{\theta} + u'_2 \\
\dot{x}_4 &= f_4(x_4) + F_4(x_4)\hat{\theta} + F_4(x_4)\tilde{\theta} + u'_3,
\end{aligned} \tag{47}$$

where

$$f_1(x_1) = \begin{bmatrix} d'_{11}(x_{41} - x_{11}) \\ -x_{12} - x_{11}x_{13} + d'_{12}(x_{42} - x_{12}) \\ x_{11}x_{12} + d'_{13}(x_{43} - x_{13}) \end{bmatrix},$$

$$F_1(x_1) = \begin{bmatrix} x_{11} & x_{12} & 0 & 0 \\ 0 & 0 & x_{11} & 0 \\ 0 & 0 & 0 & x_{13} \end{bmatrix}$$

$$f_2(x_2) = \begin{bmatrix} d'_{21}(x_{11} - x_{21}) \\ -x_{22} - x_{21}x_{23} + d'_{22}(x_{12} - x_{22}) \\ x_{21}x_{22} + d'_{23}(x_{13} - x_{23}) \end{bmatrix},$$

$$F_2(x_2) = \begin{bmatrix} x_{21} & x_{22} & 0 & 0 \\ 0 & 0 & x_{21} & 0 \\ 0 & 0 & 0 & x_{23} \end{bmatrix}$$

$$f_3(x_3) = \begin{bmatrix} d'_{31}(x_{21} - x_{31}) \\ -x_{32} - x_{31}x_{33} + d'_{32}(x_{22} - x_{32}) \\ x_{31}x_{32} + d'_{33}(x_{23} - x_{33}) \end{bmatrix},$$

$$F_3(x_3) = \begin{bmatrix} x_{31} & x_{32} & 0 & 0 \\ 0 & 0 & x_{31} & 0 \\ 0 & 0 & 0 & x_{33} \end{bmatrix}$$

$$f_4(x_4) = \begin{bmatrix} d'_{41}(x_{31} - x_{41}) \\ -x_{42} - x_{41}x_{43} + d'_{42}(x_{32} - x_{42}) \\ x_{41}x_{42} + d'_{43}(x_{33} - x_{43}) \end{bmatrix},$$

$$F_4(x_4) = \begin{bmatrix} x_{41} & x_{42} & 0 & 0 \\ 0 & 0 & x_{41} & 0 \\ 0 & 0 & 0 & x_{43} \end{bmatrix}.$$

For the antisynchronization, the error vectors

$$\begin{aligned} e_{r1} &= \begin{bmatrix} e_{r11} \\ e_{r12} \\ e_{r13} \end{bmatrix}, \\ e_{r2} &= \begin{bmatrix} e_{r21} \\ e_{r22} \\ e_{r23} \end{bmatrix}, \\ e_{r3} &= \begin{bmatrix} e_{r31} \\ e_{r32} \\ e_{r33} \end{bmatrix} \end{aligned} \quad (49)$$

are

$$\begin{aligned} e_{r1} &= x_2 + x_1, \\ e_{r2} &= x_3 + x_2, \\ e_{r3} &= x_4 + x_3. \end{aligned} \quad (50)$$

Therefore

$$\begin{aligned} \begin{bmatrix} \dot{e}_{r1} \\ \dot{e}_{r2} \\ \dot{e}_{r3} \end{bmatrix} &= \begin{bmatrix} (F_1(x_1) + F_2(x_2))\hat{\theta} + f_1(x_1) + f_2(x_2) \\ (F_2(x_2) + F_3(x_3))\hat{\theta} + f_2(x_2) + f_3(x_3) \\ (F_3(x_3) + F_4(x_4))\hat{\theta} + f_3(x_3) + f_4(x_4) \end{bmatrix} \\ &+ \begin{bmatrix} F_1(x_1) + F_2(x_2) \\ F_2(x_2) + F_3(x_3) \\ F_3(x_3) + F_4(x_4) \end{bmatrix} \tilde{\theta} \\ &+ \begin{bmatrix} 1 & 0 & 0 \\ 1 & 1 & 0 \\ 0 & 1 & 1 \end{bmatrix} \begin{bmatrix} u'_1 \\ u'_2 \\ u'_3 \end{bmatrix}. \end{aligned} \quad (48)$$

Choose

$$\begin{aligned} \begin{bmatrix} u'_1 \\ u'_2 \\ u'_3 \end{bmatrix} &= \begin{bmatrix} 1 & 0 & 0 \\ 1 & 1 & 0 \\ 0 & 1 & 1 \end{bmatrix}^{-1} \\ &\cdot \left\{ - \begin{bmatrix} f_2(x_2) + f_1(x_1) + (F_2(x_2) + F_1(x_1))\hat{\theta} \\ f_3(x_3) + f_2(x_2) + (F_3(x_3) + F_2(x_2))\hat{\theta} \\ f_4(x_4) + f_3(x_3) + (F_4(x_4) + F_3(x_3))\hat{\theta} \end{bmatrix} \right. \\ &\left. + \begin{bmatrix} e_{r2} \\ e_{r3} \\ v \end{bmatrix} \right\}, \end{aligned} \quad (52)$$

where v is the new input vector.

We have

$$\begin{bmatrix} \dot{e}_{r1} \\ \dot{e}_{r2} \\ \dot{e}_{r3} \end{bmatrix} = \begin{bmatrix} e_{r2} \\ e_{r3} \\ v \end{bmatrix} + \begin{bmatrix} F_2(x_2) + F_1(x_1) \\ F_3(x_3) + F_2(x_2) \\ F_4(x_4) + F_3(x_3) \end{bmatrix} \tilde{\theta} \quad (53)$$

or

$$\begin{aligned} \dot{e}_{r1} &= e_{r2} + (F_2(x_2) + F_1(x_1))\tilde{\theta} \\ \dot{e}_{r2} &= e_{r3} + (F_3(x_3) + F_2(x_2))\tilde{\theta} \\ \dot{e}_{r3} &= v + (F_4(x_4) + F_3(x_3))\tilde{\theta}. \end{aligned} \quad (54)$$

The nominal system for (54) is

$$\begin{aligned} \dot{e}_{r1} &= e_{r2} \\ \dot{e}_{r2} &= e_{r3} \\ \dot{e}_{r3} &= v_0. \end{aligned} \quad (55)$$

The Hurwitz sliding surface vector for nominal system (55) can be defined as

$$\sigma_0 = e_{r1} + 2e_{r2} + e_{r3}, \quad (56)$$

where

$$\sigma_0 = \begin{bmatrix} \sigma_{01} \\ \sigma_{02} \\ \sigma_{03} \end{bmatrix} = \begin{bmatrix} e_{r11} + 2e_{r21} + e_{r31} \\ e_{r12} + 2e_{r22} + e_{r32} \\ e_{r13} + 2e_{r23} + e_{r33} \end{bmatrix}. \quad (57)$$

Then the derivative of the above system is $\dot{\sigma}_0 = \dot{e}_{r1} + 2\dot{e}_{r2} = e_{r2} + 2e_{r3} + v_0$. By choosing $v_0 = -e_{r2} - 2e_{r3} - k\sigma_0 - k \text{sign}(\sigma_0)$, $k > 0$, we have $\dot{\sigma}_0 = -k \text{sign}(\sigma_0) - k\sigma_0$. So the error dynamics (55) are asymptotically stable.

Sliding surface for the system (55) is described as $\sigma = \sigma_0 + z = e_{r1} + 2e_{r2} + e_{r3} + z$, where $z = [z_1 \ z_2 \ z_3]^T$ is some integral term, by choosing $z(0)$ in such a way that $\sigma(0) = 0$. Select $v = v_0 + v_s$, where $v_0 = [v_{01} \ v_{02} \ v_{03}]^T$ is the nominal input and $v_s = [v_{s1} \ v_{s2} \ v_{s3}]^T$ is compensator term computed later.

The system (54) can be rewritten as

$$\begin{aligned} \dot{e}_{r11} &= e_{r21} + \tilde{a}x_{21} + \tilde{b}x_{22} + \tilde{a}x_{11} + \tilde{b}x_{12} \\ \dot{e}_{r12} &= e_{r22} + \tilde{c}x_{21} + \tilde{c}x_{11} \\ \dot{e}_{r13} &= e_{r23} + \tilde{d}x_{23} + \tilde{d}x_{13} \\ \dot{e}_{r21} &= e_{r31} + \tilde{a}x_{31} + \tilde{b}x_{32} + \tilde{a}x_{21} + \tilde{b}x_{22} \\ \dot{e}_{r22} &= e_{r32} + \tilde{c}x_{31} + \tilde{c}x_{21} \\ \dot{e}_{r23} &= e_{r33} + \tilde{d}x_{33} + \tilde{d}x_{23} \\ \dot{e}_{r31} &= v_{01} + v_{s1} + \tilde{a}x_{41} + \tilde{b}x_{42} + \tilde{a}x_{31} + \tilde{b}x_{32} \\ \dot{e}_{r32} &= v_{02} + v_{s2} + \tilde{c}x_{41} + \tilde{c}x_{31} \\ \dot{e}_{r33} &= v_{03} + v_{s3} + \tilde{d}x_{43} + \tilde{d}x_{33}. \end{aligned} \quad (58)$$

Then $\dot{\sigma} = \dot{e}_{r1} + 2\dot{e}_{r2} + \dot{e}_{r3} + \dot{z}$ gives

$$\begin{aligned} \dot{\sigma}_1 &= \dot{e}_{r11} + 2\dot{e}_{r21} + \dot{e}_{r31} + \dot{z}_1 \\ &= e_{r21} + \tilde{a}x_{21} + \tilde{b}x_{22} + \tilde{a}x_{11} + \tilde{b}x_{12} + 2e_{r31} \\ &\quad + 2\tilde{a}x_{31} + 2\tilde{b}x_{32} + 2\tilde{a}x_{21} + 2\tilde{b}x_{22} + v_{01} + v_{s1} \\ &\quad + \tilde{a}x_{41} + \tilde{b}x_{42} + \tilde{a}x_{31} + \tilde{b}x_{32} + \dot{z}_1 \\ \dot{\sigma}_2 &= \dot{e}_{r12} + 2\dot{e}_{r22} + \dot{e}_{r32} + \dot{z}_2 \\ &= e_{r22} + \tilde{c}x_{21} + \tilde{c}x_{11} + 2e_{r32} + 2\tilde{c}x_{31} + 2\tilde{c}x_{21} \\ &\quad + v_{02} + v_{s2} + \tilde{c}x_{41} + \tilde{c}x_{31} + \dot{z}_2 \\ \dot{\sigma}_3 &= \dot{e}_{r13} + 2\dot{e}_{r23} + \dot{e}_{r33} + \dot{z}_3 \\ &= e_{r23} + \tilde{d}x_{23} + \tilde{d}x_{13} + 2e_{r33} + 2\tilde{d}x_{33} + 2\tilde{d}x_{23} \\ &\quad + v_{03} + v_{s3} + \tilde{d}x_{43} + \tilde{d}x_{33} + \dot{z}_3 \end{aligned} \quad (59)$$

or

$$\begin{aligned} \dot{\sigma}_1 &= e_{r21} + 2e_{r31} + \tilde{a} \{x_{11} + 3x_{21} + 3x_{31} + x_{41}\} \\ &\quad + \tilde{b} \{x_{12} + 3x_{22} + 3x_{32} + x_{42}\} + v_{01} + v_{s1} \\ &\quad + \dot{z}_1 \\ \dot{\sigma}_2 &= e_{r22} + 2e_{r32} + \tilde{c} \{x_{11} + 3x_{21} + 3x_{31} + x_{41}\} + v_{02} \\ &\quad + v_{s2} + \dot{z}_2 \\ \dot{\sigma}_3 &= e_{r23} + 2e_{r33} + \tilde{d} \{x_{13} + 3x_{23} + 3x_{33} + x_{43}\} + v_{03} \\ &\quad + v_{s3} + \dot{z}_3. \end{aligned} \quad (60)$$

Choose the Lyapunov function: $V = (1/2)\{\sigma_1^2 + \sigma_2^2 + \sigma_3^2 + \tilde{a}^2 + \tilde{b}^2 + \tilde{c}^2 + \tilde{d}^2\}$.

Then $\dot{V} < 0$ if the adaptive laws for $\tilde{a}, \tilde{b}, \tilde{c}, \tilde{d}, \hat{a}, \hat{b}, \hat{c}, \hat{d}$ and v_{so} , $o = 1, 2, 3$ are chosen as

$$\begin{aligned} \dot{z}_1 &= -e_{r21} - 2e_{r31} - v_{01}, \\ v_{s1} &= -k_1 s_1 \\ \dot{z}_2 &= -e_{r22} - 2e_{r32} - v_{02}, \\ v_{s2} &= -k_2 s_2 \\ \dot{z}_3 &= -e_{r23} - 2e_{r33} - v_{03}, \\ v_{s3} &= -k_3 s_3 \\ \dot{\tilde{a}} &= -\sigma_1 (x_{11} + 3x_{21} + 3x_{31} + x_{41}) - k_4 \tilde{a}, \\ \dot{\hat{a}} &= -\tilde{a} \\ \dot{\tilde{b}} &= -\sigma_1 (x_{12} + 3x_{22} + 3x_{32} + x_{42}) - k_5 \tilde{b}, \\ \dot{\hat{b}} &= -\tilde{b} \\ \dot{\tilde{c}} &= -\sigma_2 (x_{11} + 3x_{21} + 3x_{31} + x_{41}) - k_6 \tilde{c}, \\ \dot{\hat{c}} &= -\tilde{c} \\ \dot{\tilde{d}} &= -\sigma_3 (x_{13} + 3x_{23} + 3x_{33} + x_{43}) - k_7 \tilde{d}, \\ \dot{\hat{d}} &= -\tilde{d}, \end{aligned} \quad (61)$$

$$k_o > 0, \quad o = 1, \dots, 7.$$

From this we conclude that $\tilde{a}, \tilde{b}, \tilde{c}, \tilde{d}, \sigma_1, \sigma_2, \sigma_3, \tilde{d} \rightarrow 0$. Since $\sigma_o \rightarrow 0$, $o = 1, 2, 3$, therefore $e_{r1}, e_{r2}, e_{r3} \rightarrow 0$. Thus antisynchronization is achieved.

For complete synchronization, the errors are $e'_{r1} = x_3 - x_1$, $e'_{r2} = x_4 - x_2$ which can be written as

$$\begin{aligned} e'_{r1} &= x_3 - x_1 = x_3 + x_2 - x_2 - x_1 = e_{r2} - e_{r1} \\ e'_{r2} &= x_4 - x_2 = x_4 + x_3 - x_3 - x_2 = e_{r3} - e_{r2}. \end{aligned} \quad (62)$$

As $e_{r1}, e_{r2}, e_{r3} \rightarrow 0$ therefore $e'_{r1}, e'_{r2} \rightarrow 0$; thus complete synchronization is achieved. Simulation results are shown in Figures 5-7.

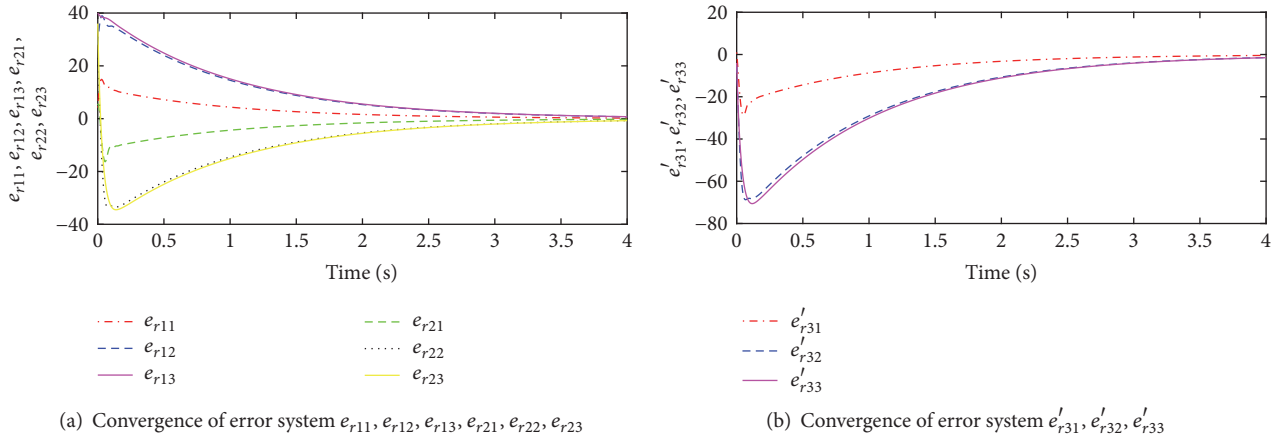


FIGURE 2

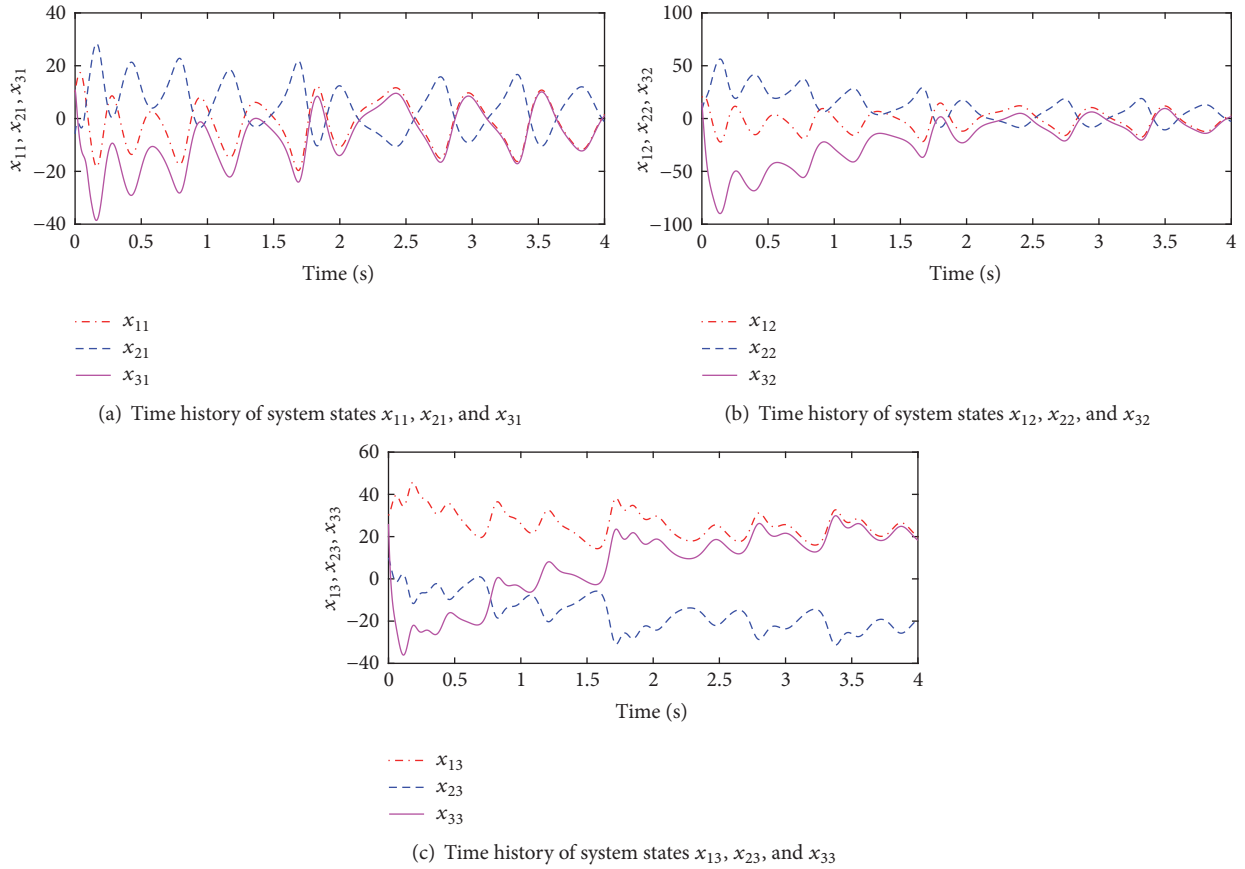
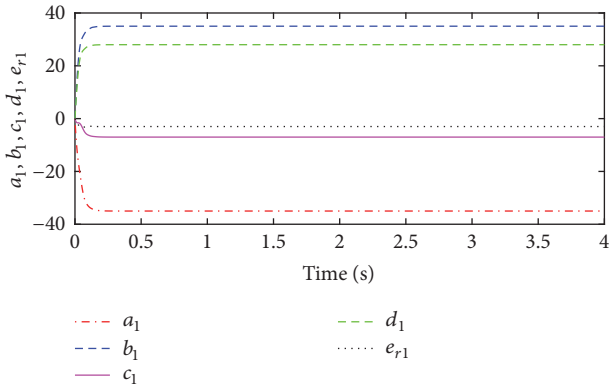


FIGURE 3

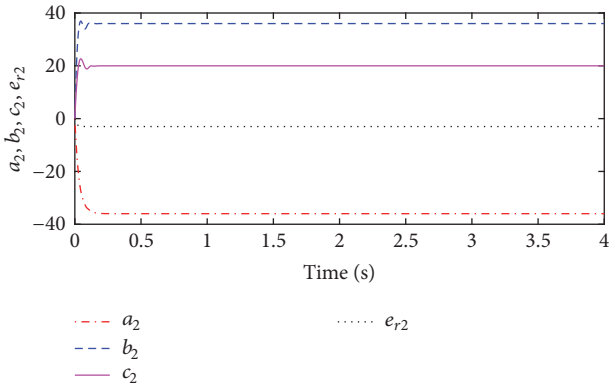
5. Simulation Results and Discussion

Figures 2–4 show simulation results for Example 1 with $M = 3$. The initial (starting point) conditions are chosen as $(x_{11}(0) = 10, x_{12}(0) = 20, x_{13}(0) = 30), (x_{21}(0) = -5.8, x_{22}(0) = 8, x_{23}(0) = 10),$ and $(x_{31}(0) = 11, x_{32}(0) = 15, x_{33}(0) = 26)$. The coupling parameters are chosen as $d_{11} = d_{21} = d_{13} = d_{23} = d_{31} = d_{33} = 0, d_{12} = 10, d_{22} = 11$ and $d_{32} = 1$. Figure 2(a) shows that the errors $e_{r11}, e_{r12},$

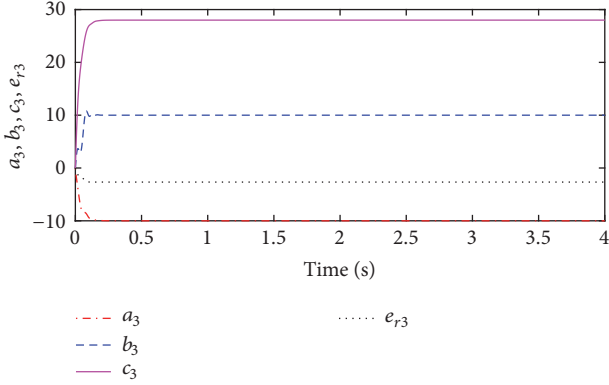
$e_{r13}, e_{r21}, e_{r22},$ and e_{r23} asymptotically go to zero. Figure 2(b) displays the errors $e'_{r31}, e'_{r32},$ and $e'_{r33},$ converging to origin. Figure 3(a) shows system states $x_{11}, x_{21}, x_{31},$ Figure 3(b) shows system states $x_{12}, x_{22},$ and $x_{32},$ and Figure 3(c) shows system states $x_{13}, x_{23},$ and $x_{33}.$ From these figures we can see that systems $x_1(t)$ and $x_2(t),$ and systems $x_2(t)$ and $x_3(t)$ achieve the antisynchronization, and systems $x_1(t)$ and $x_3(t)$ attain complete synchronization and therefore milestone is attained, that is, hybrid synchronization. Figure 4 shows the



(a) Parameter estimation $a_1, b_1, c_1, d_1,$ and e_{r1}



(b) Parameter estimation $a_2, b_2, c_2,$ and e_{r2}

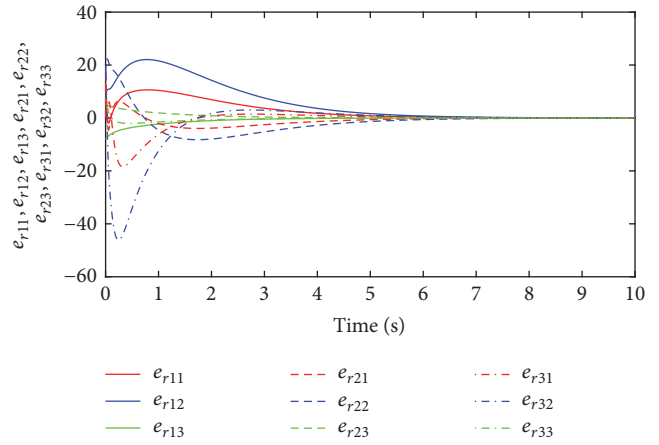


(c) Parameter estimation $a_3, b_3, c_3,$ and e_{r3}

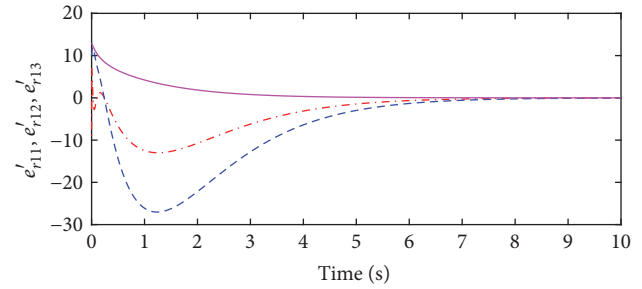
FIGURE 4

adaptive estimation of parameters $a, b, c, d,$ and e_r for the three systems. Figure 4(a) shows the estimation of $a_1, b_1, c_1, d_1,$ and e_{r1} , the parameters of the first system, which converge to their true values of $-35, 35, -7, 28,$ and $-3,$ respectively. Figure 4(b) shows the estimation of $a_2, b_2, c_2,$ and e_{r2} , and the parameters of the second system, which converges to their true values of $-36, 36, 20,$ and $3,$ respectively. Figure 4(c) shows the estimation of $a_3, b_3, c_3,$ and e_{r3} , the parameters of the third system, which converges to their true values $-10, 10, 28,$ and $-8/3,$ respectively.

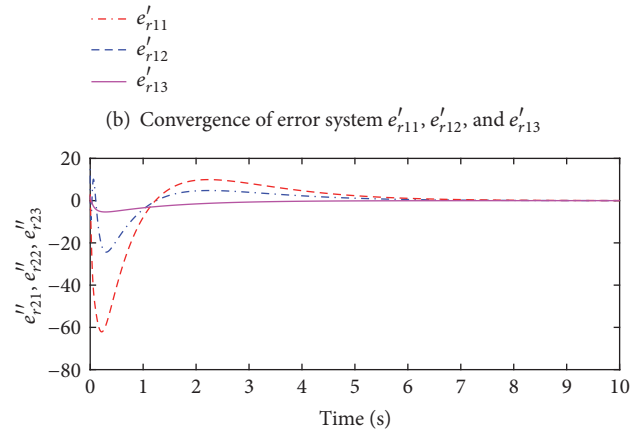
Figures 5–7 show simulation results for Example 2 with $M = 4$. The initial (starting point) conditions are chosen as



(a) Convergence of error system $e_{r11}, e_{r12}, e_{r13}, e_{r21}, e_{r22}, e_{r23}, e_{r31}, e_{r32},$ and e_{r33}



(b) Convergence of error system $e'_{r11}, e'_{r12},$ and e'_{r13}



(c) Convergence of error system $e''_{r21}, e''_{r22},$ and e''_{r23}

FIGURE 5

$(x_{11}(0) = 4, x_{12}(0) = 5, x_{13}(0) = -3), (x_{21}(0) = 5, x_{22}(0) = 2, x_{23}(0) = -5), (x_{31}(0) = 11, x_{32}(0) = 15, x_{33}(0) = 10),$ and $(x_{41}(0) = 4, x_{42}(0) = 5, x_{43}(0) = -3)$. The coupling parameters are chosen as $d_{12} = d_{22} = d_{32} = d_{13} = d_{23} = d_{33} = d_{42} = d_{43} = 0, d_{11} = d_{21} = 1$ and $d_{31} = d_{41} = -1$. Figure 5(a) shows the errors $e_{r11}, e_{r12}, e_{r13}, e_{r21}, e_{r22}, e_{r23}, e_{r31}, e_{r32},$ and e_{r33} asymptotically converge to zero. Figure 5(b) shows the errors $e'_{r11}, e'_{r12},$ and e'_{r13} asymptotically converge to zero. Figure 5(c) shows the errors $e''_{r21}, e''_{r22},$ and e''_{r23}

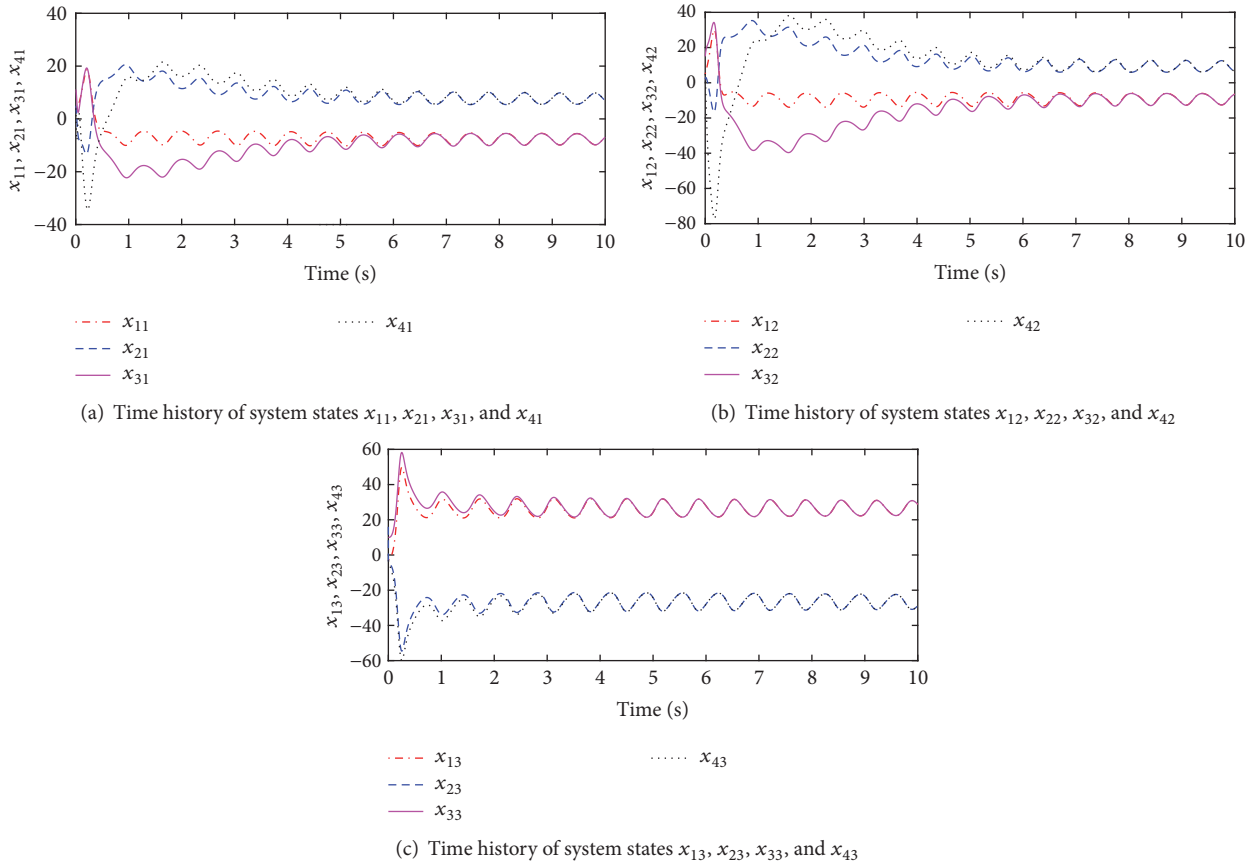
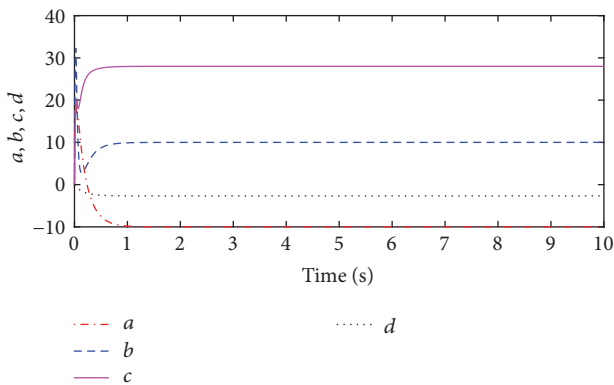


FIGURE 6



asymptotically converge to zero. Figure 6(a) shows system states x_{11} , x_{21} , x_{31} , and x_{41} , Figure 6(b) shows system states x_{12} , x_{22} , x_{32} , and x_{42} , and Figure 6(c) shows system states x_{13} , x_{23} , x_{33} , and x_{43} . From these figures we can see that systems $x_1(t)$ and $x_2(t)$, systems $x_2(t)$ and $x_3(t)$, and systems $x_3(t)$ and $x_4(t)$ achieve the antisynchronization, and systems $x_1(t)$ and $x_3(t)$ and systems $x_2(t)$ and $x_4(t)$ attained the complete synchronization and hence hybrid synchronization is attained. Figure 7 shows an adaptive estimation of parameters a , b , c ,

and d for four systems which converge to their true values of -10 , 10 , 28 , and $-8/3$ respectively.

6. Conclusion

In this article, we presented control design method for parameter identification and synchronization/antisynchronization of many attached chaotic systems connected in the ring topology. The methodology is created using adaptive integral SMC. The error system was transformed into a special structure containing nominal part and some unknown terms. The unknown terms were computed adaptively. Then the error system was stabilized using integral sliding mode control. The stabilizing controller for the error system is created that contains the nominal control and the compensator control. Simulation results show that antisynchronization and complete synchronization were achieved with the proposed control laws and that the uncertain parameters converge to their actual values.

Conflicts of Interest

The authors do not have any conflicts of interest regarding the publication of this paper.

References

- [1] L. M. Pecora and T. L. Carroll, "Synchronization in chaotic systems," *Physical Review Letters*, vol. 64, no. 8, pp. 821–824, 1990.
- [2] H. Serrano-Guerrero, C. Cruz-Hernandez, R. M. Lopez-Gutiérrez, L. Cardoza-Avendano, and R. A. Chávez-Páez, "Chaotic synchronization in nearest-neighbor coupled Networks of 3D CNNs," *Journal of Applied Research and Technology*, vol. 11, no. 1, pp. 26–41, 2013.
- [3] L. Jin, Y. Zhang, and L. Li, "One-to-many chaotic synchronization with application in wireless sensor network," *IEEE Communications Letters*, vol. 17, no. 9, pp. 1782–1785, 2013.
- [4] V. Dronov, *Application of Chaotic Synchronization and Controlling Chaos to Communications*, Diss, 2005.
- [5] S. Das, U. Halder, and D. Maity, "Chaotic dynamics in social foraging swarms-an analysis," *IEEE Transactions on Systems, Man, and Cybernetics, Part B: Cybernetics*, vol. 42, no. 4, pp. 1288–1293, 2012.
- [6] Y. Yu and H.-X. Li, "Adaptive generalized function projective synchronization of uncertain chaotic systems," *Nonlinear Analysis: Real World Applications*, vol. 11, no. 4, pp. 2456–2464, 2010.
- [7] G. M. Mahmoud, E. E. Mahmoud, and A. A. Arafat, "On projective synchronization of hyperchaotic complex nonlinear systems based on passive theory for secure communications," *Physica Scripta*, vol. 87, no. 5, Article ID 055002, 2013.
- [8] J. Zhou, J.-a. Lu, and J. Lu, "Adaptive synchronization of an uncertain complex dynamical network," *Institute of Electrical and Electronics Engineers Transactions on Automatic Control*, vol. 51, no. 4, pp. 652–656, 2006.
- [9] J. Sun, Q. Yin, and Y. Shen, "Compound synchronization for four chaotic systems of integer order and fractional order," *EPL (Europhysics Letters)*, vol. 106, no. 4, Article ID 40005, 2014.
- [10] J. Sun, Y. Shen, X. Wang, and J. Chen, "Finite-time combination-synchronization of four different chaotic systems with unknown parameters via sliding mode control," *Nonlinear Dynamics*, vol. 76, no. 1, pp. 383–397, 2014.
- [11] C. Jiang and S. Liu, "Synchronization and antisynchronization of N-coupled complex permanent magnet synchronous motor systems with ring connection," *Complexity*, vol. 2017, Article ID 6743184, 15 pages, 2017.
- [12] Q. Wei, X.-Y. Wang, and X.-P. Hu, "Hybrid function projective synchronization in complex dynamical networks," *AIP Advances*, vol. 4, no. 2, Article ID 027128, 2014.
- [13] C. Li, Q. Chen, and T. Huang, "Coexistence of anti-phase and complete synchronization in coupled chen system via a single variable," *Chaos, Solitons & Fractals*, vol. 38, no. 2, pp. 461–464, 2008.
- [14] F. Nian and W. Liu, "Hybrid synchronization of heterogeneous chaotic systems on dynamic network," *Chaos, Solitons & Fractals*, vol. 91, pp. 554–561, 2016.
- [15] S. Wang, Y. Yu, and G. Wen, "Hybrid projective synchronization of time-delayed fractional order chaotic systems," *Nonlinear Analysis: Hybrid Systems*, vol. 11, pp. 129–138, 2014.
- [16] C.-H. Chen, L.-J. Sheu, H.-K. Chen et al., "A new hyper-chaotic system and its synchronization," *Nonlinear Analysis: Real World Applications*, vol. 10, no. 4, pp. 2088–2096, 2009.
- [17] M. Hu, Z. Xu, R. Zhang, and A. Hu, "Parameters identification and adaptive full state hybrid projective synchronization of chaotic (hyper-chaotic) systems," *Physics Letters A*, vol. 361, no. 3, pp. 231–237, 2007.
- [18] X. Wu and H. Lu, "Hybrid synchronization of the general delayed and non-delayed complex dynamical networks via pinning control," *Neurocomputing*, vol. 89, pp. 168–177, 2012.
- [19] Q. Song, J. Cao, and F. Liu, "Pinning-controlled synchronization of hybrid-coupled complex dynamical networks with mixed time-delays," *International Journal of Robust and Nonlinear Control*, vol. 22, no. 6, pp. 690–706, 2012.
- [20] Y. Xu, W. Zhou, J. Fang, W. Sun, and L. Pan, "Adaptive synchronization of stochastic time-varying delay dynamical networks with complex-variable systems," *Nonlinear Dynamics*, vol. 81, no. 4, pp. 1717–1726, 2015.
- [21] W. Yu, J. Cao, and J. Lü, "Global synchronization of linearly hybrid coupled networks with time-varying delay," *SIAM Journal on Applied Dynamical Systems*, vol. 7, no. 1, pp. 108–133, 2008.
- [22] C. Jiang and S. Liu, "Generalized combination complex synchronization of new hyperchaotic complex Lü-like systems," *Advances in Difference Equations*, vol. 2015, no. 1, article no. 214, 2015.
- [23] N. Cai, Y. Jing, and S. Zhang, "Generalized projective synchronization of different chaotic systems based on antisymmetric structure," *Chaos, Solitons & Fractals*, vol. 42, no. 2, pp. 1190–1196, 2009.
- [24] I. M. Kyprianidis and I. N. Stouboulos, "Chaotic synchronization of three coupled oscillators with ring connection," *Chaos, Solitons & Fractals*, vol. 17, no. 2-3, pp. 327–336, 2003.
- [25] Q. Song and J. Cao, "Synchronization and anti-synchronization for chaotic systems," *Chaos, Solitons & Fractals*, vol. 33, no. 3, pp. 929–939, 2007.
- [26] G. M. Mahmoud and E. E. Mahmoud, "Phase and antiphase synchronization of two identical hyperchaotic complex nonlinear systems," *Nonlinear Dynamics*, vol. 61, no. 1-2, pp. 141–152, 2010.
- [27] S. B. Wang, X. Y. Wang, X. Y. Wang, and Y. F. Zhou, "Adaptive generalized combination complex synchronization of uncertain real and complex nonlinear systems," *AIP Advances*, vol. 6, no. 4, Article ID 045011, 2016.
- [28] T. Dahms, J. Lehnert, and E. Schöll, "Cluster and group synchronization in delay-coupled networks," *Physical Review E: Statistical, Nonlinear, and Soft Matter Physics*, vol. 86, no. 1, part 2, Article ID 016202, 2012.
- [29] M. Jiménez-Martín, J. Rodríguez-Laguna, O. D’Huys, J. de la Rubia, and E. Korutcheva, "Synchronization of fluctuating delay-coupled chaotic networks," *Physical Review E: Statistical, Nonlinear, and Soft Matter Physics*, vol. 95, no. 5, article 052210, 2017.
- [30] Y. Sun, W. Li, and J. Ruan, "Generalized outer synchronization between complex dynamical networks with time delay and noise perturbation," *Communications in Nonlinear Science and Numerical Simulation*, vol. 18, no. 4, pp. 989–998, 2013.
- [31] J. Lu, D. W. Ho, and J. Cao, "Synchronization in an array of nonlinearly coupled chaotic neural networks with delay coupling," *International Journal of Bifurcation and Chaos*, vol. 18, no. 10, pp. 3101–3111, 2008.
- [32] X. Chen, J. Qiu, J. Cao, and H. He, "Hybrid synchronization behavior in an array of coupled chaotic systems with ring connection," *Neurocomputing*, vol. 173, pp. 1299–1309, 2016.
- [33] V. Utkin and J. Shi, "Integral sliding mode in systems operating under uncertainty conditions," in *Proceedings of the 35th IEEE Conference on Decision and Control*, vol. 4, pp. 4591–4596, 1996.

Research Article

Fixed-Time Stability of the Hydraulic Turbine Governing System

Caoyuan Ma,¹ Chuangzhen Liu ,¹ Xuezi Zhang,¹ Yongzheng Sun ,²
Wenbei Wu ,¹ and Jin Xie¹

¹School of Electrical and Power Engineering, China University of Mining and Technology, Xuzhou 221116, China

²School of Mathematics, China University of Mining and Technology, Xuzhou 221008, China

Correspondence should be addressed to Yongzheng Sun; yzsun@cumt.edu.cn

Received 11 August 2017; Revised 16 December 2017; Accepted 21 December 2017; Published 30 January 2018

Academic Editor: Ton D. Do

Copyright © 2018 Caoyuan Ma et al. This is an open access article distributed under the Creative Commons Attribution License, which permits unrestricted use, distribution, and reproduction in any medium, provided the original work is properly cited.

This paper studies the problem of fixed-time stability of hydraulic turbine governing system with the elastic water hammer nonlinear model. To control and improve the quality of hydraulic turbine governing system, a new fixed-time control strategy is proposed, which can stabilize the water turbine governing system within a fixed time. Compared with the finite-time control strategy where the convergence rate depends on the initial state, the settling time of the fixed-time control scheme can be adjusted to the required value regardless of the initial conditions. Finally, we numerically show that the fixed-time control is more effective than and superior to the finite-time control.

1. Introduction

Hydropower, as a low-cost, zero-polluting, and renewable energy source, has been deeply developed since the twentieth century [1]. With the reserves of coal, natural gas, and other nonrenewable energy sources decreasing gradually and the serious environmental problems caused by power generation, hydropower is becoming an increasingly large proportion of the electricity structure. According to the current projections provided by international hydropower industries referring to the next thirty years, a significant growth in the sector is expected [2]. As a typical nonlinear complex system and an important part of hydraulic power generation system, hydraulic turbine governing system is a hydraulic, mechanical, electrical integrated control system [3]. The normal operation of the water turbine governing system is essential to the whole hydraulic power system, and it even affects the safe and stable operation of the related power grid, thus affecting the power quality and the power consumption experience of the users. In view of the high proportion of the hydropower system in the electricity structure, the research of the hydraulic turbine governing system is of great importance.

At present, the control method commonly used in water turbine control system mainly includes the following:

nonlinear control [4–7], sliding mode control [8–10], PID control [11–13], fuzzy control [14], fault tolerant control [15], predictive control [16, 17], and finite-time control [18]. These control methods have important theoretical and practical significance for the control of hydraulic turbine governing system, but they also have their own defects. For example, feedback control has the time delay problem. The nonlinear control is targeted, and each nonlinear control strategy is only suitable for solving some special nonlinear system control problems. PID control is difficult to balance the stability time and overshoot. When the initial state of the system deviates from the equilibrium point, it is difficult for the control system to restore the system to the equilibrium point; fuzzy control is difficult to adapt to the requirements of large-scale adjustment, and it needs to constantly adjust the control rules and parameters. The effect of fault tolerant control is greatly influenced by the delay of fault detection and separation, and the long time delay will cause serious stability problem. Predictive control's accuracy is not very high, and the optimization process needs to be performed online repeatedly; in finite-time control, the stability of the system is affected by the initial state of the system. All the above control strategies can ensure the exponential stability of the system, while the adjustment time affected by the initial state of the system is not always short enough. The

fixed-time stability control not only ensures the exponential stability and the shorter adjustment time but also has stronger robustness and disturbance rejection ability than the above control strategies.

The definition of the fixed-time stability was firstly proposed by Polyakov in [19], and this definition was evolved from the definition of finite-time stability. Finite-time control theory has been widely used in Cucker-Smale systems [20], complex dynamic network systems [21], PMSM [22], delay neural networks systems [23], chaotic systems [24], and so forth. Compared with the finite-time control, the fixed-time control has the characteristic that the maximum adjustment time is not affected by the initial conditions. In view of many advantages of fixed-time control, the control method has been widely used in multiagent systems [25], aircraft systems [26], robot systems [27], neural network systems [28–31], and chaotic systems [32, 33].

In [16], a six-dimensional nonlinear mathematical model for the elastic water hammer of hydraulic turbine governing system is presented. Based on the six-dimensional nonlinear mathematical model, this paper analyzes the system running state without controllers. Comparing the operation status of the system under the fixed-time control strategy and the finite-time control strategy, we find that the control strategy used in this paper can directly calculate the system's settling time. The settling time is independent of the initial state of the system. In conclusion, whether the initial state of the system changes or not, we can use the fixed-time control strategy to make the system achieve stable state quickly.

2. Fixed-Time Stability of Hydraulic Turbine Governing System

2.1. System Modeling and Preliminaries. For the convenience of analysis, we give some necessary definitions and lemmas in advance.

Definition 1 (see [19]). Consider the following nonlinear dynamic system:

$$\dot{x} = f(x), \quad (1)$$

where $x \in R^n$ is the system state, f is a smooth nonlinear function. If, for any initial condition, there exists a fixed settling time T_0 , which is not connected with initial condition, such that

$$\lim_{t \rightarrow T_0} \|x(t)\| = 0 \quad (2)$$

and $\|x(t)\| \equiv 0$, if $t \geq T_0$, then this nonlinear dynamic system is said to be fixed-time stable.

Lemma 2 (see [34]). *Suppose there exists a continuous function such that $V(t) : [0, \infty) \rightarrow [0, \infty)$ such that*

- (1) V is positive definite,
- (2) there exist real numbers $c > 0$ and $0 < \rho < 1$, such that

$$\dot{V}(t) \leq -cV^\rho(t), \quad t \geq t_0 \quad (3)$$

and then one has

$$V^{1-\rho}(t) \leq V^{1-\rho}(t_0) - c(1-\rho)(t-t_0), \quad t_0 \leq t \leq t^*, \quad (4)$$

$$V(t) = 0, \quad t \geq t^*,$$

of which

$$t^* = t_0 + \frac{V^{1-\rho}(t_0)}{c(1-\rho)}. \quad (5)$$

Lemma 3 (see [19]). *If there exists a continuous radically unbounded function $V : R^n \rightarrow R_+ \cup \{0\}$, such that*

- (1) $V(x) = 0 \Leftrightarrow x = 0$,
- (2) any solution $x(t)$ satisfied the inequality $D^*V(x(t)) \leq -\alpha V^p(x(t)) - \beta V^q(x(t))$ for some α, β , and $p = 1 - 1/2\gamma$, $q = 1 + 1/2\gamma$, and $\gamma > 1$, where $D^*V(x(t))$ denotes the upper right-hand derivative of the function $V(x(t))$,

Then the origin is globally fixed-time stable and the following estimate holds:

$$T(x_0) \leq T_{\max} := \frac{\pi\gamma}{\sqrt{\alpha\beta}}, \quad \forall x_0 \in R^N. \quad (6)$$

Lemma 4 (see [35]). *If $x_1, x_2, \dots, x_N \geq 0$, then*

$$\begin{aligned} \sum_{i=1}^N x_i^\eta &\geq \left(\sum_{i=1}^N x_i \right)^\eta, \quad 0 < \eta \leq 1, \\ \sum_{i=1}^N x_i^\theta &\geq N^{1-\theta} \left(\sum_{i=1}^N x_i \right)^\theta, \quad \theta > 1. \end{aligned} \quad (7)$$

2.2. Main Results. Here, we use the nonlinear model of the water turbine strike system proposed in [18]:

$$\begin{aligned} \dot{x}_1 &= x_2 \\ \dot{x}_2 &= x_3 \\ \dot{x}_3 &= -a_0x_1 - a_1x_2 - a_2x_3 + y \\ \dot{\delta} &= \omega_0\omega \\ \dot{\omega} &= \frac{1}{T_{ab}} [m_t - D\omega - P_e] \\ \dot{y} &= -\frac{y}{T_y}, \end{aligned} \quad (8)$$

where

$$\begin{aligned} P_e &= \frac{E'_q V_s}{x'_{d\Sigma}} \sin \delta + \frac{V_s^2}{2} \frac{x'_{d\Sigma} - x_{q\Sigma}}{x'_{d\Sigma} x_{q\Sigma}} \sin 2\delta \\ m_t &= b_3 y + (b_0 - a_0 b_3) x_1 + (b_1 - a_1 b_3) x_2 \\ &\quad + (b_2 - a_2 b_3) x_3 \end{aligned}$$

$$\begin{aligned}
x'_{d\Sigma} &= x'_d + x_T + \frac{1}{2}x_L \\
x_{q\Sigma} &= x_q + x_T + \frac{1}{2}x_L \\
b_0 &= \frac{24e_y}{e_{qh}h_\omega T_r^3}, \\
b_1 &= -\frac{24ee_y}{e_{qh}T_r^2}, \\
b_2 &= \frac{3e_y}{e_{qh}h_\omega T_r}, \\
b_3 &= -\frac{ee_y}{e_{qh}}, \\
a_0 &= \frac{24}{e_{qh}h_\omega T_r^3}, \\
a_1 &= \frac{24}{T_r^2}, \\
a_2 &= \frac{3}{e_{qh}h_\omega T_r}.
\end{aligned} \tag{9}$$

x_1 , x_2 , and x_3 are state variables; δ is the generator rotor angle, ω is the relative value of generator speed, y is the incremental deviation of the guide vane opening, D is generator damping coefficient, e is intermediate variable, e_{qh} is the first-order partial derivative value of flow rate with respect to water head, e_y is the first-order partial derivative value of torque with respect to wicket gate, E'_q is the transient internal voltage of the armature, h_ω is characteristic coefficient of water diversion system, m_t is torque relative value of hydraulic turbine, T_y is relay reaction time constant, x'_d is the direct axis transient reactance, x_q is the quartered axis reactance, x_T is the short circuit reactance of the transformer, x_L is the reactance of the electric transmission line, and V_s is the bus voltage at infinity.

From system (8), we can see that $P(0, 0, 0, m, 0, 0)$ is a point of equilibrium of the system, where m is a constant. In order to make the system fast and stable to the equilibrium point P , the fifth and sixth subsystems of model (8) are added with the controllers u_ω and u_y , and the controlled system is formed as follows:

$$\begin{aligned}
\dot{x}_1 &= x_2 \\
\dot{x}_2 &= x_3 \\
\dot{x}_3 &= -a_0x_1 - a_1x_2 - a_2x_3 + y \\
\dot{\delta} &= \omega_0\omega \\
\dot{\omega} &= \frac{1}{T_{ab}} [m_t - D\omega - P_e] + u_\omega \\
\dot{y} &= \frac{1}{T_y} (-y + u_y).
\end{aligned} \tag{10}$$

Theorem 5. *The hydraulic turbine governing system (10) can become stable in a fixed time, under the following controllers:*

$$\begin{aligned}
u_y &= -k_1 \text{sign}(y) |y|^\alpha - k_1 \text{sign}(y) |y|^\beta \\
u_\omega &= -\frac{m_t - P_e - b_3 \cdot y}{T_{ab}} - k_2 \text{sign}(\omega) |\omega|^\alpha \\
&\quad - k_2 \text{sign}(\omega) |\omega|^\beta,
\end{aligned} \tag{11}$$

where the parameters α and β satisfy $0 < \alpha < 1$ and $\beta > 1$ and the parameters k_1 and k_2 are tuning parameters of the terminal attractor.

Proof. Here, we use the two-step method of two steps to prove that the system is stable for the fixed time; for the sixth subsystem of system (10), we put u_y into the controlled subsystem, and we can have the following relationship:

$$\frac{dy}{dt} = \frac{1}{T_y} (-y - k_1 \text{sign}(y) |y|^\alpha - k_1 \text{sign}(y) |y|^\beta). \tag{12}$$

The Lyapunov function is constructed as follows:

$$V_1(t) = \frac{y^2}{2}. \tag{13}$$

The derivative along the trajectory of the sixth subsystem in (10) can be obtained:

$$\begin{aligned}
\frac{dV_1(t)}{dt} &= y \frac{dy}{dt} = \frac{y}{T_y} [-y - k_1 \text{sign}(y) |y|^\alpha \\
&\quad - k_1 \text{sign}(y) |y|^\beta] = -\frac{1}{T_y} (y^2 + k_1 |y|^{\alpha+1} \\
&\quad + k_1 |y|^{\beta+1}) \leq -\frac{k_1}{T_y} [(y^2)^{(\alpha+1)/2} + (y^2)^{(\beta+1)/2}] \\
&= -\frac{k_1}{T_y} \left[\left(\frac{y^2}{2} \right)^{(\alpha+1)/2} \cdot \left(\frac{1}{2} \right)^{-(\alpha+1)/2} + \left(\frac{y^2}{2} \right)^{(\beta+1)/2} \right. \\
&\quad \cdot \left(\frac{1}{2} \right)^{-(\beta+1)/2} \left. \right] = -\frac{k_1}{T_y} \cdot 2^{(\alpha+1)/2} V_1^{(\alpha+1)/2}(t) - \frac{k_1}{T_y} \\
&\quad \cdot 2^{(\beta+1)/2} V_1^{(\beta+1)/2}(t),
\end{aligned} \tag{14}$$

where

$$\begin{aligned}
m &= \frac{k_1}{T_y} \cdot 2^{(\alpha+1)/2}, \\
n &= \frac{k_1}{T_y} \cdot 2^{(\beta+1)/2}, \\
p &= \frac{\alpha + 1}{2}, \\
q &= \frac{\beta + 1}{2}.
\end{aligned} \tag{15}$$

According to Lemma 3, we know that the sixth subsystem in model (10) is stable in fixed time:

$$t_1 = \frac{\pi T_y}{k_1 (\beta - \alpha) \cdot 2^{(\alpha+\beta-2)/4}} \quad (16)$$

which means that the system state variable y satisfies the following relation $y = 0$ when $t \geq t_1$. And

$$\begin{aligned} \dot{x}_1 &= x_2 \\ \dot{x}_2 &= x_3 \\ \dot{x}_3 &= -a_0 x_1 - a_1 x_2 - a_2 x_3 \\ \dot{\delta} &= \omega_0 \omega \\ \dot{\omega} &= \frac{1}{T_{ab}} [(b_0 - a_0 b_3) x_1 + (b_1 - a_1 b_3) x_2 \\ &\quad + (b_2 - a_2 b_3) x_3 - D\omega - P_e] + u_\omega. \end{aligned} \quad (17)$$

To this end, we select the following Lyapunov function:

$$V_2(t) = \frac{\omega^2}{2}. \quad (18)$$

Thus,

$$\begin{aligned} \frac{dV_2(t)}{dt} &= \omega \frac{d\omega}{dt} = \omega \left[-\frac{D\omega}{T_{ab}} - k_2 \text{sign}(\omega) |\omega|^\alpha \right. \\ &\quad \left. - k_2 \text{sign}(\omega) |\omega|^\beta \right] = -\frac{D\omega^2}{T_{ab}} - k_2 |\omega|^{\alpha+1} \\ &\quad - k_2 |\omega|^{\beta+1} \leq -k_2 |\omega|^{\alpha+1} - k_2 |\omega|^{\beta+1} \\ &= -k_2 \left[2^{(\alpha+1)/2} \cdot \left(\frac{\omega^2}{2} \right)^{(\alpha+1)/2} + 2^{(\beta+1)/2} \right. \\ &\quad \left. \cdot \left(\frac{\omega^2}{2} \right)^{(\beta+1)/2} \right] = -k_2 \cdot 2^{(\alpha+1)/2} V_2^{(\alpha+1)/2}(t) - k_2 \\ &\quad \cdot 2^{(\beta+1)/2} V_2^{(\beta+1)/2}(t), \end{aligned} \quad (19)$$

where

$$\begin{aligned} m &= k_2 \cdot 2^{(\alpha+1)/2}, \\ n &= k_2 \cdot 2^{(\beta+1)/2}, \\ p &= \frac{\alpha+1}{2}, \\ q &= \frac{\beta+1}{2}. \end{aligned} \quad (20)$$

According to Lemma 3, we can show that the fourth and fifth subsystems in model (10) are stable in fixed time:

$$t_2 = \frac{\pi}{k_2 (\beta - \alpha) \cdot 2^{(\alpha+\beta-2)/4}} \quad (21)$$

which means that when $t \geq t_2$, then $\omega = 0$ and $\dot{\delta} = 0$. In other words, when $t \geq t_1 + t_2$, the value of δ tends to be stable.

To sum up, when $t \geq t_3$, where $t_3 = t_1 + t_2 + \Delta t$ and Δt is the time from $y = 0$ to u_ω acting on model (10), the hydraulic turbine governing system (10) is stable under the controllers u_y and u_ω . That is, the system is stable in a fixed time, and the theorem is proved. \square

3. Numerical Simulations

In this section, numerical results are provided to verify the theoretical results. The system parameters and controller parameters in this paper are $\omega_0 = 314$, $T_{ab} = 8.0$, $D = 0.5$, $E'_q = 1.35$, $x'_{d\Sigma} = 1.15$, $x_{q\Sigma} = 1.474$, $T_y = 0.1$, $V_s = 1.0$, $e_{qh} = 0.5$, $e_y = 1.0$, $T_r = 1.0$, $h_\omega = 2.0$, $r = 0$, $a_0 = 24$, $a_1 = 24$, $a_2 = 3$, $b_0 = 24$, $b_1 = 33.6$, $b_2 = 3$, and $b_3 = -1.4$, respectively. The simulation sampling time is 0.0001 s, and the initial states are $(x_1, x_2, x_3, \delta, \omega, y) = (0.1, 0.1, 0.1, 0.1, 0.1, 0.1)$.

Figures 1(a)–1(c) are the response curves of the system variables δ , ω , and y when the hydraulic turbine governing system is not controlled. From Figure 1, it is clear that the steady state of the system state variable y is about 0.6 s before being controlled. The state of the system variables δ and ω are aperiodic and are always in a state of instability.

Figures 2(a)–2(b) are the response curves of the fixed-time controllers u_ω and u_y , respectively. In this simulation, u_y acts on the hydraulic turbine governing system in 0.3 s, and u_ω acts on the hydraulic turbine governing system in 0.75 s. Figures 3(a)–3(c) are the response curves of the system variables δ , ω , and y after the fixed-time controllers u_y and u_ω are applied to the hydraulic turbine governing system, respectively. From Figure 3, it is clear that when the system is coupled with u_y in 0.3 s and u_ω in 0.75 s, the system state variable y reaches a stable state at 0.326 s, and the system state variables δ and ω achieve stable state at 2 s, simultaneously. The simulation results show that the system can achieve a stable state in a short time by fixed-time controllers, and the control effect is achieved.

In order to make a fair comparison between fixed-time control and finite-time control, the parameters, initial conditions, and the tuning parameters of the terminal attractor are the same in this paper. Figures 4(a)–4(c) are the comparison of response curves of system state variables δ , ω , and y with fixed-time controllers and finite-time controllers, respectively. From Figure 4, it is obvious that the settling time of system state variable y under the action of fixed-time controllers is mostly equal to the settling time of system state variable y under the action of the finite-time controllers. The system state variables δ and ω achieve stable state at 2 s under the action of fixed-time controllers, simultaneously. And the system state variables δ and ω achieve stable state at 2.07 s under the action of finite-time controllers, simultaneously. The fixed-time controllers stabilize the nonlinear system faster than finite-time controllers do. Thus, the fixed-time method has the better capacity to handle a nonlinear system in a short time.

To explore the relationship between the settling time and the values of the parameters α and β experimentally, we

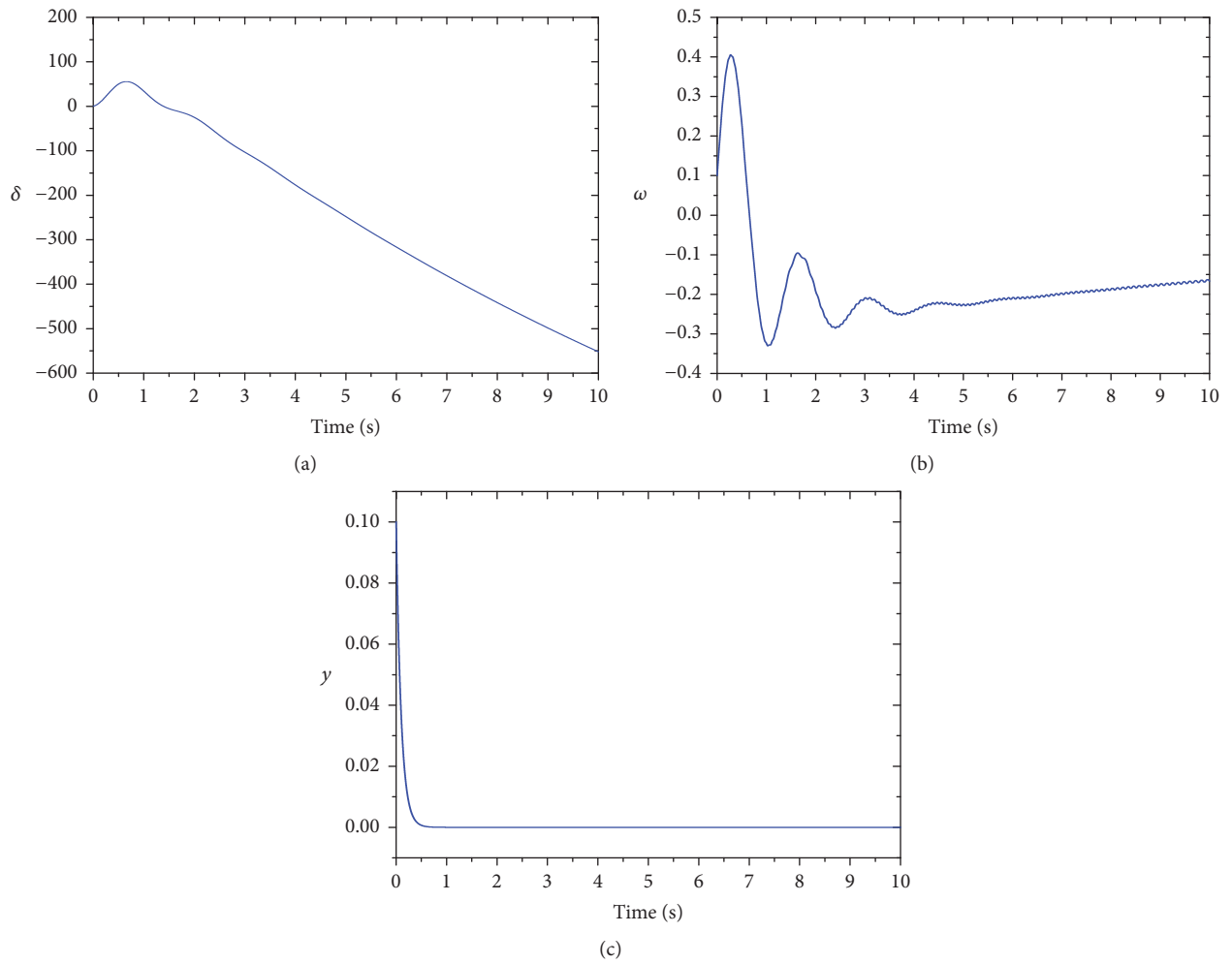


FIGURE 1: The response of the system without controller.

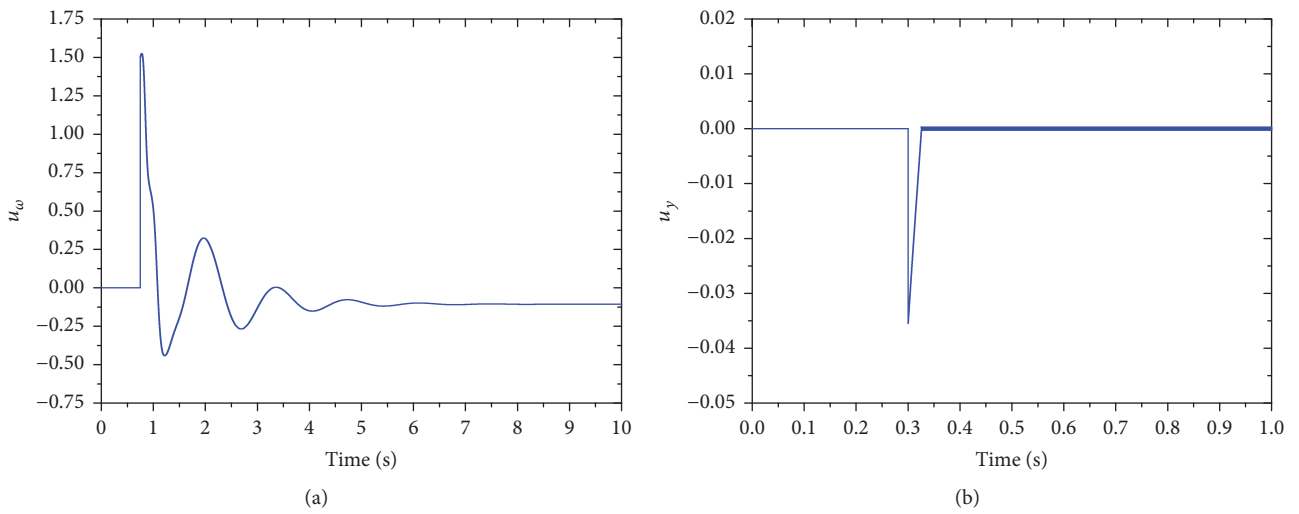


FIGURE 2: The response of the fixed-time controllers u_ω and u_y .

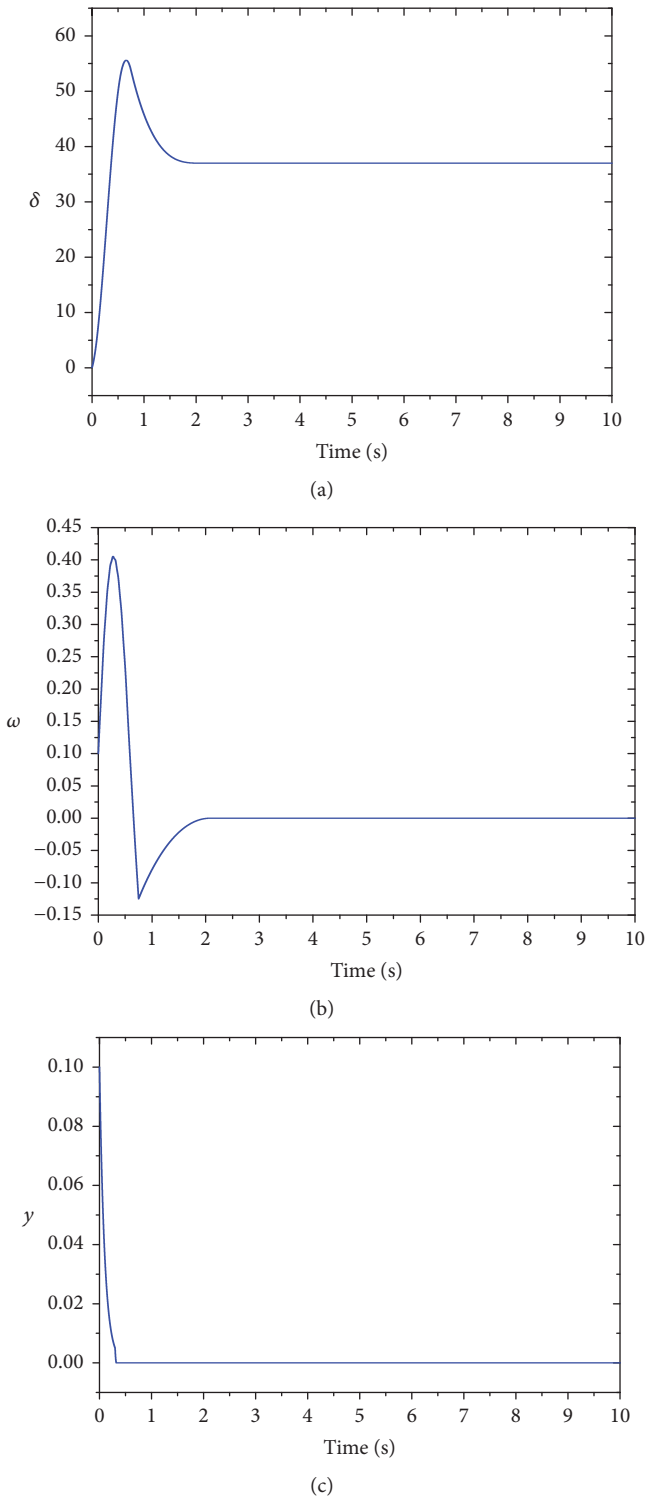


FIGURE 3: The response of the system with fixed-time controllers.

select system state variables δ , ω , and y to demonstrate the settling time. Figures 5(a)–5(c) and Figures 6(a)–6(c) are, respectively, the effects of different control parameters α and β on the state variables δ , ω , and y under the fixed-time controllers. In Figure 5, the parameter values are $\beta = 1.5$ and $\alpha = 0.3, 0.4, 0.5, 0.6, 0.7$. In Figure 6, the parameter values

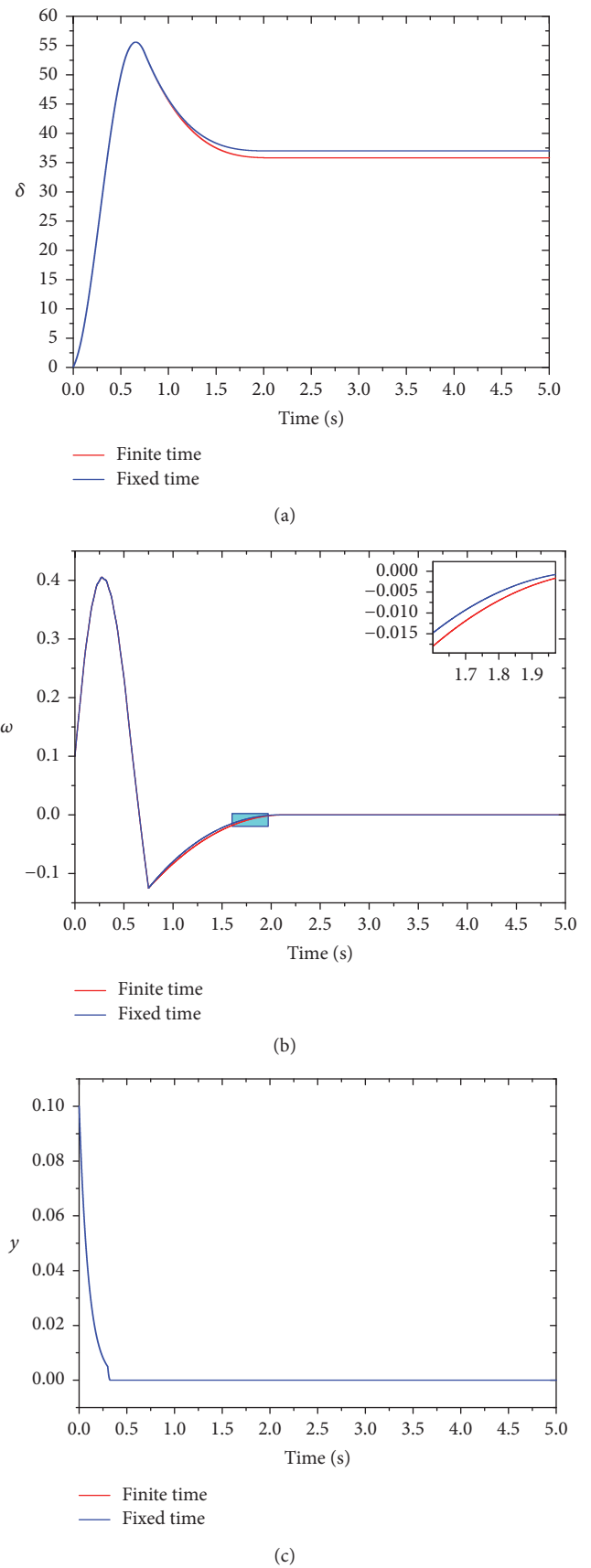


FIGURE 4: Comparison of converging speed of fixed-time and finite-time controllers.

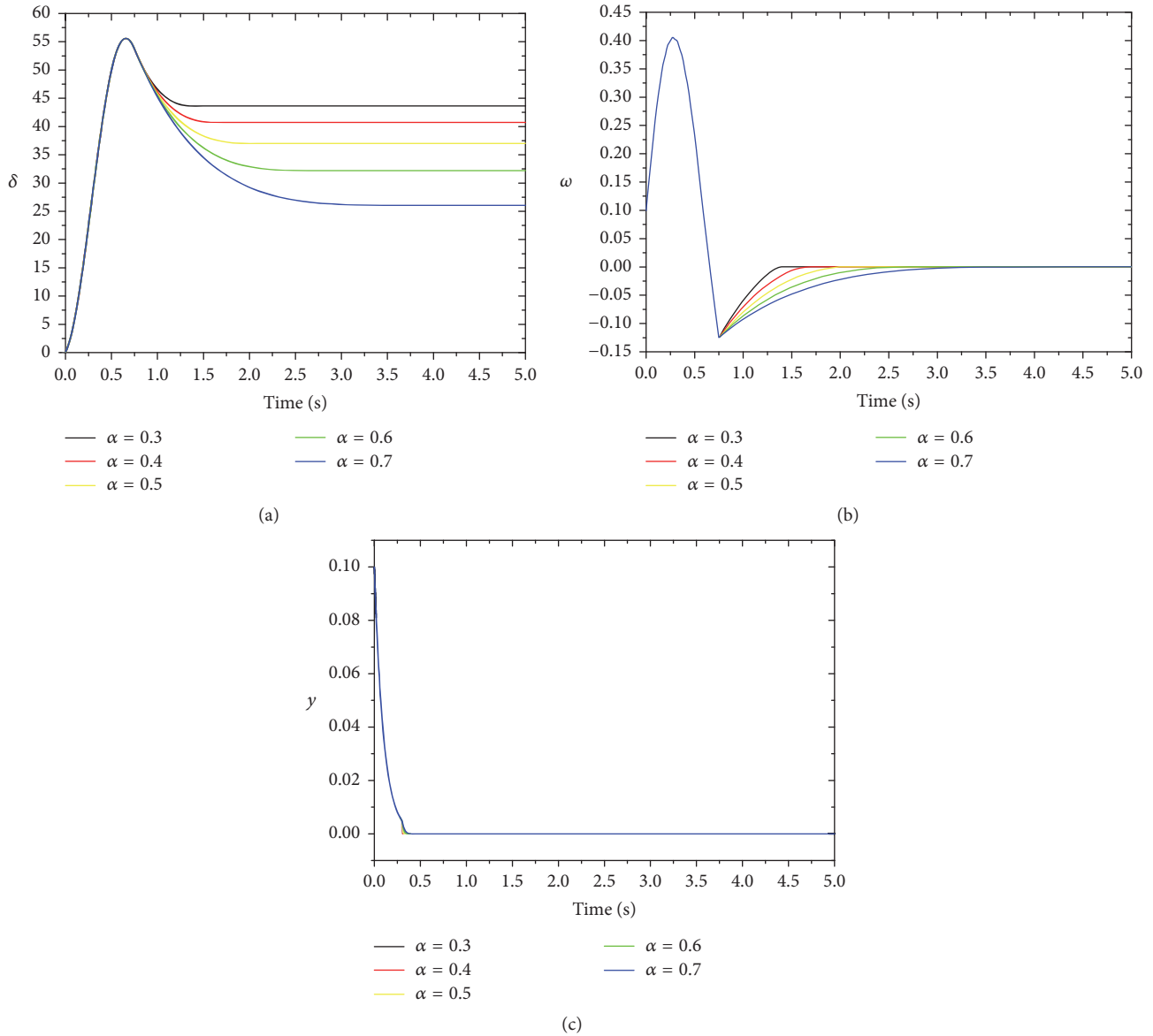


FIGURE 5: Response of α of the system controlled by fixed-time controllers.

are $\alpha = 0.5$ and $\beta = 1.1, 1.3, 1.5, 1.7, 1.9$. In Figures 5 and 6, the system parameters and other controller parameters and tuning parameters of the terminal attractor are consistent with the previous sections. The simulation results clearly show that changing the controller parameters α and β can change the time of the system state variables δ and ω to reach the steady state. But the time of the system state variable y to reach the steady state is almost the same. And the smaller the α and β value of the system are, the faster the settling time will be. Moreover, the influence of β on the settling time of the system state variables δ and ω is less than the influence of α on the settling time of the system state variables δ and ω . The simulation results are consistent with the theoretical analysis of the maximum stable time t_3 of the system in the previous section. Moreover, the values of α and β also affect the stability value of the system state variable δ . That is to

say, we can get the size of the system state variable δ to the numerical value we need by controlling the size of α and β .

In order to explore the effect of the initial state of hydropower system with fixed-time controllers, we compared the response of three different initial conditions of the hydropower system. Figures 7(a)–7(c) show the response of the system state variables δ , ω , and y at different initial conditions with the fixed-time controllers u_ω and u_y , respectively. From Figures 7(a)–7(c), it is clear that when the initial states of system are $S1 = (0.08, 0.08, 0.08, 0.08, 0.08, 0.08)$, $S2 = (0.1, 0.1, 0.1, 0.1, 0.1, 0.1)$, and $S3 = (0.12, 0.12, 0.12, 0.12, 0.12, 0.12)$ and the system is coupled with u_y at 0.3 s and u_ω at 0.75 s, the system state variables δ are stable at 1.92 s, 2 s, and 2.22 s, respectively. The system states variables ω are also stable at 1.92 s, 2 s, and 2.22 s, respectively. The system state variables y are all stable

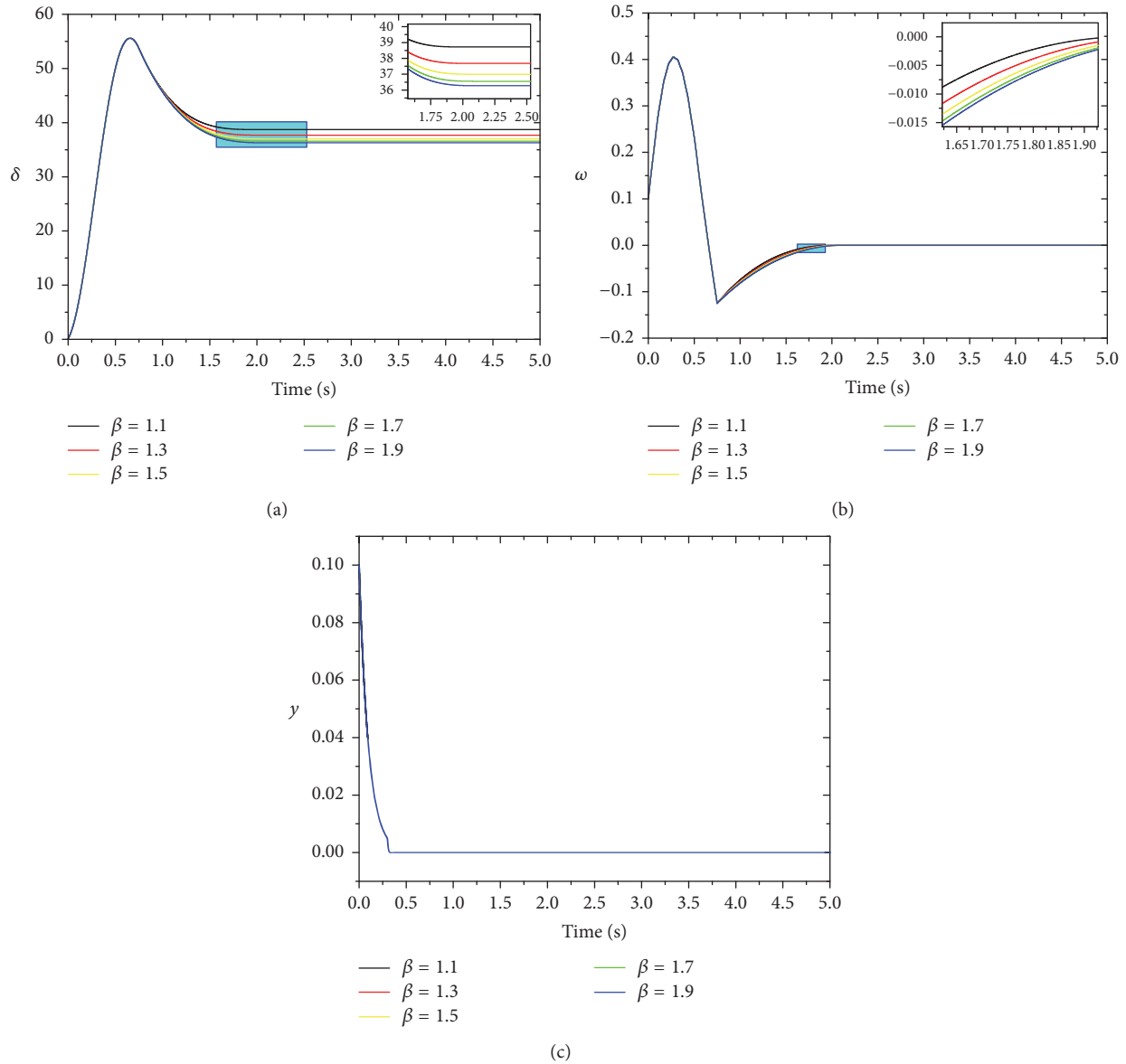


FIGURE 6: Response of β of the system controlled by fixed-time controllers.

at 0.326 s. These simulation results show that when the initial state of the system changes, the settling times of the system state variables have changed, but they are not more than theoretical deduction time t_3 . That is to say, the simulation results are consistent with the theoretical derivation.

4. Conclusions

In this paper, to ensure the safe and stable operation of hydraulic turbine governing system, a new control method based on the fixed-time theory is proposed. Compared with the finite-time control method, the hydraulic turbine governing system under the fixed-time controllers has more advantages: better robustness, fast response ability, and the setting time to reach the stable state being regardless of the initial state. Finally, the effectiveness and superiority of

the proposed control method are verified by the simulation results. Note that time delay may influence the dynamic behavior of the system; the fixed-time control of hydraulic turbine governing system with time delay is our future direction.

Conflicts of Interest

The authors declare no conflicts of interest regarding the publication of this paper.

Authors' Contributions

Caoyuan Ma, Yongzheng Sun, and Chuangzhen Liu conceived and designed the experiments; Chuangzhen Liu, Xuezi Zhang, Wenbei Wu, and Jin Xie performed the experiments

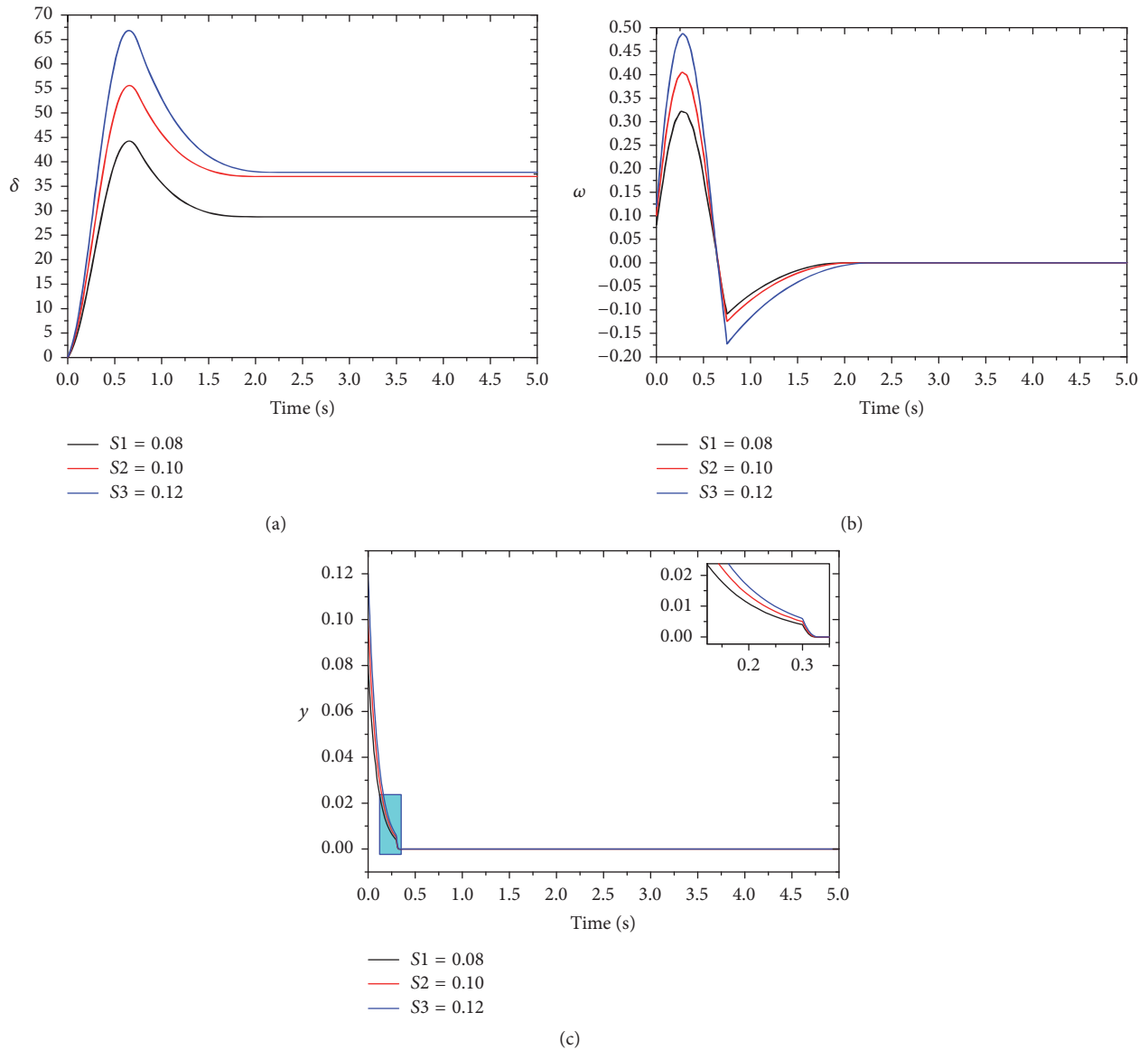


FIGURE 7: The response of the system with the different S .

and analyzed the data; Chuangzhen Liu and Xuezi Zhang wrote the paper.

Acknowledgments

This work is supported by the Fundamental Research Funds for the Central Universities (Grant no. 2017XKZD11).

References

- [1] R. E. Grumbine and J. Xu, "Mekong hydropower development," *Science*, vol. 332, no. 6026, pp. 178-179, 2011.
- [2] B. Xu, D. Chen, H. Zhang, F. Wang, X. Zhang, and Y. Wu, "Hamiltonian model and dynamic analyses for a hydro-turbine governing system with fractional item and time-lag," *Communications in Nonlinear Science and Numerical Simulation*, vol. 47, pp. 35-47, 2017.
- [3] D. J. Ling and Y. Tao, "An analysis of the Hopf bifurcation in a hydroturbine governing system with saturation," *IEEE Transactions on Energy Conversion*, vol. 21, no. 2, pp. 512-515, 2006.
- [4] H. Mesnage, M. Alami, N. Perrissin-Fabert, and Q. Alloin, "Nonlinear model-based control for minimum-time start of hydraulic turbines," *European Journal of Control*, vol. 34, pp. 24-30, 2017.
- [5] W. C. Guo, J. D. Yang, M. J. Wang, and X. Lai, "Nonlinear modeling and stability analysis of hydro-turbine governing system with sloping ceiling tailrace tunnel under load disturbance," *Energy Conversion and Management*, vol. 106, pp. 127-138, 2015.
- [6] D. Chen, C. Ding, Y. Do, X. Ma, H. Zhao, and Y. Wang, "Nonlinear dynamic analysis for a Francis hydro-turbine governing system and its control," *Journal of The Franklin Institute*, vol. 351, no. 9, pp. 4596-4618, 2014.

- [7] H. H. Li, D. Y. Chen, H. Zhang, F. Wang, and D. Ba, "Nonlinear modeling and dynamic analysis of a hydro-turbine governing system in the process of sudden load increase transient," *Mechanical Systems and Signal Processing*, vol. 80, pp. 414–428, 2016.
- [8] C. Xu and D. Qian, "Governor design for a hydropower plant with an upstream surge tank by GA-based Fuzzy reduced-order sliding mode," *Energies*, vol. 8, no. 12, pp. 13442–13457, 2015.
- [9] X. Yuan, Z. Chen, Y. Yuan, and Y. Huang, "Design of fuzzy sliding mode controller for hydraulic turbine regulating system via input state feedback linearization method," *Energy*, vol. 93, pp. 173–187, 2015.
- [10] X. Yuan, Z. Chen, Y. Yuan, Y. Huang, X. Li, and W. Li, "Sliding mode controller of hydraulic generator regulating system based on the input/output feedback linearization method," *Mathematics and Computers in Simulation*, vol. 119, pp. 18–34, 2016.
- [11] C. Li, N. Zhang, X. Lai, J. Zhou, and Y. Xu, "Design of a fractional-order PID controller for a pumped storage unit using a gravitational search algorithm based on the Cauchy and Gaussian mutation," *Information Sciences*, vol. 396, pp. 162–181, 2017.
- [12] Y. Xu, J. Zhou, X. Xue, W. Fu, W. Zhu, and C. Li, "An adaptively fast fuzzy fractional order PID control for pumped storage hydro unit using improved gravitational search algorithm," *Energy Conversion and Management*, vol. 111, pp. 67–78, 2016.
- [13] C. Li, Y. Mao, J. Zhou, N. Zhang, and X. An, "Design of a fuzzy-PID controller for a nonlinear hydraulic turbine governing system by using a novel gravitational search algorithm based on Cauchy mutation and mass weighting," *Applied Soft Computing*, vol. 52, pp. 290–305, 2017.
- [14] S. Simani, S. Alvisi, and M. Venturini, "Data-driven design of a fault tolerant fuzzy controller for a simulated hydroelectric system," *IFAC-PapersOnLine*, vol. 28, no. 21, pp. 1090–1095, 2015.
- [15] S. Simani, S. Alvisi, and M. Venturini, "Fault tolerant control of a simulated hydroelectric system," *Control Engineering Practice*, vol. 51, pp. 13–25, 2016.
- [16] R. Zhang, D. Chen, and X. Ma, "Nonlinear predictive control of a hydropower system model," *Entropy*, vol. 17, no. 9, pp. 6129–6149, 2015.
- [17] Z. Xiao, S. Meng, N. Lu, and O. P. Malik, "One-Step-Ahead Predictive Control for Hydroturbine Governor," *Mathematical Problems in Engineering*, vol. 2015, Article ID 382954, 2015.
- [18] B. Wang, L. Yin, S. Wang, S. Miao, T. Du, and C. Zuo, "Finite time control for fractional order nonlinear hydroturbine governing system via frequency distributed model," *Advances in Mathematical Physics*, vol. 2016, Article ID 7345325, 2016.
- [19] A. Polyakov, "Nonlinear feedback design for fixed-time stabilization of linear control systems," *Institute of Electrical and Electronics Engineers Transactions on Automatic Control*, vol. 57, no. 8, pp. 2106–2110, 2012.
- [20] Y. Sun and W. Lin, "A positive role of multiplicative noise on the emergence of flocking in a stochastic Cucker-Smale system," *Chaos: An Interdisciplinary Journal of Nonlinear Science*, vol. 25, no. 8, Article ID 083118, 2015.
- [21] Y. Z. Sun, S. Y. Leng, Y. C. Lai, C. Grebogi, and W. Lin, "Closed-loop control of complex networks: a trade-off between time and energy," *Physical Review Letters*, vol. 119, no. 19, Article ID 198301, 2017.
- [22] Y. Sun, X. Wu, L. Bai, Z. Wei, and G. Sun, "Finite-time synchronization control and parameter identification of uncertain permanent magnet synchronous motor," *Neurocomputing*, 2015.
- [23] J. Huang, C. Li, T. Huang, and X. He, "Finite-time lag synchronization of delayed neural networks," *Neurocomputing*, vol. 139, pp. 145–149, 2014.
- [24] J. Wu, Z.-c. Ma, Y.-z. Sun, and F. Liu, "Finite-time synchronization of chaotic systems with noise perturbation," *Kybernetika*, vol. 51, no. 1, pp. 137–149, 2015.
- [25] H. F. Hong, W. W. Yu, G. H. Wen, and X. H. Yu, "Distributed robust fixed-time consensus for nonlinear and disturbed multiagent systems," *IEEE Transactions on Systems, Man, and Cybernetics: Systems*, vol. 47, no. 7, pp. 1464–1473, 2017.
- [26] J. Gao and Y. Cai, "Fixed-time control for spacecraft attitude tracking based on quaternion," *Acta Astronautica*, vol. 115, article no. 5463, pp. 303–313, 2015.
- [27] Y. N. Yang, C. C. Hua, J. P. Li, and X. P. Guan, "Fixed-time coordination control for bilateral telerobotics system with asymmetric time-varying delays," *Journal of Intelligent Robotic Systems*, vol. 86, no. 3-4, pp. 447–466, 2017.
- [28] X. Ding, J. Cao, A. Alsaedi, F. E. Alsaedi, and T. Hayat, "Robust fixed-time synchronization for uncertain complex-valued neural networks with discontinuous activation functions," *Neural Networks*, vol. 90, pp. 42–55, 2017.
- [29] C. Hu, J. Yu, Z. Chen, H. Jiang, and T. Huang, "Fixed-time stability of dynamical systems and fixed-time synchronization of coupled discontinuous neural networks," *Neural Networks*, vol. 89, pp. 74–83, 2017.
- [30] J. D. Cao and R. X. Li, "Fixed-time synchronization of delayed memristor-based recurrent neural networks," *Science China Information Sciences*, vol. 60, no. 3, Article ID 032201, 2017.
- [31] Y. Wan, J. Cao, G. Wen, and W. Yu, "Robust fixed-time synchronization of delayed Cohen-Grossberg neural networks," *Neural Networks*, vol. 73, pp. 86–94, 2016.
- [32] J. Ni, L. Liu, C. Liu, X. Hu, and S. Li, "Fast fixed-time nonsingular terminal sliding mode control and its application to chaos suppression in power system," *IEEE Transactions on Circuits and Systems II: Express Briefs*, vol. 64, no. 2, pp. 151–155, 2017.
- [33] J. Ni, L. Liu, C. Liu, X. Hu, and T. Shen, "Fixed-time dynamic surface high-order sliding mode control for chaotic oscillation in power system," *Nonlinear Dynamics*, vol. 86, no. 1, pp. 401–420, 2016.
- [34] S. P. Bhat and D. S. Bernstein, "Finite-time stability of continuous autonomous systems," *SIAM Journal on Control and Optimization*, vol. 38, no. 3, pp. 751–766, 2000.
- [35] H. K. Khalil, and J.W.Grizzle, *Nonlinear systems third edition*, Prentice Hall, Upper Saddle River, 2002.

Research Article

Adaptive Backstepping Based MTPA Sensorless Control of PM-Assisted SynRM with Fully Uncertain Parameters

Yang Yu ¹, Da Chang,¹ Xiaoming Zheng,² Zengqiang Mi,² Xiaolong Li,³ and Chenjun Sun³

¹Hebei Key Laboratory of Distributed Energy Storage and Micro-Grid, North China Electric Power University, Baoding, Hebei 071003, China

²State Key Laboratory of Alternate Electrical Power System with Renewable Energy Sources, North China Electric Power University, Baoding 071003, China

³Department of Technology and Information, State Grid Hebei Electric Power Company, Shijiazhuang, Hebei 050022, China

Correspondence should be addressed to Yang Yu; ncepu_yy@163.com

Received 5 September 2017; Revised 3 December 2017; Accepted 25 December 2017; Published 29 January 2018

Academic Editor: Ton D. Do

Copyright © 2018 Yang Yu et al. This is an open access article distributed under the Creative Commons Attribution License, which permits unrestricted use, distribution, and reproduction in any medium, provided the original work is properly cited.

A nonlinear and robust adaptive backstepping based maximum torque per ampere speed sensorless control scheme with fully uncertain parameters is proposed for a permanent magnet-assisted synchronous reluctance motor. In the design of the controller, the relation to d - q -axis currents constrained by maximum torque per ampere control is firstly derived. Then, a fully adaptive backstepping control method is employed to design control scenario and the stability of the proposed control scenario is proven through a proper Lyapunov function candidate. The derived controller guarantees tracking the reference signals of change asymptotically and has good robustness against the uncertainties of motor parameters and the perturbation of load torque. Moreover, in allusion to the strong nonlinearity of permanent magnet-assisted synchronous reluctance motor, an active flux based improved reduced-order Luenberger speed observer is presented to estimate the speed. Digital simulations testify the feasibility and applicability of the presented control scheme.

1. Introduction

Drive system is vital for various industrial applications. One of the important trends for the drive field is that direct current (DC) motor drive systems are being replaced by alternate current (AC) motor drive system due to low cost, convenient control, and superior performance of AC motor drive systems. A permanent magnet-assisted synchronous reluctance motor (PMA-SynRM) based drive system is a unique state-of-the-art technology, where permanent magnets are equipped in magnetic barrier of rotor. Permanent magnet synchronous motor (PMSM) incorporated with synchronous reluctance motor makes PMA-SynRM appeal to the public in high efficiency, good utilization of the inverter, and wide range of flux-weak regulation. The uniqueness in structure of PMA-SynRM attracts the investigator's attention of optimizing the design of motor body and putting forward more diverse and fascinating structures [1, 2].

As for its control, it is a bottleneck problem researched insufficiently. The synchronous change of speed and frequency for PMA-SynRM makes speed be regulated by adjusting voltage or frequency, which leads to three commonly used approaches to control: voltage-to-frequency control (VFC), direct torque control (DTC), and vector control (VC). VFC is a scalar and open-loop control, and its voltage regulated by space vector modulation always follows the change of given value. Low cost and ease of use are the prominent superiorities of VFC [3]. However, the weaknesses of slow response, poor performance of control, and insufficient utilization of torque hinder its successful development. Takahashi and Noguchi [4] and Depenbrock [5] studied DTC about 30 years ago, which was applied to control asynchronous motor first and was gradually introduced in PMSM until it had been developed and matured [6]. In terms of space vector and stator flux orientation, a hysteresis comparator is designed to control flux and torque. Through comparison of feedback

value and given value in flux and torque, respectively, the states of converter switches are produced and torque output with high performance and rapid response is gained ultimately. Definite physical meaning of control signals and quick torque response are the remarkable assets for DTC. But torque ripple, current impulse, and massive online computations restrict its application [7]. VC is originated from the principle of flux orientation and enables controlling flux and torque to be decoupled like DC motor [8]. Therefore, it is famous for flexibility, high accuracy, and stable performance in low speed. For PMA-SynRM, maximum torque per ampere (MTPA) vector control has great advantages of large torque in low speed, small capacity in inverter unit, and facility to utilize reluctance torque compared to $i_d = 0$ vector control [9, 10]. The essence of MTPA control is to allocate d - q -axis currents appropriately. The relationship of constrained d - q -axis currents in MTPA principle is multiple, high-order, and nonlinear. The d - q -axis reference currents predetermined through offline method are a good solution. One of the representative offline methods is look-up table method [11], which is easy to execute but adds burden to store and requires extra offline effort [12]. Additionally, conventional MTPA control relies heavily on precise modeling parameters. Variation of parameters directly worsens its control performance. Especially for PMA-SynRM, previous investigations clearly demonstrate that its resistance, inductance, and flux linkage are directly related to operating temperature [13]. Hence, research on MTPA control with uncertain parameters is a hot and thorny issue. Niazi and Toliyat [14] estimated d - q -axis inductances and flux linkage of PMA-SynRM under multiple reference frame and [15] proposed a robust MTPA control scheme of PMA-SynRM for variation of d - q -axis inductances. The actuality is that only partial system uncertainties are considered, which desires the other system parameters to be known.

Backstepping control (BC) is a new style recursive technology for uncertain nonlinear plant [16, 17]. With the aid of virtual control variables and plenty of recursive steps, the ultimate controller can be completed systematically and original high-order plant is reduced to a lower dimension. Furthermore, integration of backstepping control with adaptive control and uncertain plant parameters can be estimated through selecting a suitable Lyapunov function. A robust nonlinear controller based on BC and MTPA has been proposed for speed control of interior PMSM [18, 19]. Nevertheless, to the best of our knowledge, previous researches on employment of BC into PMA-SynRM have not been found. A majority of control schemes utilize conventional PID control [20]. Moreover, three intrinsic deficiencies in traditional BC should be mentioned as follows:

- (A1) Linear treatment of uncertain plant parameters results in solving highly complicated regression matrices in the design of control; utilization of various linearization theories may ignore some beneficial nonlinearities of the plant.
- (A2) Partial parameters uncertainties considered cause to the designed control scenario vulnerable to variation of extra values.

- (A3) Determination of control parameters in the last time derivative of ultimate Lyapunov function requires the positive definite terms which only include partial model information. Once the derivative is induced to be positive definite by these positive terms, the asymptotic stability of the controller will be damaged and unfortunately it is nearly impossible to discover.

The innovation of the study is firstly to propose a new nonlinear and fully adaptive BC approach with no problems of overparameterization and singularity for an uncertain PMA-SynRM and hence (A1) is excluded. Previous researches such as that in [21] cannot resolve full parameter uncertainties, and the problems of overparameterization and singularity cannot be complete to be coped with. Furthermore, the paper enables overcoming the shortcomings of conventional BC, and totally seven parameter uncertainties of six motor parameters and one load parameter are taken into account, which construct a full adaptive structure and eliminate (A2) and (A3). Merely the number of pole pairs is considered to be known, due to the fact that it does not change in operation and can be acquired from nameplate. The other novelty in the context is that adaptive BC is introduced into MTPA control through implicit and symbolic computation methodology. Additionally, an active flux based improved reduced-order Luenberger speed observer is developed to estimate the speed of PMA-SynRM, resisting its strong and high nonlinearity of dynamic model. The remainder of the paper is arranged as follows: the dynamics of PMA-SynRM with fully uncertain parameters are introduced in Section 2. The relation constrained in d - q -axis currents under MTPA control is explicitly derived in Section 3. Section 4 discloses the design scenario of the proposed controller with relation to Lyapunov stability analysis. An improved Luenberger speed observer on the basis of active flux is developed in Section 5 to estimate the speed. The effectiveness and correctness of the proposed algorithm are validated in Section 6 and the simulation results are discussed. The final section sums up the paper.

2. Dynamics of PMA-SynRM with Fully Uncertain Parameters

The model of a typical PMA-SynRM is expressed in rotating d - q -axis coordinate system as follows [22]:

Stator Voltage Equations

$$\begin{aligned} u_d &= R_s i_d + \frac{d\psi_d}{dt} - n_p \omega_r \psi_q, \\ u_q &= R_s i_q + \frac{d\psi_q}{dt} + n_p \omega_r \psi_d. \end{aligned} \quad (1)$$

Flux Linkage Equations

$$\begin{aligned} \psi_d &= L_d i_d, \\ \psi_q &= L_q i_q - \psi_f. \end{aligned} \quad (2)$$

(3)

Electromagnetic Torque

$$T_e = \frac{3}{2} \frac{n_p}{2} [\psi_f i_d + (L_d - L_q) i_d i_q]. \quad (4)$$

Thus, the dynamic model of a PMA-SynRM can be described as

$$\frac{di_d}{dt} = -\frac{R_s}{L_d} i_d + \frac{n_p L_q}{L_d} \omega_r i_q - \frac{n_p \psi_f}{L_d} \omega_r + \frac{1}{L_d} u_d, \quad (5)$$

$$\frac{di_q}{dt} = -\frac{R_s}{L_q} i_q - \frac{n_p L_d}{L_q} \omega_r i_d + \frac{1}{L_q} u_q, \quad (6)$$

$$\frac{d\omega_r}{dt} = \frac{1}{J_m} (T_e - B_m \omega_r - T_L), \quad (7)$$

where i_d and i_q are the d - q -axis currents, u_d and u_q are the d - q -axis voltages, ψ_d and ψ_q are the d - q -axis flux linkages, L_d and L_q are the d - q -axis inductors, R_s is the stator resistance, n_p is the number of pole pairs, ω_r is the mechanical speed of rotor, ψ_f is the flux linkage of permanent magnet, J_m is the moment of inertia of rotor, B_m is the viscous damping coefficient, and T_L is the load torque denoting external torque disturbance.

Due to the existence of product terms between electrical stator currents and mechanical rotor speed in (5) and (6), PMA-SynRM as an electromechanical coupling system belongs to a highly nonlinear plant. With regard to the various electrical parameters R_s , L_d , L_q , and ψ_f , it should be noted that they could be directly measured or calculated, but their values may vary with operating and experimental conditions such as temperature, humidity, and flux saturation. The remaining mechanical parameters J_m and B_m are even more difficult, which are improbable to measure or calculate. The final load torque T_L is frequently uncertain. It follows that PMA-SynRM suffers from inevitable parameter uncertainties and immeasurable disturbances. For this purpose, nonlinear adaptive control should be introduced to eliminate uncertainties and reject disturbances.

3. Parameter Constraint Relation in MTPA Control

The key of MTPA is to pursue electromagnetic torque as large as possible through reasonable distribution of d - q -axis stator currents. This problem can be transformed into an extreme problem in the following:

$$\begin{aligned} \min: \quad & i_s = \sqrt{i_d^2 + i_q^2}, \\ \text{condition:} \quad & T_e = \frac{3}{2} \frac{n_p}{2} [\psi_f i_d + (L_d - L_q) i_d i_q], \end{aligned} \quad (8)$$

where i_s is the stator current.

Through introduction of a Lagrangian multiplier ξ , the extreme problem given in (8) is converted into an auxiliary function solution problem in the following:

$$F = \sqrt{i_d^2 + i_q^2} + \xi \left\{ T_e - \frac{3}{2} \frac{n_p}{2} [\psi_f i_d + (L_d - L_q) i_d i_q] \right\}. \quad (9)$$

Using partial derivatives of i_d , i_q , and ξ in (9), respectively, we can obtain

$$\begin{aligned} \frac{\partial F}{\partial i_d} &= \frac{i_d}{\sqrt{i_d^2 + i_q^2}} - \frac{3}{4} \xi n_p [\psi_f + (L_d - L_q) i_q], \\ \frac{\partial F}{\partial i_q} &= \frac{i_q}{\sqrt{i_d^2 + i_q^2}} - \frac{3}{4} \xi n_p (L_d - L_q) i_d, \\ \frac{\partial F}{\partial \xi} &= T_e - \frac{3}{2} \frac{n_p}{2} [\psi_f i_d + (L_d - L_q) i_d i_q]. \end{aligned} \quad (10)$$

Let (10) be equal to zero; then the relation constrained in d - q -axis currents in MTPA control can be derived as

$$i_q = -\frac{\psi_f}{2(L_d - L_q)} + \sqrt{i_d^2 + \left(\frac{\psi_f}{2(L_d - L_q)} \right)^2}. \quad (11)$$

Equation (11) indicates that if i_d is acquired, i_{qref} will be determined.

4. Nonlinear Adaptive Backstepping Controller

The control target of the study is to guarantee all the signals to be bounded and ensures the speed and currents to track their respective references precisely and rapidly in spite of full parameter uncertainties in PMA-SynRM and load disturbance. For achievement of the goal, the designed controller enables tracking the variations of parameters uncertainties. Hence, online parameter estimation laws for fully uncertain parameters with no problems of overparameterization and singularity should be conducted and vary with actual parameters adaptively.

4.1. Designed Nonlinear and Fully Adaptive Backstepping Controller. The tracking errors e_ω , e_d , and e_q of ω_r , i_d , and i_q are defined as follows:

$$e_\omega = \omega_{ref} - \omega_r, \quad (12)$$

$$e_d = i_{dref} - i_d, \quad (13)$$

$$e_q = i_{qref} - i_q, \quad (14)$$

where ω_{ref} , i_{dref} , and i_{qref} are the references of ω_r , i_d , and i_q , respectively.

Step 1. By derivative of e_ω in (12) and integration of (13) and (14), the dynamics of speed tracking errors can be given by

$$\begin{aligned} \dot{e}_\omega &= \dot{\omega}_{ref} - \dot{\omega}_r = \dot{\omega}_{ref} - \frac{T_e}{J_m} + \frac{B_m \omega_r}{J_m} + \frac{T_L}{J_m} = \dot{\omega}_{ref} \\ &\quad - \frac{3n_p [\psi_f i_d + (L_d - L_q) i_d i_q]}{4J_m} + \frac{B_m \omega_r}{J_m} + \frac{T_L}{J_m} \\ &= \dot{\omega}_{ref} + \frac{B_m \omega_r}{J_m} + \frac{T_L}{J_m} - \frac{3n_p}{4J_m} [\psi_f i_{dref} + (L_d - L_q) \end{aligned}$$

$$\begin{aligned}
& \cdot i_{dref} i_{qref}] + \frac{3n_p}{4J_m} [\psi_f + (L_d - L_q) i_{qref}] e_d \\
& + \frac{3n_p}{4J_m} (L_d - L_q) i_{dref} e_q - \frac{3n_p}{4J_m} (L_d - L_q) e_d e_q \\
& = \frac{[\psi_f + (L_d - L_q) i_{qref}]}{J_m} \left(\frac{J_m}{[\psi_f + (L_d - L_q) i_{qref}]} \right. \\
& \cdot \dot{\omega}_{ref} + \frac{B_m}{[\psi_f + (L_d - L_q) i_{qref}]} \omega_r \\
& + \frac{T_L}{[\psi_f + (L_d - L_q) i_{qref}]} - \frac{3n_p}{4} i_{dref} + \frac{3n_p}{4} e_d \\
& + \frac{3n_p (L_d - L_q)}{4 [\psi_f + (L_d - L_q) i_{qref}]} i_{dref} e_q \\
& \left. - \frac{3n_p (L_d - L_q)}{4 [\psi_f + (L_d - L_q) i_{qref}]} e_d e_q \right). \tag{15}
\end{aligned}$$

Supposing that $B_m/[\psi_f + (L_d - L_q) i_{qref}] = \theta_1$, $T_L/[\psi_f + (L_d - L_q) i_{qref}] = \theta_2$, $(L_d - L_q)/[\psi_f + (L_d - L_q) i_{qref}] = \theta_3$, and $J_m/[\psi_f + (L_d - L_q) i_{qref}] = \theta_4$, (15) can be rearranged as

$$\begin{aligned}
\dot{e}_\omega &= \frac{1}{\theta_4} \left((\hat{\theta}_4 - \tilde{\theta}_4) \dot{\omega}_{ref} + (\hat{\theta}_1 - \tilde{\theta}_1) \omega_r + (\hat{\theta}_2 - \tilde{\theta}_2) \right. \\
& - \frac{3n_p}{4} i_{dref} + \frac{3n_p}{4} e_d + \frac{3n_p}{4} (\hat{\theta}_3 - \tilde{\theta}_3) i_{dref} e_q \\
& - \frac{3n_p}{4} (\hat{\theta}_3 - \tilde{\theta}_3) e_d e_q \left. \right) = \frac{1}{\theta_4} \left((\hat{\theta}_4 \dot{\omega}_{ref} - \tilde{\theta}_4 \dot{\omega}_{ref}) \right. \\
& + (\hat{\theta}_1 \omega_r - \tilde{\theta}_1 \omega_r) + (\hat{\theta}_2 - \tilde{\theta}_2) - \frac{3n_p}{4} i_{dref} + \frac{3n_p}{4} e_d \\
& + \frac{3n_p}{4} (\hat{\theta}_3 i_{dref} e_q - \tilde{\theta}_3 i_{dref} e_q) - \frac{3n_p}{4} (\hat{\theta}_3 - \tilde{\theta}_3) e_d e_q \left. \right) \\
& = \frac{1}{\theta_4} \left((\hat{\theta}_4 \dot{\omega}_{ref} + \hat{\theta}_1 \omega_r + \hat{\theta}_2 - \frac{3n_p}{4} i_{dref}) - (\tilde{\theta}_4 \dot{\omega}_{ref} \right. \\
& + \tilde{\theta}_1 \omega_r + \tilde{\theta}_2 - \frac{3n_p}{4} e_d - \frac{3n_p}{4} \tilde{\theta}_3 i_{dref} e_q \\
& \left. + \frac{3n_p}{4} \tilde{\theta}_3 i_{dref} e_q + \frac{3n_p}{4} (\hat{\theta}_3 - \tilde{\theta}_3) e_d e_q \right), \tag{16}
\end{aligned}$$

where $\hat{\theta}_1 = \tilde{\theta}_1 + \theta_1$, $\hat{\theta}_2 = \tilde{\theta}_2 + \theta_2$, $\hat{\theta}_3 = \tilde{\theta}_3 + \theta_3$, and $\hat{\theta}_4 = \tilde{\theta}_4 + \theta_4$, $\hat{\theta}_1$, $\hat{\theta}_2$, $\hat{\theta}_3$, and $\hat{\theta}_4$ are the estimations of θ_1 , θ_2 , θ_3 , and θ_4 , and $\tilde{\theta}_1$, $\tilde{\theta}_2$, $\tilde{\theta}_3$, and $\tilde{\theta}_4$ are the estimation errors of θ_1 , θ_2 , θ_3 , and θ_4 .

Through some mathematical operations, (16) is arranged and consisted of two parts. In terms of (16), selection of i_{dref} is depicted in the following:

$$i_{dref} = \frac{4}{3n_p} (\hat{\theta}_4 \dot{\omega}_{ref} + \hat{\theta}_1 \omega_r + \hat{\theta}_2 + k_\omega e_\omega), \tag{17}$$

where k_ω is the positive feedback gain.

Substituting (17) into (16),

$$\begin{aligned}
\dot{e}_\omega &= \frac{1}{\theta_4} \left(-k_\omega e_\omega - \omega_r \tilde{\theta}_1 - \tilde{\theta}_2 \right. \\
& + \left(\frac{3n_p}{4} e_d e_q - \frac{3n_p}{4} i_{dref} e_q \right) \tilde{\theta}_3 - \dot{\omega}_{ref} \tilde{\theta}_4 + \frac{3n_p}{4} e_d \\
& \left. + \frac{3n_p}{4} \tilde{\theta}_3 i_{dref} e_q - \frac{3n_p}{4} \tilde{\theta}_3 e_d e_q \right). \tag{18}
\end{aligned}$$

Let

$$\begin{aligned}
\boldsymbol{\varphi}_1 &= \left[-\omega_r, -1, \left(\frac{3n_p}{4} e_d e_q - \frac{3n_p}{4} i_{dref} e_q \right), -\dot{\omega}_{ref} \right]^T, \\
\tilde{\boldsymbol{\theta}}_1 &= [\tilde{\theta}_1, \tilde{\theta}_2, \tilde{\theta}_3, \tilde{\theta}_4]^T. \tag{19}
\end{aligned}$$

Substituting (19) into (18),

$$\begin{aligned}
\dot{e}_\omega &= \frac{1}{\theta_4} \left(-k_\omega e_\omega + \frac{3n_p}{4} e_d + \frac{3n_p}{4} \tilde{\theta}_3 i_{dref} e_q \right. \\
& \left. - \frac{3n_p}{4} \tilde{\theta}_3 e_d e_q + \tilde{\boldsymbol{\theta}}_1^T \cdot \boldsymbol{\varphi}_1 \right). \tag{20}
\end{aligned}$$

Step 2. By derivative of e_d in (13), the dynamics of d -axis current tracking error can be obtained as

$$\begin{aligned}
\dot{e}_d &= i_{dref} - \dot{i}_d \\
&= i_{dref} + \frac{R_s}{L_d} i_d - \frac{n_p L_q}{L_d} \omega_r i_q + \frac{n_p \psi_f}{L_d} \omega_r - \frac{1}{L_d} u_d, \tag{21}
\end{aligned}$$

where

$$i_{dref} = \frac{4}{3n_p} (\hat{\theta}_4 \dot{\omega}_{ref} + \hat{\theta}_4 \ddot{\omega}_{ref} + \hat{\theta}_1 \dot{\omega}_r + \hat{\theta}_1 \dot{\omega}_r + \hat{\theta}_2 + k_\omega \dot{e}_\omega). \tag{22}$$

Let $R_s = \theta_5$, $L_q = \theta_6$, $\psi_f = \theta_7$, and $L_d = \theta_8$, and $\tilde{\theta}_5 = \hat{\theta}_5 - \theta_5$, $\tilde{\theta}_6 = \hat{\theta}_6 - \theta_6$, $\tilde{\theta}_7 = \hat{\theta}_7 - \theta_7$, and $\tilde{\theta}_8 = \hat{\theta}_8 - \theta_8$, where $\hat{\theta}_5$, $\hat{\theta}_6$, $\hat{\theta}_7$, and $\hat{\theta}_8$ are the estimations of θ_5 , θ_6 , θ_7 , and θ_8 ; $\tilde{\theta}_5$, $\tilde{\theta}_6$, $\tilde{\theta}_7$, and $\tilde{\theta}_8$ are the estimation errors of θ_5 , θ_6 , θ_7 , and θ_8 .

Then, (21) can be rewritten as

$$\begin{aligned}
\dot{e}_d &= i_{dref} - \dot{i}_d \\
&= \frac{1}{L_d} (\hat{\theta}_8 i_{dref} + \hat{\theta}_5 i_d - n_p \hat{\theta}_6 \omega_r i_q + n_p \hat{\theta}_7 \omega_r - u_d) \\
& - \frac{1}{L_d} (i_d \tilde{\theta}_5 - n_p \omega_r i_q \tilde{\theta}_6 + n_p \omega_r \tilde{\theta}_7 + i_{dref} \tilde{\theta}_8). \tag{23}
\end{aligned}$$

By derivative of e_q in (14), the dynamics of q -axis current tracking error can be obtained as

$$\dot{e}_q = \dot{i}_{qref} - \dot{i}_q = \dot{i}_{qref} + \frac{R_s}{L_q} i_q + \frac{n_p L_d}{L_q} \omega_r i_d - \frac{1}{L_q} u_q, \quad (24)$$

where

$$\dot{i}_{qref} = i_d \dot{i}_d \left\{ i_d^2 + \left[\frac{\psi_f}{2(L_d - L_q)} \right]^2 \right\}^{-1/2}. \quad (25)$$

In terms of $R_s = \theta_5$, $L_q = \theta_6$, and $L_d = \theta_8$, (24) can be arranged as

$$\begin{aligned} \dot{e}_q &= \dot{i}_{qref} - \dot{i}_q \\ &= \frac{1}{L_q} (\hat{\theta}_6 \dot{i}_{qref} + \hat{\theta}_5 i_q + n_p \hat{\theta}_8 \omega_r i_d - u_q) \\ &\quad - \frac{1}{L_q} (i_q \tilde{\theta}_5 + i_{qref} \tilde{\theta}_6 + n_p \omega_r i_d \tilde{\theta}_8). \end{aligned} \quad (26)$$

For reaching the control goal and stabilizing the tracking error terms, the control inputs can be designed as follows:

$$\begin{aligned} u_d &= \hat{\theta}_8 \dot{i}_{dref} + \hat{\theta}_5 i_d - n_p \hat{\theta}_6 \omega_r i_q + n_p \hat{\theta}_7 \omega_r + k_d e_d \\ &\quad + \frac{3n_p}{4} e_\omega, \end{aligned} \quad (27)$$

$$\begin{aligned} u_q &= \hat{\theta}_6 \dot{i}_{qref} + \hat{\theta}_5 i_q + n_p \hat{\theta}_8 \omega_r i_d + k_q e_q + \frac{3n_p}{4} \hat{\theta}_3 i_{dref} e_\omega \\ &\quad - \frac{3n_p}{4} \hat{\theta}_3 e_d e_\omega, \end{aligned} \quad (28)$$

where k_d and k_q are two positive feedback gains.

Substituting (27) and (28) into (23) and (26), respectively, we can obtain

$$\begin{aligned} \dot{e}_d &= -\frac{1}{L_d} k_d e_d - \frac{3n_p}{4L_d} e_\omega \\ &\quad - \frac{1}{L_d} (i_d \tilde{\theta}_5 - n_p \omega_r i_q \tilde{\theta}_6 + n_p \omega_r \tilde{\theta}_7 + i_{dref} \tilde{\theta}_8), \\ \dot{e}_q &= -\frac{1}{L_q} k_q e_q - \frac{3n_p}{4L_q} \hat{\theta}_3 i_{dref} e_\omega + \frac{3n_p}{4L_q} \hat{\theta}_3 e_d e_\omega \\ &\quad - \frac{1}{L_q} (i_q \tilde{\theta}_5 + i_{qref} \tilde{\theta}_6 + n_p \omega_r i_d \tilde{\theta}_8). \end{aligned} \quad (29)$$

Step 3. The positive definite Lyapunov function candidate is defined as follows:

$$V_1 = \frac{1}{2} \theta_4 e_\omega^2 + \frac{1}{2} L_d e_d^2 + \frac{1}{2} L_q e_q^2. \quad (30)$$

Derivative of the Lyapunov function yields

$$\begin{aligned} \dot{V} &= -k_\omega e_\omega^2 - k_d e_d^2 - k_q e_q^2 + e_\omega \tilde{\theta}_1^T \cdot \boldsymbol{\varphi}_1 \\ &\quad - (i_d e_d + i_q e_q) \tilde{\theta}_5 + (n_p \omega_r i_q e_d - i_{qref} e_q) \tilde{\theta}_6 \\ &\quad - n_p \omega_r e_d \tilde{\theta}_7 - (i_{dref} e_d + n_p \omega_r i_d e_q) \tilde{\theta}_8. \end{aligned} \quad (31)$$

Choose

$$\begin{aligned} \tilde{\theta}_2 &= [\tilde{\theta}_5, \tilde{\theta}_6, \tilde{\theta}_7, \tilde{\theta}_8]^T, \\ \boldsymbol{\varphi}_2 &= [-i_d e_d - i_q e_q, n_p \omega_r i_q e_d - i_{qref} e_q, -n_p \omega_r e_d, \\ &\quad - i_{dref} e_d - n_p \omega_r i_d e_q]^T. \end{aligned} \quad (32)$$

By substituting (32) into (31), the derivative of the Lyapunov function can be simplified as follows after some mathematical computations:

$$\dot{V}_1 = -k_\omega e_\omega^2 - k_d e_d^2 - k_q e_q^2 + e_\omega \tilde{\theta}_1^T \cdot \boldsymbol{\varphi}_1 + \tilde{\theta}_2^T \cdot \boldsymbol{\varphi}_2, \quad (33)$$

where k_ω , k_d , and k_q are the positive control gains.

Suppose that

$$\tilde{\theta}^T \cdot \boldsymbol{\varphi} = e_\omega \tilde{\theta}_1^T \cdot \boldsymbol{\varphi}_1 + \tilde{\theta}_2^T \cdot \boldsymbol{\varphi}_2, \quad (34)$$

where

$$\tilde{\theta} = [\tilde{\theta}_1, \tilde{\theta}_2, \tilde{\theta}_3, \tilde{\theta}_4, \tilde{\theta}_5, \tilde{\theta}_6, \tilde{\theta}_7, \tilde{\theta}_8]^T, \quad (35)$$

$$\begin{aligned} \boldsymbol{\varphi} &= \left[-\omega_r, -1, \left(\frac{3n_p}{4} e_d e_q - \frac{3n_p}{4} i_{dref} e_q \right), -\dot{\omega}_{ref}, \right. \\ &\quad - i_d e_d - i_q e_q, n_p \omega_r i_q e_d - i_{qref} e_q, -n_p \omega_r e_d, -i_{dref} e_d \\ &\quad \left. - n_p \omega_r i_d e_q \right]^T. \end{aligned} \quad (36)$$

The final Lyapunov function is selected as

$$V = \frac{1}{2} \theta_4 e_\omega^2 + \frac{1}{2} L_d e_d^2 + \frac{1}{2} L_q e_q^2 + \frac{1}{2} \tilde{\theta}^T \cdot \boldsymbol{\tau}^{-1} \cdot \tilde{\theta}, \quad (37)$$

where $\boldsymbol{\tau}$ is an eighth-order positive definite diagonal matrix; the diagonal elements are described as $\tau_1, \tau_2, \tau_3, \tau_4, \tau_5, \tau_6, \tau_7$, and τ_8 .

Then, the derivative of the Lyapunov function yields

$$\begin{aligned} \dot{V} &= \theta_4 e_\omega \dot{e}_\omega + L_d e_d \dot{e}_d + L_q e_q \dot{e}_q + \tilde{\theta}^T \cdot \boldsymbol{\tau}^{-1} \cdot \dot{\tilde{\theta}} \\ &= -k_\omega e_\omega^2 - k_d e_d^2 - k_q e_q^2 + \tilde{\theta}^T \cdot \boldsymbol{\varphi} + \tilde{\theta}^T \cdot \boldsymbol{\tau}^{-1} \cdot \dot{\tilde{\theta}}. \end{aligned} \quad (38)$$

Letting

$$\tilde{\theta}^T \cdot \boldsymbol{\varphi} + \tilde{\theta}^T \cdot \boldsymbol{\tau}^{-1} \cdot \dot{\tilde{\theta}} = 0, \quad (39)$$

we can obtain

$$\dot{\tilde{\theta}} = -\boldsymbol{\tau} \cdot \boldsymbol{\varphi}. \quad (40)$$

In terms of (36) and (40), the adaptive law depicting the uncertainties for the fully uncertain parameters can be written as

$$\begin{aligned}
\dot{\hat{\theta}}_1 &= \tau_1 \omega_r e_\omega, \\
\dot{\hat{\theta}}_2 &= \tau_2 e_\omega, \\
\dot{\hat{\theta}}_3 &= -\tau_3 e_\omega \left(\frac{3n_p}{4} e_d e_q - \frac{3n_p}{4} i_{d\text{ref}} e_q \right), \\
\dot{\hat{\theta}}_4 &= \tau_4 \dot{\omega}_{\text{ref}}, \\
\dot{\hat{\theta}}_5 &= \tau_5 (i_d e_d + i_q e_q), \\
\dot{\hat{\theta}}_6 &= -\tau_6 (n_p \omega_r i_q e_d - \dot{i}_{q\text{ref}} e_q), \\
\dot{\hat{\theta}}_7 &= \tau_7 n_p \omega_r e_d, \\
\dot{\hat{\theta}}_8 &= -\tau_8 (\dot{i}_{d\text{ref}} e_d + n_p \omega_r i_d e_q).
\end{aligned} \tag{41}$$

By substituting (40) into (38), the derivative of the final Lyapunov function can be rewritten as

$$\dot{V} = -k_\omega e_\omega^2 - k_d e_d^2 - k_q e_q^2 \leq 0. \tag{42}$$

Equation (42) represents that there exists a positive definite Lyapunov function V and its derivative \dot{V} with respect to time being nonpositive for the closed-loop system.

Additionally, in terms of (41), the fully uncertain parameters of PMa-SynRM and load torque disturbance can be estimated and represented as

$$\begin{aligned}
\hat{L}_d &= \hat{\theta}_8, \\
\hat{L}_q &= \hat{\theta}_6, \\
\hat{R}_s &= \hat{\theta}_5, \\
\hat{\psi}_f &= \hat{\theta}_7, \\
\hat{J}_m &= \hat{\theta}_4 [\hat{\psi}_f + (\hat{L}_d - \hat{L}_q) i_{q\text{ref}}], \\
\hat{B}_m &= \hat{\theta}_1 [\hat{\psi}_f + (\hat{L}_d - \hat{L}_q) i_{q\text{ref}}], \\
\hat{T}_L &= \hat{\theta}_2 [\hat{\psi}_f + (\hat{L}_d - \hat{L}_q) i_{q\text{ref}}].
\end{aligned} \tag{43}$$

4.2. Stability Analysis

Theorem 1. *For the dynamics of PMa-SynRM described in (5)–(7) with parameter uncertainties and external load disturbance, the proposed controller shown in (27) with the adaptive law of fully uncertain parameters given in (41) enables ensuring the tracking error signals in (12)–(14) to converge to (0, 0, 0) asymptotically through Barbalat's Lemma.*

To prove this theorem, by integration of (42) in its both sides from 0 to $+\infty$, we can give

$$\begin{aligned}
&\int_0^\infty \dot{V}(t) dt \\
&= -\int_0^\infty (k_\omega e_\omega^2(t) + k_d e_d^2(t) + k_q e_q^2(t)) dt.
\end{aligned} \tag{44}$$

Thus,

$$\begin{aligned}
&\int_0^\infty (k_\omega e_\omega^2(t) + k_d e_d^2(t) + k_q e_q^2(t)) dt \\
&= V(\mathbf{0}) - V(\infty).
\end{aligned} \tag{45}$$

It follows that

$$\begin{aligned}
&\sqrt{\int_0^\infty (k_\omega e_\omega^2(t)) dt} \\
&\leq \sqrt{\int_0^\infty (k_\omega e_\omega^2(t) + k_d e_d^2(t) + k_q e_q^2(t)) dt} \leq V(\mathbf{0}) \\
&< \infty, \\
&\sqrt{\int_0^\infty (k_d e_d^2(t)) dt} \\
&\leq \sqrt{\int_0^\infty (k_\omega e_\omega^2(t) + k_d e_d^2(t) + k_q e_q^2(t)) dt} \leq V(\mathbf{0}) \\
&< \infty, \\
&\sqrt{\int_0^\infty (k_q e_q^2(t)) dt} \\
&\leq \sqrt{\int_0^\infty (k_\omega e_\omega^2(t) + k_d e_d^2(t) + k_q e_q^2(t)) dt} \leq V(\mathbf{0}) \\
&< \infty.
\end{aligned} \tag{46}$$

Furthermore, $V(t)$ is uniformly continuous and $\dot{V}(t)$ is finite. Through Barbalat's Lemma [23], it gives that

$$\lim_{t \rightarrow \infty} V(t) = 0, \tag{47}$$

which proves that the tracking errors (e_ω, e_d, e_q) can converge to (0, 0, 0) asymptotically under full parameters' uncertainties and uncertain load torque disturbance for any initial condition. It is worth mentioning that the choices of control parameter and adaption gain are no restriction for use, except for positive definite terms. Previous studies have shown that control gains are frequently necessary to satisfy inequality relation with uncertain parameters [21] and selection of adaptation gains in multiparameter estimation situation is complicated [24] as (A3) encountered. The relaxation of control and adaptation gains is beneficial for implementation of the proposed control scheme apparently.

5. Proposed Luenberger Speed Observer

Luenberger speed observer is an excellent linear estimation method. The product term of $i_d i_q$ in (4) represents the model nonlinearity of PMA-SynRM, which results in the fact that Luenberger speed observer cannot be used directly. Hence, an active flux ψ_{af} is firstly introduced to linearize (4) as follows:

$$\psi_{af} = \psi_f + (L_d - L_q) i_q. \quad (48)$$

Then, the torque equation (4) can be rewritten as

$$T_e = \frac{3}{2} \frac{n_p}{2} \psi_{af} i_d. \quad (49)$$

By substituting (48) into (3), we can obtain

$$\psi_q = L_q i_q - \psi_{af} + (L_d - L_q) i_q = L_d i_q - \psi_{af}. \quad (50)$$

In terms of (2) and (50), the components of ψ_{af} in rotating d - q -axis coordinate system are

$$\psi_{af,d} = \psi_d - L_d i_d = 0, \quad (51)$$

$$\psi_{af,q} = \psi_q - L_d i_q = L_d i_q - \psi_{af} - L_d i_q = -\psi_{af}.$$

Equation (51) indicates that active flux is oriented on q -axis, which is shown in Figure 1.

Furthermore, for the mathematical model (see (5) and (6)), new input variables are introduced as

$$\begin{aligned} v_d &= \frac{n_p L_q}{L_d} \omega_r i_q + \frac{1}{L_d} u_d, \\ v_q &= -\frac{n_p L_d}{L_q} \omega_r i_d + \frac{1}{L_q} u_q. \end{aligned} \quad (52)$$

By substituting (52) and (51) into (5)–(7), we can get

$$\frac{di_d}{dt} = -\frac{R_s}{L_d} i_d - \frac{n_p \psi_f}{L_d} \omega_r + v_d, \quad (53)$$

$$\frac{di_q}{dt} = -\frac{R_s}{L_q} i_q + v_q, \quad (54)$$

$$\frac{d\omega_r}{dt} = \frac{1}{J_m} \left(\frac{3}{2} \frac{n_p}{2} \psi_{af} i_d - B_m \omega_r - T_L \right). \quad (55)$$

Equations (53)–(55) manifest that the nonlinear model of the original system has been linearized. Additionally, ω_r is only related to i_d and the linearized reduced-order observer can be constructed to estimate the speed. Through utilization of the simplified rotor motion equation (55) and d -axis current equation (53), the reduced-order matrix equation can be given as

$$\begin{aligned} \begin{pmatrix} \frac{di_d}{dt} \\ \frac{d\omega_r}{dt} \end{pmatrix} &= \begin{pmatrix} -\frac{R_s}{L_d} & -\frac{n_p \psi_f}{L_d} \\ \frac{3n_p \psi_{af}}{4J_m} & -\frac{B_m}{J_m} \end{pmatrix} \begin{pmatrix} i_d \\ \omega_r \end{pmatrix} + \begin{pmatrix} 1 \\ 0 \end{pmatrix} v_d \\ &+ \begin{pmatrix} 0 \\ -\frac{T_L}{J_m} \end{pmatrix}. \end{aligned} \quad (56)$$

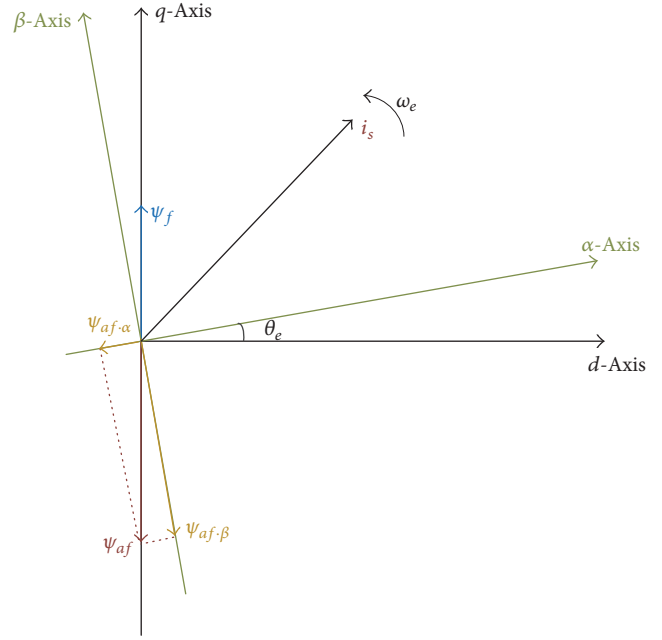


FIGURE 1: Distribution of active flux in $dq0$ coordinated system.

For the above matrix equation, linear Luenberger observer is designed as

$$\begin{aligned} \begin{pmatrix} \frac{d\hat{i}_d}{dt} \\ \frac{d\hat{\omega}_r}{dt} \end{pmatrix} &= \begin{pmatrix} -\frac{R_s}{L_d} & -\frac{n_p \psi_f}{L_d} \\ \frac{3n_p \psi_{af}}{4J_m} & -\frac{B_m}{J_m} \end{pmatrix} \begin{pmatrix} \hat{i}_d \\ \hat{\omega}_r \end{pmatrix} + \begin{pmatrix} 1 \\ 0 \end{pmatrix} v_d \\ &+ \begin{pmatrix} \gamma \\ 0 \end{pmatrix} (i_d - \hat{i}_d) + \begin{pmatrix} 0 \\ -\frac{T_L}{J_m} \end{pmatrix}, \end{aligned} \quad (57)$$

where \hat{i}_d and $\hat{\omega}_r$ are the estimations of d -axis current and speed, respectively, and γ is the feedback gain of designed Luenberger observer.

By subtracting (57) from (56), we can get

$$\begin{aligned} \begin{pmatrix} \frac{de_{od}}{dt} \\ \frac{de_{ow}}{dt} \end{pmatrix} &= \begin{pmatrix} -\frac{R_s}{L_d} - \gamma & -\frac{n_p \psi_f}{L_d} \\ \frac{3n_p \psi_{af}}{4J_m} & -\frac{B_m}{J_m} \end{pmatrix} \begin{pmatrix} e_{od} \\ e_{ow} \end{pmatrix}, \end{aligned} \quad (58)$$

where e_{od} and e_{ow} are estimation errors: $e_{od} = i_d - \hat{i}_d$ and $e_{ow} = \omega_r - \hat{\omega}_r$.

Replacements of B_m/J_m , ψ_{af}/J_m , R_s/L_d , and ψ_f/L_d with $\hat{\theta}_1/\hat{\theta}_4$, $1/\hat{\theta}_4$, $\hat{\theta}_5/\hat{\theta}_8$, and $\hat{\theta}_7/\hat{\theta}_8$, respectively, (58) can be rewritten as

$$\begin{aligned} \begin{pmatrix} \frac{de_{od}}{dt} \\ \frac{de_{ow}}{dt} \end{pmatrix} &= \begin{pmatrix} -\frac{\hat{\theta}_5}{\hat{\theta}_8} - \gamma & -n_p \frac{\hat{\theta}_7}{\hat{\theta}_8} \\ \frac{3n_p}{4\hat{\theta}_4} & -\frac{\hat{\theta}_1}{\hat{\theta}_4} \end{pmatrix} \begin{pmatrix} e_{od} \\ e_{ow} \end{pmatrix}. \end{aligned} \quad (59)$$

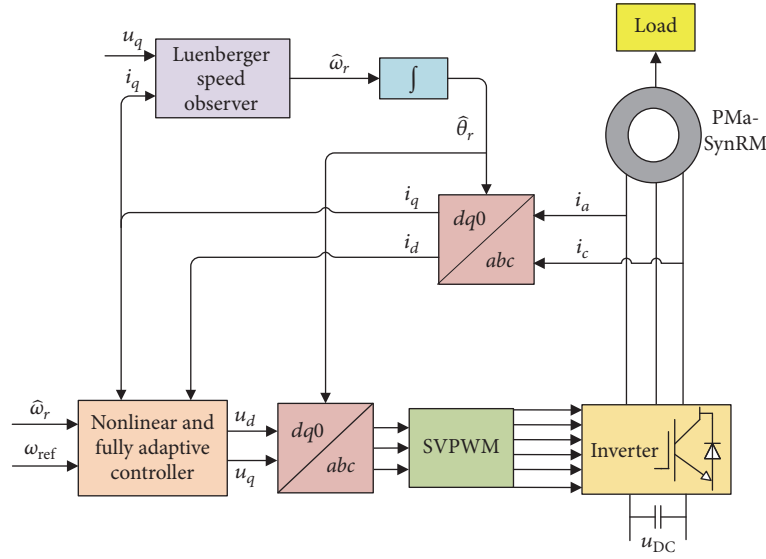


FIGURE 2: The overall configuration diagram of the proposed control scenario.

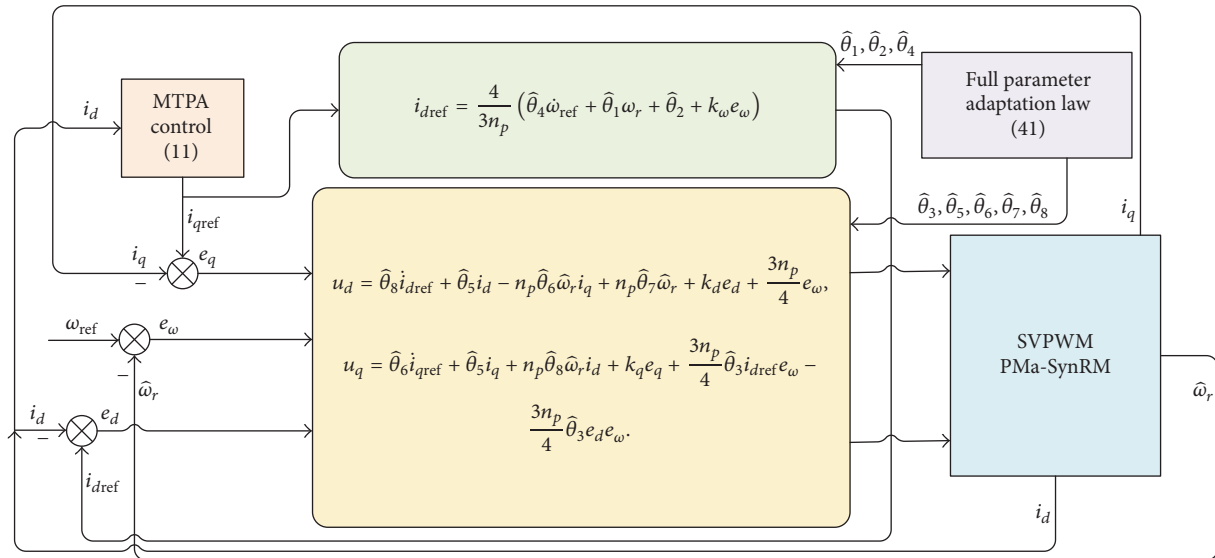


FIGURE 3: The concrete nonlinear backstepping controller with full adaptation law.

Equation (59) shows that the observed error of speed enables converging to zero through selecting a suitable parameter γ to configurate the eigenvalue of matrix. Moreover, due to the fact that the designed speed observer is of first order, the computational burden is decreased distinctly.

6. Digital Simulation Analysis and Discussion

The overall configuration diagram of the proposed control scenario and concrete nonlinear backstepping controller with full adaptation law are shown in Figures 2 and 3, respectively.

The digital simulations to validate the control scheme are implemented in MATLAB and the rated and nominal parameters of PMA-SynRM are described in the following:

per phase stator resistance, 2.875Ω , d -axis and q -axis inductances, 0.133 H and 0.058 H , respectively, viscous damping coefficient, 0.005 N/rad/s , permanent magnet flux, 0.38 Wb , moment of inertia, 0.03 kg m^2 , and number of pole pairs, 10 . The controller and adaption gains are selected as $k_\omega = 75$, $k_d = 150$, and $k_q = 5000$, and $\tau_1 = 0.005$, $\tau_2 = 0.01$, $\tau_3 = 0.05$, $\tau_4 = 0.05$, $\tau_5 = 0.1$, $\tau_6 = 0.02$, $\tau_7 = 35$, and $\tau_8 = 0.01$. The feedback gain of designed Luenberger observer γ is 20 .

To testify the superiority of the controller, adaption laws, and Luenberger speed observer adequately, the simulations consist of three groups.

Case 1. Due to the fact that very low speed regulation of PMA-SynRM is a complicated issue in control field, to validate the performance of the proposed controller and Luenberger

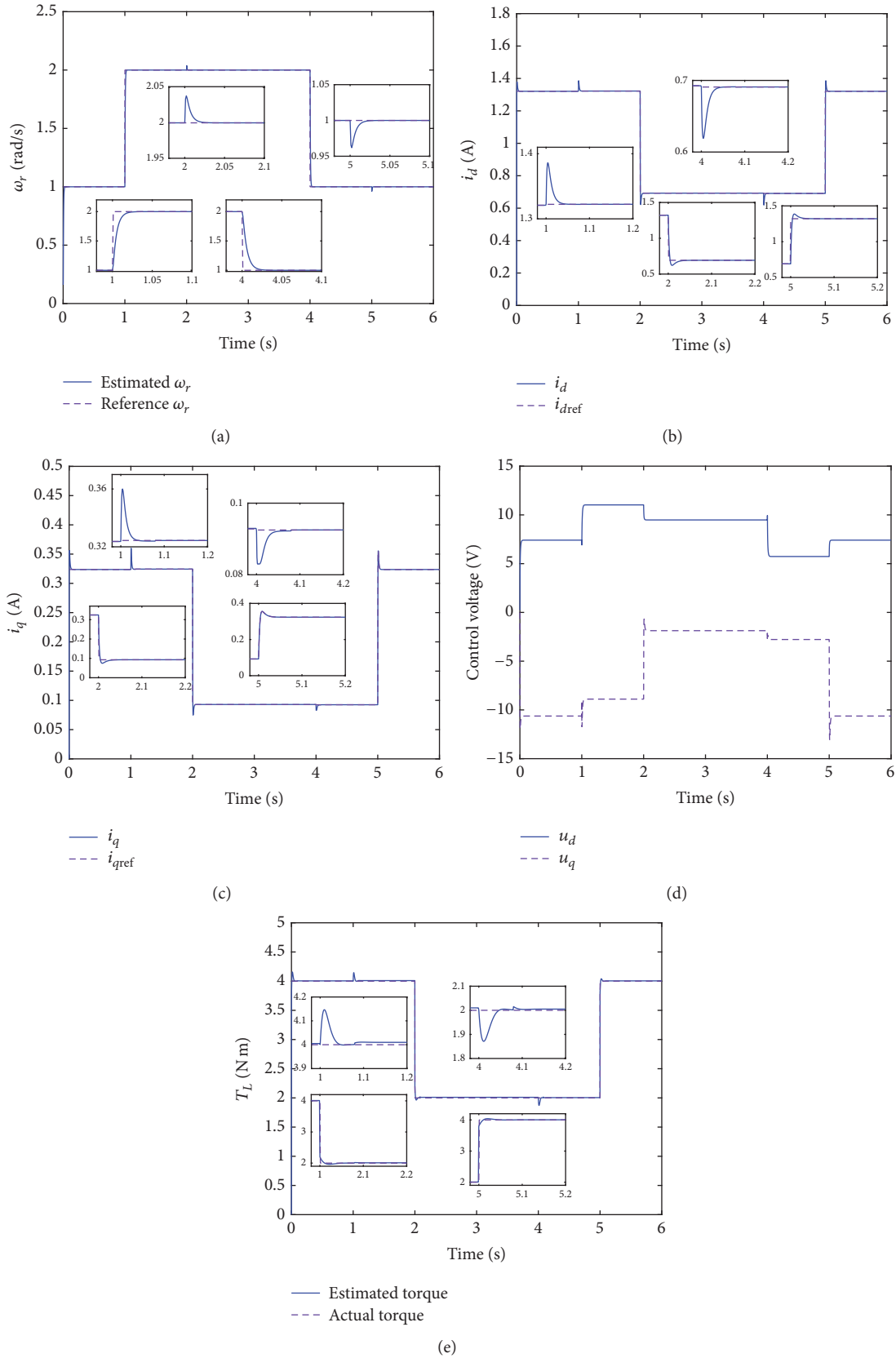


FIGURE 4: The simulation results in Case 1. (a) The estimated speed and its reference; (b) d -axis current and its reference; (c) q -axis current and its reference; (d) d - q -axis control voltages; (e) torque and its estimation.

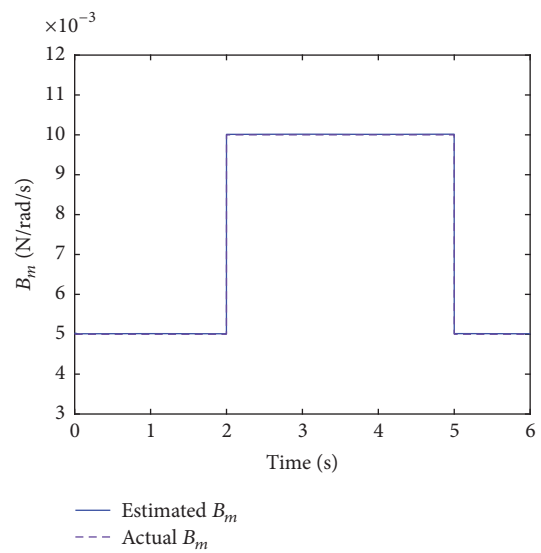
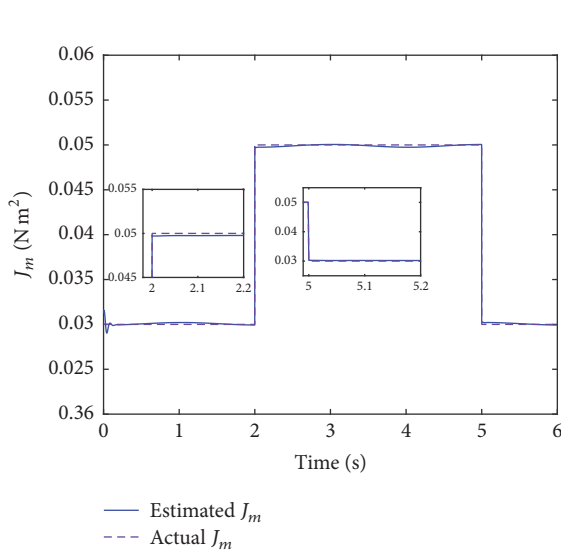
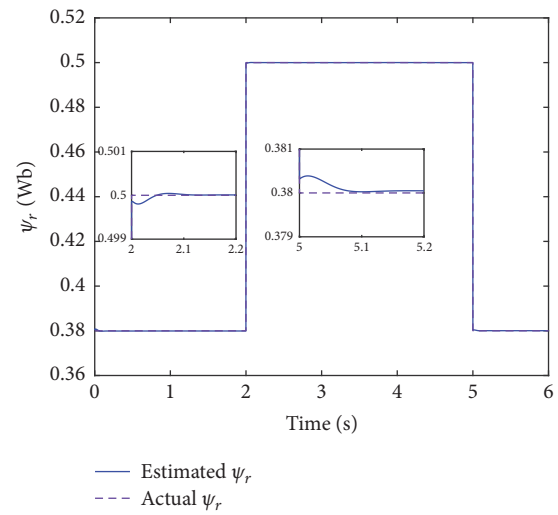
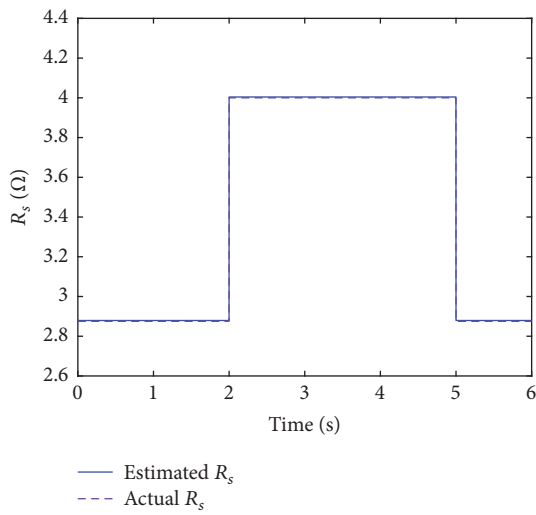
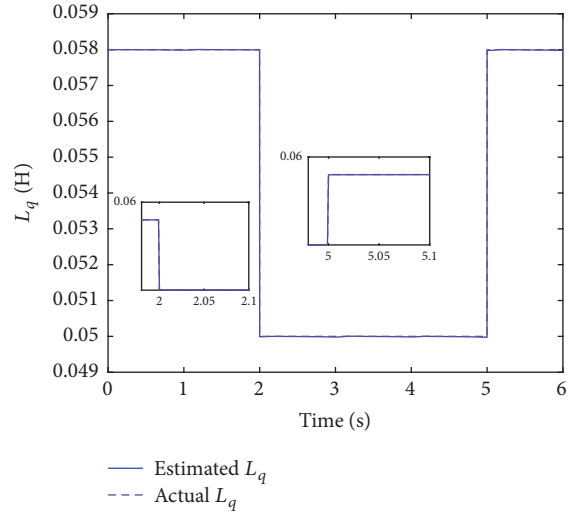
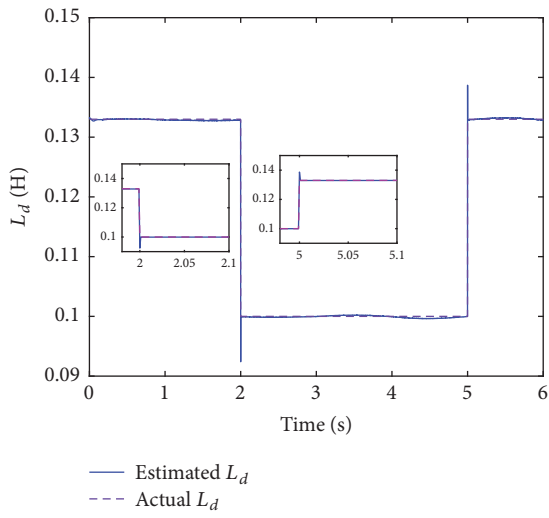


FIGURE 5: Continued.

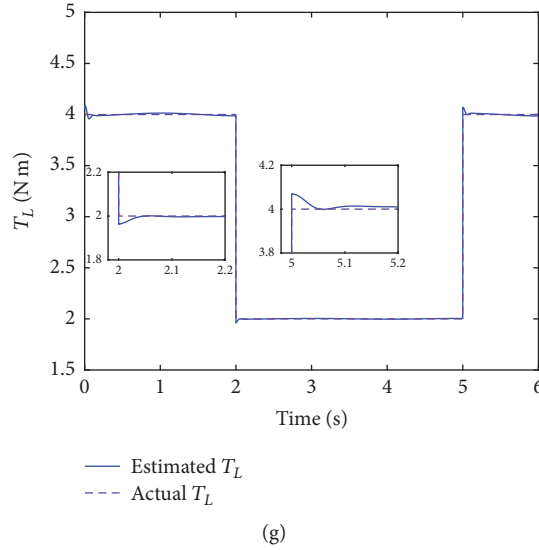


FIGURE 5: The simulation results in Case 2. (a) L_d and its estimation; (b) L_q and its estimation; (c) R_s and its estimation; (d) ψ_r and its estimation; (e) J_m and its estimation; (f) B_m and its estimation; (g) T_L and its estimation.

speed observer, the speed reference is set to a very low and changing value, which is 1 rad/s between 0 and 1 s, 2 rad/s between 1 s and 4 s, and 1 rad/s between 4 s and 6 s. That is to say that the simulation time in the first simulation is 6 s. Simultaneously, the sudden variation of load torque is taken into account and is abruptly applied to the motor as 4 N·m from 0 to 2 s, 2 N·m from 2 to 5 s, and 4 N·m from 5 s to 6 s.

The simulation results responding to the speed variation and torque disturbance are indicated in Figures 4(a)–4(e). The estimated speed and its reference are shown in Figure 4(a). The dynamic tracking responses of d - q -axis currents and their references are in Figures 4(b) and 4(c) individually. The control inputs of d - q -axis voltages are displayed in Figure 4(d). The estimated load torque and its reference are demonstrated in Figure 4(e).

Figures 4(a)–4(c) indicate that the proposed controller can guarantee the output signals to track their respective references correctly and rapidly. Furthermore, Figure 4(a) verifies the effectiveness of the designed Luenberger speed observer. From Figure 4(e), the load torque is estimated precisely.

Case 2. To illustrate the capability of the adaption law and testify the robustness of the control scheme retaining the full parameter perturbations furthermore, the parameter perturbations are described as follows: per phase stator resistance increases from 2.875 Ω to 4 Ω at 2 s and changes to 2.875 Ω at 5 s, d -axis and q -axis inductances decrease from 0.133 H and 0.058 H to 0.1 H and 0.05 H, respectively, at 2 s and return to their respective initial value at 5 s, viscous damping coefficient varies from 0.005 N/rad/s to 0.01 N/rad/s at 2 s and returns to 0.005 N/rad/s at 5 s, permanent magnet flux changes from 0.38 Wb to 0.5 Wb at 2 s and changes to 0.38 Wb at 5 s, and moment of inertia increases from 0.03 kg m² to 0.05 kg m² at 2 s and changes to 0.03 kg m² at 5 s. Additionally, in terms of the persistency of excitation condition, a good result with

parameter estimation requires abundant signals, where the speed reference is chosen as $\omega_{ref} = 2 \sin(\pi t)$, and simulation time is also 6 s. The load torque is the same as in Case 1. Figures 5(a)–5(g) plot the estimated errors of fully uncertain parameters, which clarify that all the uncertain and varied parameters are estimated by the adaption law rightly. As a consequence, the simulation results shown in Figure 5 exhibit the accuracy of the adaption law and reveal the good robustness of the presented control scenario.

Simultaneously, for demonstrating the influence of each parameter variation on the presented control scheme, the dynamic responses of speed tracking are displayed in Figure 6 when changing each parameter of the following parameters: L_d , L_q , R_s , ψ_r , J_m , B_m , and T_L . The range of variation for each parameter is set to $\pm 50\%$ rated value. Figure 6 indicates that the speed of the motor tracks the reference precisely with the aid of the controller and the tracking errors approach zero. Hence, the proposal controller goes against all the parameter perturbations. Merely, when the parameter deviates from its rated value, the waveform responses of speed at startup will become larger, especially for ψ_r , B_m , and T_L . In other words, the variations of these parameters ψ_r , B_m , and T_L have a more significant influence on the speed response. However, all the speed responses in Figure 6 converge to their expected values within 0.3 s.

Case 3. For various applications in usual, the motor operates at medium speed or high speed is indispensable. Therefore, this case indicates the simulation results in high speed condition. The speed reference is selected as 300 rad/s from zero to 1 s and 600 rad/s from 1 s to 4 s. After 4 s, the speed reference returns to 300 rad/s. Meanwhile, the load torque changes from 4 N·m to 2 N·m at 2 s and returns to 4 N·m at 5 s.

The results in this case are demonstrated in Figure 7. It is implied that, under the high speed condition, the estimated

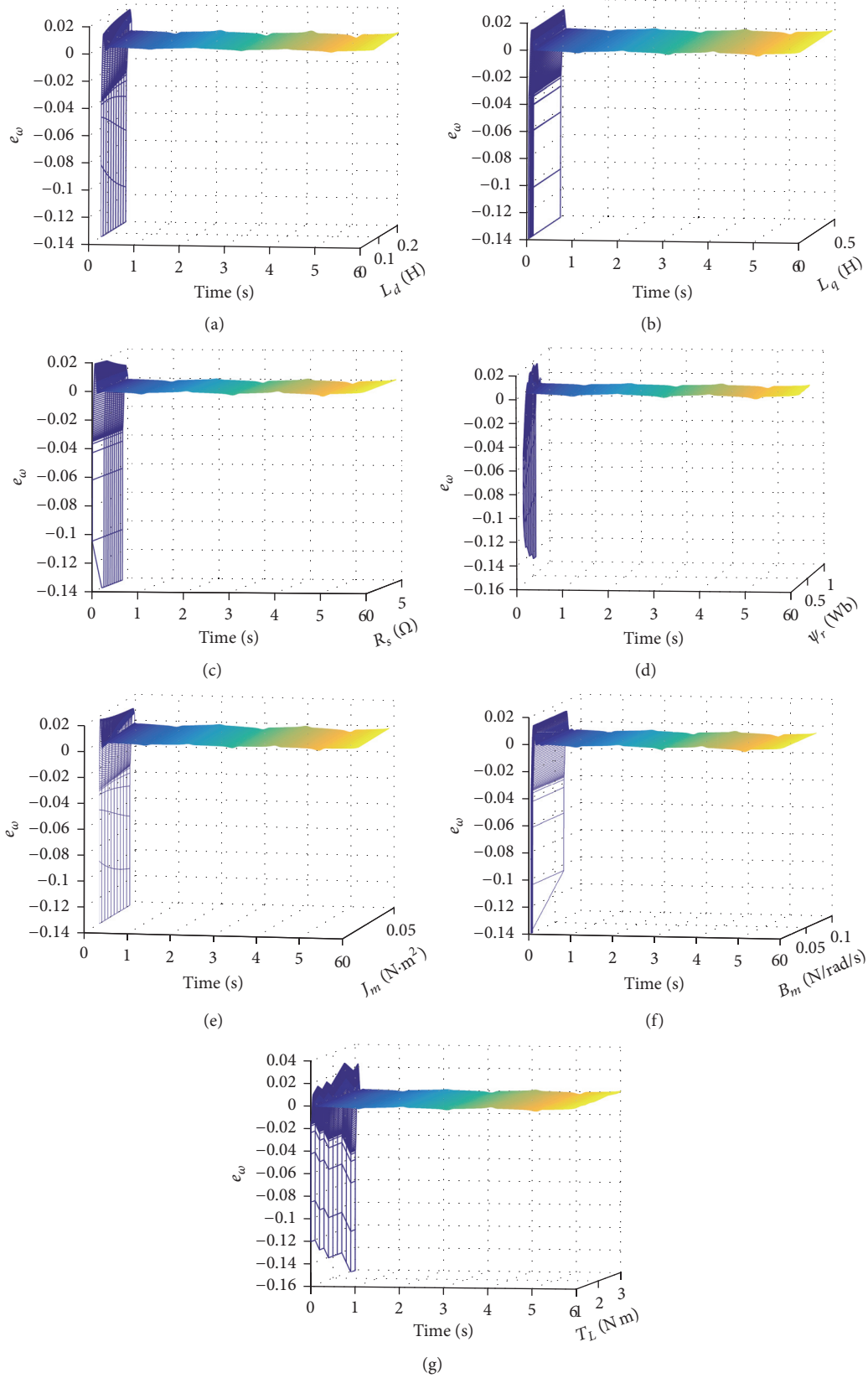


FIGURE 6: Speed tracking responses with the parameters variation. (a) Variation of L_d . (b) Variation of L_q . (c) Variation of R_s . (d) Variation of ψ_r . (e) Variation of J_m . (f) Variation of B_m . (g) Variation of T_L .

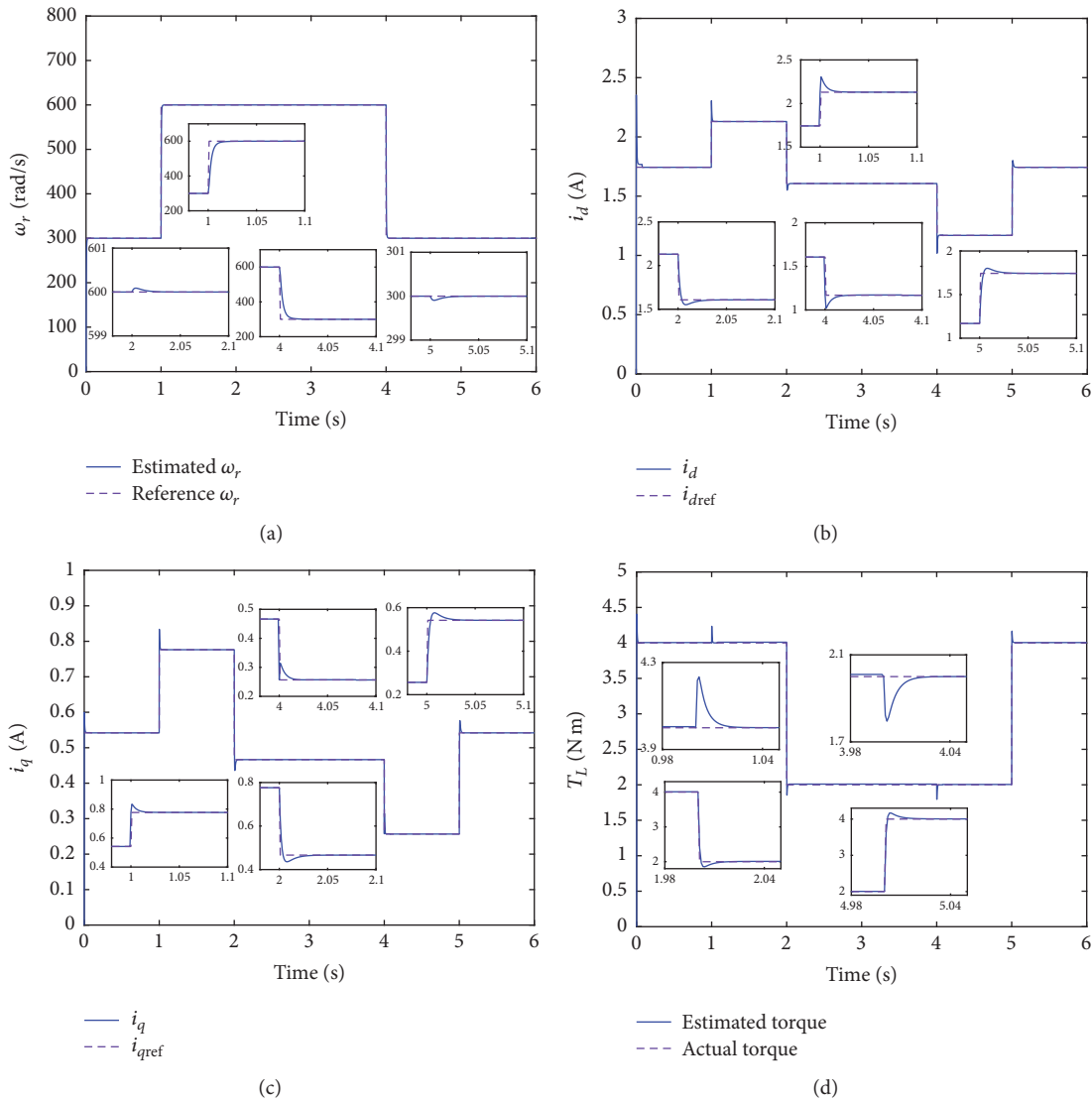


FIGURE 7: The simulation results in Case 3. (a) The estimated speed and its reference; (b) d -axis current and its reference; (c) q -axis current and its reference; (d) torque and its estimation.

speed shown in Figure 7(a) is also controlled to track the speed reference fast and correctly. The stator currents i_d and i_q are regulated to their reference signals individually.

Consequently, the presented control algorithm in the context achieves the closed-loop control of rotor speed and stator current and performs the estimations of fully unknown parameters for PMA-SynRM.

7. Conclusions

In this paper, on the basis of nonlinear dynamic model and parameter relation constrained in MTPA control, a nonlinear and robust adaptive backstepping speed sensorless control scheme with mismatched fully uncertain parameters is proposed for a PMA-SynRM. All the parameters of the motor and load torque are thought as uncertain except for

the number of pole pairs of rotor. The design of the control scheme avoids solving complex regression matrices and the only prerequisite for all controller and adaption gains is positive definite, which reduces the workload of choice of feedback gains tremendously and ensures the asymptotic stability of the controller readily. Additionally, an active flux based Luenberger speed observer is developed. The speed observer resolves the nonlinearity of dynamic model for PMA-SynRM effectively. The proposed controller fulfills the global asymptotic tracking of a varying speed reference and d - q -axis current references constrained by MTPA control. Simultaneously, the designed controller is of great robustness against uncertainties in both PMA-SynRM and load torque perturbation. Digital simulations have been implemented to verify the correctness and feasibility of the proposed control scheme well.

Conflicts of Interest

The authors declare that there are no conflicts of interest.

Acknowledgments

This work was partially supported by the National Natural Science Foundation of China (Grant no. 51407077), the Exploring Research Funds for the State Key Laboratory of Alternate Electrical Power System with Renewable Energy Sources (Grant no. LAPS2016-28), the Science and Technology Project of State Grid Corporation of China (headquarter) (Grant no. 5204BB16000F), and the Fundamental Research Funds for the Central Universities of China (Grant no. 2017MS095).

References

- [1] W.-H. Kim, K.-S. Kim, S.-J. Kim et al., "Optimal PM design of PMA-SynRM for wide constant-power operation and torque ripple reduction," *IEEE Transactions on Magnetics*, vol. 45, no. 10, pp. 4660–4663, 2009.
- [2] M. Sanada, Y. Inoue, and S. Morimoto, "Structure and characteristics of high-performance PMASynRM with ferrite magnets," *Electrical Engineering in Japan (English translation of Denki Gakkai Ronbunshi)*, vol. 187, no. 1, pp. 42–50, 2014.
- [3] E. Suárez and G. Bortolotto, "Voltage-frequency control of a self excited induction generator," *IEEE Transactions on Energy Conversion*, vol. 14, no. 3, pp. 394–401, 1999.
- [4] I. Takahashi and T. Noguchi, "A new quick-response and high-efficiency control strategy of an induction motor," *IEEE Transactions on Industry Applications*, vol. IA-22, no. 5, pp. 820–827, 1986.
- [5] M. Depenbrock, "Direct self-control (DSC) of inverter-fed induction machine," *IEEE Transactions on Power Electronics*, vol. 3, no. 4, pp. 420–429, 1988.
- [6] L. Zhong, M. F. Rahman, W. Y. Hu, and K. W. Lim, "Analysis of direct torque control in permanent magnet synchronous motor drives," *IEEE Transactions on Power Electronics*, vol. 12, no. 3, pp. 528–536, 1997.
- [7] A. Sikorski and M. Korzeniewski, "Improved algorithms of direct torque control method," *Automatika – Journal for Control, Measurement, Electronics, Computing and Communications*, vol. 54, no. 2, pp. 188–198, 2013.
- [8] M. O. E. Aboelhassan, T. Raminosa, A. Goodman, L. De Lillo, and C. Gerada, "Performance evaluation of a vector-control fault-tolerant flux-switching motor drive," *IEEE Transactions on Industrial Electronics*, vol. 60, no. 8, pp. 2997–3006, 2013.
- [9] S. Kim, Y.-D. Yoon, S.-K. Sul, and K. Ide, "Maximum torque per ampere (MTPA) control of an IPM machine based on signal injection considering inductance saturation," *IEEE Transactions on Power Electronics*, vol. 28, no. 1, pp. 488–497, 2013.
- [10] M. Preindl and S. Bolognani, "Optimal state reference computation with constrained MTPA criterion for PM motor drives," *IEEE Transactions on Power Electronics*, vol. 30, no. 8, pp. 4524–4535, 2015.
- [11] C. B. Butt, M. A. Hoque, and M. A. Rahman, "Simplified fuzzy logic based MTPA speed control of IPMSM drive," *IEEE Transactions on Industry Applications*, vol. 40, no. 6, pp. 1529–1535, 2004.
- [12] N. Yang, G. Luo, W. Liu, and K. Wang, "Interior permanent magnet synchronous motor control for electric vehicle using look-up table," in *Proceedings of the 2012 IEEE 7th International Power Electronics and Motion Control Conference - ECCE Asia, IPEMC 2012*, pp. 1015–1019, China, June 2012.
- [13] T. Sebastian, "Temperature effects on torque production and efficiency of PM motors using NdFeB magnets," *IEEE Transactions on Industry Applications*, vol. 31, no. 2, pp. 353–357, 1995.
- [14] P. Niazi and H. A. Toliyat, "Online parameter estimation of permanent-magnet assisted synchronous reluctance motor," *IEEE Transactions on Industry Applications*, vol. 43, no. 2, pp. 609–615, 2007.
- [15] P. Niazi, H. A. Toliyat, and A. Goodarzi, "Robust maximum torque per ampere (MTPA) control of PM-assisted SynRM for traction applications," *IEEE Transactions on Vehicular Technology*, vol. 56, no. 4 I, pp. 1538–1545, 2007.
- [16] M. Chen, B. Jiang, and R. Cui, "Actuator fault-tolerant control of ocean surface vessels with input saturation," *International Journal of Robust and Nonlinear Control*, vol. 26, no. 3, pp. 542–564, 2016.
- [17] M. Wang, Z. Zhang, and Y. Liu, "Adaptive backstepping control that is equivalent to tuning functions design," *International Journal of Control, Automation, and Systems*, vol. 14, no. 1, pp. 90–98, 2016.
- [18] G. M. Schoonhoven and M. N. Uddin, "MTPA and FW based robust nonlinear speed control of IPMSM drive using Lyapunov stability criterion," in *Proceedings of the 2014 IEEE Industry Application Society Annual Meeting, IAS 2014*, Canada, October 2014.
- [19] Y. Jeon, S. Jung, I. Choy, and W. Cho, "Nonlinear and adaptive back-stepping speed control of IPMSM," *The Transactions of the Korean Institute of Power Electronics*, vol. 18, no. 1, pp. 18–25, 2013.
- [20] A. K. Chakali, H. A. Toliyat, and H. Abu-Rub, "Observer-based sensorless speed control of PM-assisted SynRM for direct drive applications," in *Proceedings of the 2010 IEEE International Symposium on Industrial Electronics, ISIE 2010*, pp. 3095–3100, Italy, July 2010.
- [21] M. Karabacak and H. I. Eskikurt, "Speed and current regulation of a permanent magnet synchronous motor via nonlinear and adaptive backstepping control," *Mathematical and Computer Modelling*, vol. 53, no. 9-10, pp. 2015–2030, 2011.
- [22] R. Lohninger, H. Grabner, G. Weidenholzer, S. Silber, and W. Amrhein, "Modeling, simulation, and design of a permanent-magnet-assisted synchronous reluctance machine," *IEEE Transactions on Industry Applications*, vol. 51, no. 1, pp. 196–203, 2015.
- [23] M. Krstic, I. Kanellakopoulos, and P. V. Kokotovic, *Nonlinear and Adaptive Control Design*, John Wiley and Sons, NY, New York, USA, 1995.
- [24] J. Slotine and W. Li, *Applied Nonlinear Control*, Prentice-Hall, NJ, USA, 1991.

Research Article

Time-Varying Noise Statistic Estimator Based Adaptive Simplex Cubature Kalman Filter

Zhaoming Li,¹ Wenge Yang,² and Dan Ding²

¹Graduate School, Academy of Equipment, Beijing 101416, China

²Department of Optical and Electrical Equipment, Academy of Equipment, Beijing 101416, China

Correspondence should be addressed to Zhaoming Li; lizhaomingzbxxy@163.com

Received 25 September 2017; Accepted 26 November 2017; Published 14 December 2017

Academic Editor: Ton D. Do

Copyright © 2017 Zhaoming Li et al. This is an open access article distributed under the Creative Commons Attribution License, which permits unrestricted use, distribution, and reproduction in any medium, provided the original work is properly cited.

To address the problem that filtering accuracy is reduced with the inaccurate time-varying noise statistic in conventional cubature Kalman filter, a noise statistic estimator based adaptive simplex cubature Kalman filter is put forward in this paper. First, the simplex cubature rule is adopted to approximate the intractable nonlinear Gaussian weighted integral in the filter. Secondly, a suboptimal unbiased constant noise statistic estimator is derived based on the maximum a posteriori estimation criterion. For the time-varying noise, the above estimator is modified using an exponential weighted attenuation method to realize the oblivion of stale data which results in a fading memory estimator, which has the ability to estimate the time-varying noise statistic to revise the filter online. The simulation results indicate that the proposed filter can achieve higher accuracy than conventional filters with inaccurate noise statistic.

1. Introduction

Control accuracy is generally affected by the state feedback accuracy in a closed-loop control system. On account of the state feedback being easily contaminated by noise or being prevented from being measured directly, the optimal estimate of the state should be considered. The Kalman filter is a type of real-time signal processing method which adopts the state space method to model linear systems and achieve the minimum variance estimate of the state in the form of recursion [1] and has been widely used in control systems.

In practical applications, the actual systems generally contain nonlinear characteristics which are described by nonlinear models. Correspondingly, the system states are required to be estimated using the nonlinear Kalman filters of which the extended Kalman filter (EKF) has been most widely used over the past few decades [2, 3]. The EKF adopts the Taylor series expansion to obtain the linear approximation of the nonlinear systems, and then the standard Kalman filter is applied. However, the accuracy of EKF is unsatisfactory for strong nonlinear systems in which the linearity error of the model may seriously affect filtering accuracy and even lead to the filter divergence [4]. Moreover, the EKF requires

differentiation of the nonlinear system models where the Jacobian matrix needs to be calculated, which is computationally cumbersome in many applications [5].

Julier et al. [6] propose the unscented transformation (UT) based unscented Kalman filter (UKF), which has third-degree filtering accuracy [7, 8]. The UKF is a deterministic filter where a series of sigma points are selected according to the certain criteria and the a posteriori mean and covariance are approximated using nonlinear propagation of these sigma points [9]. The UKF is a derivative-free filter which has no restrictions on the system models. However, as the core of the UKF, UT has some tunable parameters, and the selection of which lacks a rigorous mathematical basis. As for high-dimensional systems, the weight on the center point is negative and the semidefinite of the covariance cannot be guaranteed, which may reduce the numerical stability of the system [10].

Arasaratnam et al. [11, 12] propose the cubature Kalman filter (CKF) based on the cubature rule (CR). By means of coordinate transformation, the intractable Gaussian weighted integral is decomposed into the spherical integral and radial integral, which are approximated using various numerical rules to deduce the CR. The CKF uses a set of cubature

points with equal weights to approximate the a posteriori mean and covariance and achieves higher stability than the UKF [13–15]. Furthermore, the CKF can be regarded as a special case of the UKF with $\kappa = 0$ [16, 17], whereas the CKF gives the reason for $\kappa = 0$ theoretically for the first time from another perspective. In the calculation framework of the CKF, Wang et al. [18] and Shovan and Swati [19, 20] modify the spherical integral and radial integral, respectively, and put forward the spherical simplex-radial cubature Kalman filter and the cubature quadrature Kalman filter, both of which have better performance compared with the CKF.

The prior noise statistic is required exactly for the above-mentioned filters. However, in practical applications, the system noise statistic is often unknown and varies as a function of time, so the estimate accuracy may be significantly reduced. In order to address the problem that the filtering accuracy of the conventional filters reduces in the case of inaccurate time-varying noise statistic, a noise statistic estimator based adaptive simplex cubature Kalman filter (ASCKF) is proposed in this paper. The spherical simplex rule and the first-order generalized Gauss-Laguerre quadrature rule are adopted to derive the simplex cubature rule, which is used to approximate the a posteriori mean and covariance in the nonlinear Kalman filter framework. The noise statistic estimator is designed based on the maximum a posteriori (MAP) estimation criterion [21], and the fading memory exponential weighted attenuation method is utilized to achieve the oblivion of stale data and emphasize the new data. This allows the online real-time estimation of the time-varying noise statistic. The designed noise statistic estimator is used to revise the filter and to improve the filtering accuracy with the inaccurate noise statistic. Simulation results have verified the validity of the proposed filter.

The rest of this paper is organized as follows: the simplex cubature Kalman filter is provided in Section 2. The noise statistic estimator is derived in Section 3. The simulation results and analysis are presented in Section 4. The conclusions are given in Section 5.

2. Simplex Cubature Kalman Filter

2.1. Simplex Cubature Rule. The key problem in nonlinear Kalman filter is to calculate the intractable nonlinear Gaussian weighted integral as $I_N = \int_{\mathbf{R}^n} \mathbf{g}(\mathbf{x})N(\mathbf{x}; \bar{\mathbf{x}}, \mathbf{P}_x) d\mathbf{x}$, where $\mathbf{x} \in \mathbf{R}^n$, $\mathbf{g}(\mathbf{x})$ represents the arbitrary nonlinear function, and $N(\mathbf{x}; \bar{\mathbf{x}}, \mathbf{P}_x)$ denotes the Gaussian distribution with mean $\bar{\mathbf{x}}$ and covariance \mathbf{P}_x . It is generally difficult to obtain the analytical solution of I_N ; hence the high accuracy numerical approximation method should be taken into account.

2.1.1. Spherical Simplex Rule for Spherical Integral. Specifically, the coordinate transformation for integral of the form $I_g = \int_{\mathbf{R}^n} \mathbf{g}(\mathbf{x})\exp(-\mathbf{x}^T \mathbf{x}) d\mathbf{x}$ is considered first [11]. Let $\mathbf{x} = r\mathbf{s}$, where $\mathbf{s} = (s_1, s_2, \dots, s_n)^T$ represents the direction vector such that $\mathbf{s}^T \mathbf{s} = 1$ with $r = \sqrt{\mathbf{x}^T \mathbf{x}} \geq 0$. Then I_g can be decomposed

into the following two types of integrals, namely, the spherical integral $S(r)$ and the radial integral R , respectively.

$$S(r) = \int_{U_n} \mathbf{g}(r\mathbf{s}) d\sigma(\mathbf{s}) \quad (1)$$

$$R = \int_0^\infty S(r) r^{n-1} \exp(-r^2) dr, \quad (2)$$

where $U_n = \{\mathbf{s} \in \mathbf{R}^n : s_1^2 + s_2^2 + \dots + s_n^2 = 1\}$ represents the spherical surface and $\sigma(\cdot)$ denotes the area element on U_n .

The third-degree spherical simplex rule [18], which consists of $2n+2$ points, is adopted to approximate the spherical integral $S(r)$ in (1) as follows.

$$S(r) \approx \frac{T_n}{2(n+1)} \sum_{i=1}^{n+1} [\mathbf{g}(r\mathbf{a}_i) + \mathbf{g}(-r\mathbf{a}_i)], \quad (3)$$

where $T_n = 2\sqrt{\pi^n}/\Gamma(n/2)$ is the surface area of unit sphere and $\Gamma(x) = \int_0^\infty \exp(-t)t^{x-1} dt$ denotes the Gamma function. The vectors $\mathbf{a}_i = (a_{i,1}, a_{i,2}, \dots, a_{i,n})^T$, $i = 1, 2, \dots, n+1$ are the vertices of the n -dimensional simplex, and the elements are defined as follows.

$$a_{i,j} = \begin{cases} -\sqrt{\frac{n+1}{n(n-j+2)(n-j+1)}}, & j < i \\ \sqrt{\frac{(n+1)(n-i+1)}{n(n-i+2)}}, & i = j \\ 0, & j > i. \end{cases} \quad (4)$$

2.1.2. Generalized Gauss-Laguerre Quadrature Rule for Radial Integral. As for the radial integral shown in (2), let $r = \sqrt{t}$ and $R = (1/2) \int_0^\infty S(\sqrt{t})t^{n/2-1} \exp(-t) dt$ is deduced. Further, R can be written in the form of $R = (1/2) \int_0^\infty \tilde{S}(t)t^\beta \exp(-t) dt$ by letting $\tilde{S}(t) = S(\sqrt{t})$ with $\beta = n/2 - 1$, and it is convenient to use the generalized Gauss-Laguerre quadrature rule [19] for approximation as follows.

$$\int_0^\infty \tilde{S}(t) t^\beta \exp(-t) dt \approx \sum_{i=1}^p \tilde{\omega}_i \tilde{S}(t_i), \quad (5)$$

where t_i and $\tilde{\omega}_i$ denote the quadrature points and the corresponding weights, respectively. p represents the number of the points. The points t_i can be obtained by solving the following m -order Chebyshev-Laguerre polynomial [20].

$$L_p^\beta(t) = (-1)^p t^{-\beta} \exp(t) \frac{d^p}{dt^p} (t^{\beta+p} \exp(-t)) = 0. \quad (6)$$

The weights $\tilde{\omega}_i$ are calculated using

$$\tilde{\omega}_i = \frac{p! \Gamma(\beta + p + 1)}{t_i [L_p^\beta(t_i)]^2}. \quad (7)$$

For the third-degree accuracy of the radial integral, p should be chosen 1, and $t_1 = n/2$ with $\tilde{\omega}_1 = \Gamma(n/2)$ are obtained; thus the radial integral turns to be the following form.

$$R \approx \frac{1}{2} \tilde{\omega}_1 \tilde{S}(t_1) = \frac{1}{2} \Gamma\left(\frac{n}{2}\right) S\left(\sqrt{\frac{n}{2}}\right). \quad (8)$$

2.1.3. *Simplex Cubature Rule.* The integral I_g is approximated by substituting (3) into (8) as follows.

$$I_g \approx \frac{\sqrt{\pi^n}}{2(n+1)} \sum_{i=1}^{n+1} \left[\mathbf{g} \left(\sqrt{\frac{n}{2}} \mathbf{a}_i \right) + \mathbf{g} \left(-\sqrt{\frac{n}{2}} \mathbf{a}_i \right) \right]. \quad (9)$$

I_N has the following equivalent form:

$$I_N = \frac{1}{\sqrt{\pi^n}} \int_{\mathbf{R}^n} \mathbf{g} \left(\sqrt{2\mathbf{P}_x} \mathbf{x} + \hat{\mathbf{x}} \right) \exp(-\mathbf{x}^T \mathbf{x}) d\mathbf{x}. \quad (10)$$

The simplex cubature rule, which is used to approximate the nonlinear Gaussian weighted integral, is derived by combining (9) and (10) as follows.

$$\begin{aligned} I_N & \approx \frac{1}{2(n+1)} \sum_{i=1}^{n+1} \left[\mathbf{g} \left(\hat{\mathbf{x}} + \sqrt{n\mathbf{P}_x} \mathbf{a}_i \right) + \mathbf{g} \left(\hat{\mathbf{x}} - \sqrt{n\mathbf{P}_x} \mathbf{a}_i \right) \right] \\ & = \sum_{i=1}^{2n+2} \omega_i \mathbf{g} \left(\hat{\mathbf{x}}^{(i)} \right), \end{aligned} \quad (11)$$

where the cubature points $\hat{\mathbf{x}}^{(i)}$ and the weights ω_i are given as follows:

$$\hat{\mathbf{x}}^{(i)} = \hat{\mathbf{x}} + \sqrt{n\mathbf{P}_x} [\mathbf{a}_i, -\mathbf{a}_i], \quad i = 1, 2, \dots, 2n+2 \quad (12)$$

$$\omega_i = \frac{1}{2(n+1)}, \quad i = 1, 2, \dots, 2n+2, \quad (13)$$

where $\mathbf{a} = [\mathbf{a}_1, \mathbf{a}_2, \dots, \mathbf{a}_{n+1}]$ and the matrix subscript $[\cdot]_i$ represents the i th column.

2.2. *The Simplex Cubature Kalman Filter.* The following discrete-time nonlinear system is taken into account.

$$\mathbf{x}_k = \mathbf{f}(\mathbf{x}_{k-1}) + \mathbf{w}_k \quad (14)$$

$$\mathbf{z}_k = \mathbf{h}(\mathbf{x}_k) + \mathbf{v}_k,$$

where $\mathbf{x}_k \in \mathbf{R}^n$ and $\mathbf{z}_k \in \mathbf{R}^q$ denote the state and measurement vectors, respectively, and \mathbf{w}_k and \mathbf{v}_k represent the white Gaussian process noise and measurement noise, respectively, with the mean being \mathbf{q}_k and \mathbf{r}_k , respectively, and the covariance being \mathbf{Q}_k and \mathbf{R}_k , respectively.

In the nonlinear Kalman filter framework, the a posteriori mean and covariance are calculated using the simplex cubature rule given in (11), and the simplex cubature Kalman filter (SCKF) is derived as follows.

The a posteriori state estimate $\hat{\mathbf{x}}_{k-1}^+$ and covariance \mathbf{P}_{k-1}^+ at time $k-1$ are used instead of $\hat{\mathbf{x}}$ and \mathbf{P}_x in (12) to calculate the cubature points $\hat{\mathbf{x}}_{k-1}^{(i)}$, which are propagated using the nonlinear function $\mathbf{f}(\cdot)$ to obtain the following points $\mathbf{X}_k^{(i)}$.

$$\mathbf{X}_k^{(i)} = \mathbf{f} \left(\hat{\mathbf{x}}_{k-1}^{(i)} \right) + \mathbf{q}_{k-1}. \quad (15)$$

The prior state estimate $\hat{\mathbf{x}}_k^-$ at time k is calculated using the propagated points $\mathbf{X}_k^{(i)}$ as follows.

$$\hat{\mathbf{x}}_k^- = \sum_{i=1}^{2n+2} \omega_i \mathbf{X}_k^{(i)}, \quad (16)$$

where ω_i is given in (13).

The prior error covariance \mathbf{P}_k^- at time k is calculated as follows.

$$\mathbf{P}_k^- = \sum_{i=1}^{2n+2} \omega_i \left(\mathbf{X}_k^{(i)} - \hat{\mathbf{x}}_k^- \right) \left(\mathbf{X}_k^{(i)} - \hat{\mathbf{x}}_k^- \right)^T + \mathbf{Q}_{k-1}. \quad (17)$$

The prior state estimate $\hat{\mathbf{x}}_k^-$ and covariance \mathbf{P}_k^- at time k are used instead of $\hat{\mathbf{x}}$ and \mathbf{P}_x in (12) to calculate the cubature points $\hat{\mathbf{x}}_k^{(i)}$, which are propagated using the nonlinear function $\mathbf{h}(\cdot)$ to obtain the following points $\mathbf{Z}_k^{(i)}$.

$$\mathbf{Z}_k^{(i)} = \mathbf{h} \left(\hat{\mathbf{x}}_k^{(i)} \right) + \mathbf{r}_k. \quad (18)$$

The predicted measurement $\hat{\mathbf{z}}_k$ is calculated using the propagated points $\mathbf{Z}_k^{(i)}$ as follows.

$$\hat{\mathbf{z}}_k = \sum_{i=1}^{2n+2} \omega_i \mathbf{Z}_k^{(i)}. \quad (19)$$

The measurement covariance $\mathbf{P}_{z,k}$ is calculated as follows.

$$\mathbf{P}_{z,k} = \sum_{i=1}^{2n+2} \omega_i \left(\mathbf{Z}_k^{(i)} - \hat{\mathbf{z}}_k \right) \left(\mathbf{Z}_k^{(i)} - \hat{\mathbf{z}}_k \right)^T + \mathbf{R}_k. \quad (20)$$

The cross covariance $\mathbf{P}_{xz,k}$ is calculated as follows.

$$\mathbf{P}_{xz,k} = \sum_{i=1}^{2n+2} \omega_i \left(\hat{\mathbf{x}}_k^{(i)} - \hat{\mathbf{x}}_k^- \right) \left(\mathbf{Z}_k^{(i)} - \hat{\mathbf{z}}_k \right)^T. \quad (21)$$

The Kalman filter gain \mathbf{K}_k is calculated as follows.

$$\mathbf{K}_k = \mathbf{P}_{xz,k} \mathbf{P}_{z,k}^{-1}. \quad (22)$$

The a posteriori state estimate $\hat{\mathbf{x}}_k^+$ at time k is calculated as follows.

$$\hat{\mathbf{x}}_k^+ = \hat{\mathbf{x}}_k^- + \mathbf{K}_k \left(\mathbf{z}_k - \hat{\mathbf{z}}_k \right). \quad (23)$$

The a posteriori error covariance \mathbf{P}_k^+ is calculated as follows.

$$\mathbf{P}_k^+ = \mathbf{P}_k^- - \mathbf{K}_k \mathbf{P}_{z,k} \mathbf{K}_k^T. \quad (24)$$

It can be seen from (15), (17), (18), and (20) that the exact noise statistics are required in SCKF, and the filtering accuracy may reduce if the inaccurate noise statistics are substituted.

3. Noise Statistic Estimator

In this section, two noise statistic estimators, including the constant noise statistic estimator and the time-varying noise statistic estimator, are given to realize the online estimation of the noise statistic.

3.1. *Constant Noise Statistic Estimator.* The MAP estimates of \mathbf{q} , \mathbf{Q} , \mathbf{r} , \mathbf{R} , and \mathbf{X}_k can be obtained by calculating the maximum value of the following conditional probability density function [21].

$$\tilde{L} = p(\mathbf{X}_k, \mathbf{q}, \mathbf{Q}, \mathbf{r}, \mathbf{R} | \mathbf{Z}_k), \quad (25)$$

where $\mathbf{X}_k = (\mathbf{x}_0, \mathbf{x}_1, \dots, \mathbf{x}_k)$ and $\mathbf{Z}_k = (\mathbf{z}_1, \mathbf{z}_2, \dots, \mathbf{z}_k)$.

According to the property of the conditional probability function, (25) has the equivalent form as $\tilde{L} = p(\mathbf{X}_k, \mathbf{q}, \mathbf{Q}, \mathbf{r}, \mathbf{R}, \mathbf{Z}_k) / p(\mathbf{Z}_k)$, and the problem is transformed into calculating the maximum value of the following equation on account of $p(\mathbf{Z}_k)$ being independent of the optimization.

$$L = p(\mathbf{X}_k, \mathbf{q}, \mathbf{Q}, \mathbf{r}, \mathbf{R}, \mathbf{Z}_k) = p(\mathbf{Z}_k | \mathbf{X}_k, \mathbf{q}, \mathbf{Q}, \mathbf{r}, \mathbf{R}) \cdot p(\mathbf{X}_k | \mathbf{q}, \mathbf{Q}, \mathbf{r}, \mathbf{R}) p(\mathbf{q}, \mathbf{Q}, \mathbf{r}, \mathbf{R}), \quad (26)$$

where $p(\mathbf{q}, \mathbf{Q}, \mathbf{r}, \mathbf{R})$ can be regarded as a constant since it is obtained using the prior information.

The terms $p(\mathbf{X}_k | \mathbf{q}, \mathbf{Q}, \mathbf{r}, \mathbf{R})$ and $p(\mathbf{Z}_k | \mathbf{X}_k, \mathbf{q}, \mathbf{Q}, \mathbf{r}, \mathbf{R})$ in (26) can be calculated using the multiplicative theorem of conditional probability as follows.

$$\begin{aligned} p(\mathbf{X}_k | \mathbf{q}, \mathbf{Q}, \mathbf{r}, \mathbf{R}) &= p(\mathbf{x}_0) \prod_{j=1}^k p(\mathbf{x}_j | \mathbf{x}_{j-1}, \mathbf{q}, \mathbf{Q}) \\ &= M_1 |\mathbf{P}_0|^{-1/2} \cdot |\mathbf{Q}|^{-k/2} \exp \left\{ -\frac{1}{2} \left[\|\mathbf{x}_0 - \hat{\mathbf{x}}_0^+\|_{\mathbf{P}_0^+}^2 \right. \right. \\ &\quad \left. \left. + \sum_{j=1}^k \|\mathbf{x}_j - \mathbf{f}(\mathbf{x}_{j-1}) - \mathbf{q}\|_{\mathbf{Q}^{-1}}^2 \right] \right\}, \end{aligned} \quad (27)$$

where $M_1 = 1/(2\pi)^{n(k+1)/2}$ represents a constant, $|\cdot|$ denotes the determinant, and $\|\mathbf{u}\|_{\mathbf{A}}^2 = \mathbf{u}^T \mathbf{A} \mathbf{u}$ is the quadratic.

$$\begin{aligned} p(\mathbf{Z}_k | \mathbf{X}_k, \mathbf{q}, \mathbf{Q}, \mathbf{r}, \mathbf{R}) &= \prod_{j=1}^k p(\mathbf{z}_j | \mathbf{x}_j, \mathbf{r}, \mathbf{R}) \\ &= M_2 |\mathbf{R}|^{-k/2} \exp \left[-\frac{1}{2} \sum_{j=1}^k \|\mathbf{z}_j - \mathbf{h}(\mathbf{x}_j) - \mathbf{r}\|_{\mathbf{R}^{-1}}^2 \right], \end{aligned} \quad (28)$$

where $M_2 = 1/(2\pi)^{qk/2}$ denotes a constant.

Then, by substituting (27) and (28) into (26), we have

$$\begin{aligned} L &= \mathbf{M} |\mathbf{Q}|^{-k/2} \cdot |\mathbf{R}|^{-k/2} \\ &\quad \cdot \exp \left\{ -\frac{1}{2} \left[\sum_{j=1}^k \|\mathbf{x}_j - \mathbf{f}(\mathbf{x}_{j-1}) - \mathbf{q}\|_{\mathbf{Q}^{-1}}^2 \right. \right. \\ &\quad \left. \left. + \sum_{j=1}^k \|\mathbf{z}_j - \mathbf{h}(\mathbf{x}_j) - \mathbf{r}\|_{\mathbf{R}^{-1}}^2 \right] \right\}, \end{aligned} \quad (29)$$

where $\mathbf{M} = M_1 M_2 |\mathbf{P}_0|^{-1/2} p(\mathbf{q}, \mathbf{Q}, \mathbf{r}, \mathbf{R}) \exp(-(1/2)\|\mathbf{x}_0 - \hat{\mathbf{x}}_0^+\|_{\mathbf{P}_0^+}^2)$, and taking the logarithm of (29), we obtain that

$$\begin{aligned} \ln L &= -\frac{k}{2} \ln |\mathbf{Q}| - \frac{k}{2} \ln |\mathbf{R}| \\ &\quad - \frac{1}{2} \sum_{j=1}^k \|\mathbf{x}_j - \mathbf{f}(\mathbf{x}_{j-1}) - \mathbf{q}\|_{\mathbf{Q}^{-1}}^2 \\ &\quad - \frac{1}{2} \sum_{j=1}^k \|\mathbf{z}_j - \mathbf{h}(\mathbf{x}_j) - \mathbf{r}\|_{\mathbf{R}^{-1}}^2 + \ln \mathbf{M}. \end{aligned} \quad (30)$$

Note that (29) and (30) share the same extreme points; the following partial differentials are taken.

$$\begin{aligned} \frac{\partial \ln L}{\partial \mathbf{q}} \Big|_{\mathbf{q}=\hat{\mathbf{q}}_k}^{\mathbf{x}_{j-1}=\hat{\mathbf{x}}_{j-1}^+, \mathbf{x}_j=\hat{\mathbf{x}}_{j|k}^+} &= 0 \\ \frac{\partial \ln L}{\partial \mathbf{Q}} \Big|_{\mathbf{Q}=\hat{\mathbf{Q}}_k}^{\mathbf{x}_{j-1}=\hat{\mathbf{x}}_{j-1}^+, \mathbf{x}_j=\hat{\mathbf{x}}_{j|k}^+} &= 0 \\ \frac{\partial \ln L}{\partial \mathbf{r}} \Big|_{\mathbf{r}=\hat{\mathbf{r}}_k}^{\mathbf{x}_j=\hat{\mathbf{x}}_{j|k}^+} &= 0 \\ \frac{\partial \ln L}{\partial \mathbf{R}} \Big|_{\mathbf{R}=\hat{\mathbf{R}}_k}^{\mathbf{x}_j=\hat{\mathbf{x}}_{j|k}^+} &= 0, \end{aligned} \quad (31)$$

where $\hat{\mathbf{x}}_{j-1|k}^+$ and $\hat{\mathbf{x}}_{j|k}^+$ represent the smooth values, which are replaced by the filtering estimates $\hat{\mathbf{x}}_{j-1}^+$ and $\hat{\mathbf{x}}_j^+$, or predicted estimate $\hat{\mathbf{x}}_j^-$, and the suboptimal MAP noise statistic estimator is deduced in a recursive form as follows.

$$\begin{aligned} \hat{\mathbf{q}}_k &= \frac{1}{k} \left[(k-1) \hat{\mathbf{q}}_{k-1} + \hat{\mathbf{x}}_k^+ - \sum_{i=1}^{2n+2} \omega_i \mathbf{f}(\hat{\mathbf{x}}_{k-1}^{(i)}) \right] \\ \hat{\mathbf{Q}}_k &= \frac{1}{k} \left[(k-1) \hat{\mathbf{Q}}_{k-1} + \mathbf{K}_k \mathbf{e}_k \mathbf{e}_k^T \mathbf{K}_k^T + \mathbf{P}_k^+ \right. \\ &\quad \left. - \sum_{i=1}^{2n+2} \omega_i (\mathbf{X}_k^{(i)} - \hat{\mathbf{x}}_k^-) (\mathbf{X}_k^{(i)} - \hat{\mathbf{x}}_k^-)^T \right] \\ \hat{\mathbf{r}}_k &= \frac{1}{k} \left[(k-1) \hat{\mathbf{r}}_{k-1} + \mathbf{z}_k - \sum_{i=1}^{2n+2} \omega_i \mathbf{h}(\hat{\mathbf{x}}_k^{(i)}) \right] \\ \hat{\mathbf{R}}_k &= \frac{1}{k} \left[(k-1) \hat{\mathbf{R}}_{k-1} + \mathbf{e}_k \mathbf{e}_k^T \right. \\ &\quad \left. - \sum_{i=1}^{2n+2} \omega_i (\mathbf{Z}_k^{(i)} - \hat{\mathbf{z}}_k) (\mathbf{Z}_k^{(i)} - \hat{\mathbf{z}}_k)^T \right], \end{aligned} \quad (32)$$

where $\mathbf{e}_k = \mathbf{z}_k - \hat{\mathbf{z}}_k$ is the filtering residual.

3.2. *Time-Varying Noise Statistic Estimator.* For the time-varying noise statistic, we should emphasize the effect of new data and gradually forget the effect of the stale data, so as to

achieve the online real-time estimation of the time-varying noise statistic. For this, the fading memory exponential weighted attenuation method is considered. The weighting factor μ_i is selected such that $\mu_i = \mu_{i-1}\gamma$, $\sum_{i=1}^k \mu_i = 1$, where $0 < \gamma < 1$ denotes the forgetting factor, and then we have

$$\begin{aligned}\mu_i &= \rho_k \gamma^{i-1} \\ \rho_k &= \frac{1 - \gamma}{1 - \gamma^k}.\end{aligned}\quad (33)$$

Each term in (32) is multiplied by μ_{k+1-j} to replace the original factor $1/k$, and the fading memory time-varying noise statistic estimator is derived as follows.

$$\begin{aligned}\hat{\mathbf{q}}_k &= (1 - \rho_k) \hat{\mathbf{q}}_{k-1} + \rho_k \left[\hat{\mathbf{x}}_k^+ - \sum_{i=1}^{2n+2} \omega_i \mathbf{f}(\hat{\mathbf{x}}_{k-1}^{(i)}) \right] \\ \hat{\mathbf{Q}}_k &= (1 - \rho_k) \hat{\mathbf{Q}}_{k-1} + \rho_k \left[\mathbf{K}_k \mathbf{e}_k \mathbf{e}_k^T \mathbf{K}_k^T + \mathbf{P}_k^+ \right. \\ &\quad \left. - \sum_{i=1}^{2n+2} \omega_i (\mathbf{X}_k^{(i)} - \hat{\mathbf{x}}_k^-) (\mathbf{X}_k^{(i)} - \hat{\mathbf{x}}_k^-)^T \right]\end{aligned}$$

$$\hat{\mathbf{q}}_k = (1 - \rho_k) \hat{\mathbf{q}}_{k-1} + \rho_k \left[\hat{\mathbf{x}}_k^+ - \sum_{i=1}^{2n+2} \omega_i \mathbf{f}(\hat{\mathbf{x}}_{k-1}^{(i)}) \right]$$

$$\hat{\mathbf{Q}}_k = \begin{cases} (1 - \rho_k) \hat{\mathbf{Q}}_{k-1} + \rho_k \left[\mathbf{K}_k \mathbf{e}_k \mathbf{e}_k^T \mathbf{K}_k^T + \mathbf{P}_k^+ - \sum_{i=1}^{2n+2} \omega_i (\mathbf{X}_k^{(i)} - \hat{\mathbf{x}}_k^-) (\mathbf{X}_k^{(i)} - \hat{\mathbf{x}}_k^-)^T \right], & \text{positive semi-definite} \\ (1 - \rho_k) \hat{\mathbf{Q}}_{k-1} + \rho_k \mathbf{K}_k \mathbf{e}_k \mathbf{e}_k^T \mathbf{K}_k^T, & \text{negative definite} \end{cases}\quad (36)$$

$$\hat{\mathbf{r}}_k = (1 - \rho_k) \hat{\mathbf{r}}_{k-1} + \rho_k \left[\mathbf{z}_k - \sum_{i=1}^{2n+2} \omega_i \mathbf{h}(\hat{\mathbf{x}}_k^{(i)}) \right]$$

$$\hat{\mathbf{R}}_k = \begin{cases} (1 - \rho_k) \hat{\mathbf{R}}_{k-1} + \rho_k \left[\mathbf{e}_k \mathbf{e}_k^T - \sum_{i=1}^{2n+2} \omega_i (\mathbf{Z}_k^{(i)} - \hat{\mathbf{z}}_k) (\mathbf{Z}_k^{(i)} - \hat{\mathbf{z}}_k)^T \right], & \text{positive definite} \\ (1 - \rho_k) \hat{\mathbf{R}}_{k-1} + \rho_k \mathbf{e}_k \mathbf{e}_k^T, & \text{nonpositive definite.} \end{cases}$$

The above derived time-varying noise statistic estimator is used in the SCKF to carry out the online estimation of the unknown noise and results in the ASCKF, whose specific calculation steps are given below.

Step 1 (filter initialization). One has the initial values $\hat{\mathbf{x}}_0^+$, \mathbf{P}_0^+ , $\hat{\mathbf{q}}_0$, $\hat{\mathbf{Q}}_0$, $\hat{\mathbf{r}}_0$, $\hat{\mathbf{R}}_0$.

Cycle $k = 1, 2, \dots$, and complete the following steps.

Step 2 (time update). The cubature points $\hat{\mathbf{x}}_{k-1}^{(i)}$ are calculated as SCKF in Section 2.2, and the noise estimator $\hat{\mathbf{q}}_{k-1}$ is used instead of \mathbf{q}_{k-1} to obtain the propagated points $\mathbf{X}_k^{(i)}$ as follows.

$$\mathbf{X}_k^{(i)} = \mathbf{f}(\hat{\mathbf{x}}_{k-1}^{(i)}) + \hat{\mathbf{q}}_{k-1}.\quad (37)$$

$$\hat{\mathbf{r}}_k = (1 - \rho_k) \hat{\mathbf{r}}_{k-1} + \rho_k \left[\mathbf{z}_k - \sum_{i=1}^{2n+2} \omega_i \mathbf{h}(\hat{\mathbf{x}}_k^{(i)}) \right]$$

$$\hat{\mathbf{R}}_k = (1 - \rho_k) \hat{\mathbf{R}}_{k-1} + \rho_k \left[\mathbf{e}_k \mathbf{e}_k^T - \sum_{i=1}^{2n+2} \omega_i (\mathbf{Z}_k^{(i)} - \hat{\mathbf{z}}_k) (\mathbf{Z}_k^{(i)} - \hat{\mathbf{z}}_k)^T \right].\quad (34)$$

However, for the high-dimensional systems, $\hat{\mathbf{Q}}_k$ and $\hat{\mathbf{R}}_k$ may dissatisfy the semipositive definite and positive definite conditions, respectively, and result in the filter divergence. To solve this problem, the following modified noise statistic estimator can be used instead to ensure positivity all through the process of recursion.

$$\begin{aligned}\hat{\mathbf{Q}}_k &= (1 - \rho_k) \hat{\mathbf{Q}}_{k-1} + \rho_k \mathbf{K}_k \mathbf{e}_k \mathbf{e}_k^T \mathbf{K}_k^T \\ \hat{\mathbf{R}}_k &= (1 - \rho_k) \hat{\mathbf{R}}_{k-1} + \rho_k \mathbf{e}_k \mathbf{e}_k^T.\end{aligned}\quad (35)$$

From the above, the time-varying noise statistic estimator, which is suitable for nonlinear filter, is summarized in the recursive form as follows.

The prior state estimate $\hat{\mathbf{x}}_k^-$ at time k is calculated as (16). The prior error covariance \mathbf{P}_k^- at time k is calculated using the noise estimator $\hat{\mathbf{Q}}_{k-1}$ as follows.

$$\mathbf{P}_k^- = \sum_{i=1}^{2n+2} \omega_i (\mathbf{X}_k^{(i)} - \hat{\mathbf{x}}_k^-) (\mathbf{X}_k^{(i)} - \hat{\mathbf{x}}_k^-)^T + \hat{\mathbf{Q}}_{k-1}.\quad (38)$$

Step 3 (measurement update). The cubature points $\hat{\mathbf{x}}_k^{(i)}$ are calculated as SCKF in Section 2.2, and the noise estimator $\hat{\mathbf{r}}_k$ is used instead of \mathbf{r}_k to obtain the propagated points $\mathbf{Z}_k^{(i)}$ as follows.

$$\mathbf{Z}_k^{(i)} = \mathbf{h}(\hat{\mathbf{x}}_k^{(i)}) + \hat{\mathbf{r}}_k.\quad (39)$$

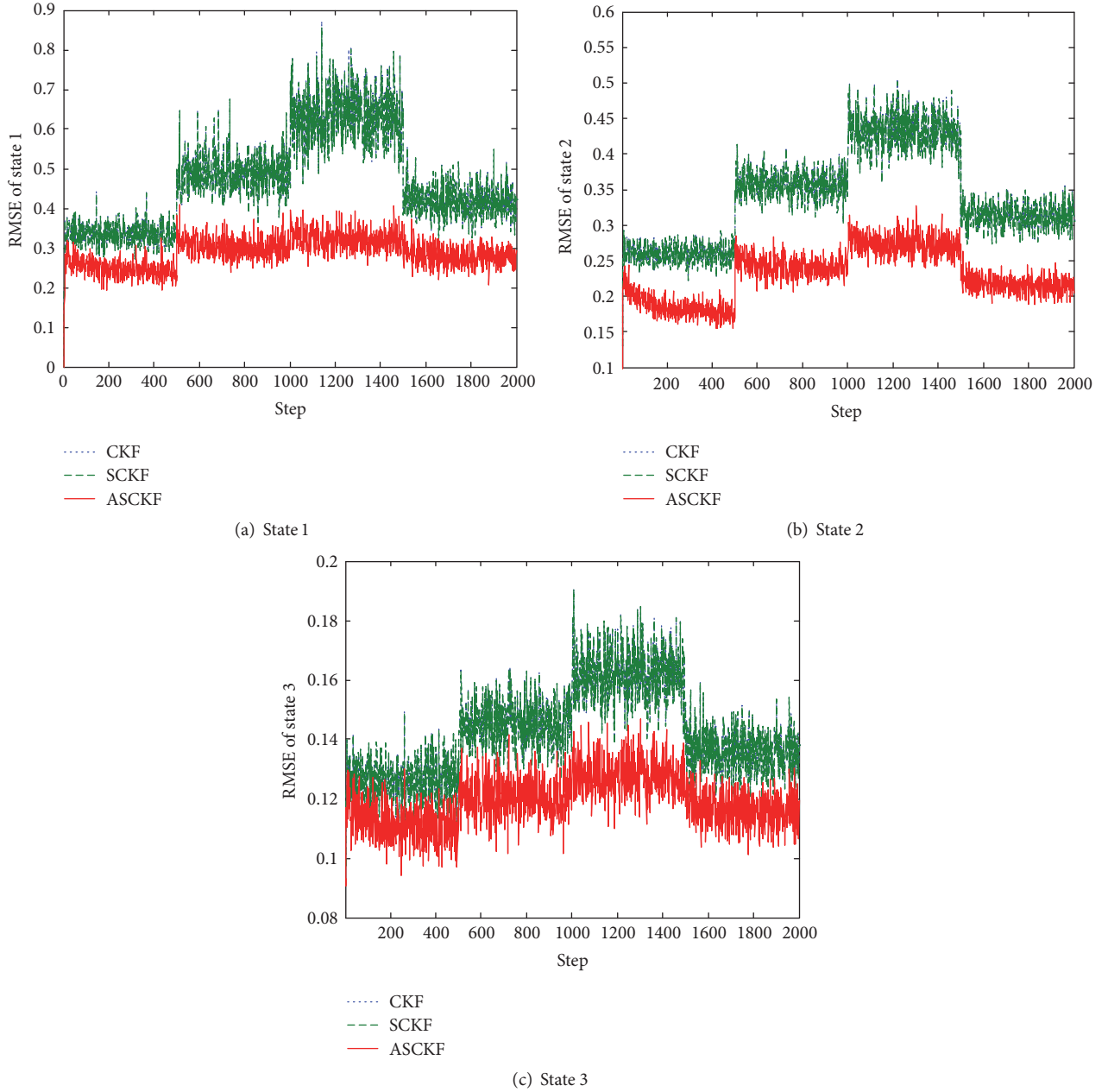


FIGURE 1: RMSEs of the three filters.

The predicted measurement \hat{z}_k is calculated as (19).

The measurement covariance $\mathbf{P}_{z,k}$ is calculated using the noise estimator $\hat{\mathbf{R}}_k$ as follows.

$$\mathbf{P}_{z,k} = \sum_{i=1}^{2n+2} \omega_i (\mathbf{Z}_k^{(i)} - \hat{\mathbf{z}}_k) (\mathbf{Z}_k^{(i)} - \hat{\mathbf{z}}_k)^T + \hat{\mathbf{R}}_k. \quad (40)$$

The cross covariance $\mathbf{P}_{xz,k}$, the Kalman filter gain \mathbf{K}_k , the a posteriori state estimate $\hat{\mathbf{x}}_k^+$, and the a posteriori error covariance \mathbf{P}_k^+ are calculated as (21) to (24), respectively.

Step 4 (noise statistic estimator update). The noise statistic estimator is updated using (36).

On account of the recursion equations of noise statistic estimator being not independent, the noise \mathbf{w}_k and \mathbf{v}_k cannot

be estimated at the same time in general; otherwise it may cause the filtering divergence.

4. Simulation Results

In this section, a three-dimensional nonlinear system is taken into account to test the performance of the proposed filter. The nonlinear system model is given as follows.

$$\begin{bmatrix} x_{1,k+1} \\ x_{2,k+1} \\ x_{3,k+1} \end{bmatrix} = \begin{bmatrix} 3 \cos(x_{2,k}) \\ x_{1,k} x_{3,k} \\ 0.1 x_{1,k} (x_{2,k} + x_{3,k}) \end{bmatrix} + \mathbf{w}_k \quad (41)$$

$$z_k = x_{1,k} x_{2,k} + x_{3,k} + v_k,$$

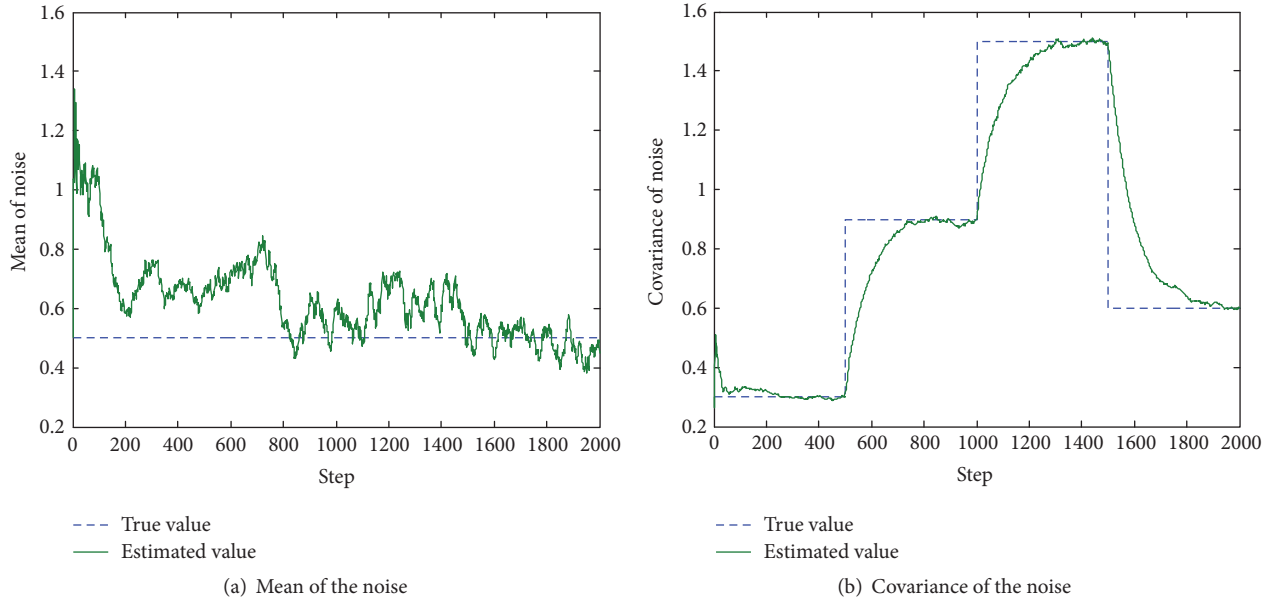


FIGURE 2: The true noise statistic and the estimated one.

where $\mathbf{x}_k = (x_{1,k}, x_{2,k}, x_{3,k})^T$ denotes the system state, \mathbf{w}_k represents the process noise with the mean and covariance being zero and \mathbf{Q}_k , respectively, and v_k is the measurement noise with the mean and covariance being r_k and R_k , respectively.

In this simulation, the true initial state and covariance are set to be $\mathbf{x}_0 = (0.2, 0.5, 0.2)^T$ and $\mathbf{Q}_k = 0.01\mathbf{I}_3$, respectively. The true values of the noise, including the mean and the time-varying covariance, are set to be $r_k = 0.5$ and R_k given below.

$$R_k = \begin{cases} 0.3, & 0 < k \leq 500 \\ 0.9, & 500 < k \leq 1000 \\ 1.5, & 1000 < k \leq 1500 \\ 0.6, & 1500 < k \leq 2000. \end{cases} \quad (42)$$

However, the true values of the noise are supposed to be unknown in application, so that the mean and the covariance of the noise used in the filters are chosen to be 0 and 0.1, respectively, which are inaccurate. The initial state and covariance of the filter are $\hat{\mathbf{x}}_0^+ = (0.2, 0.5, 0.2)^T$ and $\mathbf{P}_0^+ = 0.01\mathbf{I}_3$, respectively. The initial values of the noise statistic estimator are chosen to be $\hat{r}_0 = 0$ and $\hat{R}_0 = 0.1$, respectively. The forgetting factor, $\gamma = 0.99$, and the total steps are set to be 2000.

The proposed ASCKF is compared with the CKF and SCKF, and the estimation accuracy is evaluated using the root mean square error (RMSE), which is defined below.

$$\text{RMSE}_k = \sqrt{\frac{1}{M} \sum_{i=1}^M (x_k^i - \hat{x}_k^i)^2}, \quad k = 1, 2, \dots, 2000, \quad (43)$$

where M is the Monte Carlo run times and x_k^i and \hat{x}_k^i represent the true state and the estimated state in the i th run, respectively.

TABLE 1: Mean RMSEs of the three filters.

Filters	State 1	State 2	State 3
CKF	0.4693	0.3410	0.1423
SCKF	0.4677	0.3404	0.1421
ASCKF	0.2874	0.2294	0.1191

The simulation results based on 200 Monte Carlo runs are shown in Figures 1 and 2. It can be seen from Figure 1 that the RMSEs obtained by the ASCKF are significantly smaller than those of the other two filters, indicating that the proposed ASCKF can achieve higher estimation accuracy compared with CKF and SCKF. The reason is that the mean and time-varying covariance of the noise can be estimated online effectively to revise the filter by the noise statistic estimator in ASCKF, as shown in Figure 2. However, CKF and SCKF have no ability to revise the inaccurate noise.

The mean RMSEs of the three filters are listed in Table 1. It can be seen from the table that the three states of ASCKF are improved by 38.55%, 32.61%, and 16.19%, respectively, compared with the SCKF, thus verifying the validity of the proposed filter.

5. Conclusion

In this paper, a noise statistic estimator based adaptive simplex cubature Kalman filter is proposed to address the problem that the filtering accuracy reduces in the case of inaccurate time-varying noise statistic. The nonlinear Gaussian weighted integral in the filter is approximated using the simplex cubature rule, and the time-varying noise statistic estimator is designed based on the maximum a posteriori estimation criterion and the fading memory exponential weighted attenuation method. The simulation results show

that the proposed ASCKF has achieved better performance compared with the CKF and the SCKF in the case of inaccurate time-varying noise statistic, and the validity of the proposed filter has been verified.

Conflicts of Interest

The authors declare that they have no conflicts of interest.

Acknowledgments

This work is supported partly by the National High Technology Research and Development Program of China (2015AA7026085).

References

- [1] S. M. Persson and I. Sharf, "Invariant trapezoidal Kalman filter for application to attitude estimation," *Journal of Guidance, Control, and Dynamics*, vol. 36, no. 3, pp. 721–733, 2013.
- [2] K. Reif, S. Gunther, E. Yaz, and R. Unbehauen, "Stochastic stability of the discrete-time extended Kalman filter," *Institute of Electrical and Electronics Engineers Transactions on Automatic Control*, vol. 44, no. 4, pp. 714–728, 1999.
- [3] N. Filipe, M. Kontitsis, and P. Tsiotras, "Extended Kalman filter for spacecraft pose estimation using dual quaternions," *Journal of Guidance, Control, and Dynamics*, vol. 38, no. 9, pp. 1625–1641, 2015.
- [4] L. Jia-qiang, Z. Rong-hua, C. Jin-li, Z. Chun-yan, and Z. Yan-ping, "Target tracking algorithm based on adaptive strong tracking particle filter," *IET Science, Measurement & Technology*, vol. 10, no. 7, pp. 704–710, 2016.
- [5] H. Wang, J. Xu, A. Zhang, C. Li, and H. Yao, "Support vector regression-based adaptive divided difference filter for nonlinear state estimation problems," *Journal of Applied Mathematics*, vol. 2014, Article ID 139503, 10 pages, 2014.
- [6] S. Julier, J. Uhlmann, and H. F. Durrant-Whyte, "A new method for the nonlinear transformation of means and covariances in filters and estimators," *Institute of Electrical and Electronics Engineers Transactions on Automatic Control*, vol. 45, no. 3, pp. 477–482, 2000.
- [7] H. M. Menegaz, J. Y. Ishihara, G. A. Borges, and A. N. Vargas, "A systematization of the unscented Kalman filter theory," *Institute of Electrical and Electronics Engineers Transactions on Automatic Control*, vol. 60, no. 10, pp. 2583–2598, 2015.
- [8] K. Xiong, H. Y. Zhang, and C. W. Chan, "Performance evaluation of UKF-based nonlinear filtering," *Automatica*, vol. 42, no. 2, pp. 261–270, 2006.
- [9] K.-M. Roh, S.-Y. Park, and K.-H. Choi, "Orbit determination using the geomagnetic field measurement via the unscented kalman filter," *Journal of Spacecraft and Rockets*, vol. 44, no. 1, pp. 246–253, 2007.
- [10] J. Zarei and E. Shokri, "Convergence analysis of non-linear filtering based on cubature Kalman filter," *IET Science, Measurement & Technology*, vol. 9, no. 3, pp. 294–305, 2015.
- [11] I. Arasaratnam and S. Haykin, "Cubature Kalman filters," *Institute of Electrical and Electronics Engineers Transactions on Automatic Control*, vol. 54, no. 6, pp. 1254–1269, 2009.
- [12] I. Arasaratnam, S. Haykin, and T. R. Hurd, "Cubature Kalman filtering for continuous-discrete systems: theory and simulations," *IEEE Transactions on Signal Processing*, vol. 58, no. 10, pp. 4977–4993, 2010.
- [13] J. Chen, N. Wang, L. Ma, and B. Xu, "Extended target probability hypothesis density filter based on cubature Kalman filter," *IET Radar, Sonar & Navigation*, vol. 9, no. 3, pp. 324–332, 2015.
- [14] L. Zhang, H. Yang, H. Lu, S. Zhang, H. Cai, and S. Qian, "Cubature Kalman filtering for relative spacecraft attitude and position estimation," *Acta Astronautica*, vol. 105, no. 1, pp. 254–264, 2014.
- [15] B. Xu, Y. P. Xiao, W. Gao, Y. G. Zhang, Y. L. Liu, and Y. Liu, "Dual-model reverse CKF algorithm in cooperative navigation for USV," *Mathematical Problems in Engineering*, vol. 2014, Article ID 186785, 17 pages, 2014.
- [16] K. P. B. Chandra, D.-W. Gu, and I. Postlethwaite, "Square root cubature information filter," *IEEE Sensors Journal*, vol. 13, no. 2, pp. 750–758, 2013.
- [17] L. Chang, B. Hu, A. Li, and F. Qin, "Transformed unscented Kalman filter," *Institute of Electrical and Electronics Engineers Transactions on Automatic Control*, vol. 58, no. 1, pp. 252–257, 2013.
- [18] S. Wang, J. Feng, and C. K. Tse, "Spherical simplex-radial cubature Kalman filter," *IEEE Signal Processing Letters*, vol. 21, no. 1, pp. 43–46, 2014.
- [19] B. Shovan and Swati, "Cubature quadrature Kalman filter," *IET Signal Processing*, vol. 7, no. 7, pp. 533–541, 2013.
- [20] B. Shovan and Swati, "Square-root cubature-quadrature Kalman filter," *Asian Journal of Control*, vol. 16, no. 2, pp. 617–622, 2014.
- [21] L. Zhao, *Nonlinear System Filtering Theory*, National Defense Industry Press, Beijing, China, 2012.